technische universität
dortmund

Dissertation zur Erlangung des akademischen Grades
Doktor der Naturwissenschaften

Semiconductor Detectors and their Applications: From High-Energy Physics Experiments to Proton Therapy

vorgelegt von
Valerie Vanessa Knodel
geboren in Unna

- Dezember 2024 -

AG Kröninger
Fakultät Physik
Technische Universität Dortmund

Diese Dissertation wurde der Fakultät Physik der Technischen Universität Dortmund zur Erlangung des akademischen Grades eines Doktors der Naturwissenschaften vorgelegt.

Erstgutachter:	Prof. Dr. Kevin Kröninger
Zweitgutachter:	Prof. Dr. Dr. Wolfgang Rhode
Vorsitzender der Prüfungskommission:	Prof. Dr. Heinrich Päs
Vertretung der wiss. Mitarbeiter:	Dr. Bärbel Siegmann

Datum des Einreichens der Arbeit:	18. Dezember 2024
Datum der mündlichen Prüfung:	22. April 2025

Kurzfassung

Halbleiterdetektoren werden seit langem in der Hochenergie-Teilchenphysik eingesetzt. Durch die ständige Erweiterung der Experimente werden immer leistungsfähigere Sensoren benötigt. In dieser Arbeit wird die Charakterisierung verschiedener Sensoren gezeigt, um die Qualität der gelieferten Sensoren beurteilen zu können. Dies dient als Unterstützung bei der endgültigen Auswahl der Hersteller. Beide untersuchten Hersteller wurden für die Herstellung von Sensoren für das ATLAS Experiment qualifiziert.
Das Wissen über Siliziumsensoren kann auch für medizinisch-physikalische Anwendungen genutzt werden. In dieser Arbeit wurde für schnelle Siliziumsensoren bestätigt, dass sie in einem Flugzeitmesssystem zur Bestimmung der Energie von durchfliegenden Teilchen eingesetzt werden können. Dazu wurden an der TU Dortmund systematisch die Zeitauflösung verschiedener Sensoren untersucht und neue Auswertungsverfahren entwickelt. Zum Schluss werden die Planung und der Bau eines Prototyps sowie erste Messungen unter realen Bedingungen im Protonenstrahl einer Behandlungsanlage vorgestellt.

Abstract

Semiconductor detectors have long been used in high-energy particle physics. Due to continuous improvements of experiments, more efficient sensors are required. The characterisation of different sensors is presented in this thesis in order to estimate the quality of the delivered sensors. This study supports the decision to select the final manufacturers. Both investigated manufacturers are qualified to produce sensors for the ATLAS experiment.
Knowledge of silicon sensors is also useful for medical applications. In this thesis, fast silicon sensors are characterised to be useful for a time-of-flight system in order to measure the energy of traversing particles. For this purpose, the time resolution of different sensors is systematically investigated at the TU Dortmund University and new analysis methods are developed. Finally, the design and construction of a prototype is presented as well as first measurements under real conditions in the proton beam of a treatment facility.

Contents

1 Introduction **1**

2 Silicon Particle Detectors **3**
2.1 Semiconductors . . . 3
2.2 Particle Detection . . . 11
2.3 Radiation Damage . . . 17
2.4 Hybrid Pixel Detectors . . . 20

3 Market Survey for ITk Sensors **28**
3.1 ITk Upgrade . . . 28
3.2 Tests of Bare Sensors . . . 36
3.3 Tests of Modules . . . 80

4 Low Gain Avalanche Detectors in a Time-of-Flight System **105**
4.1 Avalanche Diodes and LGADs . . . 105
4.2 Electrical Properties . . . 108
4.3 Time Resolution . . . 112
4.4 Time-of-Flight System . . . 124

5 Conclusion and Outlook **144**
5.1 Market Survey . . . 144
5.2 Low Gain Avalanche Diodes . . . 146
5.3 Time-of-Flight System . . . 147

Bibliography **149**

Danksagung **161**

A Additional Measurements for the ITk Market Survey **163**
A.1 Measurements of Complete Wafers . . . 163
A.2 Measurements of Diced Sensors . . . 170

B Parameters for Testbeam Software **205**
B.1 EUTelescope . . . 205
B.2 TBMon2 . . . 210

C Appendix **212**
C.1 Conference Contributions 213
C.2 (Co-)Supervised Theses 213

1 Introduction

During the second half of the last century, a theory called the Standard Model of particle physics (SM) was developed. It describes the elementary particles and three of the four fundamental forces between them. With the Higgs boson, which was discovered a decade ago, the Higgs mechanism is also included in the Standard Model [1, 2]. The Standard Model was used for predictions, for example of the existence of new particles, which were then successfully verified by experiments. However, it still leaves some questions unanswered. It does not include dark matter, dark energy or gravity and it does not include neutrino masses.
To find out more about the Standard Model and to answer these questions, new theories need to be tested with experimental data. Collider experiments which observe a large number of particle collisions per time at high energies, have become crucial to produce the required data. The currently most powerful particle accelerator is the Large Hadron Collider (LHC) located at the European Organization for Nuclear Research (CERN). To study different theories in more detail, it is often beneficial to have higher energies or a larger number of collisions per time. With the upgrades of the accelerator, the different detectors at the accelerator need to be upgraded to cope with the new, often times harsher, environment.

The first way to enhance the performance of the detectors is the usage of further developed, long known and well understood technology. An example of this is hybrid planar silicon pixel modules. The fundamentals to understand this technology are summarised in chapter 2. These modules are currently used in the ATLAS experiment, which is a general-purpose detector at the LHC at CERN. The innermost parts, which are needed to track the produced particles, will be replaced by new planar silicon pixel sensors. The chapter 3 focuses on an international market survey. The aim of this survey is to investigate the quality of the sensors and to identify potential suppliers. Therefore, the upgrade of the inner part of the ATLAS experiment is described and the performed measurements for the market survey and the results are presented in this chapter.

The second way to improve the detectors is the usage of completely new technologies. After the upgrade of the LHC, Low Gain Avalanche Detectors (LGADs) will also be used in the ATLAS experiment. The LGADs are a further development of the simple diode concept. These special detectors have very good temporal resolution,

which cannot be provided by the planar silicon pixel sensors. In chapter 4, crucial properties of such sensors are analysed. Furthermore, the new experimental setup at the TU Dortmund University and the analysis scheme for the measurements are presented.
The sensors that will be used in experiments at the LHC are designed to be very radiation tolerant. This is particularly true for the pixel sensors and the LGADs, which are placed close to the collision point. Radiation tolerance is a property that is also useful in another environment: particle therapy for the treatment of cancer. The knowledge and technology available in the high energy physics community can be transferred to medical applications to improve the quality of treatment. So chapter 4 presents the concept of a time-of-flight system with LGADs as well. This system could be a potential part of a larger system for proton computed tomography. The theoretical basics and the construction process of a prototype of the time-of-flight system are presented. An insight into the first measurement and simulations of this system is also given.

2 Silicon Particle Detectors

Semiconductor detectors, especially position sensitive detectors, are employed in several fields. In addition to their usage in high-energy physics experiments, they are also utilised in radiation therapy and in material testing applications. This extensive use is made possible by the huge silicon processing industry. The chip production technology has reached for smaller and smaller structures, which allows pixelated electrodes in the order of a few tens of µm. Thanks to this industrial sector, silicon position sensitive detectors can be fabricated both cost-efficient and with high precision. Therefore, they are well suited as particle detectors. In high-energy physics experiments, their good position resolution of only a few µm is beneficial to perform precise measurements of the position of traversing particles.

In the following, the fundamentals of semiconductor physics and the working principle of silicon detectors are presented. Finally, the last section deals with a complex detector type, the hybrid detector that consists of a sensor and a readout chip, which is an often used system in high-energy physics experiments. Detailed information can be found in several resources. Most of the presented facts are extracted from textbooks [3, 4, 5]. Additionally, reference [6] was consulted for details about the electronic characteristics.

2.1 Semiconductors

Solids can be classified as conductors, insulators or semiconductors, according to their electrical properties. This distinction is done based on the distribution of the energy levels of the electrons in the corresponding atom bonds. While in an isolated atom the electrons have discrete energy levels, the electrons in a lattice are influenced by the neighbouring atoms. Therefore, the discrete energy levels known from an isolated atom are split up. Since the different levels are only a few meV apart, several energy levels are considered as energy bands instead of single levels. The distance between two energy bands is called band gap. The most important energy gap, regarding to the electrical properties, is the distance between the valence and the conduction band. The valence band defines the highest energies of the electrons at the temperature $T = 0\,\mathrm{K}$, whereas the conduction band, which is above the valence band, is defined by the lowest energies of free electrons. Electrons with

the first-mentioned energies are bound to the atoms, whereas the electrons in the latter case move freely in the lattice. Depending on the size of the gap between those two bands, solids are distinguished.

In an insulator, the valence band is completely filled, while all states in the conduction band are empty. Since the electrons bound strongly between neighbouring atoms a lot of energy is needed to break these bonds. This energy, typically in the order of 9 eV or even more [3], is only very rarely delivered by thermal excitation. Therefore, no electrical current can be observed, because only free charge carriers, for example electrons in the conduction band, contribute to this.
On the other hand, conductors can have either a partially filled conduction band or the valence band and conduction band overlap with one another. In both cases, current can be conducted easily, because free electrons in the conduction band are always available.
In semiconductors, the structure is similar to insulators, but the electrons are not bound as strongly as in insulators. Only for $T = 0\,\mathrm{K}$ all electrons are in the valence band and no electrical current is possible. With rising temperature, thermal excitation is sufficient to pass enough energy to an electron in the valence band to get into the conduction band. This is possible, since the band gap is at room temperature only about 1 eV [3]. The electron leaves a hole in the valence band, which can be seen as a positive charge carrier. Both, the electron in the conduction band and the hole in the valence band, contribute to the electrical current.

2.1.1 Silicon

One of the most widely used materials for semiconductor detectors is silicon. It is an element in the carbon group of the periodic table and forms a diamond cubic crystal structure. In this structure, each silicon atom has four neighbours in a distance of roughly 5.5 Å [3] with which the valence electrons form covalent bonds. The band gap for silicon is 1.12 eV [5] at room temperature and normal pressure. Since temperature and pressure affect the distance of the atoms in the lattice and therefore their bonding, changes of these two parameters cause a change of the size of the band gap. For silicon, the distance between the atoms, and therefore, the band gap, decreases with rising temperature and pressure.
Silicon is an indirect semiconductor. This means that in the energy-momentum representation of the energy levels, the holes in the maximum of the valence band and the electrons in the minimum of the conduction band have different momenta. A phonon, which is an excitation of the lattice, is additionally required in the process of lifting an electron from the valence band to the conduction band to preserve energy and momentum conservation. Therefore, the mean energy to generate an

electron-hole pair in silicon is 3.65 eV [3], which is more than the energy of the band gap. If the holes in the maximum of the valence band and the electrons in the minimum of the conduction band have the same momentum, the material is called a direct band gap.

2.1.2 Doping

Although silicon is an intrinsic semiconductor, meaning it can conduct current in its pure form, the electrical properties can also be adjusted. Since electrons and holes contribute to the electrical current, the insertion of atoms which have a different number of valence electrons than silicon in the lattice is beneficial. This process is called doping and examples of the modified lattices are shown in Figure 2.1. With the incorporated impurities in the lattice, the silicon becomes an extrinsic semiconductor.

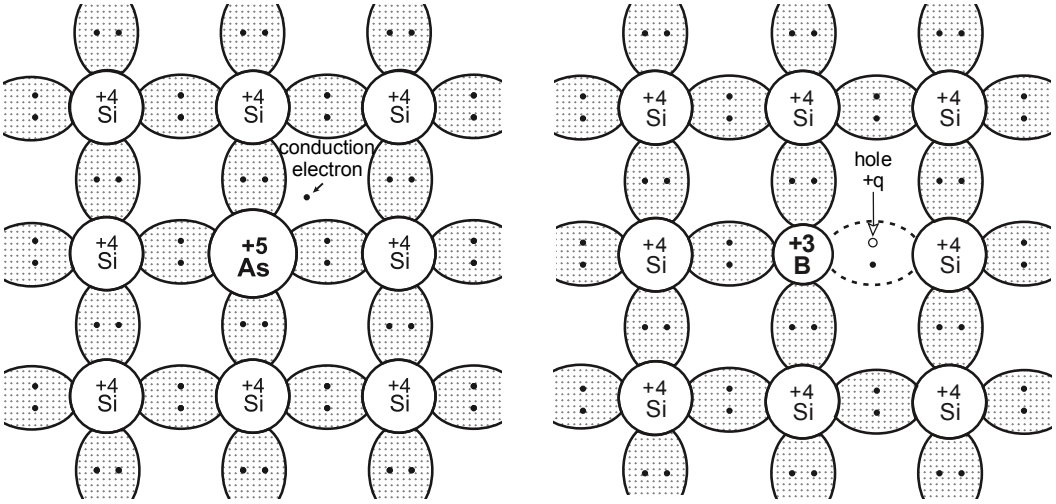

(a) n-type doped material. **(b)** p-type doped material.

Figure 2.1: Sketches of impurity atoms inserted in a lattice of silicon atoms ([3], adapted).

As shown in Figure 2.1a, atoms with more valence electrons than silicon, for example phosphorus or arsenic, can be inserted. Since silicon has four valence electrons, all electrons in a pure silicon lattice are in covalent bonds. The inserted atoms, so-called donors, have an additional electron each that is not bounded to the other atoms in the lattice. These free conduction electrons contribute to the electrical current. The energy level of these electrons is close to the lowest energy of the conduction band. Because the introduction of atoms like arsenic results in an excess of free electrons

in the lattice, such materials are called n-type doped.
In contrast to the insertion of atoms with more valence electrons than silicon, atoms with less valence electrons can be inserted as well. This is shown in Figure 2.1b. The so-called acceptors, for example boron atoms, introduce an excess of holes into the lattice because one electron of the neighbouring silicon atom stays in an unbound state. Since the holes behave like positive charges, this process enhances the electrical conductivity of the material as well. Such materials are called p-type doped.

2.1.3 p-n Junction

Doped silicon is one of the most widely used basis for semiconductor detectors. To detect particles, semiconductor detectors are realised as diodes. This means that p-type doped and n-type doped silicon parts are brought in direct contact and form a p-n junction.
Since the n-type doped and p-type doped materials have different concentrations of free electrons and holes, a concentration difference exists over the junction. This concentration difference of charge carriers leads to a diffusion current I_{diff}. Therefore, the free electrons from the n-side move to the p-side, whereas the holes move inversely from the p-side to the n-side. At the junction, the moving electrons and holes recombine. The recombination of the free charge carriers leads to a depletion zone around the junction, where nearly no mobile charge carriers are present. This is very important for the usage as a particle detector, because in the depletion zone much less free charge carriers are present than in intrinsic silicon. The ions of the dopants are bound to the lattice and are thus immobile. Since the dopants at the p-side of the junction gain an electron, they become negatively charged. Vice versa, the dopants at the n-side lose their electron, so they become positively charged. Due to these stationary ions, an electric field with a built-in potential difference U_{bi} between the p-side and the n-side is created. The electric field forces the free charge carriers to drift. The direction of the drift current I_{drift} is opposite to the diffusion current, so it counteracts further diffusion of free charge carriers.
Without external disturbances, like applied electric fields, both currents are in thermal equilibrium. In this state, the thickness of the depletion region d depends only on the doping concentrations N_{A} and N_{D} of the two doped materials:

$$d = \sqrt{\frac{2\epsilon\epsilon_0(N_{\text{A}} + N_{\text{D}})}{eN_{\text{A}}N_{\text{D}}}U_{\text{bi}}}, \tag{2.1}$$

with $\epsilon = 11.9$ [3] for silicon and the vacuum permittivity ϵ_0. Typical values for the doping of silicon are $N_{\text{A}} = 1 \times 10^{19}\,1/\text{cm}^3$ and $N_{\text{D}} = 1 \times 10^{12}\,1/\text{cm}^3$ [3]. These

doping concentrations lead to a built-in potential difference U_{bi} between the p-side and the n-side of 0.6 V to 0.8 V and a width of the depletion zone of approximately 20 µm [3].
The same potential differences can not only be built with p-n junctions, but also with junctions of two materials doped with the same type of impurities. In this case, the two parts need different doping concentrations to allow for a diffusion of free electrons from the higher doped material (often labelled as n^+ or p^+, respectively) to the lower doped material (labelled as n or p, respectively).

(a) p-n junction in thermal equilibrium.

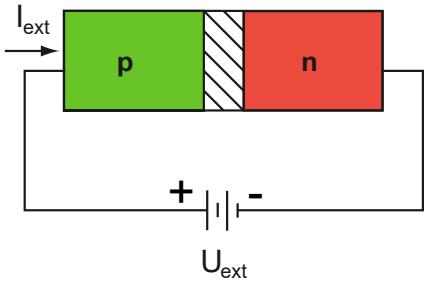

(b) p-n junction forward biased.

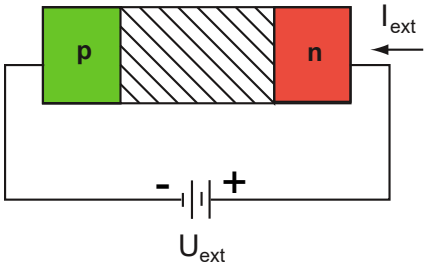

(c) p-n junction reverse biased.

Figure 2.2: Sketches of p-n junctions **(a)** without and **(b)** and **(c)** with applied external electric fields ([3], adapted). The depletion zone is the shaded part between the p- and n-side. The external current flow is indicated by arrows on the side of the sketches.

The sensitive part of a p-n junction for the detection of particles is the depletion zone. Since it is in thermal equilibrium only a few µm wide, the junction has to be widened by external influences. One possibility to adjust the width of the depletion zone is the application of an external electric field. As shown in Figure 2.2, an external bias voltage U_{ext} leads to either a reduction or an increase of the depletion zone depending on its polarity.
If the p-type doped side is connected to the positive contact with respect to the n-type doped side, the bias is in forward direction. In this configuration, the potential difference is decreased by the value of U_{ext} and the drift current gets smaller compared to the diffusion current. Therefore, the depletion zone becomes narrower compared to its width in the equilibrium state. This is shown in Figure 2.2b.
To increase the width of the depletion zone, the p-n junction needs to be reverse-biased as shown in Figure 2.2c. The p-type part is then connected to the negative

contact of the voltage supply, whereas the n-type part is connected to the positive contact. Therefore, the free charge carriers are pulled away from the p-n junction. This configuration increases the potential difference between the two sides by the value of U_{ext} and thus the diffusion current decreases with respect to the drift current. To calculate the modified width of the depletion zone, the built-in potential U_{bi} has to be replaced with $U_{\text{bi}} - U_{\text{ext}}$, with $U_{\text{ext}} < 0$, in Equation 2.1.

Current Characteristics

In thermal equilibrium, the number of thermally generated electron-hole pairs and the recombination of electron-hole pairs is equally. Therefore, no current is generated in the depletion zone. The current voltage characteristic of a p-n junction biased with an external voltage consists of three parts: the forward current, the reverse current I_{L}, which is also called leakage current, and the breakdown. Overall, the total current characteristic, except the breakdown, is described by the Shockley ideal diode equation:

$$I = I_{\text{S}} \left[\exp\left(\frac{eU_{\text{ext}}}{k_{\text{B}}T} \right) - 1 \right], \tag{2.2}$$

with the saturation current I_{S}, the elementary charge e, the Boltzmann constant k_{B} and the temperature T given in Kelvin. The saturation current originates from diffusions of the electrons and holes to the different doped segments. It depends on the surface area of the p-n junction. More details about the saturation current can be found in reference [4].
With an applied forward biased voltage, the forward current rises exponentially. After the so-called knee in the current-voltage characteristic at U_{bi}, the current rises noticeably. With an applied reverse voltage, the current-voltage characteristic consists of the leakage current and the breakdown behaviour. Given Equation 2.2, the current converges to a constant value of $-I_{\text{S}}$ up to the breakdown, which is discussed later in more detail.

However, the leakage current is not a constant in real p-n junctions. It consists of two contributions: the bulk and the surface current. The latter originates from damage of the surface or depositions on it from production processes, whereas the bulk current results mainly from the thermal generation of electron-hole pairs in the depletion zone. These charge carriers drift towards the different electrodes and contribute to the measurable leakage current. With a higher temperature, more electron-hole pairs are generated thermally, so the bulk current depends on the temperature as follows:

$$I_{\text{L}} \propto T^2 \exp\left(-\frac{E_{\text{G}}}{2k_{\text{B}}T} \right). \tag{2.3}$$

In this formula, E_G is the band gap energy. Moreover, in a greater volume more electron-hole pairs can be created and as a result, the bulk current depends on the volume of the depletion zone. Generally, the bulk current contributes much more to the overall leakage current I_L than the surface current.

For high external voltages, the electric field inside the p-n junction leads to an electrical breakdown. At that point, the leakage current increases abruptly. Some devices, for example silicon diodes, can be operated with bias voltages above the breakdown voltage. However, this is only possible in that regime, where the depletion zone is not physically destroyed by the generated heat due to the power dissipation. The breakdown is caused by two different mechanisms. In general, the Zener effect is the main reason for the breakdown at breakdown voltages below 6 V, whereas for breakdown voltages above this value, the avalanche effect causes the breakdown [6]. Both effects will be described in detail in the following.
The Zener effect is caused by high electric fields across the p-n junction of more than 1×10^5 V/cm [6]. With such a high electric field, valence electrons in the p-type doped region can escape their covalent bonds and tunnel to a free state in the conduction band of the n-type doped side. In this way, they contribute to the rising current. The probability of this quantum mechanical tunnel effect depends on the temperature, since the energy gap depends on the temperature. At a higher temperature, the energy gap of silicon decreases and thus less additional energy by the external field is required to free the electrons from their covalent bonds. For this reason, the specific breakdown voltage decreases for higher temperatures [5].
The second breakdown mechanism is the avalanche effect, which describes collision processes. Due to the high electric field, the thermally generated free charge carriers gain enough kinetic energy over their path through the depletion zone to ionise other lattice atoms. These newly produced electrons and holes contribute to the leakage current. In addition, they can continue the avalanche process, if they get enough energy during their drift length to ionise another atom. In this way, the avalanche effect is a self-amplifying process. As well as the Zener effect, the avalanche effect depends on the temperature. However, its temperature dependence is different. Since the free path length of the electrons decreases with a higher temperature, the probability for ionisation processes decreases. For this reason, a higher electric field is required to reach the breakdown current and therefore the breakdown voltage increases at higher temperatures [5].

Capacitance Characteristics

As mentioned before, the depletion zone of a p-n junction is the sensitive part for the detection of particles. To increase the probability to detect each traversing

particle, the p-n junction needs to be depleted completely, so that the full volume of the junction serves as the sensitive material. As the depletion zone grows with the applied reverse bias voltage, the required voltage to deplete the whole volume needs to be known in order to specify the operating voltage for the device. This can be done via the measurement of the capacitance of the p-n junction, because the p-n junction with its depletion zone can be considered as a parallel-plate capacitor filled with a dielectric. Its capacitance depends on the surface area of the electrodes A and the thickness of the depletion zone d. It is defined as:

$$\frac{C}{A} = \frac{\epsilon\epsilon_0}{d}. \tag{2.4}$$

Since the depletion zone thickness depends on $\sqrt{U_{\text{ext}}}$, as it was shown in the modified Equation 2.1, a measurement of the capacitance as a function of the applied reverse bias voltage reveals the depletion voltage U_{dep}. This depletion voltage is the minimal voltage required to deplete the whole volume of the p-n junction. In the curve progression of the measured capacitance in dependence of the applied bias voltage, the depletion voltage is indicated by the turning point of the curve at which it becomes constant. A schematic of this is presented in Figure 2.3. The capacitance reaches a specific constant value, because the depletion zone can not grow larger than the thickness of the p-n junction.

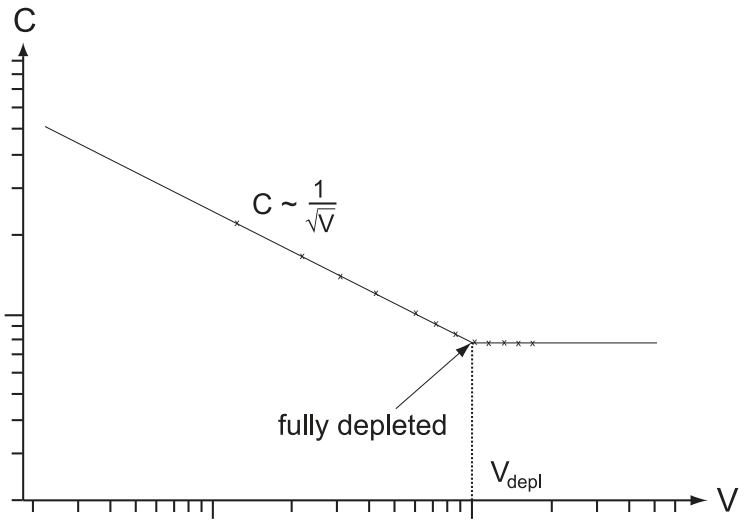

Figure 2.3: An exemplary plot of the bias voltage dependence of the capacitance ([7], adapted). Both scales are logarithmic and in arbitrary units.

2.2 Particle Detection

Generated electron-hole pairs in the depletion zone are separated by the electric field across the depleted region. Besides electron-hole pairs that are generated by thermal excitation and contribute to the leakage current, there are electron-hole pairs that are created by the energy deposited by ionising particles that traverse the semiconductor detector. The latter electron-hole pairs contribute to the signal, because they are usually generated in a much greater number than the thermally generated electron-hole pairs.
During the passage of a particle through the detector, the particle loses energy by different processes like excitation or ionisation. More about these processes can be found in the following. With the mean energy loss of a particle and the mean energy required to create an electron-hole pair, the charge that is created by a traversing particle can be calculated. The created free electrons and holes drift towards the corresponding electrodes and induce thereby a current in them which is the desired signal.

2.2.1 Energy Loss of Charged Particles

If a particle traverses matter, it interacts with the constituents, and thereby loses some fraction of its energy. Different particle types interact differently with matter and therefore, only the particle interactions with matter relevant for this thesis will be described in the following. A detailed overview about the left out particles and interactions can be found in further literature such as reference [3].

To begin with, the interaction of heavy, charged particles like protons with matter is described. In fact, the following is valid for all charged particles with a larger mass than the electron. In general, a heavy, charged particle does not interact only once with the material, but several times until it leaves the material or gets absorbed in the material due to the loss of all its kinetic energy. All of these multiple interactions are stochastically independent.
The main source for the loss of energy of a heavy, charged particle is its energy transfer to the electrons of the atomic shell of the atoms in the material. With the additional kinetic energy of the electrons, the atomic shell gets excited or even ionised. The mean energy loss per path length for heavy, relativistic, charged particles is described by the Bethe-Bloch formula:

$$-\left\langle \frac{\mathrm{d}E}{\mathrm{d}x} \right\rangle = K\frac{Z}{A}\rho\frac{z^2}{\beta^2}\left[\frac{1}{2}\ln\frac{2m_\mathrm{e}c^2\beta^2\gamma^2T_\mathrm{max}}{I^2} - \beta^2 - \frac{\delta(\beta\gamma)}{2} - \frac{C(\beta\gamma, I)}{Z}\right]. \quad (2.5)$$

The variable K sums up some natural constants and equals $0.307\,\mathrm{MeV\,cm^2/mol}$. The maximum energy transfer from the incoming particle to the shell electron, T_{max}, can be calculated assuming a frontal collision. The mean energy loss per path length depends on the material properties and on the characteristics of the incoming particle. Therefore, the target material is described with its atomic number Z and A as its mass number, whereas its density is given by ρ and the mean ionisation energy of the material with I. The parameters of the incoming particle are z as its charge and β as its velocity. Additionally, Equation 2.5 contains two correction factors. The first is δ, which is important only for very high energies of the incoming particle. In contrast to this, the second correction C/Z is important for low velocities, meaning $\beta < 0.3$ [3]. More about these corrections can be found in further literature such as reference [8].

The following discussion of the dependence of the mean energy loss per path length on the momentum focuses on the energy ranges where the correction factors do not need to be considered. This is done with respect to the energy ranges covered by the measurements for this thesis. In most cases it is useful to plot Equation 2.5 as a function of $\beta\gamma$. This is shown in Figure 2.4.
In this plot, the energy loss decreases with a $1/\beta^2$ dependence up to $\beta\gamma \approx 3$ to 4 [3]. To explain this behaviour, it is important to know that the energy loss is proportional to the square of the momentum transfer. The momentum transfer itself depends on the time that the incoming particle is near its interaction partner. This interaction time is inversely proportional to the velocity of the incoming particle, since slower particles take more time to travel the same distance. Therefore, for small values of $\beta\gamma$, the energy loss follows $1/v^2$, which is proportional to $1/\beta^2$.
After the described decrease there is a minimum of the energy loss. In silicon the mean energy loss per path length at this minimum is about $1\,\mathrm{MeV\,cm^2/g}$ to $2\,\mathrm{MeV\,cm^2/g}$ [3]. Particles with momenta in this momentum range are called Minimum Ionising Particles (MIPs). These are very important to consider, because a small energy loss per path length results in only a small energy transfer to the material. Therefore, MIPs produce the smallest possible signals in a sensor.
For values of $\beta\gamma$ greater than 4 and especially greater than 10, the energy loss increases proportional to the logarithm in Equation 2.5. This can be explained by two effects. First, the maximum energy transfer in a single collision T_{max} is proportional to γ. Second, the Lorentz transformation of the electric field of the incoming particle reduces its longitudinal component, while the transverse component increases. This affects the energy transfer in a single collision. Both effects lead to the logarithmic increase of the energy loss, until the logarithmic behaviour is stopped by radiation effects for very high energies ($\beta\gamma > 1000$ [8]).

Since electrons have a much smaller mass than the aforementioned protons, they interact differently with matter. Electrons and their antiparticles, the positrons,

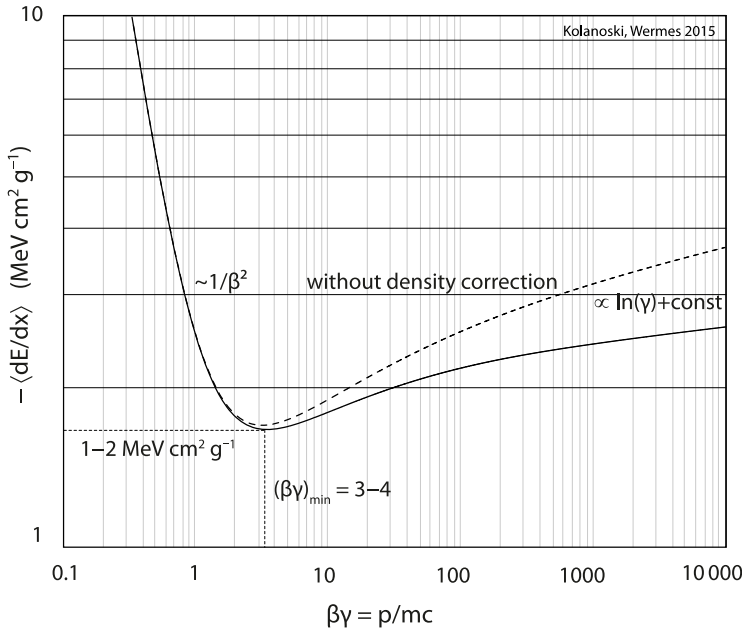

Figure 2.4: Mean energy loss per path length as a function of $\beta\gamma$ for pions in silicon [7].

lose their energy not only via ionisation of the atomic shells but also in scattering processes and through bremsstrahlung. Since the energy loss through bremsstrahlung and ionisation are independent, they can also be described independently.
For the description of the energy loss by ionisation, the Bethe-Bloch formula can be applied, but there have to be adjustments. These are necessary, since incoming electrons are indistinguishable from the electrons of the atomic shells in the matter. This has an effect on the term for the maximum energy transfer $T_{\max}$ in the Bethe-Bloch formula. In addition, especially for small energies, scattering processes have to be considered. More about this can be found for example in reference [8]. For positrons there is another additional process, called annihilation, that can occur. Since positrons are the antiparticles of electrons, an incoming positron can interact with an electron of the atomic shell. Both particles annihilate and two photons are created.
Bremsstrahlung is the most important process for the energy loss of electrons that are used throughout the measurements in this thesis. Bremsstrahlung is generated, if a charged particle is accelerated, for example in the electric field of a nucleus. The lost energy per time in this case is inversely proportional to the squared mass of the accelerated particle. Since electrons have a relatively low mass, they lose more energy in the same electric field than heavier particles like the aforementioned

protons. That is the reason why this radiation effect becomes more important at even lower energies compared to heavier particles. For electrons with energies above a few MeV, depending on the material, the energy loss by bremsstrahlung is greater than the energy loss by ionisation processes [3].

The Bethe-Bloch formula gives the mean value of the energy loss per path length, but the energy loss of individual particles fluctuates, because it is a stochastic process. In particular, so-called high energy knock-on electrons contribute to a tail of values larger than the mean value. These electrons originate from central collisions and are capable to ionise further atoms on their own. The distribution of the transferred energy follows a Landau distribution convoluted with a Gaussian distribution. An example of such a convoluted distribution is shown in Figure 2.5. The Gaussian distribution originates from many interactions where only small fractions of energy are transferred. The Landau distribution describes the long tail towards the higher energies, that originate from the knock-on electrons. In the convoluted distribution, the mean value described by the Bethe-Bloch formula and the Most Probable Value (MPV) differ due to the long tail towards high values. Therefore, the mean value itself is much higher than the MPV, because it takes into account the high energy transferred by the knock-on electrons [3].

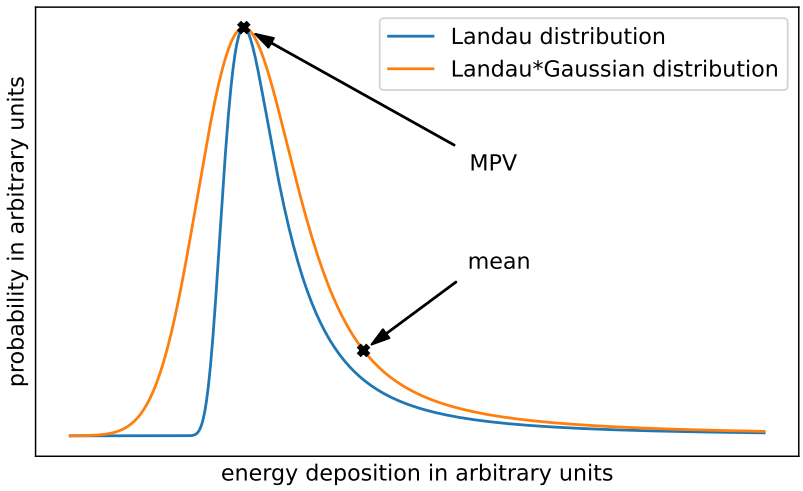

Figure 2.5: An exemplary distribution of a Landau distribution convoluted with a Gaussian distribution. The most probable value (MPV) and the mean are indicated. The code to create this distribution is taken from reference [9] and was adapted.

A particle can traverse a layer of matter until its kinetic energy is completely lost by the interactions. The length of this path in matter is called range and can be estimated with the mean energy loss. For ionisation processes, and neglecting

absorption, as it is valid for heavy, charged particles, the particle number is theoretically constant until it decreases abruptly. In reality, there is a slight decrease in the particle number due to nuclear reactions and the abrupt decrease is smeared. The smearing of the decrease is due to the so-called straggling, which describes the statistical fluctuations of the range due to fluctuations of the energy loss per path length. The width of the Gaussian distribution is only about 1% of the range [3]. The energy loss per path length as a function of the path is called the Bragg curve. A simulated Bragg curve of protons is shown in Figure 2.6. The Bragg curve reveals a striking feature, the so-called Bragg peak. This is the region where the maximum of the energy loss per path length can be seen. It forms, because the energy loss depends on $1/\beta^2$ regarding Equation 2.5. Therefore, fast moving particles lose only small fractions of their energy. With increasing numbers of interactions, the particles slow down and thus lose more energy per path length. This behaviour leads to the Bragg peak, where a particle loses most of its energy in only a small range. Especially in the irradiation of cancer this is used beneficially. Due to the precise energy loss, the tumour volume can be irradiated precisely in its width and depth.

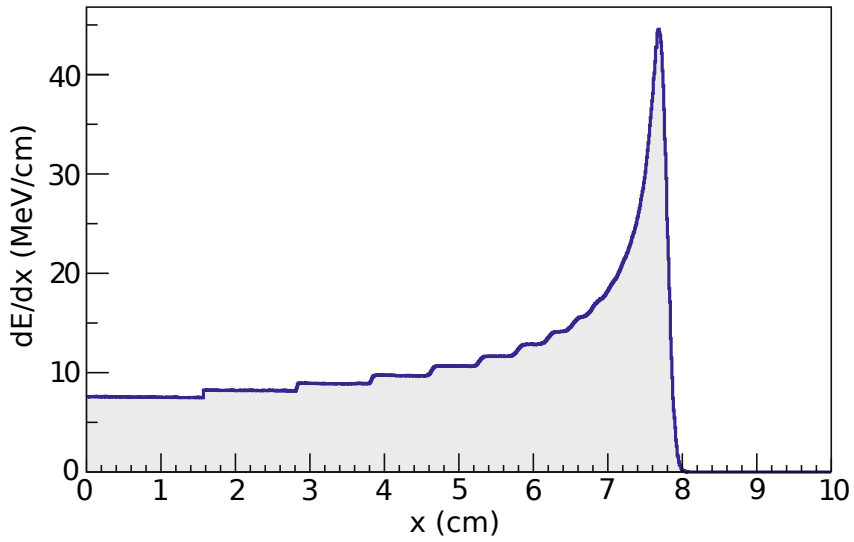

Figure 2.6: The simulated energy loss per path length for 10000 protons with an initial energy of 100 MeV in water. The simulation was done with the software package GEANT4 (graphic and simulation details taken from reference [3], adapted).

2.2.2 Energy Loss of Photons

Photons interact in different ways with matter. The kind of interaction depends highly on the energy of the photon E_γ. If the energy of the photon is less than the ionisation energy of the material, it gets only deflected in scattering processes without an energy transfer to the atoms. Above the ionisation energy there are three main processes for photons to lose their energy: the photoelectric effect, Coulomb scattering and pair production. Which of these processes is the most dominant, depends on the energy of the photon and the atomic number Z of the material. A graphic in the (E_γ, Z)-plane is shown in Figure 2.7.

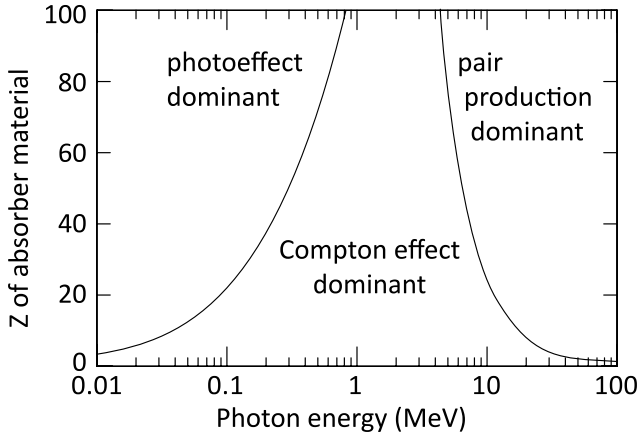

Figure 2.7: The (E_γ, Z)-plane indicates the different photon absorption processes and in which regions they are the dominant process [7].

Below an energy of 0.06 MeV [3], the photoelectric effect is dominant in silicon. The photoelectric effect describes the process of a photon absorption by an atom. The photon transfers its energy to an electron in the atomic shell, which than gets emitted with the kinetic energy $E_\gamma - E_\mathrm{B}$, where E_B corresponds to the binding energy of the electron. The probability for the photoelectric effect decreases with larger photon energies, following a dependence of E_γ^{-m} with $m \leq 3.5$ [3]. When the photoelectric effect becomes increasingly unlikely, the Coulomb scattering takes over as the dominant process.
For silicon, the Coulomb scattering is the dominant process in an energy range between 0.06 MeV and 15 MeV [3]. This process is described as an elastic scattering of a photon with a free electron. Although the electrons in matter are not free, this assumption is valid, if the energy of the photon is much larger than the binding energy. In the scattering process only a part of the photon energy gets transferred to the electron and the photon continues to traverse the material with a lower kinetic energy. The probability of Coulomb scattering decreases proportional to $1/E_\gamma$ [3].

Above 15 MeV [3] the Coulomb scattering is superseded by the pair production as the dominant process for photons to lose their energy.
Pair production is the process, where in the Coulomb field of an atomic nucleus or an electron, a photon gets converted into an electron-positron pair. This can only occur near another particle, because a partner particle is needed to meet the energy and momentum conservation. In presence of an atomic nucleus, this process happens only above energies of $E_\gamma > 2m_e c^2$. If the process happens close to an electron, the threshold energy is $E_\gamma > 4m_e c^2$ [10]. For photon energies above the corresponding threshold energy, the probability for the pair production does not depend on the energy of the photon anymore [3].

2.3 Radiation Damage

Silicon detectors are designed to detect traversing particles. For this reason they are exposed to different particle fluxes regarding their specific usage during their lifetime. However, when particles traverse the detector, they can damage the silicon lattice. Since this influences different properties of the sensor, it is important to understand the different types of radiation damage and their effects on the detector operation.
The ionising processes that take place in the depletion zone discussed in section 2.2 are reversible and are referred to as ionising energy loss. Since the ionisation process can be undone, those processes do not damage the bulk material of the sensor. In contrast, so-called Non-Ionising Energy Loss (NIEL) is irreversible and results in damage to the crystal lattice. These processes lead to a change in the properties of the sensor, for example the signal formation and the leakage current. The NIEL hypothesis allows to compare the non-ionising damage that is caused by different particle types. To do so, the damage that is caused by a neutron with an energy of 1 MeV is taken as a reference value. The particle fluence Φ, that has caused an irradiation is then given in neutron equivalent per area, $n_{\mathrm{eq}}/\mathrm{cm}^2$.
Since the damage to the crystal lattice in the bulk region of a silicon sensor has a great effect on the sensor properties, bulk damage is discussed in the following section. To complete the different types of radiation damage, a brief overview of surface damage is given after that.

2.3.1 Bulk Damage

The radiation damage of the bulk material of a silicon sensor is mainly caused by the non-ionising energy loss. As mentioned before, this leads to changes of the crystal lattice of the sensor. This is only possible, if the incoming particles collide

directly with the lattice atoms. The possible different changes of the crystal lattice are shown in Figure 2.8.

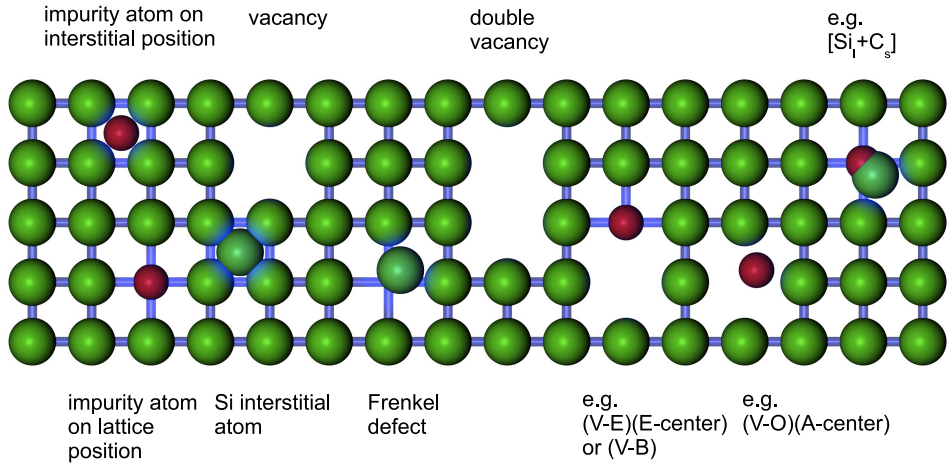

Figure 2.8: Schematic of different possible crystal defects that are caused by irradiation [11]. Possible reasons for impurity atoms are either contamination during the crystal growing or formation by nuclear transmutation of the original silicon atoms [3].

The first types of damage to be described are point like defects. These are the result of direct collisions, whose physics is described by Coulomb scattering, between the damaging particle and an atom of the bulk material. All four of the point-like defects shown on the left in Figure 2.8 can move around inside the crystal, so they may recombine. In such cases, the damage is not permanent. However, it is also possible for the point-like defects to form more complex defects. The Frenkel defect shown in Figure 2.8 is a combination of a silicon atom at an interstitial position and a vacancy. The double vacancy is formed when two single vacancies combine to a larger one. As these defects do not easily recombine, they are more stable and tend to permanently damage the bulk. A completely different type of defect is caused by neutron capture and nuclear transmutation. These processes modify slightly the chemical elements.

The above described defects in the lattice caused by NIEL may form new states in the band gap of the silicon crystal. From these new states it is easier to generate or absorb free charge carriers. An overview of the location of these new states is presented in Figure 2.9a.
When a particle passes through a detector it can create acceptor or donor centres. This happens if acceptors or donors from initial doping are electrical neutralised or their atoms are removed from the lattice. Moreover, new acceptors or donors can be

formed by nuclear transmutation. These newly formed acceptors and donors have energy states that are located near the valence or conduction band, respectively. Therefore, less energy is needed to generate new electron-hole pairs from these states. This simplified charge generation results in an increasing leakage current.
If the amount of acceptors and donors changes by the different damaging processes, the effective doping concentration of the bulk material changes as well. This results in a change of the required depletion voltage. An overview about this is given in Figure 2.9b. In addition, there is a point in the change of the doping concentration where type inversion happens. This means, that after a fluence of approximately $10^{12}\,n_{\mathrm{eq}}/\mathrm{cm}^2$ to $10^{13}\,n_{\mathrm{eq}}/\mathrm{cm}^2$ [3] n-type doped silicon acts like effective p-type doped silicon. This is a severe problem, since after the type inversion with an increasing fluence ever higher bias voltages are required to deplete the sensor volume. Moreover, due to power limits it might be possible to not be able to deplete the sensor completely any more.

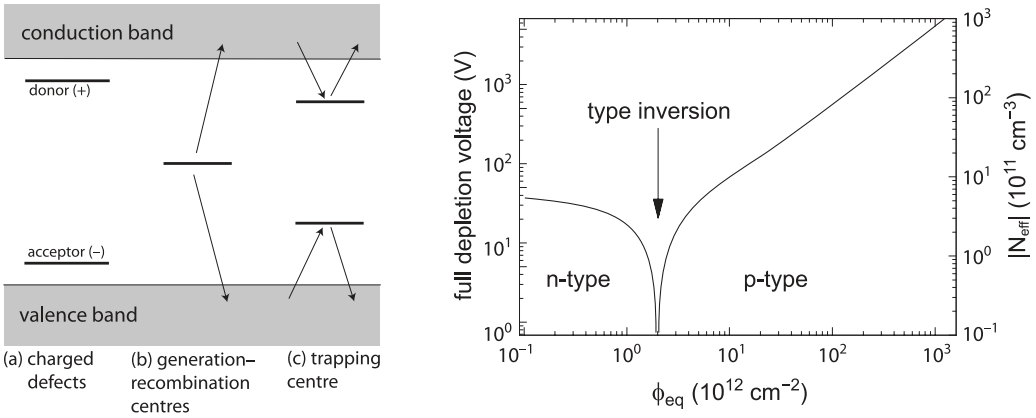

(a) New energy levels.

(b) Change of effective doping.

Figure 2.9: Results of radiation damage are **(a)** new energy levels in the band gap and **(b)** a change of the effective doping [7].

Another new state in the energy gap of silicon is formed at so-called generation-recombination centres. The generation of electron-hole pairs is simplified, since less energy is needed there to lift an electron to the conduction band. The generation centres increase the leakage current due to this effect. On the other hand, it is easier for electrons and holes to recombine at this intermediate level for the given reasons as well.
The last new states are trapping centres. In these energy levels, one type of charge carriers is captured. The trapped charge carrier might be released after some time, the so-called capture time. However, if the capture time is longer than the time for the signal acquisition (the so-called charge collection time), this charge carrier does

not contribute to the signal any more.

The microscopic defects described above lead to macroscopic changes in detector performance. First, the leakage current I_L increases in proportion to the depleted volume V and the applied neutron equivalent fluence ($\Delta I_L = \alpha \Phi_{eq} V$). Here, α is a proportional factor, the so-called damage rate. The leakage current can be problematic, because the sensor heats up as the current flow increases. This can lead to thermal runaway, where more and more thermally generated electron-hole pairs are created, which form a chain reaction that can end in the destruction of the sensor. Secondly, the deformation of the electric field within the sensor bulk results in an increasing depletion voltage. And thirdly, the signal amplitude is reduced due to the trapping of the mobile charge carriers. To ensure proper operation after certain radiation fluences, irradiated silicon sensors must be tested for their functionality.

2.3.2 Surface Damage

In contrast to the bulk damage that is caused by NIEL, the damage of the surface and boundary layers is caused by ionising energy loss. In particular, silicon dioxide (SiO_2), which forms at the contact of silicon and air [3], is affected by ionising energy loss. The reason for this is that the holes formed in it have very low mobility. Compared to electrons, their mobility is 10^6 times lower in silicon dioxide [3]. Therefore, the holes become stationary oxide charges. To reduce this effect, smaller transistor structures that come with thinner oxide layers can be used [3]. If the oxide layers are only a few nm thick, the holes can tunnel out of the oxide. In this way they do not contribute to the change in electrical behaviour. Another effect associated with the surface damage is damage to the electronic components of the readout system. The threshold characteristics of transistors change, so the circuits may not work as expected after irradiation. In addition, unwanted currents may occur.
In conclusion, bulk damage is much more relevant to the operation of the silicon sensor itself than the surface damage. This is especially true as the effects of the surface damage can be counteracted by moving to smaller structures with thin oxide layers.

2.4 Hybrid Pixel Detectors

Silicon detectors are often used in high-energy physics experiments to measure the trajectory of particles. In order to do this with a high precision, the electrodes of the diodes discussed above can be divided into parts that are smaller than the

entire surface. If the surface is divided in one direction, narrow and long rectangles, so-called strips, are the result. On the other hand, the electrode can be divided in both spatial directions, resulting in small rectangles or squares. If the edge length of the smaller structures is of the order of only a few hundred µm or even smaller, the structures are called pixels [3]. Since this thesis deals with the investigation of the quality of pixelated sensors, only these will be discussed in the following section. In order to read out the signals of the different segments individually, the sensor cells are connected to the cells of a readout chip. This combination of the connected sensor and the readout chip is called a module. More details about the different sensor types and the readout chip are given below.

2.4.1 Pixelated Sensors

There are two concepts for detecting the signal of a traversing particle with a high position sensitivity. On one hand, the generated charge in the sensor bulk can be detected with more than just one readout electrode. With the resistive charge division, the generated charge is split between two electrodes in the simplest case. The ratio depends on the distance between the position of the charge generation and the corresponding electrode. On the other hand, an easier way to get the exact position is to divide the detector into smaller, independent subdetectors [4]. The position of the traversing particle is then given, in the simplest case, by the pixel with the signal within the pixel matrix.
There are four possible combinations to achieve the independent pixels of the second alternative. The first two options use slightly n-doped silicon as the bulk material and the pixel implants can be implemented as either highly n-type or highly p-type doped silicon. The other two options are characterised by pixels as highly n-type or highly p-type doped silicon in a slightly p-type doped silicon bulk. The arrangement of the electrodes relative to the bulk defines the geometry of the sensor: either planar sensors or 3D sensors are possible.

Planar Sensors

Planar sensors are realised in a sandwich structure. The pixel implantation is on one side of the silicon bulk, while the second implant is on the other side of the bulk. In this configuration, the bulk thickness is the maximum depletion depth. This thickness also corresponds to the longest possible drift path of the generated charges within the bulk. As electrons move faster than holes in silicon [3], it is better for faster signals to read out the signal induced by electrons. This is achieved either by using highly n-type doped implants for the pixels in an n-type doped substrate,

so-called n^+-in-n sensors, or by using highly n-type doped implants in a slightly p-type doped bulk, so-called n^+-in-p sensors.
The n^+-in-p sensors have the advantage of not being affected by type inversion after irradiation. Therefore, the depletion zone in these devices always grows from the pixel side towards the back side electrode. This allows them to be used even if they are not fully depleted. This is important not only in the unirradiated state, but also in the irradiated state, where higher bias voltages are required for complete depletion. Moreover, n^+-in-p sensors are easier to produce than n^+-in-n sensors, because they have segmented parts on only one side. Therefore, they only require a single-sided production process. To get n^+-in-n sensors, the silicon has to be processed on both sides, which makes this production more expensive. The layout of n^+-in-p sensors is discussed in the next paragraph.

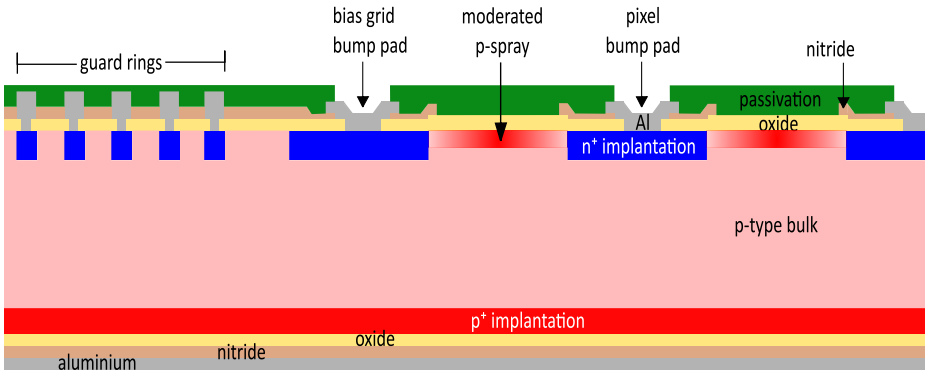

Figure 2.10: Cross section of an n^+-in-p pixel sensor. Original sketch of an n^+-in-n sensor taken from reference [12] and modified to match the n^+-in-p structure.

An n^+-in-p sensor as shown in Figure 2.10 consists of different layers above and below the silicon bulk. The layer closest to the bulk is the n^+ pixel implantation. To isolate the different pixel implantations from each other, p-spray or p-stop is applied between the pixels. More details on these techniques are given in the reference [13]. Above the pixel layer, oxide and nitride passivations are located. These are used to saturate the open bonds of the underlying silicon [4]. Vapour-deposited aluminium is used in certain areas to provide a low-resistance electrical connection to the readout chip or the outer world. The final layer is another passivation everywhere except for the metal contacts, to ensure protection against environmental influences such as humidity or mechanical damage [4]. For n^+-in-p sensors, the backside has a simpler structure than the surface. It is not divided into pixels, so there is only one large p^+ implant under the bulk. This implant is again covered by oxide and nitride passivations. The backside is completely covered with aluminium to ensure a good electrical contact.

To finish with the details of n^+-in-p pixel sensors, two specific structures for the functioning of the sensor have to be mentioned.

The first are the so-called guard rings, which can be seen close to the edge of the sensor surface in Figure 2.10. Since for n^+-in-p sensors, the n^+ pixel implant must be at a higher electrical potential than the p^+ implant, a negative bias voltage is often applied to the backside. The surface with the pixels is then held at ground level. To prevent a current flow across the edge of the sensor, guard rings are used to create a controlled voltage drop from the outer pixels to the edge of the sensor. Another advantage of this technique is that it prevents sparking between the edge of the sensor and the readout chip, which are usually at different electrical potentials. A more detailed study of the effect of guard rings can be found in the literature [12].

The other structure is the bias grid. This is a metallic grid consisting of bias rails and bias dots to connect the pixels with each other. It is used to have the same electrical potential for all the pixels of the sensor when they are not yet connected to the readout chip. The so-called punch-through effect then ensures the common potential. For this effect, the bias grid has to be connected to an additional bias ring, where the bias voltage U_{bias} is applied. Under this ring a depletion zone grows with the applied bias voltage. The depletion zone grows not only between the two electrodes, but also in the lateral direction. At a certain voltage, the so-called punch-through voltage U_{PT}, the depletion zones below the bias ring and below the closest pixel implant come into contact. For bias voltages greater than U_{PT}, the different depletion zones of the pixels and the bias ring unite and charge carriers can move freely in this connected region. The electrical potential of the pixel implant is then given by $U_{\text{bias}} - U_{\text{PT}}$. A detailed description of this effect can be found in reference [3].
Another way of contacting all the pixel cells is to use polysilicon resistors [3, 14] if no bias grid is used. These resistors are made from polycrystalline silicon. As the resistors need to minimise noise and voltage differences between the individual pixels, they are implemented in winding structures to gain more length than the direct connection of two cells. This results in a higher overall resistance. These winding structures then connect the individual pixel implantations to the bias ring. A second way to contact all pixel cells without using a bias grid is to apply a temporary metal layer [15]. The metal covers the passivation and thus shortens the individual pixels. The metal layer is removed after electrical testing.

3D Sensors

In contrast to the sandwich structure of planar sensors, 3D sensors have a completely different structure. The electrodes are highly n-type doped and p-type doped silicon columns perpendicular to the surface, surrounded by the silicon bulk. A sketch of this structure can be seen in Figure 2.11. This implementation has the advantage of a much smaller distance between the different electrodes. In currently used sensors this distance is about 67 µm [16] and will decrease to 35 µm for the next generation of 3D sensors [16]. Furthermore, since the depletion zone grows between the electrodes, its width is not linked with the thickness of the sensor any more, but to the distance between the columns.
The smaller distance between the electrodes comes with two main advantages. Firstly, to obtain complete depletion a much lower bias voltage is required, since the width of the depletion zone needs to be about a factor of 3 smaller compared to planar sensors of the same thickness [16]. Secondly, the generated charges in the sensor volume have shorter paths towards the electrodes, which results in shorter charge collection times. This effect is beneficial for irradiated sensors, since irradiation decreases the mean free path lengths of charges in the bulk material. Therefore, the effects of radiation damage get important only at higher fluences compared to planar sensors [17].

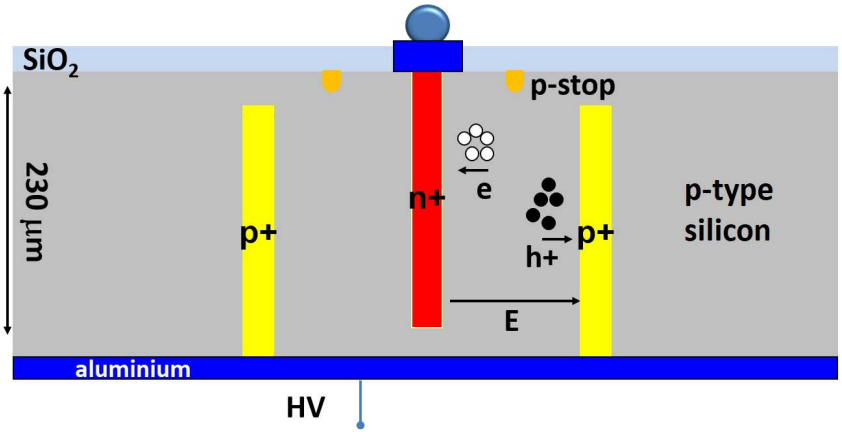

Figure 2.11: Exemplary cross section of a 3D pixel sensor, fabricated at IMB-CNM ([18], adapted). The bump contact for the connection to a readout chip is depicted as a ball at the top of the n^+ column. The p-stop is applied in a circle around the n^+ column.

Despite all these beneficial properties for particle detection in high fluence environments 3D sensors come with a downside, which is the complex production process. Usually the columns for the electrodes are etched from both sides of the substrate.

This double sided process requires more steps and masks compared to a single sided process and is therefore more expensive. However, single sided production processes are also available. Since they require additional production steps as well, even they are more expensive than the production processes for planar sensors [19].
More details about 3D sensors, from the first ideas over different fabrication processes towards recent developments, can be found in further literature [20, 21, 22, 23, 24].

2.4.2 Readout Chip

The purpose of a readout chip is diverse. Within the readout chip, the signal from the sensor gets amplified and electrically processed. Furthermore, information about the deposited energy and the timing are obtained. For further processing, the information gets digitised and the readout chip serves as a short-term storage and a forwarding device for the hit information. All those different functions can be optimised, but not all at once. So, depending on the overall purpose a trade-off of the different services needs to be realised [3].
The advantage of the hybrid detector technology is the usability of the readout chip with different sensors as long as they have the same readout design. The chip ensures an individual readout of every pixel cell of the sensor. To do so, the readout chip is bump bonded to the sensor via solder bumps, for the electrical contact between these two parts, in a flip chip process. Afterwards, the bare module is attached to a printed circuit board (PCB). This contains further circuitry and the connectors to the outer world. Generally, the readout chip is connected with wire bonds to this electrical circuit. In addition, the bias voltage for the sensor is applied via such a wire bond as well from the circuitry of the PCB.

The readout chip used during this thesis is the so-called RD53A [25], which is fabricated in 65 nm CMOS technology. It is not intended for usage in a high-energy physics experiment, but for testing purposes only.
The chip consists of readout cells with a size of $50\,\mu m \times 50\,\mu m$. These cells are placed in a matrix with 400 columns and 192 rows. However, the total size of the chip is $20\,mm \times 11.6\,mm$. This gives additional 2 mm space at the top and bottom of the readout chip. The space at the bottom is used for the global analogue and digital circuitry. It is needed for biasing and configuration of the readout chip. Moreover, at the bottom edge of the chip wire bonding pads are placed. They are separated that far from the first row of readout pixels to ensure wire bonding after the flip chip process. At the top of the pixel matrix some pads designated for specialised tests are located. Detailed information about the characterisation of the chip can be found in further literature such as reference [26].

The analogue front ends amplify the signal from the sensor pixels. The RD53A readout chip contains three different types of analogue front ends. They are called Synchronous, Linear and Differential according to the way they handle the signals. The pixel matrix is divided into three segments, with the Linear and Differential front ends covering a width of 136 readout cells and the Synchronous front ends covering a width of 128 pixels. This distribution was chosen, because the Synchronous front ends are expected to have a higher power consumption than the other two versions. The Linear and Differential versions are placed next to each other on the chip, because they share the same digital architecture and have similar functionalities. This maximises the area of the chip with the same response.
Each front end is designed to process the signal from the sensor and to convert it into digital data. To do this, different amplification circuits are implemented. Common to all three variants is the presence of a discriminator. This discriminator is used to measure the Time-Over-Threshold (ToT), which indicates the time for which a current exceeds a defined threshold. Only if the current exceeds the threshold at all is the signal treated as a hit. Detailed information about the different front ends and their overall functionality can be found in further literature [25].

Some of the parameters of the circuitry and especially the threshold values for the comparators can be adjusted via configuration bits [25]. This process is the so-called tuning [27]. It is important, since with the threshold values the smallest amount of detected charge that causes a hit is defined. Therefore, the threshold should be uniform across the pixel matrix to ensure the same response to a traversing particle in every region of the module. If the value can be set for each pixel individually, it is a so-called local tuning. On the other hand, if a certain configuration is applied to all pixels of the matrix, it is considered as a global tuning. The local tuning of the threshold is available only for the Linear and Differential part of the RD53A.

To power the analogue and digital parts of the chip, there are two possibilities. The first is the regulated mode (LDO mode), which is usually preferred. In this mode, a low-dropout regulator combined with a shunt regulator [28] is used to ensure an output voltage in the range of 1.4 V to 2.0 V to the internal voltage rails [25]. To do so, the applied external voltage has to be in the same range. The second option is the so-called direct powering. There, the regulation is bypassed. In this mode the applied external voltage has to be in the range of 1.2 V to 1.32 V [25]. Any higher applied voltage will damage the internal circuitry of the chip.

2.4.3 Spatial Resolution

The precision of the position measurement with a hybrid detector depends on the readout method and the distance between the electrodes, the so-called pitch [3, 4].

In digital readout mode only the information, whether a pixel was hit by a particle or not, is obtained. No further information about the height of the signal is available. Therefore, the hit position is always derived as the centre of the pixel, that gives the hit signal. If it is assumed that the probability of being hit is the same over the entire pixel, the measurement precision is then given by

$$\sigma = \frac{p}{\sqrt{12}}, \tag{2.6}$$

with p as the pitch of the pixels.
The spatial resolution can be improved, if analogue readout is used. Within this method, not only the occurrence of a hit, but also the information about the amplitude of the signal is recorded. The pixel pitch has to be smaller than the diffusion width of the generated charge to make advantage of this technique. Then, the generated charge is not collected only on a single electrode, but on various pixels. Since the height of the signal on the different pixels depends on the distance between the pixel and the generated charges, it is possible to calculate a centre of gravity of the signal. Then the coordinate of the origin of the signal can be obtained by interpolation, which results in a higher spatial resolution.

3 Market Survey for ITk Sensors

This chapter deals with measurements that are carried out to inspect the quality of prototypes of semiconductor sensors. The measurements of the properties of these sensors are meant to qualify manufacturers that are candidates to deliver the final sensors for the Inner Tracker (ITk) of the ATLAS experiment upgrade.

In the following section, the Large Hadron Collider (LHC) and the ATLAS experiment will be described in more detail to give some background information (section 3.1). Afterwards, the measurement techniques for qualifying the manufacturers are described and the results and conclusions are presented (section 3.2 and section 3.3).

3.1 ITk Upgrade

The Large Hadron Collider is a collider located at CERN (European Organisation for Nuclear Research) near Geneva. Hadrons with high energy are accelerated in it in bunches that reach currently a maximum energy of 6.8 TeV [29]. These bunches are brought to collision and complex experiments around the dedicated collision points measure the tracks of the emerging particles. With these experiments, theories in particle physics can be proven and new particles can be detected, which leads to a better understanding of the laws of nature. The latest most important discovery that the LHC made was the proof of the existence of the Higgs boson [1, 2].

To test theoretical predictions with a higher precision or observe rarer events, more data is required. Therefore, the luminosity, which describes the number of specific interactions per time and area, needs to be increased. This will be done in a project called High Luminosity Large Hadron Collider (HL-LHC). However, a greater luminosity produces a much harsher environment for the experiments around the collision points. As a result, some currently installed parts of these experiments need to be replaced to be able to cope with this new environment. In addition, newer technologies can be installed to maintain or even improve the performance of the detectors.

Figure 3.1 shows the current schedule for the upgrades leading towards the HL-LHC. The usage of the LHC is divided into two major parts: the periods when data

is taken (Run), and periods when a lot of upgrades take place (Long Shutdown). During the Long Shutdown 3 (LS3), which is foreseen to begin in 2026, major upgrades are foreseen for the ATLAS experiment.

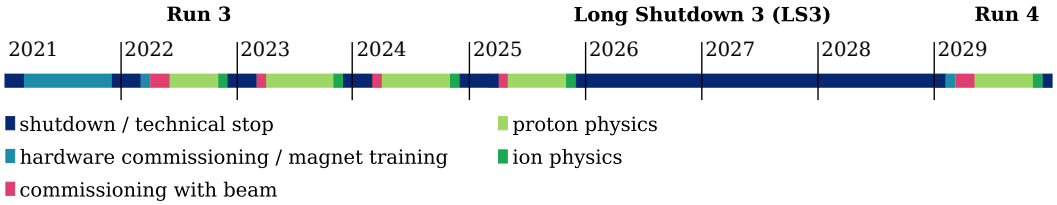

Figure 3.1: Timetable of the upgrade and physics phases at the LHC leading towards the HL-LHC. The width of the coloured boxes in the legend equals one month in the timeline. Major upgrades are usually done during the Long Shutdowns. Last updates on this plan were made in January 2022 (data taken from [30]).

3.1.1 CERN accelerator complex

With a circumference of nearly 27 km and a designed peak maximum centre of mass energy of 14 TeV per proton collision (currently 13.6 TeV are realised [29]), the Large Hadron Collider [31] is the world's most powerful particle collider. Besides protons, heavy ions, for example lead nuclei, can be used in this ring as well. The particle bunches are accelerated and circulated in two beam pipes in opposite directions. To do so, the ring is equipped with several different magnets with field strengths up to 8 T. At four points the beam pipes intersect to collide the two beams. The design peak luminosity of the LHC is $1 \times 10^{34}\,1/(\mathrm{cm}^2\,\mathrm{s})$.

To realise this high centre of mass energy, several preaccelerators form a complex system, as shown in Figure 3.2. Since 2020, the first stage is the linear accelerator LINAC4 [32]. It accelerates negative hydrogen ions gradually to 160 MeV. During injection in the Proton Synchrotron Booster (BOOSTER) [33] the hydrogen ions lose the electrons. Therefore, only the protons remain. These are subsequently accelerated up to 2 GeV in this accelerator [34]. The Proton Synchrotron Booster is followed by the Proton Synchrotron (PS) [35]. In this accelerator the energy of the protons is increased to 26 GeV. Besides of protons, this accelerator is the first ring accelerator in the injection chain that can also accelerate heavier ions, that are provided by the LINAC3 and the Low Energy Ion Ring (LEIR). The last accelerator, before the injection to the LHC happens, is the Super Proton Synchrotron (SPS) [36] where the particles can be accelerated up to 450 GeV.

There are four big experiments located at the four collision points at the LHC. One of them is the LHCb experiment [38]. Its goals are precision measurements of CP

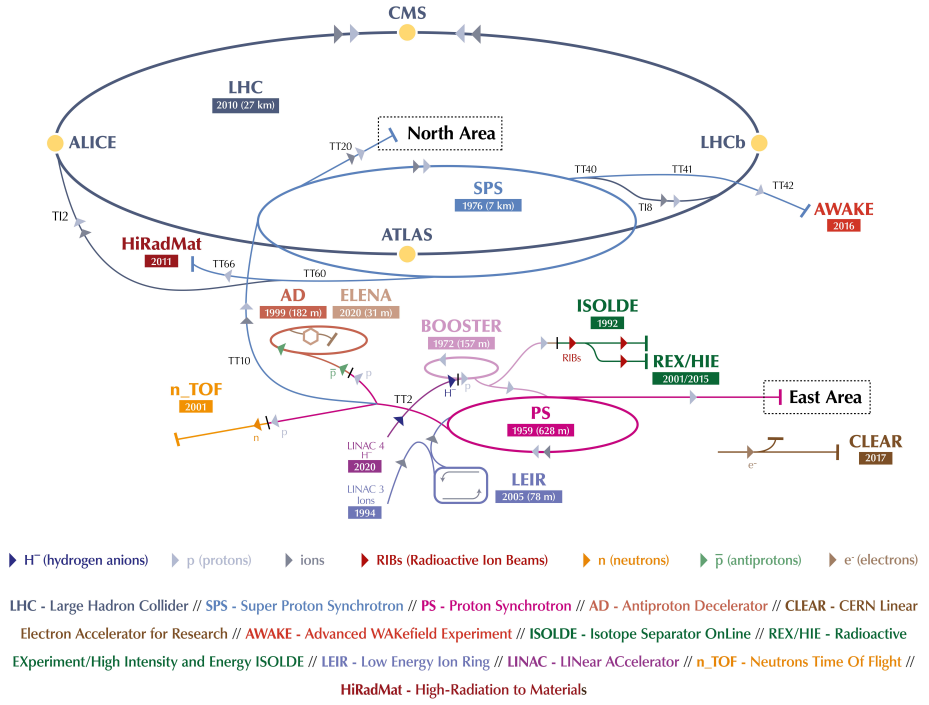

Figure 3.2: The CERN accelerator complex. Depicted are the necessary preaccelerators and the LHC (LHC in dark grey). In addition, the four collision points at the LHC are marked with yellow dots and experiments served by the complex are displayed ([37] adapted).

violation and the observation of rare decays of hadrons which contain beauty quarks. It is built as a one-armed spectrometer due to the symmetry of the production direction of the b-hadrons.
In contrast to this geometry, the other three big experiments, which are general-purpose experiments, share a cylindric, layered setup and large solid angle coverage to detect as many produced particles as possible. The most specialised of these ones is ALICE [39], because it mainly focuses on collisions of lead nuclei. In these collisions the strong interaction is studied in more detail. Additionally, data taking in proton-proton runs is also possible to ensure reference measurements for the other experiments.

The last two experiments, the CMS detector [40] and the ATLAS detector [41], have similar physics goals and can therefore combine their measurements to gain more precise results. This was done for example for the aforementioned discovery of the Higgs boson. The physics goals are the search for the Higgs boson and measurements of its properties as well as the search for new, heavier particles that are foreseen in theoretical additions to the Standard Model. Although designed as general-purpose experiments, these two experiments are suited also for precision measurements. The main difference between these two is their magnet system. Besides from this, the different subdetectors are realised with different technologies, which cause differences in the performances. Both experiments are designed to measure proton-proton collisions as well as collisions of heavy ions.

3.1.2 The ATLAS experiment

The ATLAS (**A** **T**oroidal **L**HC **A**pparatu**S**) experiment [41] is with a length of 46 m and a height and width of 25 m the largest particle detector at a particle collider. To measure different properties of the produced particles that emerge from the particle collision, the whole experiment consists of several subdetectors which are specialised for different purposes. Closest to the interaction point, the tracks of ionising particles are measured as well as the momentum of charged particles. Most of the produced particles are stopped in the calorimetry system and in that way their energy can be determined. The outermost detector subsystem is only reached by the weakest interacting particles, so its measurements are focused on muons. The subsystems are generally arranged symmetrically around the collision point in order to measure equally well in the forward and backward direction. A drawing of the ATLAS experiment and the different detector systems can be seen in Figure 3.3. The following paragraphs describe the different subsystems in more detail, going from the outside to the inside.

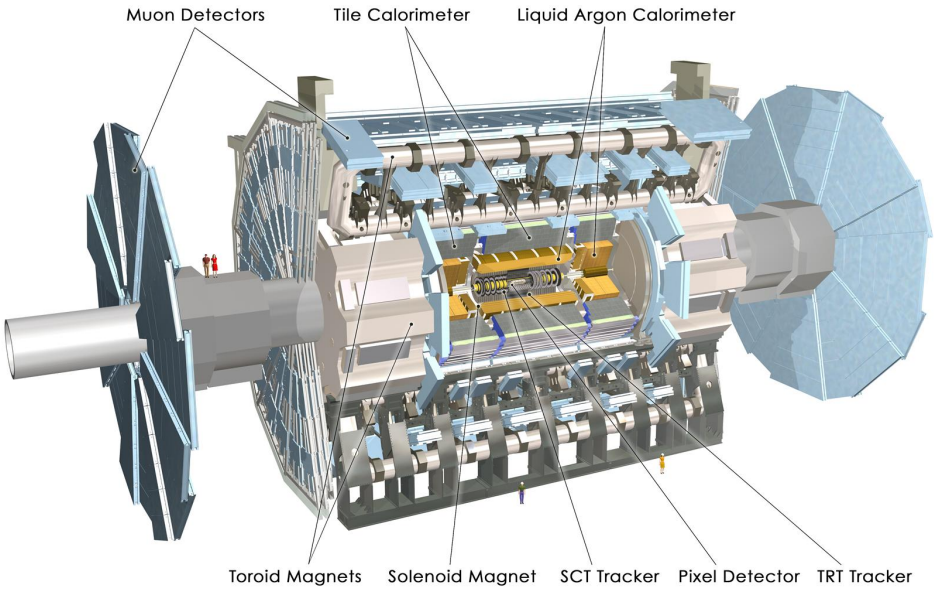

Figure 3.3: A computer generated image of the ATLAS experiment with labelled detector subsystems [42].

The momentum of charged particles is measured by the curvature of their path in a magnetic field. Inside the ATLAS experiment there are two different magnetic fields, caused by two different magnet systems. The bigger one is the toroidal system. It consists of a long barrel toroid and two end-cap toroids, which provide a magnetic field strength of 0.5 T and 1 T respectively. This magnetic field is used for bending the tracks of muons, which are measured by the muon spectrometer. The air-core toroids in the barrel and end-caps ensure a low material budget and therefore the scattering of the muons is reduced.
The smaller magnet system is the solenoid, placed between the tracking detectors close to the interaction point and the calorimeters. Its magnetic field of 2 T is used in the tracking detectors to derive the momentum and the charge of the emerging charged particles.

The aforementioned muon spectrometer is the outermost part of the ATLAS experiment. It is used for the correct identification of muons and the measurement of their charge and momentum. This is done with high precision due to three layers of different tracking chambers. In the barrel region they are arranged cylindrically, while in the end-caps they are formed as discs. Monitored Drift Tube chambers and Cathode-Strip Chambers are the position sensitive technologies for the momentum measurements. In addition to the tracking chambers, there are trigger chambers.

These are used to filter the recorded events. For this purpose, Resistive Plate Chambers are used in the barrel region, while Thin Gap Chambers are installed in the end-caps.

To measure the energy of different particles, a complex calorimetry system is placed between the solenoid and the muon system. It is divided in two major parts, because electromagnetically interacting particles have a smaller range compared to hadronically interacting particles. Thus, the electromagnetic calorimeter has to be placed in front of the hadronic calorimeter.
The electromagnetic calorimeter is designed as a sampling calorimeter which uses lead as absorber plates and liquid-argon (LAr) as the active material. It is composed of a barrel and two end-caps. Its fine granularity is suited for good energy and position measurements of electrons and photons and their correct identification.
The hadronic calorimeter, which encases the electromagnetic calorimeter, ensures a nearly complete solid angle coverage to guarantee good measurements of hadronic particles. It consists of different subsystems such as the scintillator-tile calorimeter in the barrel region. This technology uses plastic scintillating tiles as the active material and steel for the absorber. The same technology is used for two smaller extensions on either side of the barrel. The hadronic calorimeter features two wheels per end-cap to match the coverage of the electromagnetic calorimeter. In the end-caps LAr is used as the active material, while the absorber is copper.
To extend the overall coverage of the calorimetry system, ATLAS has forward calorimeters. They are built as three modules for each end-cap and all share LAr as the sensitive material. The innermost layer is optimised for electromagnetic measurements and, therefore, copper is used as the absorbing material. In the two outer layers, which are responsible for the energy measurement of hadronic particles, tungsten is the absorber.

As mentioned before, the innermost subsystem of the ATLAS experiment is intended for the accurate measurement of particle tracks. To obtain a sufficient resolution, the detectors need a fine granularity. The smallest structures in the Inner Detector (ID) are able to achieve a resolution in the order of a few µm. The used technologies in the ID need to balance the fine granularity, radiation hard material usage due to the proximity to the interaction point and only few material budget to minimise absorption of the produced particles. Thus, the tracking system of the ATLAS experiment consists of three different technologies: semiconductor detectors as pixels and strips and gaseous detectors, so-called straw tubes, in the Transition Radiation Tracker (TRT). With this complementary system the Inner Detector provides good pattern recognition, a high reconstruction efficiency and proper momentum resolution.
The TRT is intended for electron identification besides the tracking information that is gained with this part. Its straw tubes are placed parallel to the beam pipe

in the barrel region, while in the end-caps they are arranged radially in discs.
Wrapped by the TRT, the pixel and silicon microstrip trackers are located. The strip sensors form four double layers in the barrel region and nine double layered discs on each side. They are arranged as double layers back-to-back with a slight rotation against each other to enable a position measurement in two dimensions. The pitch of these strip sensors is 80 µm and the length of a single sensor is about 6 cm [43]. With these modules a position resolution of 17 µm in the smaller direction and 580 µm in the longer direction are realised [41]. This spatial resolution is surpassed by the pixel sensors. The original planar pixel sensors with a pitch of $50 \times 400\,\mu m^2$ have a spatial resolution better than 12 µm [41]. Additionally, in the long direction the spatial resolution is with approximately 115 µm four times better than that of the strip sensors [44]. The pixel sensors are arranged in three concentrically arranged layers in the barrel region and three discs in each end-cap.
The ID was upgraded with an additional layer of pixel sensors in the barrel region in 2014 [45]. This layer is the so-called Insertable B-Layer [46] and it features 3D pixel sensors and planar pixel sensors. Details about these technologies are given in subsection 2.4.1. The new pixel sensors have an even smaller pitch of $50 \times 250\,\mu m^2$. The additional IBL forms with the other pixel layers of the ID a detector system to measure precisely the origins of the produced particles, the so-called vertices.

3.1.3 Upgrade plans for the ITk

Due to the planned higher luminosity related to the HL-LHC, the current tracking system of the ATLAS experiment needs to be replaced with the new Inner Tracker (ITk) [47, 48] during the Long Shutdown 3. With the higher luminosity comes an increase of the number of proton collisions per beam crossing. This number will increase from around 60 during the last period of data taking [49] up to 200. This requires a finer granularity for the innermost tracking system to distinguish between the single vertices. In addition, with more traversing particles during the lifetime of the ITk, the radiation level for the inner layers of the new detector increases by one order of magnitude compared with the ID. To maintain the same tracking performance as the ID, new technologies have to be considered for the ITk to fulfil the requirements of the HL-LHC.

The current planned layout of the ITk can be seen in Figure 3.4. Only one quadrant of the whole detector is depicted. In contrast to the current ID, which uses different detection technologies, the new ITk is planned as an all-silicon system. Closest to the interaction point is the Pixel Detector. It is encased by the Strip Detector for a greater room coverage. The barrel parts are built cylindrically, while the end-caps are built as discs.

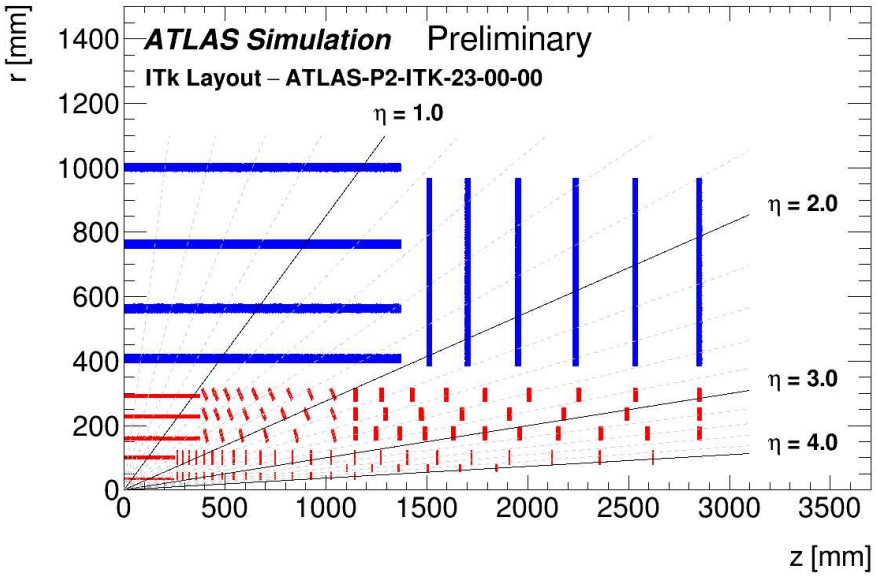

Figure 3.4: A sketch of the layout of the active elements in the planned Inner Tracker of the ATLAS experiment (blue: Strip Detector, red: Pixel Detector) [50].

The Strip Detector is divided in the barrel and the end-cap region. Its barrel region is formed by four concentrical layers of strip sensors that are arranged back-to-back. On each side of the barrel is an end-cap with six rings of strip sensors. These are also arranged as double layers.
The Pixel Detector consists of five layers in the barrel region. The pixel sensors are mounted in the central region straight and further out inclined by an angle of 75°. This inclined layout maximises the room coverage whilst ensuring at the same time a low material budget. To complete the Pixel Detector, several rings of pixel sensors form the end-caps on each side. One advantage of the ITk is the possibility to replace the two innermost pixel layers. This is needed due to the harsher radiation level during operation of the HL-LHC which calls for a replacement of these parts after a certain time.

The Pixel Detector consists of 3D and planar silicon sensors, which are used together with an additional attached readout chip as hybrid pixel detectors. The active size of the readout chip is $19.2 \times 20\,\mathrm{mm}^2$. There are different sizes of the produced detectors: so-called triplet and quad modules [51]. Triplets are three connected read-out chips that are each bump-bonded to an equally sized pixel sensor. The quads are four connected read-out chips that are connected to a single $4 \times 4\,\mathrm{cm}^2$ sensor. The triplets are used in the innermost barrel layer and in the two innermost

ring layers. All other layers are equipped with quad modules.
The innermost barrel layer and parts of the two innermost end-cap are equipped with 3D pixel sensors [52]. Their active thickness is 150 µm. However, they are produced with an additional 100 µm support structure beneath the active material to ease the handling. The 3D pixel sensors are used due to their advantages discussed in subsection 2.4.1. However, since their much more complex production process, they are more cost expensive compared with other technologies. Therefore, they are installed only in the layer closest to the interaction point. The planar sensors are produced in an n^+-in-p structure. This comes, as mentioned in subsection 2.4.1, with the advantage of a much simpler production than the currently in the ID used n^+-in-n sensors. Moreover, type inversion, that was explained as a consequence of radiation damage in subsection 2.3.1, does not occur in n^+-in-p sensors, since p-type silicon does not invert with increasing irradiation [3]. Therefore, in these sensors the depletion zone growths before and after irradiation from the pixel side to the back side. In this way, the sensors can be operated, even if the bias voltage can not be high enough to deplete the whole sensor volume. They are produced with a thickness of 100 µm and a thickness of 150 µm. The thinner ones are installed in the second innermost layer, whereas the remaining layers are equipped with the thicker sensors. The shape of the pixels can be a square with the area $50 \times 50\,\mu m^2$ or a rectangle with the area of $25 \times 100\,\mu m^2$. The rectangular pixel pitch is used in the innermost barrel pixel layer, whereas all other layers are equipped with sensors with the square pixel design [51].

To complement the ITk, the High Granularity Timing Detector (HGTD) [53] is proposed. It covers the very forward region, due to its position in the gap between the barrel and the end-cap calorimeter. This subdetector is equipped with low gain avalanche detectors with time resolutions of only a few tens of ps. This time resolution can be reached with only slight degradation during the whole foreseen operational lifetime. With this precise time information, it is possible to distinguish the vertices of a single bunch crossing that are close in time, but that occur at different locations.

3.2 Tests of Bare Sensors

This section deals with the measurements for the Step-3 qualification process of the Market Survey for the ITk sensors. The market survey is a process with three steps: first of all a self-disclosure was asked from potential manufacturers. Secondly, they were asked for dummy sensors to be tested by the market survey community to check their quality. The last step, Step-3, requires sensors that comply with the final layout. The properties of the bare planar silicon pixel sensors, especially the

measurements of the thickness and planarity of the sensors as well as tests of their electrical behaviour, are presented in this chapter. These measurements provide an overview about the usability of such sensors in the Inner Tracker. In addition, each measurement qualifies the tested sensors for the subsequent measurements or reveals operation boundaries for further tests. Finally, the documentation of possible malfunctions after each investigation step helps to disentangle the possible reasons for later failure.

Because the final design of the silicon pixel sensors was not clear in the beginning of this thesis, the manufacturers could decide to produce sensors with the two pixel sizes of $50\,\mu m \times 50\,\mu m$ or $25\,\mu m \times 100\,\mu m$. Both pixel geometries were investigated with respect to the requirements of the physics performance of the detector. Moreover, the bare sensors feature for biasing either the punch-through technology, polysilicon resistors or temporary metal (see subsubsection 2.4.1 for more information). This gives various combinations of the pixel shapes and biasing techniques. Thus, many sensors have to be tested to see differences of the performance with respect to the different combinations. Since there are quite a few manufacturers all over the world that are able to produce such sensors, the measurements for the market survey were split across numerous institutes. In this way, the time-consuming measurements were performed in parallel to accelerate the process.
The manufacturers delivered the sensors either as diced sensors or as complete wafers that include all required sensors. Within the market survey, each vendor had to deliver at least 10 sensors with Single Chip (SC) size and 20 sensors with Double Chip (DC) size. The sizes refer to the dimensions of the RD53A mentioned in subsection 2.4.2. Therefore, the SC is approximately $2 \times 1\,cm^2$ large and the DC has an area of roughly $4 \times 1\,cm^2$. Optionally, the manufacturers could provide 10 sensors with a quad size, which are $4 \times 4\,cm^2$. If the manufacturer applies for the corresponding production, all of those mentioned sensors have to be delivered for the two possible thicknesses of $100\,\mu m$ and $150\,\mu m$ that are foreseen to be used in the ITk. These large numbers of sensors give information about the uniformity of the sensor properties across a production batch. Moreover, if a manufacturer offers sensors with different layout options, they can be compared with each other.

This section covers the measurements for sensors of a manufacturer, namely FBK, who supplied two wafers, one for each thickness. These will be referred to as the thin wafer and the thick wafer in the following. To speed up the market survey process, the vendor has offered to measure the electrical properties of the structures included in the wafers. This also saves time in the later production process if the manufacturers measure the sensors themselves. In order to independently verify their measurements, the data already taken by the vendor is cross-checked at TU Dortmund University.
In the appendix, in section A.2, the results of the measurements for another manu-

facturer, namely HPK, who had provided diced sensors, are presented. This data is included because two independent institutes always check their measurements for a greater reliability. Therefore, measurements for the sensors of two manufacturers were carried out at the TU Dortmund University to be compared with the measurements done at the University of Göttingen. The names of the manufacturers were withheld during the process of the market survey to ensure an unbiased assessment of the sensor quality.

3.2.1 Visual Inspection and Metrology

The visual inspection of bare sensors is a very straightforward investigation. With this examination, the overall quality of the sensor surfaces is determined.
The first visual inspection is carried out at the reception of the sensors. The first and superficial investigation is done by eye to check whether all wafers and sensors were damaged during packaging and shipment. Typical damages due to missing protection while shipping are cracks or partially broken sensors and wafers. For both manufacturers, none of the delivered sensors or wafers showed any sign of damage caused by the shipment.
After this first inspection, the wafers are investigated under an optical microscope to check their quality in more detail. Each sensor on the wafer is photographed with a twentyfold magnification to document the actual condition of the sensor. Afterwards, the whole surface of the single sensors is studied with a hundredfold magnification. In this step, special features of the sensors are detected. Defects and irregularities are studied with an even greater magnification to work out further details. For every detected striking feature or damage an individual photograph is stored for the later documentation.

Photographs of exemplary defects and irregularities are shown in Figure 3.5. The first shown defect in Figure 3.5a is a large scratch across the sensor surface. The scratching happened during previous measurements at another facility. Since the scratch has a length of roughly 14 mm, it is visible even by eye. Nevertheless, it is also investigated under the optical microscope to see how badly the sensor is damaged. A close-up of the scratch, where the damage is shown in more detail, is depicted in Figure 3.5b. As it can be seen, the scratch is not very deep and has only damaged the metallisation of the pixels. If such scratches are deeper, they might damage the underlying implants of the sensor. If this happens, the flip chip process might fail in this region and no proper connection of the readout chip and the sensor can be obtained. Then the module would have lower to zero tracking efficiency in this region. Therefore, those severe defects need to be detected on the sensors as well as on the readout chips [54]. In addition, large scratches as the shown one

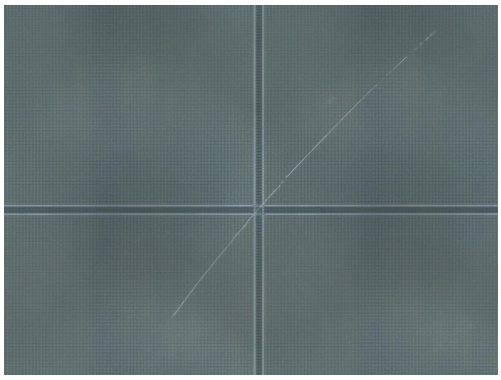

(a) Scratch, visible by eye, 20x magnification.

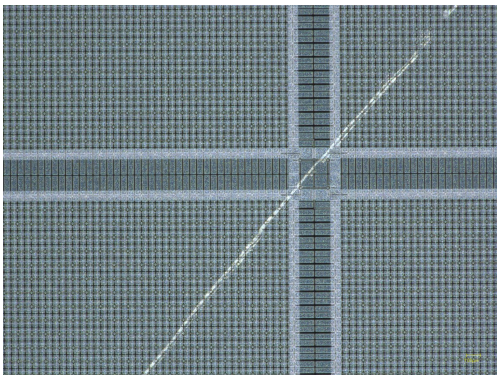

(b) Close-up of scratch, 100x magnification.

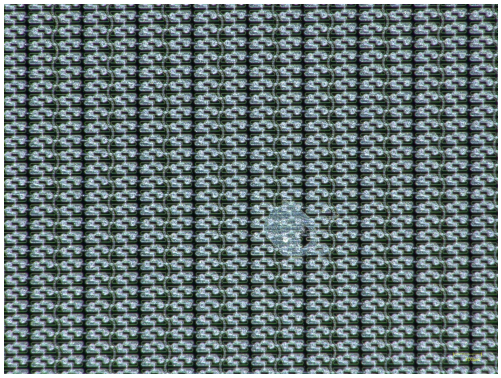

(c) Short-circuited pixels, 200x magnification.

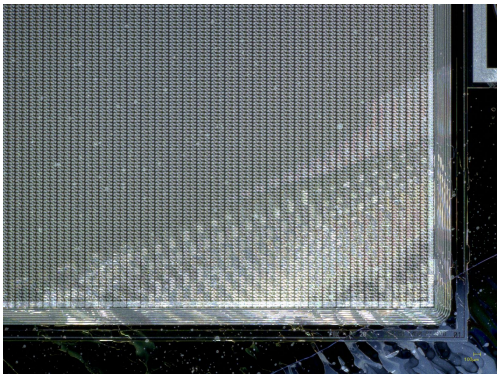

(d) Residues of a liquid, 50x magnification.

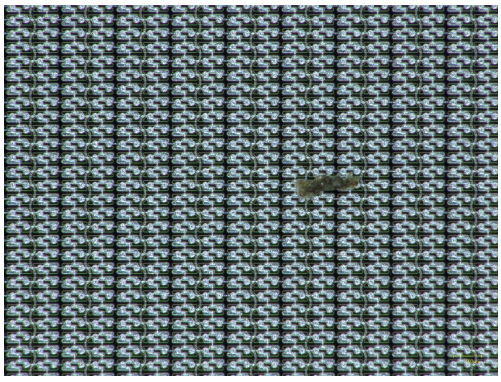

(e) Dirt or dust particle, 200x magnification.

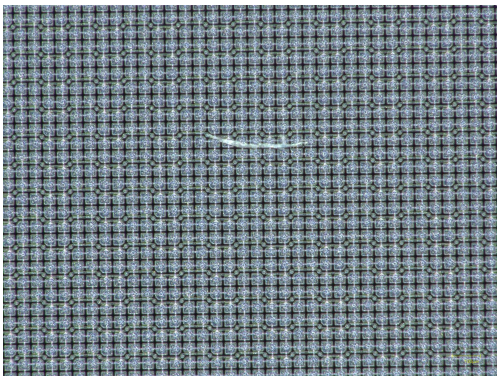

(f) Lint, 200x magnification.

Figure 3.5: Photographs of observed defects and anomalies on delivered wafers.

can lead to deterioration of the electrical behaviour of the sensor. An example for the comparison of the measured electrical properties of an undamaged sensor and the same sensor, but now with a scratch, can be found in the appendix as it was measured for the second manufacturer (see especially Table A.17 and Figure A.10). Another peculiarity, that can only be seen in greater magnification, are irregularities of the pixel matrix. One example for this is shown in Figure 3.5c. There, approximately 20 pixels in a circular region are short-circuited with their neighbours. No detailed pixel implantation can be identified in this area. Based on the colour of this region, this seems to be caused by some kind of aluminium residues. For the market survey, only the documentation of the quality is of importance, so no effort was made to find out what the origin for this irregularity is.
In Figure 3.5d, the residues of some liquid can be seen. In the bottom right corner of the picture, the larger stains look a little bit milky, but across the pixel matrix the residue appears shimmering. Additionally, several dried drops of the liquid can be seen above the pixel implants and on top of the bare silicon.
All of the above mentioned defects are permanent. In contrast to those anomalies, detected dust particles (Figure 3.5e) or fibres (Figure 3.5f) are not permanent defects. They can easily be removed from the surface with a flush of dry air. Only if the particles are very hard and scratch the surface while moving, they cause permanent damage to the sensor. However, since the cleaning of the sensor is one of the first steps in the flip chip process, no cleaning treatments of the wafers are performed at the institutes where the measurements of the market survey are carried out.

Detailed lists with the number of permanent defects found on each sensor at reception are presented in Table A.1 and Table A.2 in the appendix. These tables are used as reference to reveal possible correlations between the defects and anomalies in further measurements. The following paragraphs give an overview of the details.
For the thin wafer, only three out of 29 sensors on the wafer (which equals roughly 10%) have residues from liquids. All three structures are located next to each other at the bottom of the wafer. Therefore, it is safe to say, that the liquid has not soiled structures far away from its origin. None of the damaged sensors has scratches that are larger than 5 mm and only two show scratches smaller than 5 µm (two out of 29 is approximately 7%). Additionally, five sensors show irregularities of the pixel matrix. However, three of them have only two irregular pixels each and only two sensors feature a greater area, where approximately ten pixel implants are short-circuited (again, these two equal 7% of conspicuous sensors compared to all structures on the delivered wafer). Since ten irregular pixels compared to the total number of $400 \times 192 = 76800$ pixels in a single chip size sensor is only 0.01% (and for double chip size sensors the ratio is even smaller), this number is no reason for concern.
On the thick wafer, the same structures as on the thin wafer show residues from

a liquid. This might point to a general problem, because this is observed for two wafers in the exact same location. Additionally, the sensors on this wafer have much more scratches from previous handling. Six structures show at least one scratch smaller than 5 mm, which are 20% of all structures on this wafer. Moreover, especially one of the quad structures is heavily damaged, with five small scratches and two larger ones. Apart from this heavily damaged structure, none of the other sensors has a large scratch. There are also five sensors that have irregularities within their pixel matrix (which equals 17%). However, as stated above, the proportion of short-circuited pixels compared to the total number of pixels within a single structure is quite low.
Overall, most of the sensors on the delivered wafers seem to be in a good condition and only a small fraction shows defects from previous handling. Although some of the sensors show some severe defects like scratches across the whole surface, all of the sensors are tested electrically. With those tests, the possible influence of the damage on the electrical behaviour is studied.

Another visual inspection is done after all measurements of the market survey for the corresponding sensor or wafer are finished at one institute. In such a way, the damages caused by handling can be tracked. Lists with the numbers of all detected permanent defects are shown in Table A.3 and Table A.4 in the appendix. The differences to the number of defects right at reception are also indicated in the tables to ease the evaluation of the handling of the wafers. A general overview is given in the following.
Most of the differences to the quality at reception is one additional small scratch at the sensor, which is smaller than 5 mm. This is the case for 22 sensors on both wafers, whereas overall 26 sensors feature after all measurements more scratches than at reception. This is compared to the 58 structures on both wafers a percentage of 45% of sensors that are scratched during the measurements. Most of the additional scratches are only small and in close proximity to the contact pad. Therefore, it is likely that these scratches are caused by the needle with which the sensor is contacted for the electrical measurements. Details about the setup are shown in Figure 3.6. Since the needle probers are adjusted manually, it is easily possible to inflict more pressure and then the needle scratches across the contact pad. A photograph of the needle prober in contact with the wafer is shown in Figure 3.6b. If there are more scratches than only one additional small scratch, this is due to the fact that the sensor was contacted at different contact pads or was scratched accidently by the needle. However, none of the detected scratches is very deep and all are located at the edges of the pixel matrix.

Since no bigger additional scratch is found on the structures, this is a strong point for the cautious handling of the wafers. Additionally, there are no new residues of liquids on the surface of the wafers. Only for one sensor the number of the short-circuited

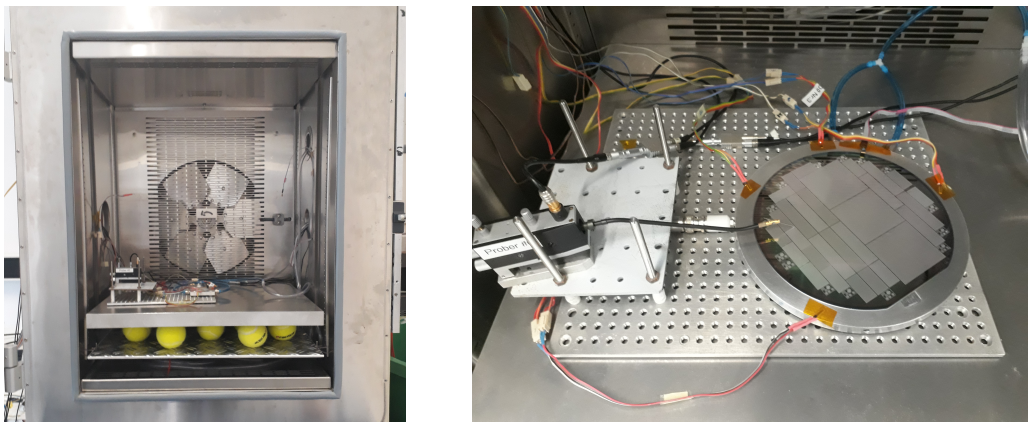

(a) The inside of the climate chamber. **(b)** Needle prober contacting the wafer.

Figure 3.6: Photographs of the setup for electrical test in the climate chamber. In **(a)** the inside of the climate chamber with a thick aluminium plate based on tennis balls can be seen and in **(b)** the manual needle prober in contact with the wafer under investigation is shown.

pixels has increased. The reason for that is not known, but in the photograph a small circular shaped mark is visible on the pixel surface, which seems to connect several pixels. However, since the total number of newly short-circuited pixels is only six, this is no matter of concern. In addition, since this has happened apparently only once, it is proven that the handling with the manual needle prober is well understood and careful handling of the wafers is carried out. A new wafer prober is now available at the TU Dortmund University. This tool overcomes the mechanical instabilities of the setup in the climate chamber as it is shown in Figure 3.6a and eliminates the need for the manual use of needle probers.
The most striking feature of the structures after all measurements is the increased number of dust particles and lints. This is expected, because the wafers are not handled exclusively in clean rooms. The normal air in the labs contains dust particles which then attach to the surfaces. The lints originate most likely from clothing, since no specially designed clothing is used during handling of the wafers. However, these particles can be removed by a flush of dry air, so their appearance is accepted.

Metrology

After the visual inspection at reception, the thickness and the bow of the wafers are measured. This is important for the later flip chip process, since only for really planar sensors a successful connection of the readout chip and the sensor is

guaranteed. The flip chip process and bump bond deposition give the limit for the maximum sensor thickness deviation. Within the market survey for planar pixel sensors, the maximum allowed thickness deviation within a single sensor is 15 µm. If the thickness is not uniform across a single sensor, the flip chip process can fail for wedge-shaped geometries. For this reason, the absolute measured thicknesses are less important than the actual geometry and the bow of the sensors for this market survey.

Since this part features the measurements of complete wafers, the maximum allowed thickness deviation of 15 µm within a single sensor is not a meaningful quantity for qualifying the wafers. However, to have at least an estimator for the quality of the wafer production, the thickness deviation of the whole wafer is compared to the same criterion as for a single sensor, i.e. 15 µm. The bow of the wafers must not exceed 100 µm for the wafers to be accepted for further processing. This requirement is valid only for the 6-inch wafers that are investigated at TU Dortmund University. If the wafers have a diameter of 8-inch, they are accepted with a maximum bow up to 150 µm.

The measurements for the market survey are carried out at various institutes, so naturally the labs are equipped differently. Therefore, the measurements have to be adjusted to the available measuring instruments. Moreover, the results have to be in a form that is comparable with other results obtained by other measurement techniques. Hence the institutes have to decide for a consistent methodology across the different laboratories.
Some of the institutes use an optical microscope to measure the height of the sensors or wafers. To do so, the so-called focus method is used. For this measurement, the height of beforehand specified measurement points at the edges of the sensor or wafer and on the underlying chuck is measured ten times. The repeated measurements are used to calculate the measurement uncertainty. To measure the bow of the device specified measurement points only across the device are used. A sketch of the distribution of the measurement points across the device and mounting chuck is shown in Figure 3.7a.
At other institutes macroscopes are available for the measurements of the thickness and the bow. With those instruments, full 3D scans can be performed to get precisely the height of the measured object. It was decided to perform only line scans with the macroscope to have a consistent methodology across the different institutes. With those scans, the measurement results of the microscope measurements and the macroscope measurements can easily be compared. The latter method of the line scans will be described in more detail in the following together with actual examples of the measurements, because at TU Dortmund University a macroscope is available.

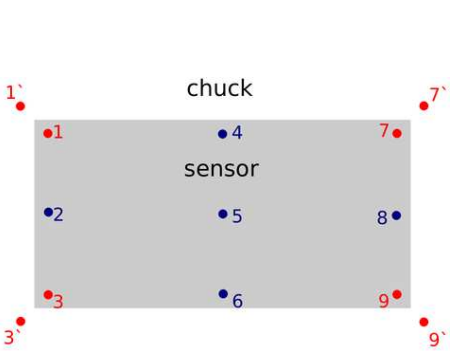

(a) Sketch for the focus method [55].

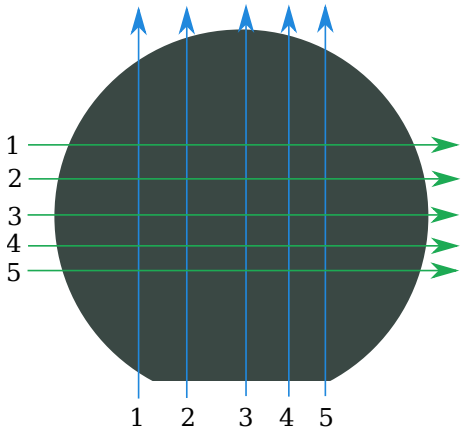

(b) Distribution of line scans.

Figure 3.7: Sketches for the different measurement techniques to determine the height and bow of devices. In **(a)** the measurement points for the focus method are shown. The red points are used to calculate the thickness of the device and the nine labelled points on the sensor are used to calculate the bow. The sketch in **(b)** shows the distribution of the line scans across a 6-inch wafer. The blue arrows indicate the vertical line scans, while the green arrows symbolise the horizontal measurements. The arrows declare the direction of the measured profile as well. The exact position is different for each measurement due to different wafer placement. Therefore, the positions in this image are not to scale.

For the measurements carried out within this thesis, the macroscope Keyence VR-3200 [56] is used. To measure the height, firstly, a metal chuck where the wafer is fixed is mounted onto the table of the macroscope. The chuck contains a number of circular grooves where vacuum can be applied to hold down the wafer. Secondly, the wafer is put in the middle of the chuck and the vacuum is applied. Therefore, the wafer is held down and its natural bow can not disturb the measurement of the height.
The data for the height measurement is collected with five line scans in the horizontal direction and five additional line scans in the vertical direction. The distribution of the line scans across the wafer is shown in Figure 3.7b. These line scans cover the whole wafer width and additionally some parts of the chuck. As a result, the data points for the height of the chuck can be used to correct the measured data, if the chuck is not mounted evenly. The Keyence VR-3200 has a measurement uncertainty of $\pm 3\,\mu m$ for the height measurements within those line scans [56]. Within the line scan, the measured heights are recorded approximately every $23\,\mu m$.

In each data set, regions on both sides of the wafer have to be assigned to the chuck to correct the possible misalignment. To do so, the first and last 42 measured heights in each data set of the line scans are chosen. These 42 measurements in the scan direction equal a measured length of approximately 1 mm. Therefore, on both sides of the wafer, a 1 mm length of the chuck data is used to estimate the base line of the corresponding measurement. A straight line of the form $y = a \cdot x + b$ is fitted to the height values y and the length of the line scan x, both given in µm, to correct the taken data. Examples of fitted parameters for the straight line fits can be found in Table A.5 in the appendix for completeness.
The values reveal only very slight misalignments of the chuck for the height measurements. However, to ensure a robust analysis scheme throughout all measurements, the original measured values for the height are nevertheless corrected in the following way:

$$y_{\text{corrected}} = y_{\text{original}} - (a \cdot x + b). \tag{3.1}$$

In this formula, y_{original} is the recorded value of the height with its measurement uncertainty of $\pm 3\,\mu m$ and x refers to the position within the line scan. The errors of the fit parameters a and b as well as the measurement uncertainty of $\pm 3\,\mu m$ of each measured original height are propagated through the analysis.

A graph with the corrected data for the heights of one line scan is shown in Figure 3.8. Since the propagated uncertainties of the data points are around $\pm 3\,\mu m$, they cannot be seen in the plot. The plateau region of the wafer reveals a length of approximately 150 mm. Since this scan line is taken close to the maximum diameter, this is in good agreement with the expected diameter of six inches, which equals 152.4 mm. The mean height in the plateau region is slightly above $600\,\mu m$. Since the wafer has

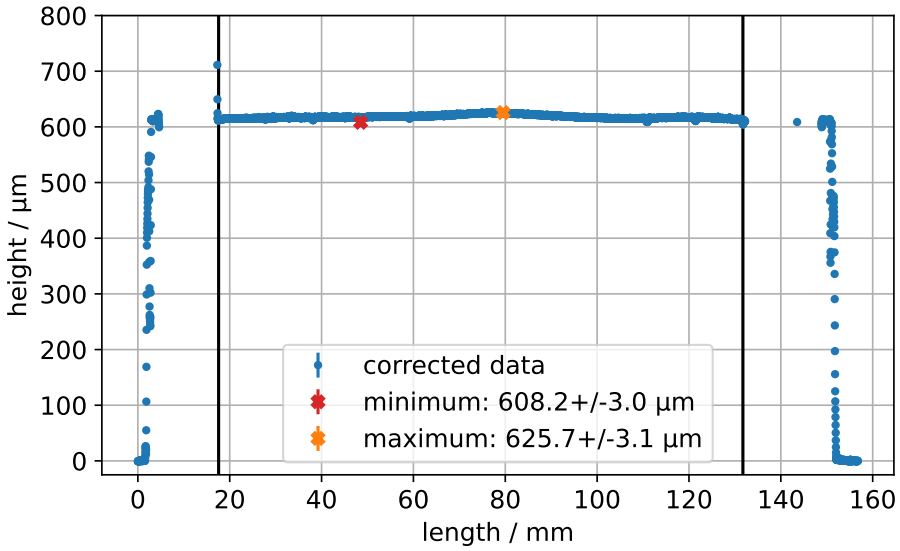

Figure 3.8: Corrected data for the height measurement of the third horizontal line scan (close to the middle of the wafer) of the thin wafer. Each measured value has a measurement uncertainty of approximately $\pm 3\,\mu m$, which is too small to be visible in this plot. The black lines indicate the beginning and end of the region of interest. Only within this region the maximum and minimum values are determined.

an expected thickness of only 100 µm, this is conspicuous. The extra 500 µm are explained by an additional support layer that is added to the backside of the wafer. Hence, the whole wafer gains more stability which eases the handling. The support layer is thinned out in further processing steps.
The most striking feature in Figure 3.8 are the gaps around 15 mm and 135 mm where no data points are present. This is due to reflections of the light of the macroscope by regions of the wafer surface where bare silicon is present. In those regions, no values are recorded for the line scan. Moreover, there are artefacts from the reflections that disturb the measurement and lead to unreasonable high (or low) values. An example for this can be seen on the right edge of the gap around the length of 15 mm.
Since these unphysical values distort the calculation of the relevant parameters, they have to be excluded. As a result, the analysis program scans the data set for missing values and removes those data pairs. Since the reflections happen only at the edges of the wafers, the data set is split in two parts. The gap at the highest x value in the first half and the gap at the lowest x value in the second half of the data set are then localised. To minimise the effect of the artefacts, the region of interest (ROI), wherein the main analysis takes place, starts roughly 0.5 mm after the last gap on the left side of the scan and ends approximately 0.5 mm before the first gap on the right side of the scan. The start and end point of the ROI can be seen as black lines in Figure 3.8.

The height of the wafer is given by the mean of all values inside the ROI. The maximum deviation of the thickness of the wafer is determined as the difference between the maximum measured height and the minimum measured height inside the ROI. For this analysis, there is no smoothing of the measured values performed. Results of the analysis are shown in Table 3.1 and discussed in the following.

The mean heights of the thin wafer differ for the different line scans only about 10 µm. Compared with the total thickness of roughly 600 µm, this is a relative deviation of approximately 1.7%. Since the production uncertainties of the applied 500 µm support layer are not known, it has to be assumed that a fraction of the additional height is caused by this layer. Therefore, the mean heights for this wafer are in compliance with the expectations.
All maximum deviations of the horizontal line scans meet the requirement of the market survey of 15 µm within their uncertainties. However, the vertical line scans show something different. The results are explained in the following paragraph.
The vertical line scans number 2 and 5 show the largest deviations with more than 30 µm. However, the maximum and minimum values, respectively, that are detected by the analysis script are only artefacts of reflections. This can be seen in Figure 3.9 in more detail. Therefore, those large values can be explained, and the real deviation, ignoring those artefacts, is smaller. The vertical line scans number 3 and 4 reveal a

Table 3.1: Relevant parameters for the market survey from the height measurements. The values refer to the five horizontal and vertical line scans.

wafer	line scan	mean height / µm	maximum deviation / µm
thin	horizontal 1	611.3 ± 0.6	16 ± 4
	horizontal 2	614.4 ± 0.6	18 ± 4
	horizontal 3	618.1 ± 0.6	18 ± 4
	horizontal 4	619.2 ± 0.6	15 ± 4
	horizontal 5	619.8 ± 0.6	14 ± 4
	vertical 1	610.0 ± 0.6	17 ± 4
	vertical 2	612.9 ± 0.6	34 ± 4
	vertical 3	615.1 ± 0.6	21 ± 4
	vertical 4	616.3 ± 0.6	19 ± 4
	vertical 5	619.5 ± 0.6	32 ± 4
thick	horizontal 1	660.9 ± 0.6	23 ± 4
	horizontal 2	664.3 ± 0.6	28 ± 4
	horizontal 3	666.2 ± 0.6	20 ± 4
	horizontal 4	665.6 ± 0.6	17 ± 4
	horizontal 5	667.5 ± 0.6	16 ± 4
	vertical 1	658.3 ± 0.6	22 ± 4
	vertical 2	659.4 ± 0.6	15 ± 4
	vertical 3	660.2 ± 0.6	17 ± 4
	vertical 4	662.3 ± 0.6	19 ± 4
	vertical 5	663.2 ± 0.6	13 ± 4

slight excess of material in the middle of the wafer. Plots of those line scans are presented in Figure 3.10a and Figure 3.10b. This excess of material of the wafer in its centre is validated by the horizontal line scans number 2 and 3, that show a similar profile with a bump in the middle. The plots of the horizontal line scans are shown in Figure 3.10c and Figure 3.10d With these four intersecting line scans, the bump on this wafer is confirmed.
The wafer is qualified overall as good, although not all maximum deviations meet the requirement of the market survey. Even the largest reasonable deviations of the measured heights are only $(21 \pm 4)\,\mu m$. This is in comparison with the total thickness a relative deviation of only 3%. Therefore, all derived values indicate a good uniformity of the thin wafer. If it would be used to dice the sensors, none of them should have natural thickness deviations that would disturb the flip chip process. From this perspective, the requirement of a maximum deviation of 15 µm across the entire wafer is too tight to be reasonable for whole wafers. To classify the planarity of whole wafers, a different requirement from that for the diced sensors is needed. Overall, the market survey community decided after discussions that the qualification as good is justified for this wafer.

For the thick wafer, the mean heights differ as well only by less than 10 µm. With regard to the overall thickness of at least 650 µm, this equals a relative deviation of roughly 1.5%. Since the production uncertainty of the support layer of 500 µm is expected to be the same for both wafers, the relative deviation of the thickness of the thick wafer is smaller compared with the thin wafer. Therefore, it can be said that the uniformity across the thick wafer is slightly better.
The maximum deviations for the vertical line scans are mainly within the market survey requirement. Only the first vertical line scan shows a higher deviation with $(22 \pm 4)\,\mu m$. Nevertheless, this profile reveals a slight bump in the second half of the wafer which can be seen in the plot in Figure 3.11a). This region is covered by the horizontal line scans number 1 and 2, which confirm the bump at that position (plots presented in Figure 3.11b and Figure 3.11c). Therefore, their higher deviations of more than 20 µm can be explained as well.
As before, since none of the deviations is a matter of concern for the flip-chip process, the wafer is qualified as good. The vendor has proven to be able to produce planar wafers for the ITk with uniform thickness. Based on the presented results, the market survey community has decided to trust the vendor to be able to produce planar wafers with the target thicknesses of 100 µm and 150 µm for the ITk.

The same setup as before is used to measure the bow of a free standing wafer (or sensor). However, the vacuum is not applied to the chuck in order to measure the bow. Hence, the wafer is not pulled down to the chuck and can stay in its natural shape. To ensure, that the measured object lies loosely on the chuck, it is slightly poked with a vacuum tweezer until its movement can be observed. Afterwards, the

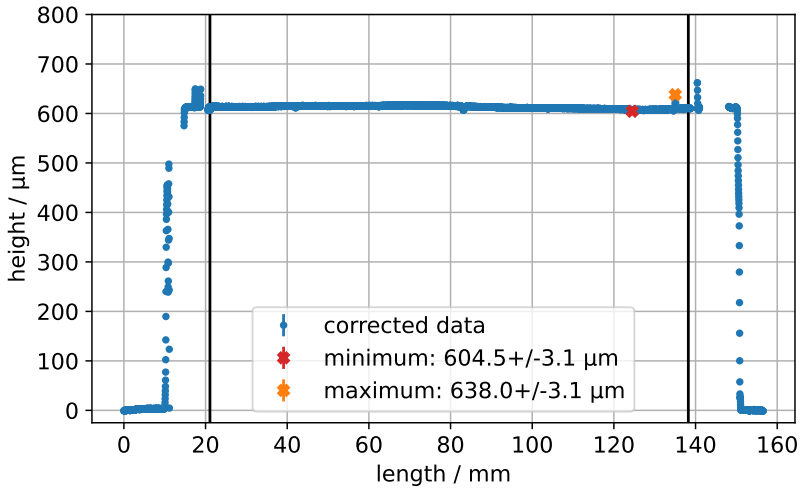

(a) Second vertical height profile.

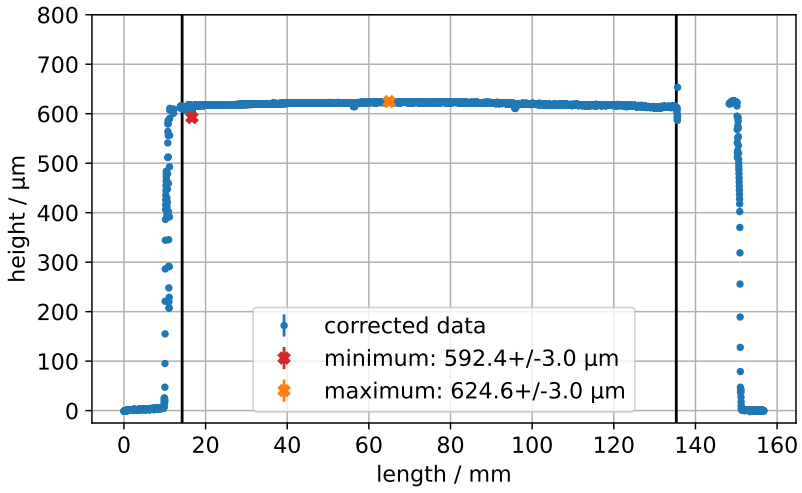

(b) Fifth vertical height profile.

Figure 3.9: Corrected data of the height measurements for the thin wafer. In **(a)** an unreasonable high value for the maximum and in **(b)** an unreasonable low value for the minimum are detected. Both extreme values are caused by artefacts from reflections near the edges.

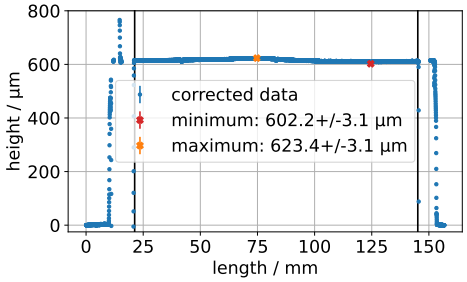

(a) Third vertical height profile.

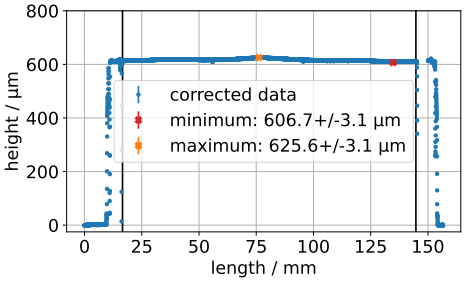

(b) Fourth vertical height profile.

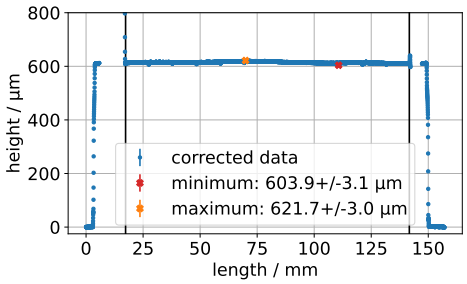

(c) Second horizontal height profile.

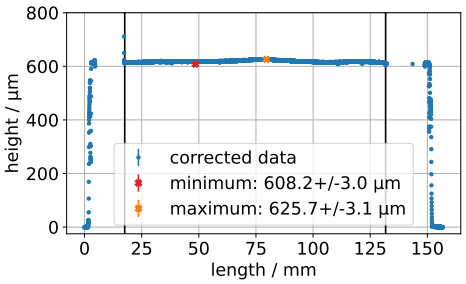

(d) Third horizontal height profile.

Figure 3.10: Corrected data of the height measurements for the thin wafer. All four line scans show a material excess in the middle of the wafer.

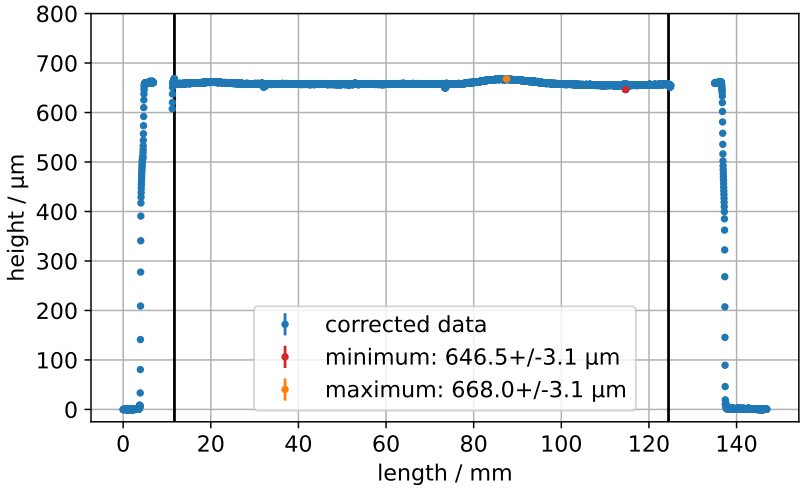

(a) First vertical height profile.

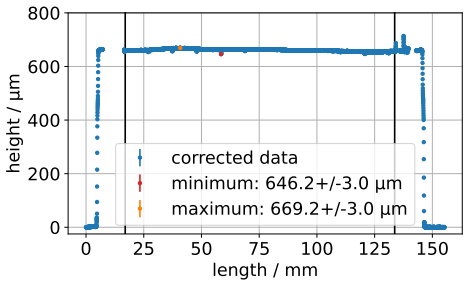

(b) First horizontal height profile.

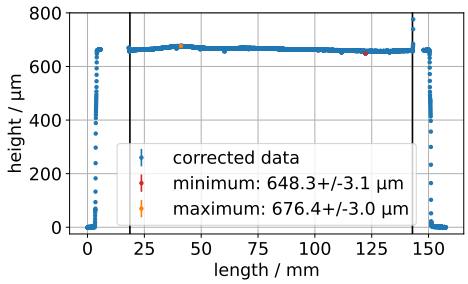

(c) Second horizontal height profile.

Figure 3.11: Corrected data of the height measurements for the thick wafer. All three line scans show a material excess on the wafer.

same measurement procedure with the macroscope as before, consisting of the five vertical and horizontal line scans, is carried out.

The first step in the analysis is again the correction of a possible misalignment of the chuck. The fitted parameters for the straight line fits can be found in Table A.6 in the appendix for completeness. Again, the values reveal a pretty good alignment, so the chuck was mounted evenly.
For the data sets, a similar analysis as before is performed. However, since the wafer is in its natural bow, no mean height of the values inside the ROI is calculated. The relevant value for the market survey is the maximum bow that the wafer shows. This bow is defined in this analysis scheme as the difference between the maximum height and the minimum height inside the ROI. In Table 3.2 the results of the analysis are presented. There, not only the maximum bows are listed, but also the detected minimum and maximum values. With this additional information, conspicuous values can be detected more easily.

Overall, the measured bows for the thin wafer are pretty low. Especially when compared with the values for the height measurements in Table 3.1, it becomes clear that this wafer is without a real bow. Only the bow for the vertical line scan number 5 is conspicuous. The measured profile of this scan is shown in Figure 3.12 in detail. The maximum value in this plot, which is the exceptional value that leads to the large bow, is caused by a sharp spike. Since this peak is in very close proximity to the detected gap which is caused by reflections, it is assumed that the peak is only an artefact of these reflections. Therefore, the measured heights within the peak region can be neglected and a maximum of approximately 650 µm is assumed. This leads to a maximum bow of roughly 35 µm which would be the largest of all measurements, but still well within the requirement of smaller than 100 µm. As a result, this wafer fulfils the market survey requirement completely.

None of the measured maximum or minimum heights for the thick wafer is unreasonable. Moreover, the maximal measured bow is 33 µm, which is only a third of the maximum allowed bow for this wafer size. Therefore, this wafer passes as well the market survey requirement and the vendor has proven its ability to produce wafers without noticeable bows.

3.2.2 Electrical Tests before Irradiation

The measurement of the electrical characteristics is mandatory for all devices that are delivered. The measurement of the current-voltage (IV) characteristic and the capacitance-voltage (VC) characteristic is relatively short with a maximum duration of approximately 30 minutes per sensor. This allows to measure these characteristics

Table 3.2: Relevant parameters from the analysis of the measurement of the wafer bow. The values refer to the five horizontal and vertical line scans.

wafer	line scan	height / µm		bow / µm
		minimum	maximum	
thin	horizontal 1	606.6 ± 3.1	630.8 ± 3.0	24 ± 4
	horizontal 2	608.7 ± 3.1	630.7 ± 3.0	22 ± 4
	horizontal 3	616.1 ± 3.1	632.3 ± 3.0	16 ± 4
	horizontal 4	615.0 ± 3.1	632.0 ± 3.0	17 ± 4
	horizontal 5	615.9 ± 3.1	633.3 ± 3.0	17 ± 4
	vertical 1	610.4 ± 3.1	624.8 ± 3.0	14 ± 4
	vertical 2	611.3 ± 3.1	627.6 ± 3.0	16 ± 4
	vertical 3	612.8 ± 3.1	630.6 ± 3.0	18 ± 4
	vertical 4	612.7 ± 3.1	632.5 ± 3.0	20 ± 4
	vertical 5	615.1 ± 3.1	1044.0 ± 3.0	429 ± 4
thick	horizontal 1	660.4 ± 3.1	689.1 ± 3.0	29 ± 4
	horizontal 2	659.7 ± 3.1	690.6 ± 3.0	31 ± 4
	horizontal 3	660.0 ± 3.1	693.0 ± 3.0	33 ± 4
	horizontal 4	664.8 ± 3.1	696.5 ± 3.0	32 ± 4
	horizontal 5	667.6 ± 3.1	699.5 ± 3.0	32 ± 4
	vertical 1	663.7 ± 3.1	681.7 ± 3.1	18 ± 4
	vertical 2	667.6 ± 3.0	686.3 ± 3.1	19 ± 4
	vertical 3	666.6 ± 3.0	688.2 ± 3.1	22 ± 4
	vertical 4	672.0 ± 3.1	690.1 ± 3.0	18 ± 4
	vertical 5	670.2 ± 3.1	690.4 ± 3.1	20 ± 4

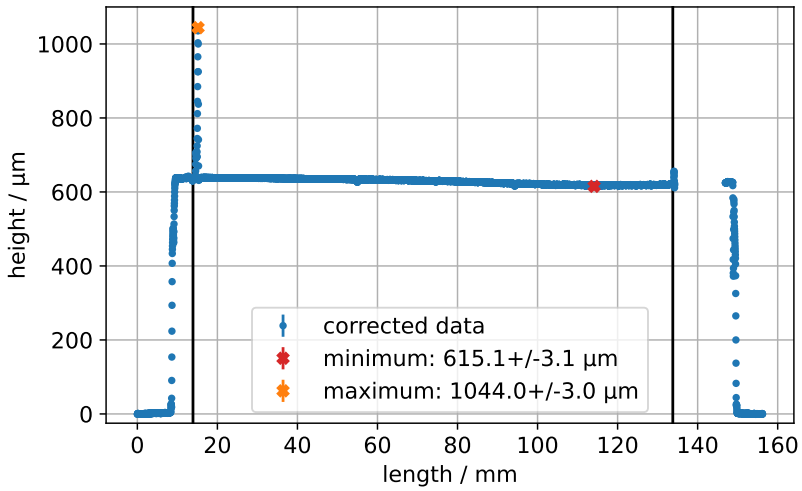

Figure 3.12: Corrected data for the bow measurement of the fifth vertical line scan of the thin wafer. Each measured value has a measurement uncertainty of approximately $\pm 3\,\mu m$, which is too small to be visible in the plot. With the close proximity of the peak and the gap on the left side, it is assumed, that the peak is an artefact of the reflections.

for all delivered devices at a single institute. Moreover, the information that is gained by those two measurements is extremely relevant for the classification of the devices as good or bad. Consequently, for all delivered devices the IV-characteristic and the CV-characteristic have to be measured. The evaluation of the long-term stability of the leakage current has to be done for only two devices. As the stability is observed for at least 48 hours, this measurement occupies most of the time of all measurements. Therefore, the number of investigated devices for this evaluation is minimised to ensure a reasonable duration of the measurements in a single institute. In the market survey, the sensors are accepted if their depletion voltage V_{depl} is less than 60 V for the 100 µm thick sensors and less than 100 V for the 150 µm sensors. These values for the depletion voltage are derived from the requirements for the later installed modules in the ITk. At typical irradiation fluences in the ITk, the resistivity of the sensor material decreases and the bias voltage needed to fully deplete the sensor increases (see subsection 2.3.1 for more details). For this reason, the sensors are initially produced with a high resistivity of the silicon substrate to allow a reasonable depletion voltage after irradiation. The combination of the resistivity requirement and a safety margin of 20 V gives the depletion voltage requirements mentioned above. The breakdown voltage V_{bd} of the sensors before irradiation has to be larger than $V_{\text{depl}} + 70\,\text{V}$ for the sensor to be accepted. Another requirement for

the market survey is the power dissipation of the sensors, so the sensors are classed as good, if their leakage current is smaller than $0.75\,\mu A/cm^2$ at a bias voltage of $V_{depl} + 50\,V$. So to use these last two requirements, it is mandatory to know the exact depletion voltage of each sensor. Therefore, the CV-characteristics are presented in this section before the other measurements, regardless of the chronological order of the actual measurements.

The ITk market survey was time-constrained. Since some deliveries delayed the process in general, quick measurements were needed. The foundry offered to measure the IV- and the CV-characteristic at their side to accelerate the procedure. The values from the foundry are cross-checked at TU Dortmund University for two reasons. Firstly, this is done to assure that no damage was done during the shipping of the sensors. Secondly, it is checked, whether the results can be repeated at a second institute. Therefore, the exact measurement procedure that is foreseen to be followed within the market survey was skipped and replaced with a shorter one, that complies with the measurements from the vendor. That is the reason why the details about the measurements differ in this part from the measurement details in subsection A.2.3 in the appendix.

Capacitance-voltage characteristic

A schematic for the used circuitry to measure the CV-characteristic is shown in Figure 3.13a. The backside of the n-in-p sensor is placed on the vacuum chuck, so the pixel implantation is facing upwards. This can be seen in the photograph in Figure 3.13b. Since the sensor needs to be reverse-biased, the potential on the p-side has to be lower than that on the n-side. Therefore, the vacuum chuck in this setup is connected to ground and the bias voltage is applied as a positive high voltage via the needle of a needle prober. The advantage of this configuration is the fact that there is no high voltage on the chuck.
The climate chamber is used to establish a controlled measurement environment by maintaining preset temperature and relative humidity. Moreover, as soon as the door of the climate chamber is closed, there is no light in the setup, which would affect the measurements. Only small inlets for cables and tubes are located at the sides. These inlets are closed with plugs and additionally sealed with tape.
Beneath the perforated plate where the mechanical components of the setup are fixed on is a 5 cm thick aluminium plate (visible in Figure 3.13b). This thick and heavy plate sits on several tennis balls which are located at the bottom of the climate chamber. The tennis balls are used as shock absorbers and the heavy aluminium plate prevents further movement of the setup caused by the vibrations of the fan of

the climate chamber. This setup reduces the transfer of movements of the climate chamber to the needle which would then scratch the probed sensor.

Following the circuitry depicted in Figure 3.13a, the sensor on the wafer is biased by a voltage source. A Keithley 2410 is used for the measurements in this thesis. To measure the capacitance of the sensor, the LCR meter uses an alternating voltage. The maximum amplitude of the used HP 4284A is $V_{\text{rms}} = 2\,\text{V}$ and the frequency is adjustable as well. The DC voltage from the voltage source and the AC voltage from the LCR meter are led to a bias box. Within the bias box, the two voltages are added.
For automated measurements, the *e4control* software [58], developed in-house, is used to control the lab hardware. It controls and reads out the used devices. With help of the software, several details such as the covered bias voltage range and current limits can be set. Moreover, the number of measurement repetitions per measurement point, the delay for starting the measurement after setting the voltage and the number of voltage steps can be adjusted. These last points are relevant to have consistent measurements between different institutes to ease the comparison of the results.
To measure the capacitance of the structures on the delivered wafers, the LCR meter was used in the $C_P - D$ mode. In this mode, the equivalent circuit is modelled in a parallel mode, since the parallel resistance has a greater effect on the reactance than the series resistance [59]. Moreover, in the same handbook the parallel mode is recommended, if the impedance of the capacitor is above $10\,\text{k}\Omega$. The impedance can be approximated as $1/(2\pi f C)$, where f is the frequency of the AC voltage from the LCR meter. Inserting a frequency of 1 kHz, the threshold capacitance, that should be measured in parallel mode results to a capacitance smaller than 16 nF. Since the investigated sensors are expected to have a much smaller capacitance, this measurement mode is the appropriate one. More details about the general measurement of the capacitance can be found in manuals of LCR meters such as [59, 60].

For the measurements, the used AC voltage has an amplitude of $V_{\text{rms}} = 100\,\text{mV}$ and a frequency of 1 kHz. All measurements are performed with five repetitions at each measurement point and the delay is set to 5 s. This delay is chosen to allow for the time it takes for the charge carriers to reach a steady state in the sensor after the high voltage is applied. The measurements for the first sensors measured, SC1 and SC2 of the thin wafer, are performed with 2.5 V steps up to a maximum bias voltage of 150 V. To reduce the measurement time, all other measurements after these have 2 V steps up to a maximum bias voltage of only 80 V. The sensor DC10 from the thick wafer was exceptionally measured up to a bias voltage of 100 V, since its capacitance saturates only at very high bias voltages. The measurement environment is set to be at 20 °C and a relative humidity of $(40 \pm 10)\%$.

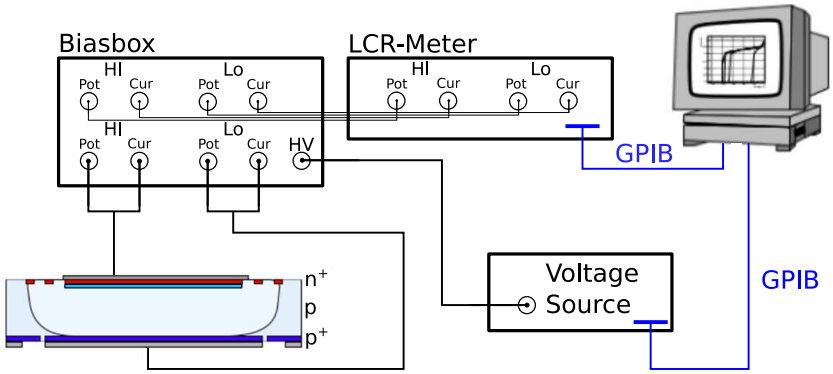

(a) Schematic of the used circuitry to measure the CV-characteristic of the different devices (original scheme by [12], adapted version taken from [57]). Besides the connections also the different used devices are displayed.

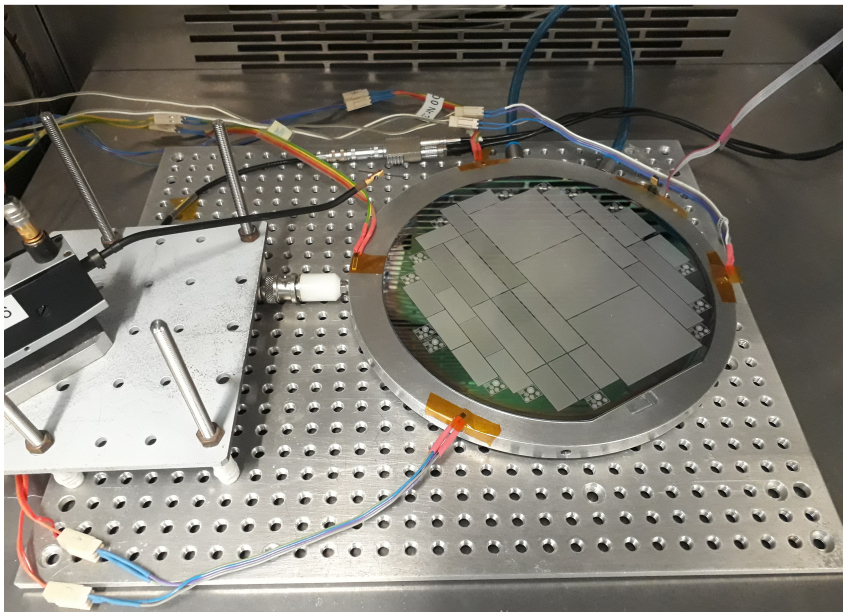

(b) Photograph of the measurement setup inside the climate chamber. The needle prober is placed on a platform left from the vacuum chuck where the wafer is placed on. At the edge of the vacuum chuck, monitoring sensors for temperature and relative humidity are visible.

Figure 3.13: Details about the measurement setup, where **(a)** shows a schematic of the used circuitry and **(b)** a photograph of the real setup inside the climate chamber.

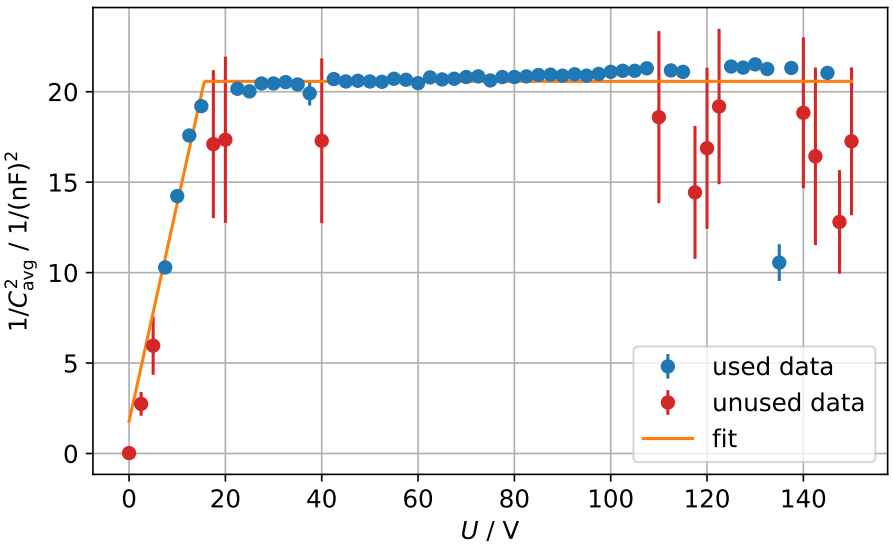

Figure 3.14: Exemplary measurement result as $1/C^2$ versus the applied bias voltage. Some of the values have comparable large measurement uncertainties and are therefore neglected in the later analysis.

Figure 3.14 shows an example of the measurement results of a CV-characteristic, depicted as $1/C^2$ versus the applied bias voltage. This format is chosen, because the depletion voltage can be easily extracted based on the modified form of Equation 2.1, where the width of the depletion zone is proportional to $\sqrt{V_{\text{bias}}}$. The values are fitted with a continuous fit consisting of two lines. The one in the beginning has a slope and the second part is a constant. The intersection point of these two lines is one of the fit parameters and gives the depletion voltage.
As it can be seen in Figure 3.14, some of the measured values of the capacitance have very large measurement uncertainties. Since it was found out, that they are caused by an internal malfunction of the bias box, these measurement points can be discarded for the analysis of the depletion voltage. To check, which measurement points are affected by this, the relative uncertainties of all measurement points are checked and histograms of this are presented in Figure 3.15. From these histograms, an overall cut-off of 5% is chosen. This means, that all measured values of the capacitance with relative measurement uncertainties greater than 5% are not included in the fitting algorithm mentioned above. This prevents those values to influence the determination of the depletion voltage.

A detailed list with the results of the analysis of the depletion voltage is shown in Table 3.3. The sensors are classified as good within the market survey, if their

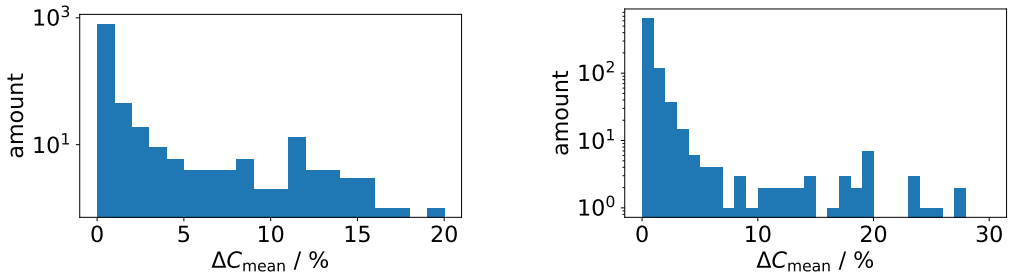

(a) Thin wafer.

(b) Thick wafer.

Figure 3.15: Logarithmic histograms of all relative measurement uncertainties of the CV measurements of the **(a)** thin and **(b)** thick wafer. Most of the measurements have very low uncertainties below 1% and only a few show large uncertainties greater than 5%.

depletion voltage is $V_{\text{depl}} < 60\,\text{V}$ for the thin sensors and $V_{\text{depl}} < 100\,\text{V}$ for the thick sensors. This is true for all measured sensors, so these sensors would be accepted for the market survey.
In addition, the manufacturer has measured the depletion voltage of the wafers on dedicated test structures and gives values of 12 V for the thin wafer and 27 V for the thick wafer. Assuming a measurement uncertainty of $\pm 1\,\text{V}$ for the measurements of the manufacturer, 13 depletion voltages of the thin wafer measured at TU Dortmund University agree within a one sigma band. Nine depletion voltages measured at TU Dortmund University are at least twice as high as stated by the manufacturer. For the thick wafer, ten measured depletion voltages agree with the values from the manufacturer within a two sigma band. Of the remaining ten measured depletion voltages, seven depletion voltages agree within a three or four sigma band. Only three depletion voltages are unusually high, with values at least twice as high as those measured by the manufacturer.

The results for the thin wafer can be grouped in two classes. One type of sensors shows a depletion voltage around 15 V and the others show depletion voltages in a broad range from 30 V to 50 V. Exemplary plots of those two classes are shown in Figure 3.16.
In Figure 3.16a it is obvious that there are two kinks in the plot of $1/C^2$ against the applied bias voltage. Therefore the aforementioned fit algorithm fails. The first kink is at a bias voltage of approximately 10 V and the second kink is at a bias voltage of about 35 V. The fit algorithm, which only fits the beginning with a slope and the end with a constant, is not suitable for describing this curve. It constantly overestimates the depletion voltage. In contrast, the curve with only the one expected kink is

Table 3.3: Results of the CV measurements of the thin wafer and the thick wafer. The column labelled *analysis* gives the results of the fit algorithm. The column labelled with *rounded* shows the values from the analysis rounded to the nearest measurement point and the stated uncertainty is given as the step width of the corresponding measurement. The fit for SC14 of the thick wafer (marked with *) fails.

	thin wafer			thick wafer	
sensor	V_{depl} / V analysis	V_{depl} / V rounded	sensor	V_{depl} / V analysis	V_{depl} / V rounded
SC1	15.6 ± 1.3	15.0 ± 2.5	SC1	30.81 ± 0.21	30 ± 2
SC2	15.15 ± 0.29	15.0 ± 2.5	SC2	21.0 ± 0.9	20 ± 2
SC3	37.5 ± 0.8	38 ± 2	SC3	21.8 ± 1.1	22 ± 2
SC4	14.59 ± 0.22	14 ± 2	SC4	23.8 ± 1.0	24 ± 2
SC5	35.7 ± 0.7	36 ± 2	SC5	30.75 ± 0.27	30 ± 2
SC6	14.86 ± 0.30	14 ± 2	SC6	-	-
SC7	14.80 ± 0.24	14 ± 2	SC7	31.03 ± 0.26	32 ± 2
SC8	-	-	SC8	-	-
SC9	14.99 ± 0.28	14 ± 2	SC9	32.73 ± 0.27	32 ± 2
SC10	14.97 ± 0.22	14 ± 2	SC10	21.4 ± 0.9	22 ± 2
SC11	44.6 ± 1.0	44 ± 2	SC11	30.28 ± 0.27	30 ± 2
SC12	37.4 ± 0.6	38 ± 2	SC12	33.08 ± 0.30	34 ± 2
SC13	37.6 ± 0.7	38 ± 2	SC13	21.0 ± 1.2	20 ± 2
SC14	55.0 ± 1.3	54 ± 2	SC14	*	*
SC15	-	-	SC15	-	-
SC16	-	-	SC16	72.4 ± 2.3	72 ± 2
DC1	-	-	DC1	29.41 ± 0.22	30 ± 2
DC2	14.50 ± 0.26	14 ± 2	DC2	28.15 ± 0.19	28 ± 2
DC3	35.3 ± 0.7	36 ± 2	DC3	28.6 ± 0.5	28 ± 2
DC4	14.86 ± 0.26	14 ± 2	DC4	-	-
DC5	13.13 ± 0.22	14 ± 2	DC5	28.05 ± 0.25	28 ± 2
DC6	14.42 ± 0.23	14 ± 2	DC6	-	-
DC7	38.2 ± 0.8	38 ± 2	DC7	-	-
DC8	-	-	DC8	23.9 ± 0.8	24 ± 2
DC9	33.5 ± 0.8	34 ± 2	DC9	60.2 ± 1.2	60 ± 2
DC10	14.1 ± 0.7	14 ± 2	DC10	80.2 ± 1.7	80 ± 2
QC1	14.63 ± 0.25	14 ± 2	QC1	-	-
QC2	-	-	QC2	30.36 ± 0.22	30 ± 2
QC3	-	-	QC3	-	-

described almost perfectly by the fit (see Figure 3.16b). The fit technique for CV-characteristics was specified by the market survey community before the first sensors were available [61]. For this reason, no adjustment to the fit algorithm is allowed, even though it is not appropriate for some of the CV-characteristics measured in the survey.
On the thin wafer, results for the CV-characteristics are obtained for 22 sensors and nine out of these 22 sensors show the behaviour with the two kinks in the representation of $1/C^2$ versus the applied bias voltage. All of these nine structures are biased through the punch-through technology. However, this cannot be the reason for the strange behaviour, since other sensors with punch-through show the expected behaviour with only one kink. Even though the details about the pixel design, biasing technique or termination are available, no common feature can be made out across those nine sensors, that can explain, why they behave differently than expected. Since they are not in proximity to each other on the wafer, even structual problems are not a reason for their different behaviour. Remeasurements of the same structures have proven, that the strange behaviour is always there and does not change in time. A possible explanation for the curve of the CV-characteristic is the depletion of structures on the surface of the sensors. This depletion stops at some point which is visible as the first kink in the plot of $1/C^2$ against the applied bias voltage. For higher bias voltages, the depletion zone grows only perpendicular to the surface, thus resulting in the second kink when the complete volume is depleted.

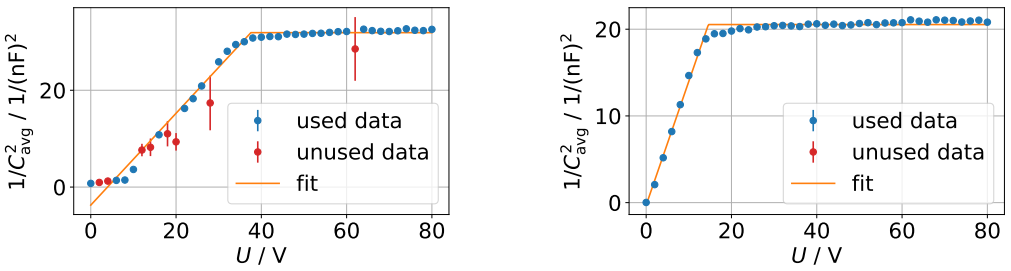

(a) SC3. **(b)** SC4.

Figure 3.16: Exemplary plots of $1/C^2$ versus the applied bias voltage for measured sensors on the thin wafer. The curve in **(a)** shows two kinks and the curve in **(b)** shows only the one expected kink.

A similar grouping can be done for the sensors on the thick wafer. There, three groups are present: the first has a depletion voltage around 20 V, the second shows depletion voltages around 30 V and the last features depletion voltages between 60 V and 80 V.
The first two groups differ only in their capacitance measured in the plateau region.

Six out of 21 sensors with appropriate measurements of the capacitance have a depletion voltage around 20 V. Eleven out of 21 sensors in total for this wafer have a depletion voltage of 30 V. These sensors have a capacitance of approximately 150 pF for the SC sized sensors in the plateau region and 300 pF for the DC sized sensors. For the sensor QC2, with an area four times as large as the DC sized sensors, a capacitance of more than 1100 pF is measured in the plateau region. This shows nicely, how the capacitance scales for sensors of the same thickness with their area, as stated in Equation 2.4.
The third group features in the representation of $1/C^2$ versus the applied bias voltage two kinks, similar to the second group of the thin wafer. The first kink is around 10 V to 15 V and the second kink is at a bias voltage of approximately 60 V. For those sensors (four out of 21 sensors), the commonly used fit algorithm does not work, so the estimated depletion voltage is always overestimated or the fit algorithm even fails. This is an indicator, that the currently used fit algorithm is not the best choice for a robust fit. One improvement could be the inclusion of an additional slope for the two first sections and then the constant for the plateau region.

To summarise the measurements of the depletion voltage, the values measured by the manufacturer and TU Dortmund University differ slightly. Nevertheless, the majority of the sensors show depletion voltages that are in good agreement with the values given by the manufacturer (mainly within a two sigma band). Furthermore, the values reported by the vendor and measured by TU Dortmund University all meet the requirements of the market survey. Therefore, the market survey community decided that it is valid to trust the manufacturer's values and to skip this measurement at the institutes for later production. As the manufacturer measured the depletion voltage on test structures on the wafer, it is expected to measure slightly higher depletion voltages for each of the structures included in the wafer. Additional information on the strange behaviour with the two kinks is not available within the scope of the market survey.

Current-voltage characteristic

The measurements for the current-voltage characteristic are carried out in the same climate chamber as the CV-measurements (as already shown in Figure 3.13b) to ensure the correct measurement environment. However, the circuit of the setup differs. The used circuit is depicted in Figure 3.17. The high voltage is applied via a needle contacting the pixel side of the sensors on the wafer and the backside is grounded on the chuck as before.
The measurements are started and controlled with the software e4control [58]. They are carried out with an increasing bias voltage in 5 V steps up to a maximum voltage

of 200 V. This procedure is only interrupted, if the leakage current increases beyond the preset limit of 1 µA. In these cases, the bias voltage is slowly ramped down. At each bias voltage, the leakage current is measured ten times. The delay after which measurements start after setting the correct bias voltage is set is 10 s. After a sudden change of the applied bias voltage, a delay is required to allow the leakage current to settle to a constant level.

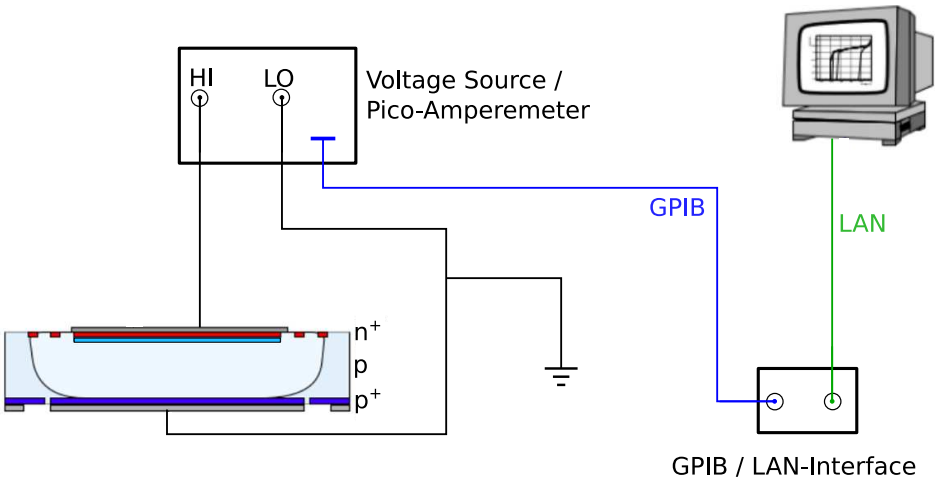

Figure 3.17: Schematic of the used circuitry to measure the IV- and It-characteristic of the different devices (taken from [57]). Besides the connections, also the different used devices are displayed.

The maximum bias voltage of 200 V is chosen, to generate measurements easily comparable to the ones from the vendor, since they have measured also up to this bias voltage. Although their measurements are carried out in 2 V steps, the measurements for this thesis are done with 5 V steps to minimise the required time. The presented measurements are not used to characterise the sensors for the market survey, but to see, whether the results of the manufacturer can be reproduced. Therefore, the measurement details differ slightly from the market survey measurements. However, to give an impression of the quality of the sensors, the original market survey requirements are used additionally to classify the sensors as good or bad.

The interesting characteristics to extract from the IV-measurements are the breakdown voltage of the sensors and the power consumption. For the latter, the relevant measurement is the leakage current I_{leak} at a specific bias voltage scaled to the sensor area A. Within the market survey, the leakage current density of a sensor has to be smaller than $0.75\,\mu\text{A/cm}^2$. It is measured at a bias voltage of $V_{\text{depl}} + 50\,\text{V}$. The areas of the different sensors are $1.94\,\text{cm}^2$ for SCs, $3.88\,\text{cm}^2$ for DCs and $15.52\,\text{cm}^2$

for the QCs. For the structures on the thin wafer, $V_{\mathrm{depl}} = 15\,\mathrm{V}$ are used, as this is the voltage, where the sensors deplete at the vendor and the university. The depletion voltage for the thicker wafer is estimated to be $V_{\mathrm{depl}} = 30\,\mathrm{V}$ as observed by the vendor and institute measurements.
There are many criteria for the breakdown voltage available. In the context of the market survey, an increase of the leakage current of more than 20% within a 5 V step is meant to be used [61]. The exact breakdown voltage is determined by the analysis script as the higher of the two voltages covering the corresponding voltage step. Within the analysis, only leakage currents at bias voltages above the depletion voltage are checked to find the breakdown voltage. The systematic error of the breakdown voltage is then given as the order of the step size. To fulfil the requirements of the market survey, the breakdown voltage V_{bd} of the sensors has to be greater than $V_{\mathrm{depl}} + 70\,\mathrm{V}$.

Most of the measured IV characteristics feature very low currents, below 20 nA. Some of these measurement points have large uncertainties (see for example Figure 3.18). Values with large uncertainties are often classified by the analysis script as the breakdown. However, since the uncertainties of these values are so large, the simple analysis foreseen for the market survey can not be trusted for those values. Therefore, an additional check of the breakdown voltage is implemented within this thesis in the script. This check tests not only the actual voltage step, but the last three consecutive voltage steps for an increase of the leakage current of more than 20%. Only if all three previous voltages steps fulfil the increase of more than 20% individually, the breakdown voltage is confirmed. The results of the analysis are presented in Table 3.4 for the thin wafer and in Table 3.5 for the thick wafer. Those sensors where the additional check of the breakdown voltage was necessary are marked with an asterisk ($*$) in the tables.
From the tables it can be seen that for many sensors, especially on the thin wafer, the definition of the market survey for the breakdown voltage is insufficient. For all marked sensors, the standard analysis script of the market survey detects breakdowns at very low bias voltages. However, the analysis with the additional check mentioned above does not confirm these breakdowns and in most of the corresponding IV curves no real breakdown is detected. Therefore, the actual analysis script for the market survey is not suitable for a robust automated analysis. Only with the additional check measurements with larger measurement uncertainties can be reliably analysed.

There are only a few sensors, where the measurement results at the institute and from the vendor differ from each other. For the thin wafer, this is the case for the quad chip sized sensor QC3. The IV characteristic measured at TU Dortmund University is shown in Figure 3.18. The original analysis script of the market survey detects a breakdown voltage of 20 V, the additional check of the three consecutive

Table 3.4: Results of the IV measurements of the thin wafer. The data from the vendor is given for comparison as well. The stated leakage currents are measured at a bias voltage of 65 V. The values that do not fulfil the market survey requirements are marked in red and those sensors where the additional check of the breakdown was used are marked with an asterisk.

	institute			vendor	
sensor	I_{leak}/A / µA/cm^2		V_{bd} / V	I_{leak}/A / µA/cm^2	V_{bd} / V
SC1 *	0.106 03	± 0.000 34	40 ± 5	0.262 911	19 ± 2
SC2 *	0.001 02	± 0.000 35	>200	0.000 821 5	>200
SC3 *	0.001 68	± 0.000 04	>200	0.001 743	>200
SC4 *	0.001 83	± 0.000 14	>200	0.001 226	194 ± 2
SC5 *	0.0014	± 0.0004	>200	0.001 499	>200
SC6 *	0.001 08	± 0.000 05	>200	0.001 275	>200
SC7 *	0.001 63	± 0.000 16	>200	0.001 505	>200
SC8	4.402	± 0.025	20 ± 5	5.392	19 ± 2
SC9 *	0.001 37	± 0.000 15	>200	0.001 304	>200
SC10 *	0.001 20	± 0.000 19	>200	0.001 108	>200
SC11 *	0.001 04	± 0.000 20	>200	0.000 948 0	>200
SC12 *	0.001 21	± 0.000 26	>200	0.001 509	>200
SC13 *	0.001 71	± 0.000 04	>200	0.001 955	>200
SC14	0.000 794	± 0.000 013	100 ± 5	0.001 058	>200
SC15		-	25 ± 5	5.00	19 ± 2
SC16	1.3010	± 0.0004	20 ± 5	5.219	19 ± 2
DC1 *	0.000 86	± 0.000 14	100 ± 5	0.000 998 8	>200
DC2 *	0.001 29	± 0.000 11	>200	0.001 191	>200
DC3 *	0.0014	± 0.0005	>200	0.001 315	>200
DC4 *	0.0014	± 0.0007	>200	0.001 039	>200
DC5 *	0.000 74	± 0.000 17	>200	0.000 883 0	>200
DC6 *	0.001 04	± 0.000 06	>200	0.001 041	>200
DC7	0.001 490	± 0.000 014	>200	0.001 999	>200
DC8	1.827 062	± 0.000 021	20 ± 5	2.829	19 ± 2
DC9 *	0.001 44	± 0.000 04	>200	0.0019	>200
DC10	0.772 68	± 0.000 13	20 ± 5	0.911 175	19 ± 2
QC1 *	0.003 34	± 0.000 10	25 ± 5	0.018 862	52 ± 2
QC2	4.0006	± 0.0013	175 ± 5	8.367	>200
QC3 *	0.000 79	± 0.000 08	25 ± 5	0.002 716	>200

Table 3.5: Results of the IV measurements of the thick wafer. The data from the vendor is given for comparison as well. The stated leakage currents are measured at a bias voltage of 80 V. The values that do not fulfil the requirements of the market survey are marked in red and those sensors where the additional check of the breakdown was used are marked with an asterisk.

	institute		vendor	
sensor	I_{leak}/A / µA/cm^2	V_{bd} / V	I_{leak}/A / µA/cm^2	V_{bd} / V
SC1	0.216 19 ± 0.000 25	35 ± 5	0.221 886	27 ± 2
SC2	0.002 93 ± 0.000 14	>200	0.003 422	>200
SC3 *	0.0037 ± 0.0004	>200	0.004 46	>200
SC4	0.003 46 ± 0.000 13	>200	0.004 409	>200
SC5	0.003 05 ± 0.000 08	>200	0.004 015	>200
SC6	0.003 46 ± 0.000 23	145 ± 5	0.004 232	>200
SC7	0.003 51 ± 0.000 19	>200	0.004 208	>200
SC8	4.558 ± 0.016	35 ± 5	8.164	19 ± 2
SC9	0.003 92 ± 0.000 19	>200	0.004 55	>200
SC10	0.003 65 ± 0.000 20	>200	0.004 762	>200
SC11	0.003 21 ± 0.000 20	>200	0.003 841	>200
SC12	0.004 051 ± 0.000 019	>200	0.005 396	>200
SC13 *	0.049 ± 0.007	155 ± 5	0.006 37	>200
SC14	0.003 50 ± 0.000 17	125 ± 5	0.004 844	>200
SC15	0.003 55 ± 0.000 11	>200	0.004 656	>200
SC16	0.0058 ± 0.0009	>200	0.006 428	98 ± 2
DC1	0.0108 ± 0.0010	>200	0.003 45	>200
DC2	0.213 02 ± 0.000 26	35 ± 5	0.241 241	19 ± 2
DC3	0.002 59 ± 0.000 05	>200	0.003 443	>200
DC4 *	0.002 95 ± 0.000 06	140 ± 5	0.003 727	>200
DC5	0.002 33 ± 0.000 11	>200	0.003 178	>200
DC6	6.3582 ± 0.0016	120 ± 5	6.393	>200
DC7	-	25 ± 5	23.59	21 ± 2
DC8	0.002 48 ± 0.000 09	>200	0.003 199	>200
DC9	0.0031 ± 0.0004	>200	0.004 146	198 ± 2
DC10	0.002 78 ± 0.000 24	115 ± 5	0.003 815	>200
QC1	-	5 ± 5	12.5	>200
QC2	0.002 27 ± 0.000 28	>200	0.006 485	>200
QC3	0.873 71 ± 0.000 29	35 ± 5	0.926 512	19 ± 2

steps with current increases gives 25 V for the breakdown voltage. However, all values that are checked within these analyses show large uncertainties. Therefore, the leakage currents at bias voltages above 25 V are checked for breakdown voltages as well. Above this bias voltage, no further breakdown with three current increases of more than 20% in a row is detected. Since the breakdown voltage is not reached below 200 V, the breakdown voltage can be assumed to be > 200 V, just as it is measured by the manufacturer.

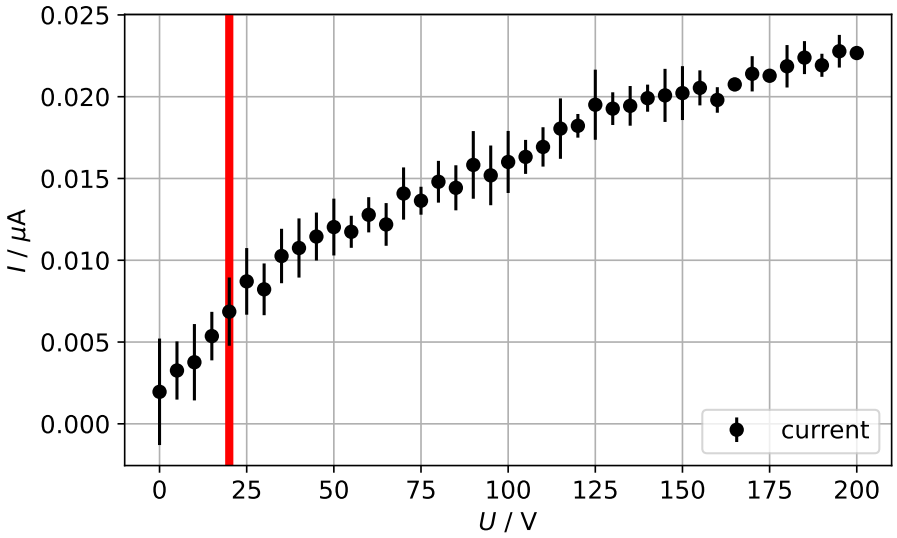

Figure 3.18: IV characteristic of sensor QC3 on the thin wafer. The red line indicates the breakdown voltage based on the analysis for an increase of the leakage current of more than 20% within a voltage step. The adapted script gives a breakdown voltage of 25 V. Given the large measurement uncertainties, an additional check for bias voltages above 25 V with the adapted script does not reveal any further breakdown.

On the thick wafer, there are two sensors, where the analysis results differ between the institute and the manufacturer. One of them is SC16, where the manufacturer has measured a high current increase for bias voltages above 100 V. This results in the low breakdown voltage of (98 ± 2) V. However, this behaviour can not be observed in the measurement at the institute. To cross-check the measurement of the institute, the measurement of the leakage current was repeated on the same day and also multiple days later. Nevertheless, all measurements at the institute showed the same course, so it was decided to trust these values.
The other sensor, where the analysis results differ, is QC1. At the institute, the leakage current at a bias voltage of 5 V is already above the set current limit and

therefore the measurement is stopped. This is then stated as a breakdown voltage of (5 ± 5) V. The manufacturer on the other hand does not find a breakdown up to 200 V. However, this is not true, if the original data from the vendor is checked. There, the measured leakage current is as well very high and in addition above the current limit. The recorded value for the current is for all measurement points above a bias voltage of 2 V the same. Therefore, the analysis script does not detect any increase and as a consequence the breakdown voltage is stated as > 200 V, although this is not the truth.

To sum up the results of the IV characteristics, all high leakage currents that do not meet the market survey requirement are detected at the institute and at the manufacturer. In addition, early breakdowns can be detected at both sites with a good accuracy. Since the classification as good or bad in the scope of the market survey is identical with the measurements done by the vendor or by TU Dortmund University, it is decided to rely on the vendor measurements in the future. Only a small fraction of sensors will be additionally cross-checked at the institutes during the production step to speed up the process.
Nevertheless, the analysis script is found to be not sufficient for an automated analysis. Within the market survey, the analysis algorithm was defined beforehand in an official document [61]. For this reason, no official change was possible while the measurements were analysed. To cope with measurements with larger measurement uncertainties, additional human checks of lots of IV curves were needed. The implemented additional check with the three consecutive steps with current increases of more than 20% is proven to be a good option to enhance the reliability of the analysis results for the breakdown voltages. Moreover, it supersedes the time consuming human checks and should be included in future analysis scripts.

Stability of the leakage current

The long-term stability of the leakage current of a sensor is of great importance. Since the sensors are biased after the installation in the ATLAS experiment, their leakage current should stay the same over the operation time. If the current increases with longer operation times, the heat that results from this process has to be transferred away from the cooling system without exceeding its power limit. Therefore, it is crucial for the silicon sensors to be tested for their long-term leakage current stability.

The manufacturer of the sensors did not perform measurements of the long term stability of the leakage current. Therefore, a comparison with their data is impossible. The measurement at TU Dortmund University is performed in the same setup as it is used for the electrical measurements presented previously (shown in Figure 3.13b

and using the power supplies shown in the sketch of Figure 3.17). The leakage current is measured at a constant applied bias voltage of $V_{\text{depl}} + 50\,\text{V}$. The market survey requires an investigation of the leakage current for 48 hours and data points every ten minutes. Therefore, every ten minutes the leakage current is measured ten times to determine the standard deviation of the mean current at this moment. If the original taken measurements cover more than 48 hours, only the first 48 hours of the data set are used for the analysis in this thesis.
Within the analysis, the variation between all points in a measurement has to be smaller than 25% to fulfil the market survey requirement. The variation is defined as the difference between the largest and smallest measured leakage current divided by the maximum measured leakage current. Since the leakage current of the sensors might show some kind of build up effect, the very first data point (measured at the beginning of the measurement) is excluded from the analysis and only data points with measurement times of more than 10 minutes are used.
The measurement is meant to be carried out at a temperature of $(20 \pm 1)°\text{C}$ and a relative humidity of $(40 \pm 10)\%$. Both requirements are fulfilled during all measurements at TU Dortmund University.

The plots of the measured leakage currents are shown in Figure 3.19 for the thin wafer and in Figure 3.20 for the thick wafer. Although the scale for the y-axis where the current is depicted differs for the plots, it is clearly visible that some data points have striking large measurement uncertainties. In some cases, the relative uncertainties are larger than 15%. One example of such a large uncertainty is the maximum measured leakage current of SC5 of the thick wafer with a relative uncertainty of about 30%. A reason for these large uncertainties is not found during the hindsight of the measurements.

The data from the vendor gives a depletion voltage of 12 V and the good CV measurements at TU Dortmund University reveal a depletion voltage of approximately 15 V for the thin wafer. Therefore, the sensors on the thin wafer are biased with 65 V for this measurement. For investigating the long-term stability of the leakage current, the single chip sized sensors SC4 and SC5 are chosen. These sensors are randomly chosen from all sensors rated good by the manufacturer.
The leakage current during the IV-measurement of SC4 is about 3 nA at a bias voltage of 65 V. In Figure 3.19a it can be seen, that the leakage current is about a factor of ten larger during the It-measurement. The IV-characteristic of this sensor was checked multiple times before the It-measurement was carried out and always showed the same behaviour back then. However, after the It-measurement, another IV-curve is taken and a larger leakage current in general and a current of roughly 32 nA at 65 V bias voltage is confirmed at this point in time. An obvious reason for this change of the behaviour is not found.
The largest leakage current for SC4 is measured near the end of the measurement

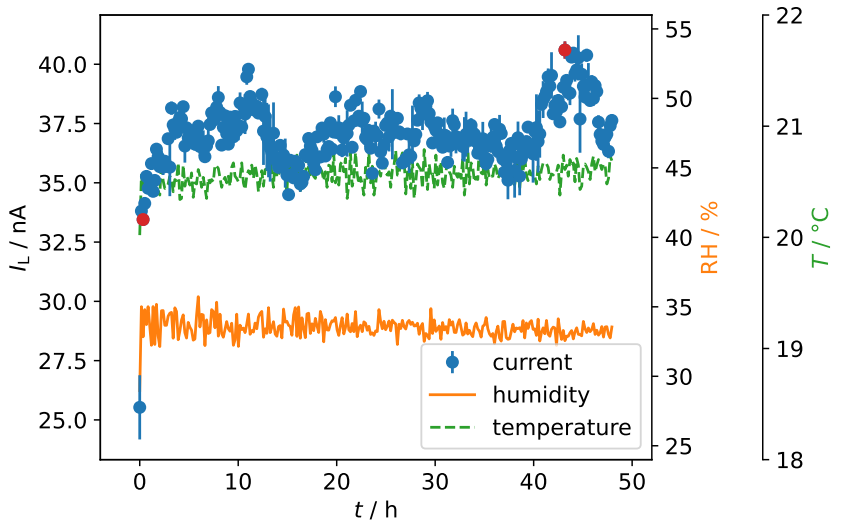

(a) Measured leakage current of SC4 at a bias voltage of 65 V.

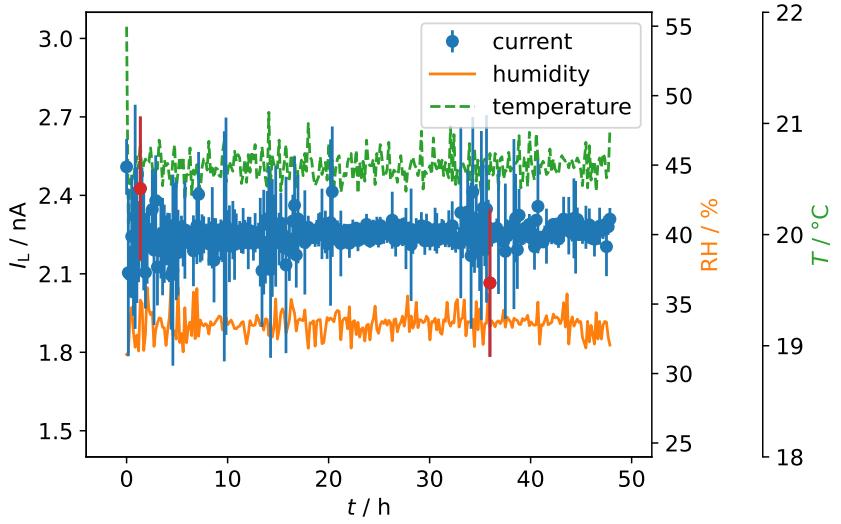

(b) Measured leakage current of SC5 at a bias voltage of 65 V.

Figure 3.19: Measured data for the investigation of the long-term stability of the leakage current over 48 hours for the thin wafer. Besides of the leakage current, the measured temperature and relative humidity are displayed as well. The data points marked in red indicate the smallest and largest measured leakage current in the corresponding data set.

time with (40.6 ± 0.4) nA. The minimum leakage current is (33.45 ± 0.26) nA which is measured right at the start of the measurement. These values result in a variation of $(17.6 \pm 1.0)\%$.
The leakage current of SC5 was found to be around 2.5 nA at a bias voltage of 65 V at previous IV-measurements. The plotted data in Figure 3.19b reveals that the leakage current stays during the long-term measurement slightly below this value. The mean leakage current during the measurement is approximately 2.2 nA. The largest leakage current is found to be (2.43 ± 0.28) nA and the minimum leakage current is (2.06 ± 0.28) nA. This gives a variation of $(15 \pm 15)\%$. The large uncertainty of this value can be explained with the Gaussian error propagation that is used for the calculation of this value. Since the uncertainties of the maximum and minimum current are in the same order, this leads to a quite high uncertainty for the variation.

For both thin sensors, the total variation within the measurement is below 25%, which is the requirement of the market survey. Therefore, both sensors pass the investigation and the thin wafer is classified as good. This decision is mainly based on the measurement of SC4. The relative measurement uncertainty of the variation of the leakage current of this sensor is only about 6%. This is small enough to trust the found value of 17%. The extreme values of SC5 show large relative uncertainties. Therefore, the measurement of this sensor is used to have a second example for the quality of the wafer to verify the found results in the measurements of SC4.
The definition of the variation of the leakage current is specified in the official market survey document [61]. As the result of SC5 shows, the ratio of the current difference (between the largest and smallest measured leakage current) and the maximum measured leakage current is very sensitive to measurements with large relative uncertainties. This is a downside for gaining reliable results. Another approach to evaluate the systematic changes in the leakage current over time would be the fit of a straight line to the measurement points. Its slope could then be used as the criterion to class the sensors as good or bad. However, during the market survey measurements in this thesis, no adjustment of the analysis is done, because the official market survey document had to be followed.

For the thick wafer, the manufacturer provided a value for the depletion voltage of 27 V. The CV-measurements verified this value and a constant bias voltage of 80 V is chosen for the long-term measurements. Since both wafers have the same layout of the structures included in them, the sensors SC4 and SC5 are chosen as well for a comparison.
The IV-characteristic of SC4 reveals an expected leakage current of 7 nA at a bias voltage of 80 V. Nevertheless, as it is clearly visible in Figure 3.20a, the measured leakage current increases with the operation time exponentially. This measurement was repeated to exclude a malfunction, but the behaviour was reproducible. The

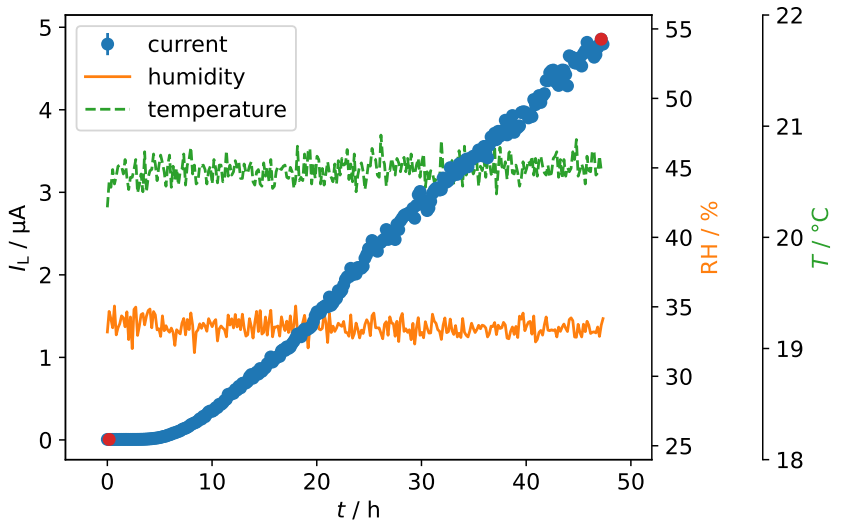

(a) Measured leakage current of SC4 at a bias voltage of 80 V.

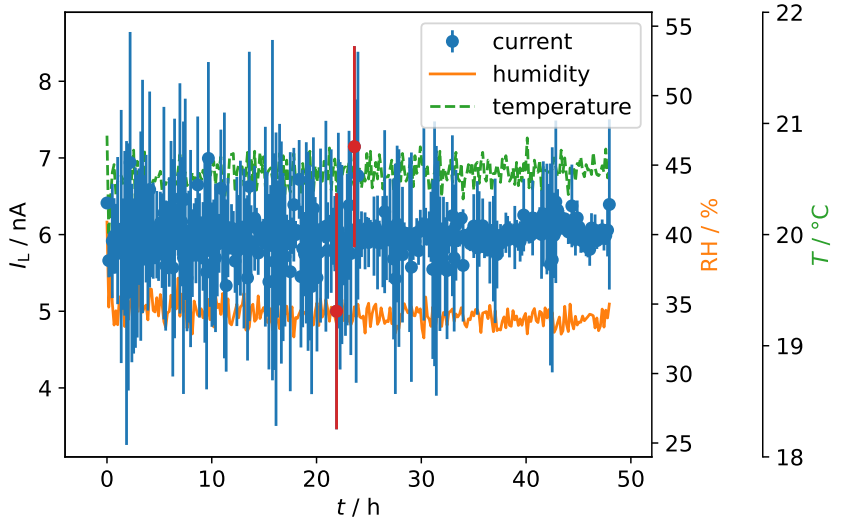

(b) Measured leakage current of SC5 at a bias voltage of 80 V.

Figure 3.20: Measured data for the investigation of the stability of the leakage current over 48 hours for the thick wafer. Besides of the leakage current, the measured temperature and relative humidity are displayed as well. The data points marked in red indicate the smallest and largest measured leakage current in the corresponding data set.

lowest measured current is found right at the beginning of the measurement time with (5.98 ± 0.16) nA. This value is within the expectation derived from the IV-characteristic. However, the current increases up to (4.86 ± 0.05) µA at the end of the measurement time. This is an increase by the factor of nearly 1000. Since this is easily visible, this measurement is stopped slightly before the for the market survey required 48 hours are over (however, only 30 minutes are skipped).
In contrast to the unexpected behaviour of SC4, the leakage current of SC5 is in the expected regime. Figure 3.20b shows a quite stable current of 6 nA which meets the value from the previous IV-characteristic. Nevertheless, over the time some fluctuations are visible, which reach from the minimum value of (5.0 ± 1.5) nA up to the maximum observed current of (7.1 ± 1.3) nA. This results in a variation of (30 ± 25)%. The reason for the relative large uncertainty is the same as before for SC5 of the thin wafer. If the standard deviations of the extreme values are taken into account, both currents are in agreement with the mean current across the whole measurement time, which is found to be (6.0 ± 0.9) nA.

The analysis script written for the market survey classes both SCs as failing the requirement. For SC4 this is very clear, but for SC5 it is worth to use some more time to investigate the data in more detail. The relative standard deviations of the found extreme values for SC5 are quite large (18% for the maximum and 30% for the minimum). Especially, if the minimum and maximum are compared to the mean of the complete data set, they agree with it within their uncertainties. Therefore, although the analysis gives a variation of more than 25%, SC5 is classified as good after a human check of the data.
No further data is available from either the vendor or a second institute for the measurement of the long-term stability of the leakage current. Therefore, no comparison is possible and the decision whether the thick wafer meets the market survey requirement is made by the market survey community. As other vendors delivered sensors with a thickness of 150 µm with much better leakage current stability, the community decided that this measured thick wafer does not fulfil the market survey requirements with these ambiguous results.

3.2.3 Electrical Tests of Irradiated Bare Sensors

Since the sensors are foreseen to be installed close to the interaction point in the ATLAS experiment, they need to be radiation hard. The radiation damage results in a reduction of the charge collection efficiency, which is mitigated by an increased bias voltage. However, the increased bias voltage results in a larger leakage current. The larger leakage current is a problem, because the analogue front-end of the readout chip can compensate only up to 10 nA per pixel cell [48]. Besides from this,

the cooling system needs to compensate the self heating of the sensor to prevent an uncontrolled current and temperature increase [48]. This effect of the mutual interference of current and temperature that results in ever higher currents and temperatures is the so-called thermal run-away. Since the cooling system has a limit for the cooling power, the temperature of the sensor and therefore also the leakage current must not be larger than specific requirements.
To evaluate if the produced sensors of the investigated vendor can cope with these requirements, some diced sensors are sent to an irradiation facility to be irradiated. The sensors of this vendor are irradiated at Birmingham at the MC40 cyclotron with protons with energies of up to 40 MeV [62]. Within the market survey, the sensors are irradiated to two reference fluences: the lower fluence is $2 \cdot 10^{15}\, n_{\mathrm{eq}}/\mathrm{cm}^2$ and the higher fluence is $5 \cdot 10^{15}\, n_{\mathrm{eq}}/\mathrm{cm}^2$. These fluences are chosen, because the pixel sensors in the barrel layer one will have to withstand a fluence of up to approximately $3.8 \cdot 10^{15}\, n_{\mathrm{eq}}/\mathrm{cm}^2$ until their end of lifetime in the replacement hypothesis [48]. Therefore, $5 \cdot 10^{15}\, n_{\mathrm{eq}}/\mathrm{cm}^2$ represents this end of lifetime fluence with an additional safety margin [63]. The lower reference fluence of $2 \cdot 10^{15}\, n_{\mathrm{eq}}/\mathrm{cm}^2$ represents the maximum fluence expected for the whole lifetime of the ITk for the sensors in the barrel layer three [63].

The electrical behaviour of the sensors is measured for all irradiated sensors that are available. Since the sensors were sent by the vendor directly to the irradiation facility, a comparison with the electrical behaviour before the irradiation is not possible. After the irradiation, the sensors undergo an annealing of 10 days at room temperature. The annealing process is then followed by the measurement of the current-voltage characteristic.
For this measurement, the same setup as for the IV measurements of the unirradiated bare sensors is used. The leakage current is measured in 5 V steps with 10 repetitions per voltage step. The delay, after which the measurement of the current starts after setting the bias voltage, is set to 10 s. This allows the current to settle after applying a new bias voltage and results in smaller measurement uncertainties due to the more stable behaviour. The measurement continues up to different bias voltages, depending on the thickness and irradiation fluence of the investigated sensor. If the measured leakage current is larger than 100 µA, the measurement is stopped and the bias voltage is ramped down. The temperature inside the climate chamber is set to $T_{\mathrm{set}} = -25\,^{\circ}\mathrm{C}$ and the relative humidity should be lower than 50% during the measurement. The set temperature of the climate chamber is chosen, because the temperature of the investigated sensor should be as close as possible to $T_{\mathrm{sensor}} = -25\,^{\circ}\mathrm{C}$. The temperature has to be precisely measured, since it has a great effect on the leakage current.

The leakage current and the breakdown voltage are the two quantities that are checked for the market survey requirements. The maximum allowed leakage current

densities and breakdown voltages for the different delivered thicknesses are listed below. The leakage current density is tested at a specific bias voltage (given in brackets in the list below) with respect to the sensor thickness and irradiation fluence.

- sensors with 100 µm thickness
  - irradiation fluence $2 \cdot 10^{15}\,n_{\mathrm{eq}}/\mathrm{cm}^2$: breakdown voltage $V_{\mathrm{bd}} > 300\,\mathrm{V}$, leakage current density I_{L}/A ($V_{\mathrm{bias}} = 300\,\mathrm{V}$) $< 20\,\mu\mathrm{A}/\mathrm{cm}^2$
  - irradiation fluence $5 \cdot 10^{15}\,n_{\mathrm{eq}}/\mathrm{cm}^2$: breakdown voltage $V_{\mathrm{bd}} > 400\,\mathrm{V}$, leakage current density I_{L}/A ($V_{\mathrm{bias}} = 400\,\mathrm{V}$) $< 35\,\mu\mathrm{A}/\mathrm{cm}^2$
- sensors with 150 µm thickness
  - irradiation fluence $2 \cdot 10^{15}\,n_{\mathrm{eq}}/\mathrm{cm}^2$: breakdown voltage $V_{\mathrm{bd}} > 400\,\mathrm{V}$, leakage current density I_{L}/A ($V_{\mathrm{bias}} = 400\,\mathrm{V}$) $< 25\,\mu\mathrm{A}/\mathrm{cm}^2$
  - irradiation fluence $5 \cdot 10^{15}\,n_{\mathrm{eq}}/\mathrm{cm}^2$: breakdown voltage $V_{\mathrm{bd}} > 600\,\mathrm{V}$, leakage current density I_{L}/A ($V_{\mathrm{bias}} = 600\,\mathrm{V}$) $< 45\,\mu\mathrm{A}/\mathrm{cm}^2$

The measured leakage current is scaled to the area of the sensor to allow a comparison, if different sized sensors are irradiated and investigated afterwards. Since the leakage current is examined at a specific bias voltage, the IV-characteristic has to be taken at least up to this point. The bias voltage is increased up to additional 200 V above the specified V_{bias} in the list above to check for the breakdown voltage.

Within the market survey, temperature scaling of the measured leakage current is not allowed. Therefore, the temperature of the sensor has to be known as precisely as possible to apply the requirements properly. This is done in the used setup by placing PT1000 temperature sensors as close as possible to the investigated sensor. This can be seen in Figure 3.21 for the different setups.
The thinner sensors are all available as bare sensors. For this reason, they are placed on a vacuum chuck. The PT1000 temperature sensor is then fixed with Kapton tape (see Figure 3.21a) in proximity to the sensor. In the depicted setup, the distance between the sensor and the temperature sensor is less than 5 mm.
The thicker sensors are glued to a PCB. Therefore, the whole PCB is placed inside the climate chamber. To protect the sensor, a cap is mounted above the sensor. As it can be seen in Figure 3.21b, there is a hole in the PCB, where the cable of the PT1000 sensor is led through. Therefore, the PT1000 sensor is in a comparable distance to the sensor as for the setup for the bare sensors. Moreover, since it is together with the sensor inside the volume of the protective cap, that is the best position for tracking the temperature of the sensor.

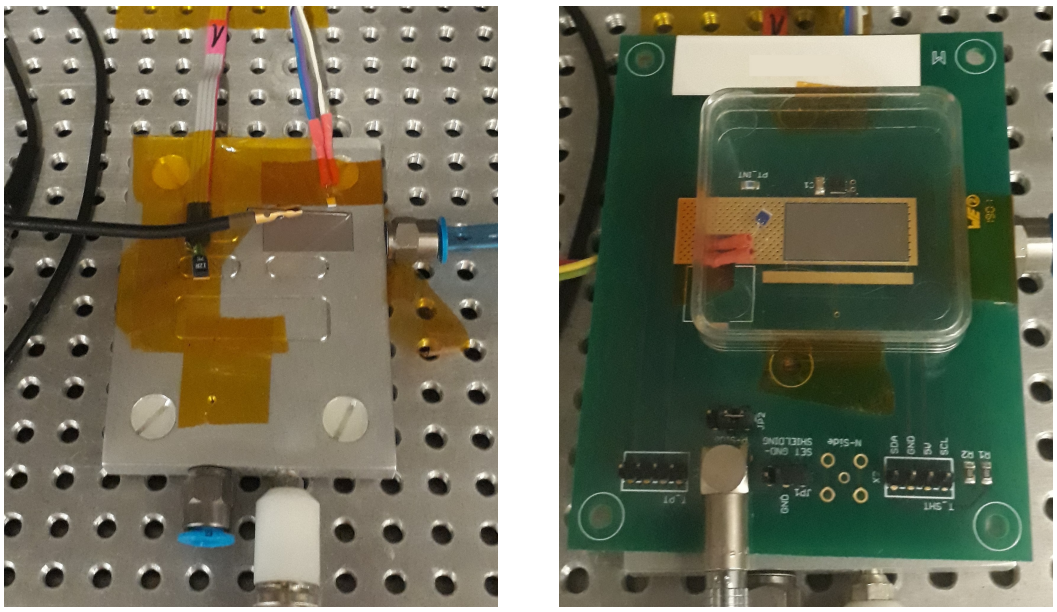

(a) Setup for the bare sensors.

(b) Setup for the sensors glued to a PCB.

Figure 3.21: Placement of PT1000 temperature sensors in **(a)** nearer than 5 mm to the sensor and **(b)** inside the protective cap.

Overall, the temperature of the investigated sensor stays in the required range of $T_{\text{sensor}} = -25\,°\text{C}$ during the whole measurement. The data for this is depicted in Figure A.1a in the appendix for reference. Although the market survey allows a deviation of $\pm 1\,°\text{C}$ of $T_{\text{sensor}} = -25\,°\text{C}$, five out of the six measurements have even smaller deviations of only $\pm 0.2\,°\text{C}$. Only one of the temperature curves indicates a small thermal run-away during the measurement. Nevertheless, even this is still within the market survey requirements. Therefore, the setup is proven to have a very good control of the temperature.
In contrast to this, the relative humidity inside the climate chamber is not as required. As it can be seen in Figure A.1b in the appendix, all measurements are carried out at humidity levels of more than 60%, although dry air is led into the chamber. A reason for this high relative humidity was not found. The high humidity causes hoar-frost and ice to form inside the chamber. When the setup is heated from the measurement temperature of $T_{\text{set}} = -25\,°\text{C}$ to room temperature to allow the removal of the investigated sensor, the ice melts, resulting in water droplets inside the climate chamber. All of the melting water is found on the thick aluminium plate at the bottom of the setup, since this part takes the longest time to adjust to new temperatures. Since the sensors are placed on the vacuum chuck, which is a few millimetres above this plate, there is no risk for the investigated sensors.

Taken these effects into account, the measurements that are performed at TU Dortmund University for the irradiated sensors of this vendor are used to validate the measurements of the second institute, because there a probe station is used which allows a better control of the environment. The measurements of the second institute are then used as the official measurements for the market survey that can be fed into a database.

The measured data for the leakage current is shown in Figure 3.22. The relevant values for the breakdown voltage and the leakage current scaled to the sensor area are additionally listed in Table 3.6.
For two of the six investigated sensors, a breakdown is detected by the analysis script. This is the case, if the measured leakage current of the consecutive bias voltage step exceeds the current of the actual bias voltage step by a factor of more than 1.2. The detected breakdown voltage for sensor B is at $(420 \pm 5)\,\mathrm{V}$ and for sensor C the breakdown voltage is at $(475 \pm 5)\,\mathrm{V}$. The systematic deviation of the detected breakdown voltage is set to the step size of the voltage increase during the measurement. The breakdown voltages for the other sensors are given as that voltage step, where the measurement stops. This happens, if either the current limit of 100 µA is reached (valid for sensors D and F) or the maximum bias voltage of the measurement is reached (valid for sensors A and E). All the sensors fulfil the breakdown voltage requirements of the market survey.
The other requirement that is specified by the market survey, is the measured leakage current per sensor area at a given bias voltage. The corresponding current limits are indicated in Figure 3.22 by a red line. All sensors irradiated to the lower fluence of $2 \cdot 10^{15}\,n_{\mathrm{eq}}/\mathrm{cm}^2$ show leakage currents of only half the height, that the limit allows. Therefore, it is easy to recognise from the plots that they fulfil the requirement of the market survey. For the thin sensors, those sensors that are irradiated to $5 \cdot 10^{15}\,n_{\mathrm{eq}}/\mathrm{cm}^2$ fulfil the requirement as well.
Only the thick sensor, irradiated to $5 \cdot 10^{15}\,n_{\mathrm{eq}}/\mathrm{cm}^2$ needs a closer look. The area of the SCs is specified as $1.939\,65\,\mathrm{cm}^2$ in the analysis script. Therefore, a maximum leakage current of 87.284 25 µA is allowed at a bias voltage of 600 V. The data reveals, that the measured leakage current at this bias voltage is about $(86.533 \pm 0.023)\,\mu\mathrm{A}$ for the sensor F. For this reason, this sensor fulfils the requirement as well and all irradiated sensors pass all the requirements for the market survey.

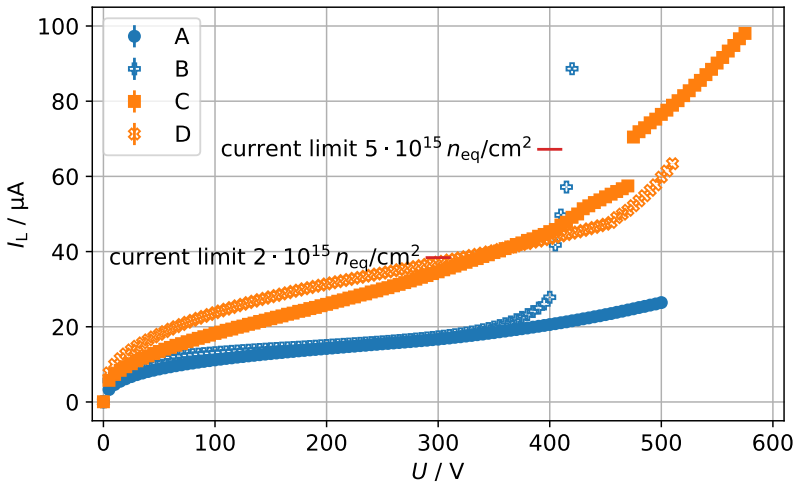

(a) Current-voltage characteristics for the thin SCs.

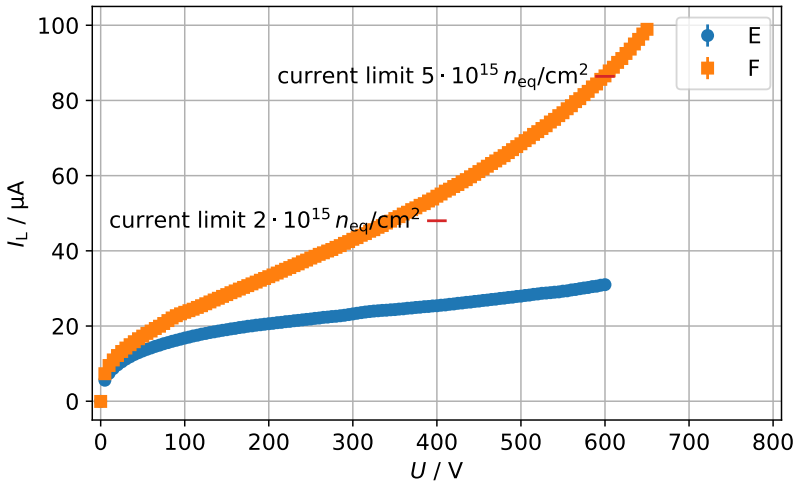

(b) Current-voltage characteristics for the thick SCs.

Figure 3.22: Current-voltage characteristics of the irradiated sensors. The blue markers in both plots refer to those sensors that are irradiated to a fluence of $2 \cdot 10^{15}\, n_{eq}/cm^2$ and the orange markers depict the sensors irradiated to the higher fluence of $5 \cdot 10^{15}\, n_{eq}/cm^2$. Additionally, the corresponding current limits are displayed in the plots. The measurement uncertainties defined as the standard deviation of the measured leakage currents per bias voltage are plotted as well, but are too small to be seen.

Table 3.6: Detailed list with the relevant data of the leakage current measurements of the irradiated sensors. Given are the values for the leakage current density I_L/A and the breakdown voltage V_{bd} of the sensors.

thickness	fluence	sensor name	(I_L/A) / µA/cm^2	V_{bd} / V
thin	$2 \cdot 10^{15}\, n_{eq}/cm^2$	A	8.6094 ± 0.0017	>500
		B	8.9370 ± 0.0010	420 ± 5
	$5 \cdot 10^{15}\, n_{eq}/cm^2$	C	23.362 ± 0.013	475 ± 5
		D	22.4062 ± 0.0028	>510
thick	$2 \cdot 10^{15}\, n_{eq}/cm^2$	E	13.0906 ± 0.0014	>600
	$5 \cdot 10^{15}\, n_{eq}/cm^2$	F	44.613 ± 0.012	>650

3.3 Tests of Modules

Besides the already tested electrical behaviour, the particle detection efficiency of the sensors has to reach a certain level for the later experiment to work well. Therefore, there are several so-called test beam facilities across the world, where the performance of modules can be measured.
This section introduces the used test beam facility located in Hamburg and gives details about the reconstruction of tracks and the later analysis. Moreover, the measurement results are presented in the end.

3.3.1 Test Beam Measurements

Test beam measurements are carried out at special test beam facilities to examine modules with high energetic particles. The facilities offer different kinds of particle beams. Such a particle beam traverses the test beam setup, which consists of a so-called beam telescope and the investigated modules, the so-called devices under test (DUTs). The beam telescope measures the trajectories of the particles with a high spatial resolution. In the later analysis, these tracks are used to extrapolate the expected position on the DUT and are compared to the measured hit position on the DUT.

Test Beam Infrastructure

The modules investigated in this thesis are measured at the DESY II Test Beam Facility [64]. There, a particle beam of either electrons or positrons with an energy of up to 6 GeV is used for the investigation. A sketch of the generation of this

particle beam is shown in Figure 3.23. Detailed information about the DESY II Test Beam Facility is given in the literature [64]. This thesis offers a brief introduction to put the measurements in a greater context.

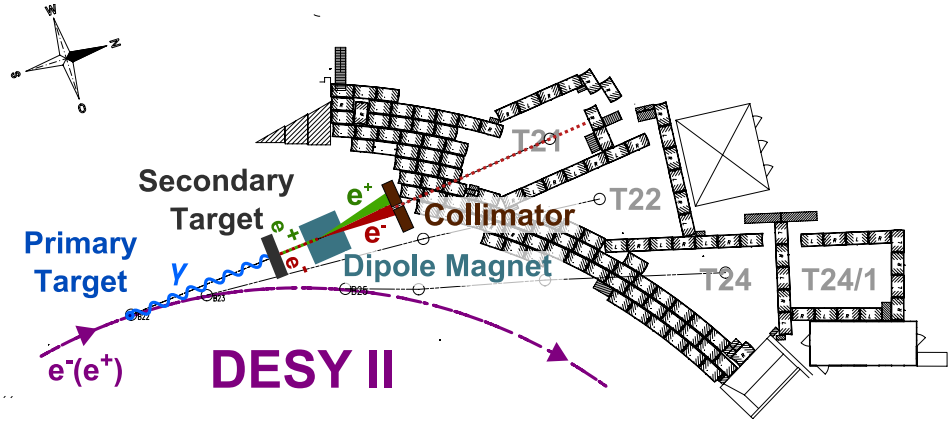

Figure 3.23: Sketch of the DESY II Test Beam Facility with the generation process for the particle beam ([64], adapted).

The primary beam consists of either electrons or positrons and originates from the DESY II synchrotron. Behind three different quadrupoles, the primary fibre targets are placed. If the leptons from the primary beam collide with this fibre, bremsstrahlung is generated and therefore the particle beam is converted to a beam of photons. Those photons collide with the secondary target, a converter target, and produce electron-positron pairs via pair production. This newly generated beam of particles then passes through a dipole magnet. The field strength and the polarity of this magnet can be set by the users to filter the particle beam for the desired particle type and energy. Before entering the final test beam areas, the beam passes a primary collimator and the beam shutter. The shutter is crucial for switching off the beam to allow access to the test beam area to change the measurement setup. An additional lead collimator can be placed inside the test beam area to change the size of the delivered particle beam for the experiment.
For the later presented measurements, a beam consisting of electrons with an energy of roughly 5 GeV is used. This energy is chosen, because it is the perfect trade-off between a high particle rate for less time for data taking and not too much multiple scattering within the measurement setup which worsens the data quality.

The most crucial part of the test beam setup is the pixel beam telescope. Pictures of the exact setup are shown in Figure 3.24. At DESY, two EUDET-type beam telescopes with the names DATURA and DURANTA are available [65]. These telescopes consist of two arms, of which each contains three planes with MIMOSA26 pixel sensors [66]. A MIMOSA26 sensor features quadratic pixels with the size of

18.4 µm × 18.4 µm. Arranged in 1152 columns and 576 rows, this gives an active area of 21.2 mm × 10.6 mm. The sensors have a thickness of only 50 µm. They are protected from environmental light by Kapton foil on both sides. This composition of thin sensors and the thin Kapton foil is used to minimise the material budget and therefore multiple scattering inside the particle trajectory.
The two arms of the beam telescope are upstream and downstream of a movable stage, on which the DUTs can be mounted. The stage is used for precise alignment of the DUTs within the surrounding telescope arms. A box made of PPE foam is mounted around the baseplate of the stage. This box serves two purposes. On the one hand, the black PPE protects the DUTs from environmental light. On the other hand, this box can be used for cooling the sensors. Therefore, it consists of two compartments. One compartment covers the DUTs and the other compartment can be used to store dry ice for the cooling of the irradiated modules. More details about the box can be found in the literature [11].

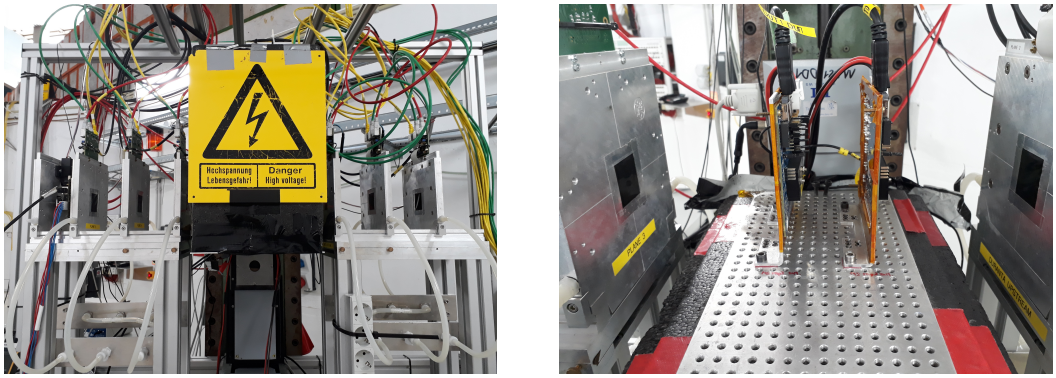

(a) Beam telescope with closed DUT box. **(b)** Closeup of two modules.

Figure 3.24: Photographs of the testbeam setup, where **(a)** shows the complete beam telescope and the DUT box. On the left side, the cables towards the reference module can be seen behind the last telescope plane. In **(b)**, two modules mounted on metal frames fixed to the baseplate can be seen. Red marks on the baseplate indicate the positions for the measurements of the market survey.

For triggering the data taking, four scintillators with areas matching the MIMOSA26 sensors are used. They are placed at the beginning and end of the telescope arms, before the first and after the last plane respectively, and in both positions two scintillators overlap each other. The data taking is only started, if a traversing particle triggers the scintillators. Which scintillators are mandatory for the triggering, can be set by the users. Usually, at least one scintillator in the beginning and one at the end of the telescope are used as the mandatory ones. The trigger signal from the used scintillators is fed into the EUDET Trigger Logic Unit (TLU) [67]. The

TLU submits information about the time of the particle passage and gives trigger numbers. For coincident signals of the scintillators, the trigger signal is distributed to the different readout systems by the TLU. Only after this, the data acquisition (DAQ) is started for the connected modules. As long as the DAQ systems send busy signals, no further trigger is submitted by the TLU.
The MIMOSA26 pixel sensors are read out in a rolling shutter mode. This means, that each row is read out one after another. This results in a quite large integration time of 115.2 µs to read out the whole pixel matrix [65]. For a finer time stamp, an n-in-n reference sensor read out with an FE-I4 readout chip [68] is placed at the end of the telescope. This module can be used for time stamps with a granularity of 25 ns, since it is read out with a frequency of 40 MHz.
The different data streams from the DUTs and the telescope are merged with the EUDAQ data acquisition framework [69]. Each particle passage with a coincident trigger signal is handled as an event and multiple events are summed up to a run. The data is stored in the raw-file format and if the data file exceeds a beforehand specified file size (usually around 1 GB), a new run is started. Changes regarding, for example, the bias voltage are done in between two runs. To ease the later reconstruction, runs taken with the same measurement conditions are called a batch. A typical change in the setup that leads to a change of the batch, is the installation of new modules.

The EUDAQ software comes with another feature: its graphical user interface is used for two different purposes. On the one hand, the different systems can be controlled, so starting and stopping the data taking is easily possible. On the other hand, an additional Online Monitor is available to monitor the data taking. This is helpful for checking the quality of the recorded data by the time it is being recorded. There are a number of plots that can be used to help identify good and bad conditions for data taking, and some of these are described below.
One of the simplest plots, which is created for every module in the setup, is the hitmap. In this plot, all hit signals from the corresponding plane are depicted in a 2D histogram of the sensor. An example of such a hitmap is shown in Figure 3.25a. With this plot, noisy pixels can be identified, because they show higher numbers of entries compared to pixels that are not noisy.
Another plot, that helps to check the noise, is the so-called LVL1 distribution. The LVL1 distribution gives information about the time difference between the trigger signal and the measured hit signal. If the hit is caused by a triggered particle, the time difference between the trigger signal and the hit signal is always the same, since the particle needs a certain time to travel from the trigger scintillator to the corresponding module, where it is detected. Therefore, a clear peak is expected in the LVL1 distribution. Noise signals do not have a fixed time correlation to the trigger signal, so their contribution to the LVL1 distribution is uniform across

the depicted time differences. An example with the clear peak and the uniform distribution caused by noise is shown in Figure 3.25b. The ratio of the peak caused by hit signals to the uniform background from noise entries is an indicator for the amount of noise in the module.

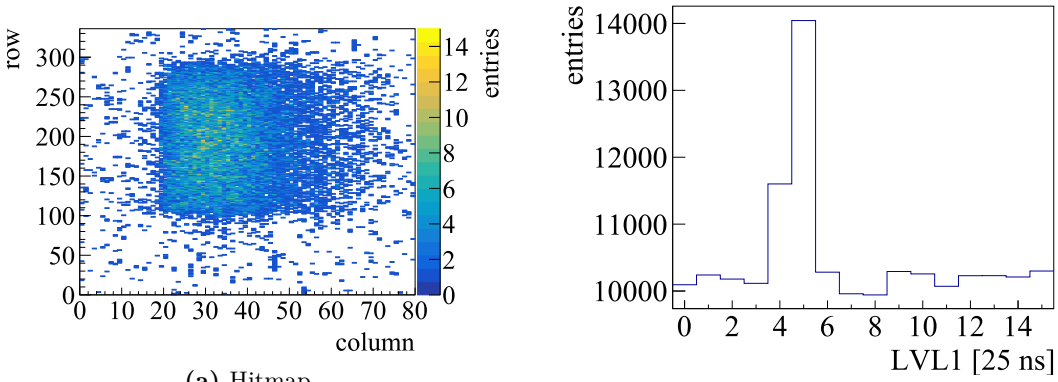

(a) Hitmap.

(b) LVL1 distribution.

Figure 3.25: Exemplary plots taken from the Online Monitor. In **(a)** a hitmap and in **(b)** a LVL1 distribution of an FE-I4 module are displayed [70].

The above-mentioned plots are useful for the detection of noisy pixels. The so-called correlation plots serve a different purpose. With these plots, the correct timing of the data streams can be observed. Exemplary plots of these are shown in Figure 3.26a and Figure 3.26b. Correlation plots are created as 2D histograms, where the hit positions of one sensor are plotted against the hit positions of a second sensor for all hits in an event. Since the position difference of a hit on different planes is constant for the same particle, a diagonal line in the 2D histogram is expected. The diagonal line is not visible or vanishes, if the hits in the two sensors are from different particles and therefore events. This can happen, if the correlation between the different readout systems is lost. This happens mainly due to noisy modules. Since only data where the timing of the data streams is correlated can be used in the later analysis, the correlation plots have to be checked thoroughly during data taking.

Reconstruction and Analysis Software

Two different software tools are needed to convert the raw data taken at testbeam campaigns, to extract the particle detection efficiency of the DUT. The first is *EUTelescope* [71, 72], which is used to reconstruct particle tracks from the raw data. The second step is done with *TBMon2* [73], which analyses the reconstructed tracks

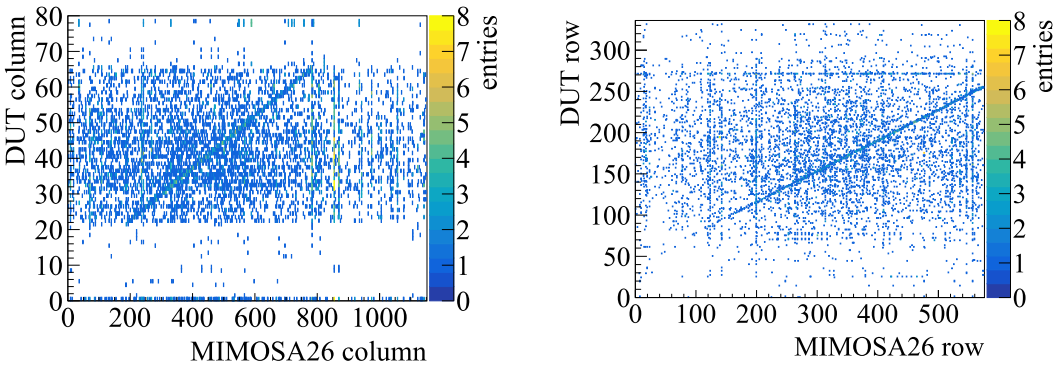

(a) Correlation in x-direction.

(b) Correlation in y-direction.

Figure 3.26: Exemplary plots taken from the Online Monitor. In **(a)** a correlation plot in x-direction and in **(b)** a correlation plot in y-direction of an FE-I4 module are displayed [70].

and gives efficiencies for the DUT. Both tools are presented in more detail in the following.

EUTelescope uses the Modular Analysis and Reconstruction for Linear Collider (MARLIN) framework. The framework is part of the International Linear Collider Software package (ILC Soft) [74] and is used, because it splits the reconstruction process into different so-called jobs. This modularity is especially beneficial, if certain jobs should be skipped or executed multiple times during the reconstruction process. This eases the usage of the reconstruction software. The parameters for the different jobs are stored in steering templates in the xml-data format. The information about the setup details like the number of modules, their position within the setup or module details are given in GEAR-files. These files have to be adjusted for every batch in a testbeam campaign individually.
The different jobs, that need to be carried out in exactly this order, are described now in more detail. The first job is the **converter**. In this step, the raw-data files are converted to the LCIO data format, which is used by EUTelescope. Moreover, within this step, noisy pixels are identified. This is done by comparing the firing frequency of each pixel with a pre-set value. All pixels with a firing frequency larger than the threshold are masked as noisy pixels.
After the conversion of the data, the hits on the different planes are grouped into clusters in the job called **clustering**. For this purpose, different algorithms are available [72]. In this work, the *SparseClustering* is used for the MIMOSA26 sensors and the *GeometricClustering* is chosen for the DUTs. The *SparseClustering* groups pixels together solely based on their indices in the x- and y-direction. The *GeometricClustering* uses the pixel layout description and approximates pixels as

rectangles. All pixels with hits in geometric proximity to the position of the initial hit are grouped to a cluster. This is especially helpful for staggered pixel matrices [75]. After the clustering process, clusters that contain at least one noisy pixel are identified and removed from the further processes.
The **hitmaker** converts the clusters to hits. To do so, the position of the cluster centre is calculated. For this, different approaches are available and in this thesis, a charge-weighted algorithm with the ToT information from pixels within a cluster [75] is used. After the determination of the hit position, the position is transformed from the local coordinate system of each plane to a global coordinate system. Afterwards, a pre-alignment is done. In this step, the positions of the modules are shifted in the x- and y-coordinate, which describe the layer that is perpendicular to the particle beam. This has to be done, because the original GEAR-file contains only information about the distances between the different modules, but no information about their x- and y-coordinate. In order to do the pre-alignment, the difference between the hits in the first plane of the telescope and in another module is calculated in the x- and y-direction. The differences are filled in a histogram and the module is then shifted by the bin with the most entries. The updated positions are saved in a new GEAR-file.
The new GEAR-file is used to **align** all modules. The distances given in the original GEAR-file are measured during the testbeam campaign only roughly with a folding rule. In the alignment, shifts in all directions are applied. This is done in the global coordinate system. The tracks are fitted based on the hit information of each module. For this thesis, the General Broken Line (GBL) algorithm [76] is used for the track fitting. It allows kinks and offsets after each passed module to take multiple scattering into account. The fitted tracks are then used by the Millepede II software [77] to align the modules. For this purpose, a least square minimisation of the whole system is done with the distances between the hit positions and the fitted tracks. The alignment job is done multiple times - three times for this thesis - to gain the best alignment possible.
The very last step of the reconstruction chain is the **fit** of the hits in an aligned system to tracks. The GBL algorithm is used again, but in this step, only the hit information of the MIMOSA26 sensors is used. This ensures unbiased tracks. The tracks have to fulfil certain requirements to be accepted. These requirements, e.g. for different residual cuts and cuts on the slope of so-called doublets (straight line fit between hit in the first and last module of one telescope arm), can be set in the configuration file. After this step, the information about the fitted tracks, the projected positions on the DUTs and the hit information of every DUT is stored in a ROOT-file to be analysed further.

The software TBMon2 uses the track information from the EUTelescope output file for the analysis of the efficiency of the DUTs. For that purpose, different

preprocessors are needed before the actual analysis takes place. The analysis is based on the distinction between tracks and hits. A track in TBMon2 is without a corresponding hit in the DUT. In contrast to this, a hit in TBMon2 is associated with a hit in the corresponding DUT. In the following, details about the preprocessors are given.
In the first preprocessor, tracks are selected that are only measured by the reference module. This is necessary, because the MIMOSA26 sensors are read out much longer than the DUTs, which are read out with a granularity of 25 ns (see subsection 2.4.2). Therefore, there are measured particles in the telescope plane, that are not detected within the time frame of the DUT. For this reason, a reference module with the same integration time as the DUT is used and only those tracks are used, that are detected by the telescope and the reference module. After the tracks with correct timing information are chosen for the analysis, another preprocessor marks dead and noisy pixels. After this, the hits on the DUTs are clustered. Within the clustering step, the cluster is marked with a flag, if it contains marked pixels from the second preprocessor or edge pixels. Within the preprocessor called ClusterMatcher, the clusters are associated with the reconstructed tracks. To do so, the distance between the cluster centre and the track position is compared to a specified value, and if the distance is smaller than the pre-set value, the cluster and track are matched. Empirical knowledge gives the rule of thumb to use twice the pixel pitch as the pre-set value. This is followed for the pixel pitches of 50 µm and 100 µm, resulting in pre-set values of 100 µm and 200 µm, respectively. For the smallest studied pixel pitch of 25 µm in this thesis, it was found, that a pre-set value that complies with the rule of thumb misses a lot of hits. Therefore, a pre-set value for the distance of 100 µm is used for this case. The last preprocessor checks the alignment of only the DUTs. For this purpose, residual plots are created from the difference between the track positions and the cluster centres. After these plots are created, shifts and rotations are applied for each run independently. More details about the latest improvements of the preprocessors can be found for example in the thesis of M. Wagner [70].

TBMon2 offers different analyses, that can be chosen individually. Only good tracks and hits are used for the calculation of the efficiency of a module. This means, that tracks have to be recognised by the reference module and that the track is not in a masked or edge region of the investigated DUT. A hit is classified as good, if the track has a cluster without masked or edge pixels associated.
Since an optimal detector would recognise all tracks as hits, the efficiency is given as the fraction of good hits n_{hits} and the number of good tracks n_{tracks}:

$$\epsilon = \frac{n_{\text{hits}}}{n_{\text{tracks}}}. \tag{3.2}$$

The statistical error of the efficiency is calculated as the standard deviation:

$$\sigma_\epsilon = \sqrt{\frac{\epsilon \cdot (1-\epsilon)}{n_{\text{tracks}}}}. \tag{3.3}$$

This basic calculation of the efficiency is used to get the global efficiency for the whole sensor area per run.
The software TBMon2 allows generating different so-called geometries, because pixels with the same layout behave the same. All pixels that share an identical layout are grouped in a geometry, and all geometries that build up a full sensor, are collected in a so-called geometry file. This allows for example to differentiate in the analysis between edge pixels and inner pixels. All track and hit positions of a single geometry are projected in one pixel-sized area by means of the geometry file. Since all recorded hits within several runs are displayed in the in-pixel map, a better insight in the efficiency distribution across the single pixel is gained.
The efficiency is calculated for every run after Equation 3.2 and Equation 3.3. Since the efficiency differs from run to run slightly, a mean efficiency is given. This is done by averaging the independent efficiencies weighted with the number of used tracks. A Clopper-Pearson confidence interval is used with a confidence level of $\gamma = 95\%$, to describe the deviations from run to run. This procedure was implemented and used for the first time in TBMon2 in the thesis of A. Gisen [78]. More detailed information about this confidence interval can be found there.

A new analysis was written for the market survey. This is necessary, because some of the investigated sensors are biased through the punch-through technology (see subsubsection 2.4.1). This technology is known to show inefficiencies around the bias dot [12]. Since this affects the overall particle hit detection efficiency of the sensor, a new analysis is written, where only tracks and hits in a fiducial region are considered. This fiducial region is chosen in a trade-off between maximising the area under investigation and simplicity of implementing in the analysis script. An example of the fiducial regions for different pixel geometries is given in Figure 3.27. In addition, the exclusion of the regions around the bias dots is justified by the fact, that the particle trajectories in the ITk are expected to pass regions around the bias dot as well as regions that are not affected by the bias dot. In such a way, the effect of the efficiency loss is reduced in the later operation of the ITk and therefore the investigation of only the fiducial region is reasonable in the scope of the market survey. With this new analysis, the overall efficiency, or global efficiency, can be compared to the efficiency of the fiducial region.

The analyses of the calculation of the efficiency per run and the efficiency for the fiducial region are combined in the course of this thesis. An example of how much the calculated efficiencies differ with respect to the different runs and the chosen

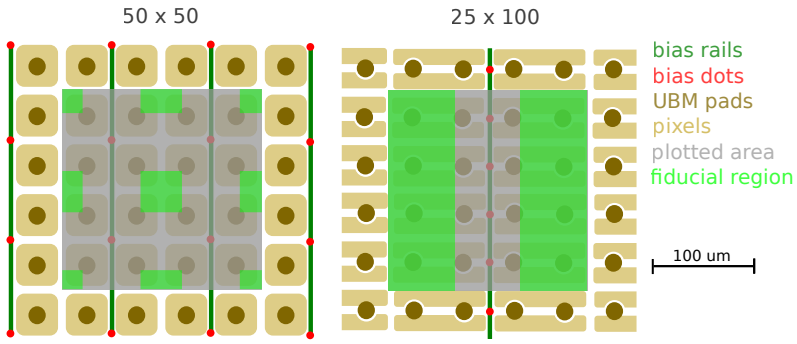

Figure 3.27: Schematic layout of the two different pixel geometries [79]. The fiducial regions are marked in green and exclude the parts affected by the biasing structure. The grey squares indicate the plotted area in hit efficiency maps.

part of the pixel matrix is shown in Figure 3.28. The analysed efficiencies of an unirradiated sensor biased with punch-through technology are displayed. For the reference module, the sensor outside the cold box, equipped with an FE-I4 readout chip, is used. For this investigated sensor, the mean efficiencies (calculated as the track-weighted average over the independent efficiencies per run) across the whole investigated pixel area, which are displayed in orange, vary around 99.3% for the different analysed runs. The mean efficiencies of only the fiducial part of the pixel area, displayed in blue, are approximately 0.5% higher. This difference seems small, but especially for irradiated sensors, where the efficiency loss around the punch-through region is more prominent, it gets larger.

Several people were responsible for choosing a robust configuration for the reconstruction and analysis software. In such a way, the process to analyse the data was standardised and reusable for all testbeam campaigns to allow for quick results. Since the amount of the measured data was very large and the results had to be ready quickly, the reconstruction and analysis were split between different people. The analysis results were always cross-checked by at least two people to ensure validity.
In the course of this thesis, the best parameters for a robust reconstruction and analysis chain are determined. Moreover, the author of this thesis was part of the team to reconstruct, analyse and cross-check the data from multiple testbeam campaigns.

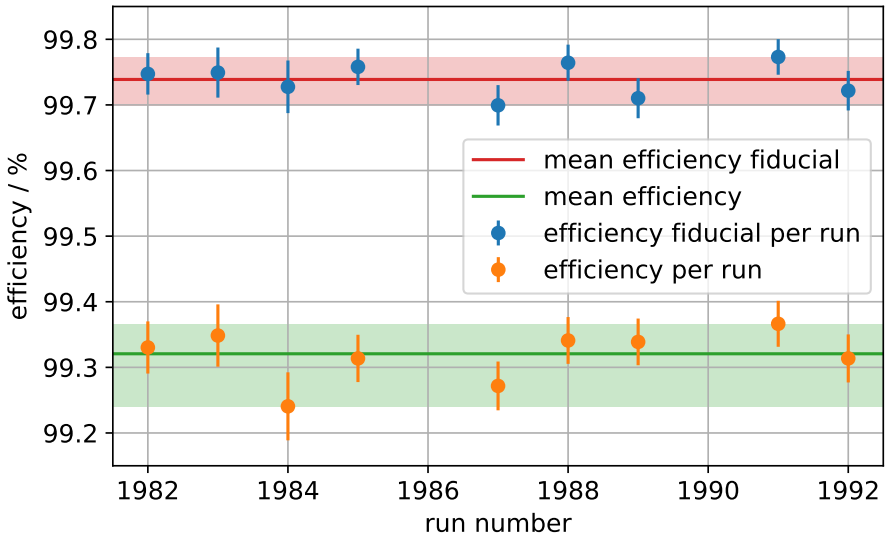

Figure 3.28: Measured efficiencies for the sensor V3S05 at a bias voltage of 80 V for the different investigated runs at the June 2020 testbeam campaign with a particle beam of 5 GeV particles. The analysis of the fiducial part of the pixel matrix is displayed with blue points and the red area, the orange data points and the green band belong to the analysis of the global efficiency.

3.3.2 Results of Test Beam Measurements

The modules used in the testbeam campaigns are read out with ITk software based on YARR [80]. Only the linear and differential parts of the module are considered for data taking and the synchronous part is masked before data acquisition. This is done, because the synchronous part is not going to be used in the ITk. During all testbeam campaigns the same setup, the same configuration in the reconstruction and the analysis are used. This is done, because only the sensor quality is important for this market survey and in this way uniform conditions are valid for all modules. To check the quality of the readout chips or the hybridisation, there are additional campaigns focusing on those.

Modules from six different vendors are investigated in several testbeam campaigns. However, this thesis only focuses on modules from those vendors whose sensors have already been investigated in the laboratory at TU Dortmund University. Therefore, all modules listed in the following part belong to either vendor three (FBK) or vendor four (HPK).
A subset of the results was already presented in the thesis of R. Taibah [81], when the market survey was still ongoing. The values given in this thesis differ from those presented here, as the correct configuration files were not yet created. The full set of measured modules and the corresponding results of the standard analysis with the fiducial region can be found in more recent theses [79, 82].

Unirradiated Modules

The measurement of unirradiated modules in a testbeam campaign is usually straight forward. Neither problems with the tuning of the readout chip nor the sensor itself are expected. Therefore, all investigated unirradiated modules are handled the same in the different testbeam campaigns.
Concerning the tuning of the readout chip, a standardised tuning procedure is chosen. This results in a threshold of 1500 electrons and a time over threshold, which is an indicator for the charge response, of seven bunch crossings (each is 25 ns) for a signal of 10000 electrons. The latter means, that an injected charge of 10000 electrons results in a signal which is for the duration of seven bunch crossings (corresponding to a total time of 175 ns) above the threshold value. This tuning is usually written as 1500e, 7ToT@10ke.
With this tuning, the hit detection efficiency of the different sensors is examined. Within the market survey, the required efficiency for non-irradiated modules is 98.5%. This value should be met at a bias voltage of $V_{\text{bias}} = V_{\text{depl}} + 50\,\text{V}$. Only

modules with a higher efficiency at this bias voltage are classified as good and pass the market survey.

All given values for the efficiency are calculated with the combined analysis of the fiducial region and the asymmetric error band. Within this thesis, no pixels at the edges of the pixel matrix are included. For unirradiated modules, the linear and differential front-end of the readout chip are tuned. Therefore, all the pixels beneath these front-end flavours are included in the analysis of the particle hit efficiency.
The analysis with TBMon2 requires a reference module. Only tracks and hits, that are detected by this reference module, are used in the analysis. The sensor equipped with the FE-I4 readout chip at the end of the telescope should be used as the reference module, since it is known to have a very good efficiency. If there are two market survey modules installed in the cold box of the setup, these two modules can be used for cross-referencing each other. This method is used to increase the statistics and is applied only, if the DUT that should serve as the alternative reference module has an efficiency of more than 90%. This efficiency is determined by the analysis, where the module that is read out with the FE-I4 serves as the reference module. Those cases where cross-referencing is used in the analysis are marked in Table 3.7.

Table 3.7: Details and results of the efficiency measurements at different testbeam campaigns for the unirradiated sensors of the vendors 3 and 4. The used beam energy is 5.6 GeV, only the sensor V3S06 is investigated with a 6 GeV beam. In the column for the geometry, the thickness and the pixel area are given. The pixel area is given in length times the width, where the length is measured parallel to the long side of the whole sensor. The given number of tracks corresponds to the used analysis (either global for sensors without punch-through technology or fiducial for those with punch-through technology). An asterisk marks the sensors where cross-referencing is used.

sensor	geometry / µm, µm × µm	PT	V_{bias} / V	tracks	ϵ_{glob} / %	ϵ_{fid} / %
V4S01*	150, 25 × 100	poly	130	50401	$99.736^{+0.014}_{-0.023}$	
V4S02*	150, 50 × 50	poly	130	97914	$99.71^{+0.07}_{-0.05}$	
V4S03*	150, 25 × 100	poly	130	120695	$99.85^{+0.05}_{-0.05}$	
V4S06*	150, 25 × 100	poly	130	61730	$99.814^{+0.038}_{-0.017}$	
V3S05	150, 100 × 25	PT	80	59196	$99.342^{+0.10}_{-0.027}$	$99.804^{+0.09}_{-0.024}$
V3S06*	150, 100 × 25	PT, split	80	1977	100^{+0}_{-0}	$99.95^{+0.06}_{-0.06}$
V3S13	100, 50 × 50	TM	80	14638	$99.801^{+0.11}_{-0.034}$	

For most of the sensors, the stated efficiencies are received with cross-referencing.

Especially, for all the modules of vendor 4 this has to be done.
This is caused by a special design of the sensors. Their pixel matrix differs in its top and bottom half. Moreover, the modules of vendor 4 are investigated in one of the first testbeam campaigns and it was later confirmed, that in this campaign there are more clusters and tracks per trigger. This was due to a different beam configuration than in other testbeam campaigns, which resulted in a higher particle flux. For those reasons, the standard analysis with the FE-I4 as the reference module is not the chosen method. Nevertheless, the sensors used as reference modules have high particle hit detection efficiencies of more than 90%.
For the investigation of V3S06, cross-referencing is also used. With this method, the number of used tracks increases by a factor of three compared to the analysis with the FE-I4 as the reference module. Since the number of tracks is still very low compared to the other measurements stated in Table 3.7, this is a reasonable choice. Furthermore, the second DUT, which is used as the reference module in this setup, has a global efficiency above 99%.
All investigated sensors fulfil the market survey requirement by having efficiencies of more than 99.7%, which is at least 1% more than the required 98.5%. Since this thesis uses another analysis as the theses before, the efficiencies are checked against the efficiencies stated in the theses of T. Fitschen and S. Möbius [79, 82]. With respect to the error bands given in Figure 3.29, all measured efficiencies are in good agreement. Only for the sensor V4S06, the efficiency is higher in this analysis than that given by T. Fitschen. However, the absolute difference is only 0.5%, which does not change anything about the classification of this sensor. Since all other values are in good agreement, the new analysis in this thesis is proven to be appropriate to give comparable results.

Apart from the measurement points necessary for the market survey, most modules are also investigated at lower bias voltages. An example of such an investigation is shown in Figure 3.30.
The sensors have different pixel designs (V3S13 has a pitch of $50\,\mu m \times 50\,\mu m$ and V3S05 has $100\,\mu m \times 25\,\mu m$) and different thicknesses (V3S13 is $100\,\mu m$ thick and V3S05 is $150\,\mu m$ thick). Even the biasing scheme is different between those two sensors, since V3S13 features temporary metal and V3S05 is biased with the punch-through technology. Nevertheless, the efficiencies do not differ much from each other. For the sensor V3S05, the efficiency is given for the fiducial region, because the areas around the bias dots worsen the overall efficiency. At least for these two sensors, there is no indication that one of the pixel pitches or the thicknesses is more beneficial than the other with respect to the particle hit detection efficiency.
Although there is a slight trend towards lower mean efficiencies at higher bias voltages, the values for all applied bias voltages are consistent in terms of their corresponding error bars. It is clear from this investigation, that the sensors have

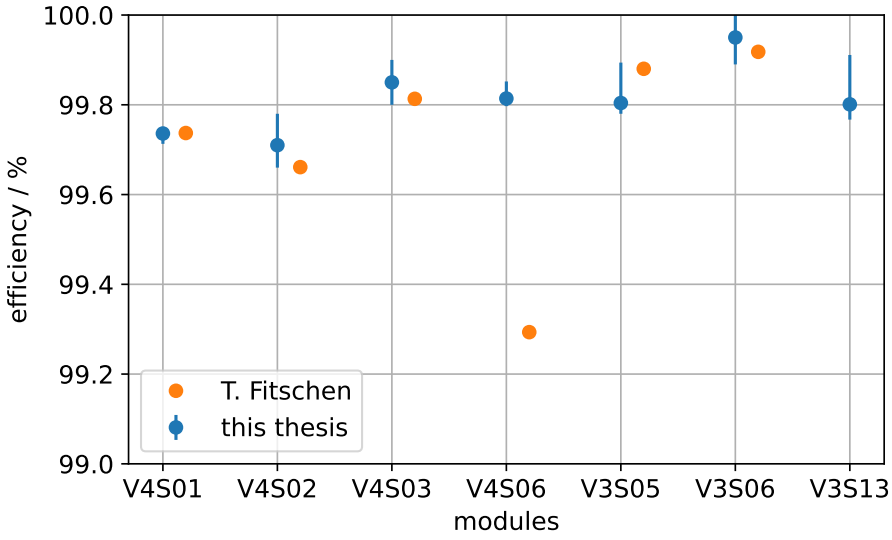

Figure 3.29: Comparison of the analysed efficiencies recorded for the market survey with the analysis used in this thesis (blue data points) and the analysis used by T. Fitschen [79] (orange data points). There is no data given for V3S13 in the thesis of T. Fitschen, so no comparison is possible. For the modules V3S05 and V3S06, the efficiency of the fiducial region is given, for the other modules the global efficiency is depicted.

high efficiencies at even lower bias voltages than required. The sensors of this vendor have been investigated in the lab before the testbeam campaign, so the depletion voltage is known to be around only 15 V for the thin sensor and only 25 V for the thick sensor. Even with the lowest applied bias voltage of 30 V, which is just slightly above the depletion voltage, an efficiency of more than 99.7% is achieved. This is well above the required efficiency of 98.5% for the market survey and proves, that the safety margin of an additional 50 V is not necessarily needed and the sensors work very well at low bias voltages before irradiation.

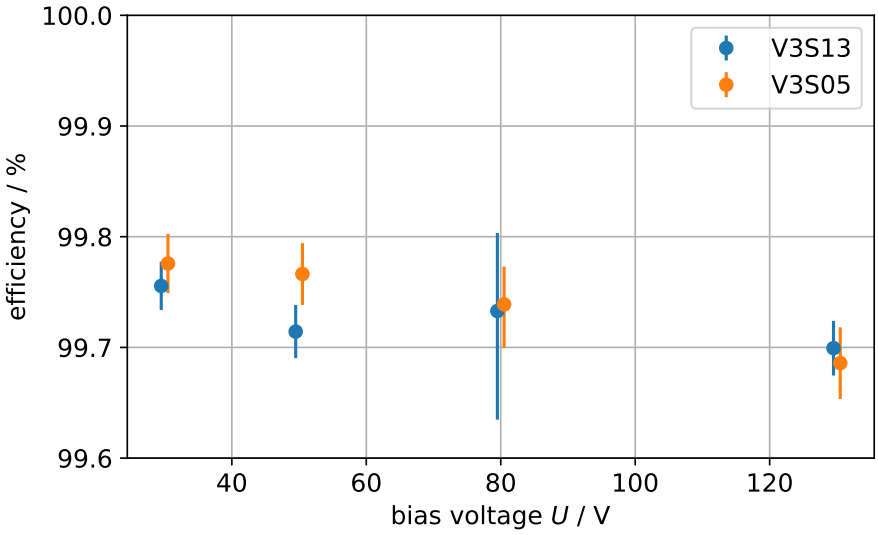

Figure 3.30: Averaged mean efficiencies for the sensors V3S13 and V3S05 at different bias voltages. For sensor V3S05, the efficiency of the fiducial region is given. The data points are plotted next to each other, but the applied bias voltages are 30 V, 50 V, 80 V and 130 V for both sensors. The tuning is always the standard tuning of 1500e, 7ToT@10ke.

Irradiated Modules

To test, whether the sensors can cope with the harsh conditions in the future HL-LHC, their particle hit detection efficiency is studied as well, after the sensors are irradiated. The fluences are the same as for the laboratory measurements for the irradiated sensors, so one set of the sensors is irradiated to $2 \cdot 10^{15}\, n_{\mathrm{eq}}/\mathrm{cm}^2$ and another set is irradiated to $5 \cdot 10^{15}\, n_{\mathrm{eq}}/\mathrm{cm}^2$. Irradiated sensors are expected to show signs of bulk damage and therefore a higher leakage current is expected. This results

in more noisy pixels, which give signals without a corresponding trigger, that affect the tuning procedure and data taking. For this reason, the tuning procedure for the irradiated modules differs from the procedure for the unirradiated ones.
For the tuning, a predefined script is prepared to ease the process. The tuning target is a threshold of 1000 electrons for all modules. For irradiated sensors, there is no tuning for the ToT value foreseen. However, as different sensors are affected differently by the irradiation, individual adjustments must be made for each module. The tuning is heavily affected by noisy pixels, so a different number of masking steps has to be performed for each module. In addition, the masking has to be repeated during different runs in the data taking process. This is necessary, because it gets warmer inside the cold box over the time after the initial setup and filling with dry ice. If the sensors and the air around them get warmer, the leakage current increases and therefore more pixels get noisy. Nevertheless, all irradiated modules are tuned to the same target value. This grants the possibility to compare the efficiencies with each other, because potential side effects from the readout chip are counteracted.

Within the market survey, the sensors are classed as good, if the measured efficiency is more than 97%. This value is a compromise between the capability of the available technology from this time and the requirements for the tracking performance of the ATLAS experiment [48]. The efficiency is examined at different applied bias voltages with respect to the thickness and the irradiation fluence of the investigated sensor. The thin sensors are measured at a bias voltage of 300 V, if they are irradiated to $2 \cdot 10^{15}\, n_{\mathrm{eq}}/\mathrm{cm}^2$ and at a bias voltage of 400 V for the higher fluence of $5 \cdot 10^{15}\, n_{\mathrm{eq}}/\mathrm{cm}^2$. The thick sensors are examined at a bias voltage of 400 V when irradiated to the lower fluence, and a bias voltage of 600 V is required for the higher irradiation fluence.

For irradiated modules, only the differential flavour of the front-end is used in the ITk market survey and the other areas of the pixel matrix are excluded from the analysis. This is done, since only this flavour is foreseen for the final readout chip and the tuning of this part of the pixel matrix is easier than for the other flavours. This saves a lot of time during the testbeam campaigns, since the tuning of an irradiated module with lots of noisy pixels can take up to two hours. Moreover, the tuning is done after the temperature inside the cold box settles and if the tuning takes more time, the temperature starts to rise again, since the chips and sensors are powered during the process and produce heat in the meantime.
In some runs, only one market survey module is installed. In this case, the sensor equipped with the FE-I4 readout chip at the end of the telescope has to be used as the reference module. All cases where cross-referencing with an additional market survey module is used are marked in Table 3.8 to be easily recognised. The analysis is performed in the same way as for the unirradiated modules, so no pixels at the edges of the pixel matrix are included. Again, the efficiencies are given for

the whole pixel area or only the fiducial part of the pixel area with respect to the corresponding biasing scheme. The analysed sensors and their efficiencies are displayed in Table 3.8. Sketches of the punch-through design straight and wavy are displayed in Figure 3.31.

Table 3.8: Details and results of the efficiency measurements at different testbeam campaigns for the irradiated sensors of the vendors FBK and HPK (FBK sensor names start with V3 and HPK sensor names start with V4). In the column for the geometry, the thickness and the pixel area are given. The pixel area is given in length times the width, where the length is measured parallel to the long side of the whole sensor. The given number of tracks corresponds to the applied analysis (either global for sensors without punch-through technology or fiducial for those with punch-through technology). The sign † is used to indicate an irradiation fluence of $2 \cdot 10^{15}\, n_{\mathrm{eq}}/\mathrm{cm}^2$, while all other sensors have an irradiation fluence of $5 \cdot 10^{15}\, n_{\mathrm{eq}}/\mathrm{cm}^2$. An asterisk marks those sensors where cross-referencing is used. Numbers printed in red indicate efficiencies that do not comply with the market survey requirement.

sensor	geometry / µm, µm × µm	PT	V_{bias} / V	tracks	ϵ_{glob} / %	ϵ_{fid} / %
V4S01†	150, 50 × 50	poly	400	98	100^{+0}_{-0}	
V4S03	150, 50 × 50	poly	600	6144	$99.58^{+0.18}_{-0.11}$	
V3S01†	150, 50 × 50	TM	400	22552	$99.75^{+0.08}_{-0.07}$	
V3S12†	100, 50 × 50	TM	300	152254	$99.46^{+0.09}_{-0.06}$	
V3S02*	150, 100 × 25	TM	600	54130	$99.61^{+0.12}_{-0.12}$	
V3S03	150, 50 × 50	TM	600	105699	$99.557^{+0.024}_{-0.027}$	
V3S14*	100, 50 × 50	PT, straight	400	58	$86.7^{+1.8}_{-1.8}$	$96.6^{+2.4}_{-2.4}$
V3S15	100, 100 × 25	PT, split	400	25707	$98.80^{+0.22}_{-0.06}$	$99.55^{+0.09}_{-0.16}$
V3S16	100, 50 × 50	PT, wavy	400	7795	$96.37^{+0.36}_{-0.5}$	$98.91^{+0.24}_{-0.29}$

Only for two modules, the cross-referencing technique is used. For the measurement of V3S14 at the required bias voltage of 400 V, this is the only choice to gain any results. At the required bias voltage, there is only one run available. In addition, there is a hiccup in the readout systems on this particular run, so there is a mismatch between the data from the DUTs and the data from the FE-I4 module. Nevertheless, the second module, that is used as the reference module in this run, has an efficiency of more than 97%, so this is a valid choice. For the module V3S02, cross-referencing is chosen to double the statistics. The second module in the setup has efficiencies of

(a) PT straight. **(b)** PT wavy.

Figure 3.31: Sketches of the sensor design for a pixel pitch of 50 µm × 50 µm with a **(a)** straight and **(b)** wavy punch-through design [83].

well above 90%.

In particular, the module V3S14 stands out in Table 3.8. Neither the global efficiency nor the fiducial efficiency reach the required efficiency of 97%. The difference between these two efficiencies is quite large with roughly 10%, which is an indicator, that the exclusion of the regions around the punch-through structures is a necessary decision. Nevertheless, the in-pixel projection for this module looks different from other sensors with a pixel pitch of 50 µm × 50 µm with biasing structures for the punch-through technology. A comparison is shown in Figure 3.32. For the module V3S16 in Figure 3.32b only the bias dot affects the efficiency. The bias dots are located in this presentation at the coordinates (50|50), (150|50), (50|150) and (150|150). The round regions with lower efficiency around these coordinates are excluded in the analysis of the fiducial regions, as it is displayed in the scheme in Figure 3.27. However, for the module V3S14, the areas with low efficiencies are arranged differently. Instead of round areas, large horizontal bands can be seen in Figure 3.32a. This is thought to be due to the different arrangement of the biasing structures (called PT (straight) in Table 3.8). The standard analysis of the fiducial region does not exclude all areas of low efficiency for this sensor design. However, as this PT design is not expected to be used for later ITk sensors anyway, no adaption of the analysis is made within the scope of the market survey.

Besides of the unusual biasing scheme, the number of used tracks for the analysis is very low for the module V3S14. Around one quarter of the pixels are masked and nearly all of them are disabled, because they are identified as noisy (see the thesis of T. Fitschen [79] for more details about the masking of modules during the market survey). The leakage current of this module at the required bias voltage of 400 V is relatively high, with more than 1 mA. The other modules V3S15 and V3S16, which feature the same pixel pitch, thickness and irradiation fluence, have leakage currents below 5 µA. Due to the high leakage current, it is possible that

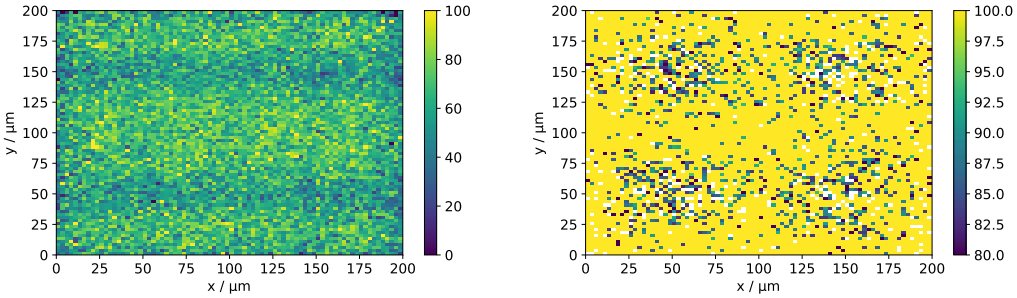

(a) V3S14, PT (straight), 300 V.

(b) V3S16, PT, 400 V.

Figure 3.32: In-pixel projection for **(a)** V3S14 and **(b)** V3S16. Both sensors have the same pixel pitch (50 µm × 50 µm), the same thickness (100 µm) and the same irradiation fluence ($5 \cdot 10^{15}\, n_{\mathrm{eq}}/\mathrm{cm}^2$). For sensor V3S14, a measurement with a bias voltage of only 300 V is displayed, because for this measurement a higher number of tracks is reconstructed (roughly 700) than for the measurement with a bias voltage of 400 V (58 tracks). Therefore, the overall efficiency is expected to be very different from that displayed for V3S16 and only the areas of low efficiency across each projection are of interest. The colormaps indicate different efficiencies for both plots.

other pixels are only slightly below the threshold to be recognised as noisy. Those pixels fire a lot without a corresponding trigger and thus overwhelm the readout system. That is the reason why the run has around one million triggers, as all other runs have, but only 350 reconstructed tracks across the whole pixel matrix and only 58 reconstructed tracks through the fiducial region of this sensor at the required bias voltage.
The results for V3S14 show very large uncertainties of roughly ±2% for both analysed efficiencies. This is at least by a factor of ten larger than the usually derived uncertainties for the other modules. An explanation for this is the low statistics, because only 58 tracks are available for the analysis of this module. Another sensor with unusual uncertainties is V4S01. For this sensor, the number of tracks is comparably small with only 98 usable tracks. The small number of tracks is a result of numerous masked pixels. Across the module, approximately 90% of the pixels are masked. This results in the unusual fact, that all of these tracks are recognised by the sensor, giving an efficiency of 100%. For this efficiency, the term $\epsilon \cdot (1 - \epsilon)$ in Equation 3.3 is always zero. For this reason, the analytical uncertainty of the efficiency is given with ±0. The sensor V4S01 is classed as good within the market survey after discussions in the market survey community. Nevertheless, a remeasurement with a greater statistics would have been beneficial to verify that classification.

There is one additional sensor, with more statistics, that should be mentioned. This is V3S16, for which the global efficiency is too low to meet the market survey requirement, but the fiducial efficiency fulfils the requirement. However, the global efficiency of 96.37% is only slightly below the threshold of 97%. This small difference proves that the loss of efficiency due to the biasing structures is not that relevant even after irradiation. As the biasing technique is not investigated in this survey, this is a good example of why it was justified to exclude the regions around the bias dots. Furthermore, the efficiency of the fiducial area of V3S16 is only slightly below the efficiencies for modules with other biasing schemes.
To sum up the results, only one module is classified as bad after the irradiation process. This can be tracked down to a special arrangement of the biasing structures. All other sensors fulfil the market survey requirement. For this reason, both vendors have proven to be able to produce sensors that can cope with the harsh environment of the HL-LHC.

The analysis used by T. Fitschen and the analysis used in this thesis are compared for the irradiated sensors as well. The corresponding plot is shown in Figure 3.33. For the modules of vendor 4, there is no comparison with the theses of T. Fitschen and S. Möbius [79, 82] possible. Although there is data for the sensors in the tables in their theses, there is a confusion in their analyses and the tracks are reconstructed and analysed with a wrong pixel implantation for the irradiated sensors V4S01 and V4S03. Since these are the only samples for irradiated modules of vendor 4, there is only a comparison between the correct reconstructed tracks and the wrongly reconstructed tracks feasible. Since this is not expected to gain information about the different used analyses in this thesis and theirs, this comparison is not done here.
In total, there are seven irradiated modules of vendor 3. Four of them are analysed to have efficiencies, that are in very good agreement with those from the former theses. These modules are V3S01, V3S02, V3S15 and V3S16. The latter two are named V3S1x1026 and V3S1x1028 in the thesis of T. Fitschen [79]. The efficiency of the sensor V3S14 is not comparable, because T. Fitschen gives the efficiency for a bias voltage of only 350 V and in this thesis the original foreseen bias voltage of the market survey of 400 V is analysed. Since the efficiency is correlated to the applied bias voltage, a comparison of these values is not reasonable. This leaves only two other sensors for the comparison: V3S12 and V3S03. For both sensors, the efficiencies in this thesis are lower than those reported by T. Fitschen. Nevertheless, if the upper edge of the error band from this thesis is compared to the values from the other theses, the absolute difference is only 0.06% (V3S12) and 0.12% (V3S03). These differences are very small and in the order of the given error band calculated in this thesis. Considering that T. Fitschen gives no uncertainties for the results, it is very likely that his efficiencies and the efficiencies in this thesis agree well with

each other. Moreover, a slightly lower efficiency is expected for the values of these sensors from this thesis, since the original reference module is used and not the cross-referencing technique. Despite all these differences, the efficiencies in this and the other theses all classify the sensors the same as either good or bad. So even for the irradiated sensors, the combined analysis gives comparable results.

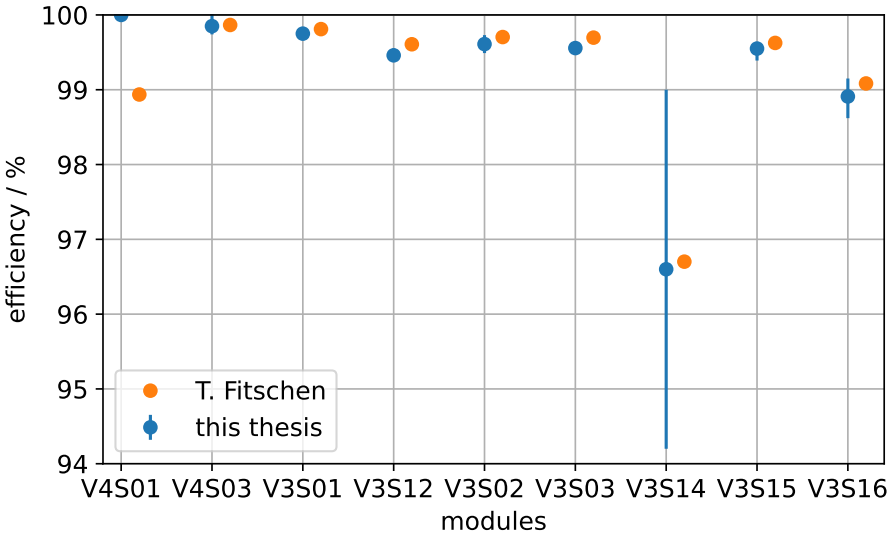

Figure 3.33: Comparison of the analysed efficiencies recorded for the market survey with the analysis used in this thesis (blue data points) and the analysis used by T. Fitschen [79] (orange data points). A comparison is not feasible for the modules of vendor 4 and for the sensor V3S14 (see the text for more details). The data points are nevertheless shown for completeness.

The sensors of vendor 4 are special, since their pixel matrix is not uniform, but divided into two parts with different designs. On each sensor, there is only one pixel pitch realised, but one half features biasing structures and the other half does not. The in-pixel projections are used to investigate, if the used polysilicon for biasing affects the particle hit detection efficiency.
Exemplary plots of the projected in-pixel maps for an unirradiated sensor with a pixel pitch of 50 µm × 50 µm and 25 µm × 100 µm are shown in Figure 3.34a and Figure 3.34b, respectively. No effect of the polysilicon used for the biasing is observed on the efficiency of the unirradiated sensors. Moreover, there is no specific pattern that is linked to the pixel implantation visible.
For the irradiated modules of vendor 4, an in-pixel projection is available only for V4S03, because the number of tracks is too small for V4S01. Even for V4S03, the in-pixel projection is not completely covered with tracks. The projection is shown in

Figure 3.34c. White areas in the projection indicate, that there are no tracks, that are folded in this area. Since the map is not completely filled, it is not possible to observe an effect of the polysilicon on the efficiency for this sample of an irradiated sensor.

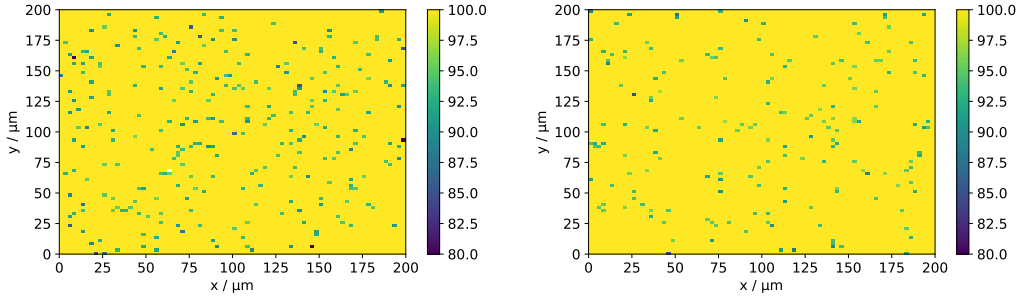

(a) V4S02, 50 µm × 50 µm, poly.

(b) V4S03, 25 µm × 100 µm, poly.

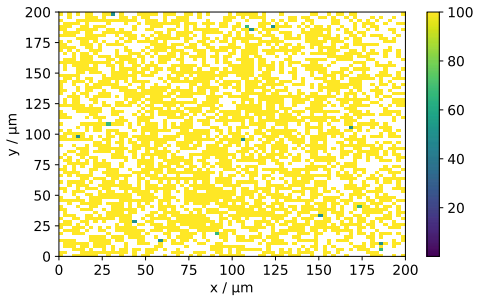

(c) V4S03, 25 µm × 100 µm, poly, irradiated to $5 \cdot 10^{15}\, n_{\mathrm{eq}}/\mathrm{cm}^2$.

Figure 3.34: In-pixel projections for unirradiated and irradiated sensors of vendor 4 with different pixel pitches. In **(c)** a different colour encoding is used in contrast to the maps for the unirradiated sensors displayed in **(a)** and **(b)**.

Vendor 3 offers different combinations of pixel pitches and biasing techniques such as punch-through technology and temporary metal (refer to subsubsection 2.4.1 for more details). An example of if and how the temporary metal affects the efficiency is depicted in Figure 3.35a and Figure 3.35b. The projections are based on pixels with a pitch of 50 µm × 50 µm. They differ in the irradiation (unirradiated and irradiated to a fluence of $5 \cdot 10^{15}\, n_{\mathrm{eq}}/\mathrm{cm}^2$) and their thickness. Nevertheless, the latter is not expected to affect the efficiency of the sensor, since the bias voltage is chosen in accordance to this parameter. From the plots, it is clearly visible, that the temporary metal does not impact the efficiency very much. This is true for the unirradiated and the irradiated module as well. In fact, the total difference between

the measured efficiencies of these two modules is only 0.3%, with the irradiated module having a slightly lower efficiency. This is reflected in the plots with more green and blue filled areas, which correspond to areas with lower efficiencies.
For the effect of the bias dot and bias rail, two in-pixel projections of sensors biased with the punch through technique are displayed in Figure 3.35c and Figure 3.35d. Both have pixels with an area of 100 µm × 25 µm, but one sensor is not irradiated and the other is irradiated to the maximum fluence that is used within the market survey. Within both projections, a straight vertical line can be seen, that is exactly in the same position where the bias rail and bias dots are located. This effect is expected and therefore, this area is excluded from the analysis. However, the efficiencies between the unirradiated and the irradiated sensor do not differ that much. The irradiated sensor has a global efficiency that is 0.5% lower than that of the unirradiated one and the fiducial efficiencies differ only about 0.3% (the irradiated sensor has the lower efficiency again). This is an indication, that the biasing structure with bias dots does not decrease the efficiency of the whole sensor stronger after the irradiation process, since the same differences of 0.3% can be observed for the sensors biased with temporary metal.
To conclude the discussion of the different combination of biasing techniques and pixel implantations, there is one last comparison left. In Figure 3.35d, the pixel pitch is 100 µm × 25 µm and in Figure 3.35e the pixel pitch is 50 µm × 50 µm, whereas the irradiation fluence and the thickness are exactly the same. The areas in which the loss of efficiency due to the biasing structures is visible are very different between these two arrangements. For the rectangular pixels, a vertical line with a width of roughly 50 µm is present. In contrast to this, four circular shaped areas, each with a diameter of at least 50 µm, are visible for the quadratic pixels. The area, where the efficiency drop is present, is about 12.5% for the rectangular pixels, whereas for the quadratic pixels this value is at least 20%. The fact, that the quadratic pixels show a lower efficiency in general after the irradiation, is supported by the values for these two sensors in Table 3.8. Results with the same tendency for the different pixel pitches are also reported in the literature [84] (although there another biasing technique is used).

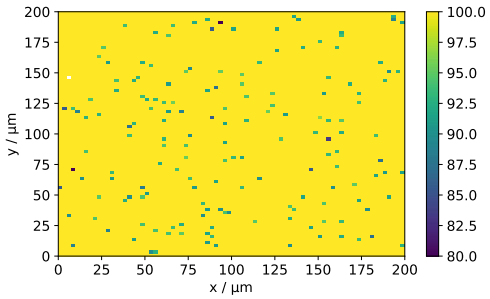

(a) V3S13, 50 µm × 50 µm, TM, unirradiated.

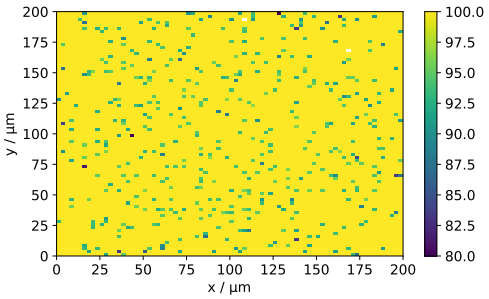

(b) V3S03, 50 µm × 50 µm, TM, irradiated to $5 \cdot 10^{15}\, n_{\mathrm{eq}}/\mathrm{cm}^2$.

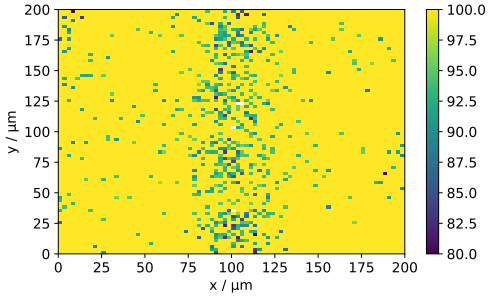

(c) V3S05, 100 µm × 25 µm, PT, unirradiated.

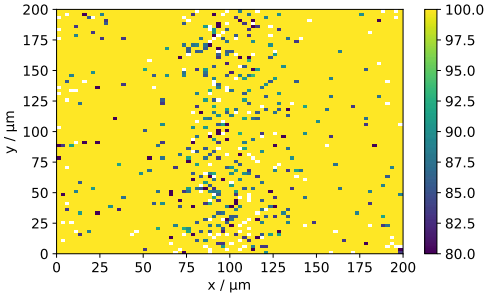

(d) V3S15, 100 µm × 25 µm, PT, irradiated to $5 \cdot 10^{15}\, n_{\mathrm{eq}}/\mathrm{cm}^2$.

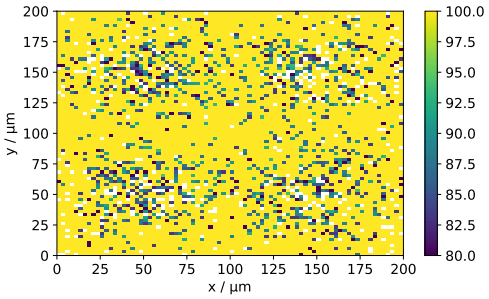

(e) V3S16, 50 µm × 50 µm, PT, irradiated to $5 \cdot 10^{15}\, n_{\mathrm{eq}}/\mathrm{cm}^2$.

Figure 3.35: In-pixel projections for sensors of vendor 3 with different pixel pitches, biasing technologies and irradiation fluences.

4 Low Gain Avalanche Detectors in a Time-of-Flight System

Low-Gain Avalanche Detectors, so-called LGADs, are a special form of avalanche diodes. LGADs have a very good time resolution of only a few tens of ps. With this quality, they are ideal candidates for high-energy physics experiments to help distinguish particle interaction points in space and time [53]. Their fast time response is also advantageous in medical applications. Examples of their more recent medical use can be found in the literature such as [85, 86, 87].
In this chapter, the working principle of LGADs and their structure are introduced. After that, different LGAD types that were studied at TU Dortmund University are described. An investigation of the the electrical properties and time resolution is presented to prove their usability for a Time-Of-Flight (ToF) system. To introduce the ToF system a brief introduction to the usage of ToF systems is presented afterwards. Theoretical calculations and considerations follow which lead to the design of a very first prototype for such a ToF system. This chapter closes with insights into the first test and simulations of the setup.

4.1 Avalanche Diodes and LGADs

Avalanche diodes, especially avalanche photo diodes (APDs), are named after their main working principle, the avalanche effect (see subsubsection 2.1.3 for more details). The needed gain is achieved by a high electric field. This high electric field is generated by an additional highly doped p-type layer [88]. Supported by an external bias voltage, the typical field strength can be up to $E \approx 10\,\mathrm{kV/cm}$ [7]. The typical gain of an APD ranges from ten to several hundreds [3].
Such detectors can be used for single particle detection. Silicon photomultipliers, that are built from arrays of APDs, can have a gain of up to 10^6 [3]. Such detectors are especially good for the detection of photons, because the large multiplied output signal does not depend on the number of initially produced electron-hole pairs and can be generated by even a single photon. Detectors with a lower gain are sufficient for the detection of individual charged particles, because the number of initially generated electron hole pairs is greater for MIPs compared to photons [4]. Low-Gain Avalanche Detectors (LGADs) as a special form of an avalanche diode have been

developed for this purpose [89]. Their structure and features will be described in the following.

Low-Gain Avalanche Detectors (LGADs) are sensors whose design is based on an n-in-p standard diode. A sketch of the typical design is shown in Figure 4.1. A highly doped n^+-layer serves as the signal collection electrode. Directly beneath this layer, a highly doped p-type layer is placed. This additional layer is the so-called multiplication layer or avalanche region. As the dopant for the avalanche region, often times Boron or Gallium are used [90]. A typical doping concentration of the dopant is about $10^{16}\,/\mathrm{cm}^3$ [91]. The active layer of an LGAD is formed together with the known p-type bulk and p^+-layer on the backside of the device. For a better handling, this active structure is often supported by a silicon support layer of a few hundreds of micrometres.
The electric field inside an LGAD differs from that in a standard n-in-p diode. As seen in Figure 4.1, the E-field can be divided into two different regions. The first reaches from the p^+-layer of the backside through the p-type bulk. In this drift region, the E-field increases only slightly (dependent on the used bias voltage). An LGAD with a thickness of 300 µm and an applied bias voltage of 600 V has an E-field with a strength of about 20 kV/cm [90] in the drift region. In the multiplication region, the electric field increases strongly. This region is quite small and covers only the first few micrometres from the n^+-layer inwards. The E-field in the multiplication region can have a strength of more than 300 kV/cm and is caused by the non-uniform doping gradient [92]. In this high electric field, the generated electrons that drift towards the n^+-electrode multiply via impact ionisation.

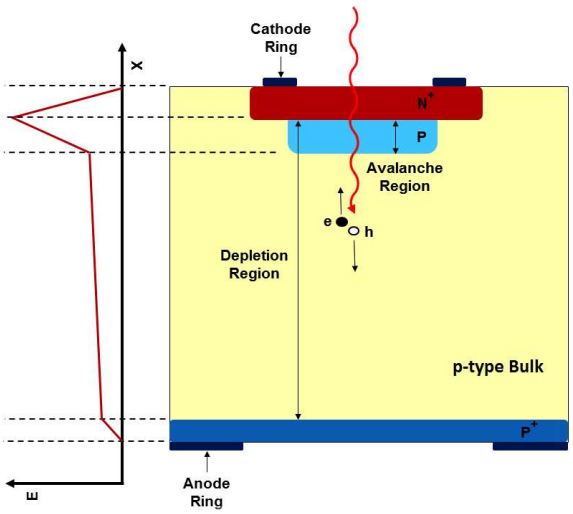

Figure 4.1: Drawing of the composition of an LGAD [93]. In addition, a sketch of the generated electric field is depicted left of the drawing of the sensor.

LGADs are considered as low gain devices, since their internal gain is only between 10 and 100 [92]. This lower gain compared to traditional APDs comes with different benefits. Firstly, the gain increases both, the signal and the sensor noise. However, with the lower gain of LGADs the total signal-to-noise ratio is enhanced, since the sensor noise is not the dominant part of the overall noise in a silicon detector [90]. Secondly, the lower gain results in a much lower power consumption.
The excellent time resolution of a few tens of ps for LGADs is not achieved with only the internal gain [92, 94]. Besides from the higher signal-to-noise ratio compared to standard silicon sensors, a higher slew rate is needed [90]. The slew rate of a signal, which describes how fast a signal increases, decreases with the sensor thickness [95, 96]. Simulations about this are shown in Figure 4.2b. The small thickness of currently available LGADs of only 30 µm to 80 µm [97] affects the rise time of the signal but not the amplitude (see Figure 4.2a). The signal current in LGADs of different thicknesses, but with the same gain, are therefore of the same height.

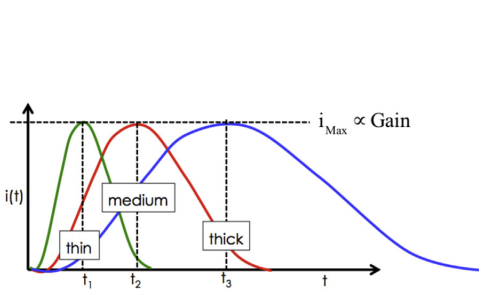

(a) Current signals.

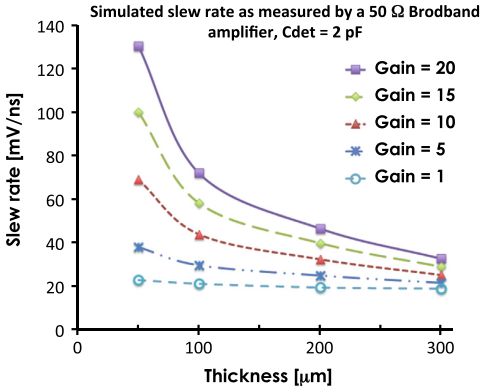

(b) Simulated slew rates.

Figure 4.2: Sketches of **(a)** current signals in sensors with different thicknesses and **(b)** slew rates versus the sensor thickness. Graphics taken from [96].

At TU Dortmund University, there are different LGADs available. All were produced by Hamamatsu Photonics (HPK) and are named HPK-Type1.1, HPK-Type1.2 and HPK-Type2. They are from a wafer with a thickness of 150 µm and their active thickness is only 35 µm [98, 57]. The pad size of these sensors is 1.3 mm × 1.3 mm. Guard rings surround the $n++$ electrode [53]. The three types differ in their bulk substrate and the gain layer.
The types HPK1.1 and 2 have a similar bulk substrate with the same resistivity. For the type HPK1.2 the bulk resistivity is higher. The gain layer implantation is the same for the types HPK1.1 and HPK1.2. Both have a deep gain implant. This means, that the gain implant is not in direct contact with the n^+-layer, but a few micrometres beneath it. The HPK2 has in contrast to those two types a broad gain

layer. In this case, the gain implant is placed directly beneath the n^+-layer. More details about the gain layer placement inside the LGAD and its effects can be found in the literature [97]. The naming scheme for the gain implants is also taken from this reference.
The various LGADs available at the TU Dortmund University come from different institutes. In order to distinguish the LGADs according to their origin in the following sections, an asterisk at the end of the name indicates that the LGADs originate from the University of Göttingen. If the name is without any modification, the corresponding LGADs were received from CERN.

4.2 Electrical Properties

The electrical properties of LGADs are of great importance for their use. For this reason, the current-voltage characteristics of the LGADs are investigated in order to extract the breakdown voltages. Moreover, the capacitance-voltage characteristics are examined to determine the depletion behaviour of the devices. The depletion voltage and breakdown voltage are important, because these two voltages define the operating range.
The data presented in this section was taken by S. Pape and described in his master thesis [57]. As this is not publicly available, a broad overview of his results is provided in the following paragraphs. This is done to contextualise further measurements taken as part of this thesis.

The IV-characteristics are measured with the same electrical circuit that is also used for the market survey. A picture of this was already presented in Figure 3.17. The data is taken at room temperature and a controlled relative humidity between 35% and 45%. The LGADs are reverse biased and the bias voltage is increased in 5 V steps. At each bias voltage, the leakage current is measured ten times. The averaged currents are presented in Figure 4.3. To ensure a proper handling of the devices, a compliance limit of 1 µA is set. If the leakage current exceeds this threshold, the measurement is stopped and the bias voltage is ramped down slowly.

The breakdown voltage V_{bd} of the measured devices is defined as the bias voltage step right before the current limit is reached. The systematic uncertainty of this value is $\pm 5\,\mathrm{V}$, because this is the step size and no finer value for the breakdown voltage is taken. All of the LGAD types available at the TU Dortmund University have a leakage current behaviour expected from a standard diode. This is consistent with the literature. The small differences between the different types are discussed in the following.
For both sensors of the LGAD type HPK-Type1.1, the breakdown voltage is found

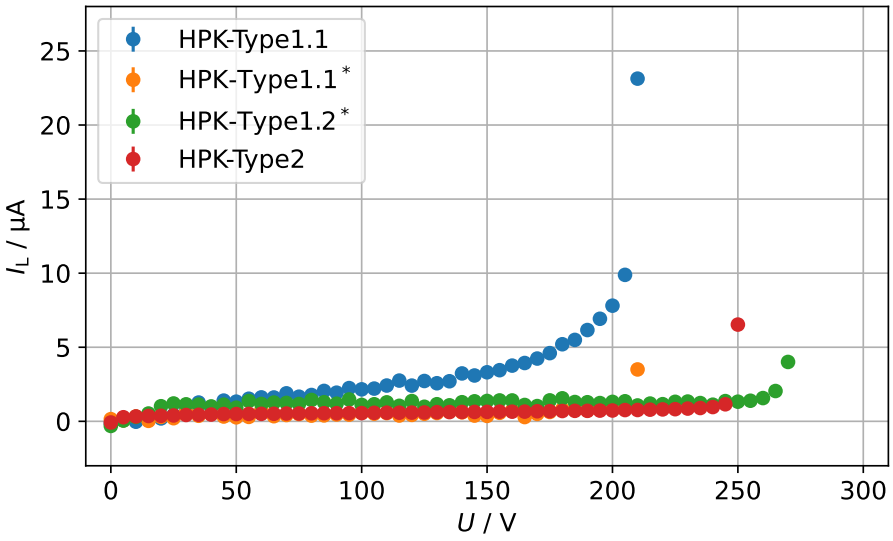

Figure 4.3: The current-voltage characteristics of different reverse biased LGAD types measured at room temperature. The data was taken by S. Pape and was first described in his master thesis [57]. The asterisk in the type names indicate that the LGADs are originally from the University of Göttingen. The other LGADs are received from CERN.

to be $V_{\mathrm{bd}} = (210 \pm 5)\,\mathrm{V}$. The difference between the two IV-characteristics is the overall magnitude of the leakage current for all set bias voltages and a linear rise before the breakdown for the sensor HPK-Type1.1. This is tracked down to scratches on the sensor surface, which result in an increased amount of surface currents.
The LGAD HPK-Type1.2 has exactly the same doping implantation as the HPK-Type1.1. However, their bulk substrates are different. The much higher breakdown voltage of $V_{\mathrm{bd}} = (270 \pm 5)\,\mathrm{V}$ is an evidence for the higher bulk resistivity of the sensor HPK-Type1.2*. This is in accordance with their earlier mentioned design description [98].
The last sensor HPK-Type2 has a breakdown voltage of $V_{\mathrm{bd}} = (250 \pm 5)\,\mathrm{V}$. Since this design has the same bulk substrate than the HPK-Type1.1, there has to be another design feature, that affects the breakdown voltage. In the course of the thesis of S. Pape [57] it was found that the HPK-Type2 has a lower doping gradient. This results in a lower internal electric field and therefore in a higher breakdown voltage.
Overall, small differences between the different LGAD types can be observed in their IV-characteristics. Every behaviour, from the height of the measured leakage current to the breakdown behaviour can be explained by sensor features like the bulk substrates, doping gradients or scratches from former handling. In addition, the results are in accordance with the results presented in the literature [98].

The CV-characteristics are measured with the same electrical circuit, that is also used for the market survey, to gain more information about the depletion behaviour of the used LGAD types. A picture of the circuitry was already presented in Figure 3.13a. The data is taken at room temperature and a controlled relative humidity between 35% and 45% inside a climate chamber. The LGADs are reverse biased and the bias voltage is increased in 2.5 V steps. At each set bias voltage, the capacitance is measured five times. The bias voltage is increased for these measurements up to the corresponding breakdown voltage of each LGAD type. The averaged capacitances are presented in Figure 4.4.

The plot in Figure 4.4 shows the measured capacitances as $1/C^2$. For all measurements, a typical LGAD curve with two kinks is observed. For the LGAD types HPK-Type1.1 and HPK-Type1.2, the first kink is around 30 V, for the LGAD type HPK-Type2 the kink is around 40 V. These voltages correspond to the depletion voltages of the avalanche region.
For the depletion of the no-gain region, i.e. the bulk substrate, a depletion voltage of 40 V is extracted for the HPK-Type1.2. For the other two types, the capacitance does not settle at a constant value, so the standard analysis does not work for these measurements. However, a depletion voltage of roughly 150 V can be defined for the LGAD HPK-Type2 from the plot. For the LGADs of type HPK-Type1.1, the depletion voltage is approximately around 200 V. The depletion voltages of

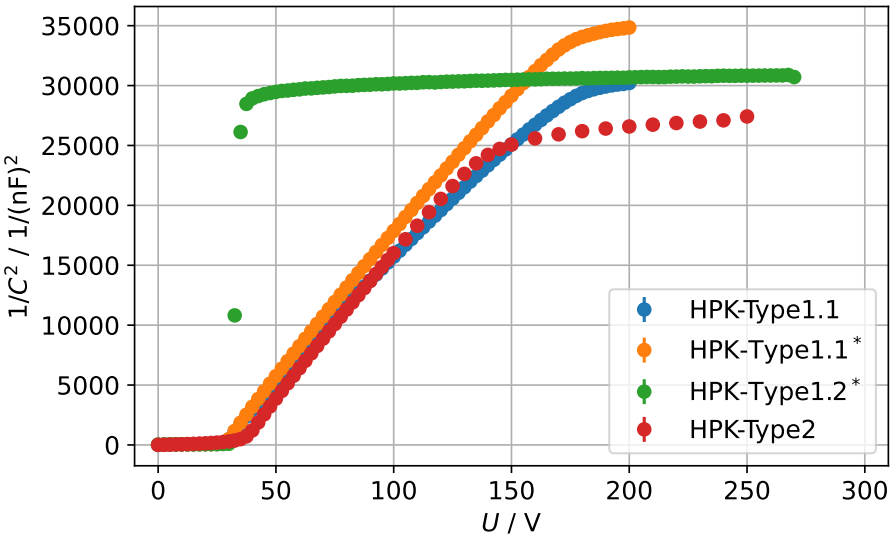

Figure 4.4: The capacitance-voltage characteristics of different reverse biased LGAD types. The data is depicted as $1/C^2$. The original data was taken by S. Pape and was first described in his master thesis [57]. The asterisk marks sensors received from the University of Göttingen, the LGAD types without the asterisk are from CERN.

the no-gain layer are also the voltages of full depletion. The extracted voltages correspond well with those found in the literature [98].

4.3 Time Resolution

The flight time of a particle that traverses a ToF system is the determining parameter for calculating its energy. Therefore, the precise measurement of the time t_0 when a signal induced by a traversing particle reaches a given threshold is of great importance. Due to various effects, this initially measured time t_0 can be shifted, thus affecting the time resolution of the device. The contributions of the effects can be summed quadratically to the total time resolution [90]:

$$\sigma_t^2 = \sigma_{\text{Time Walk}}^2 + \sigma_{\text{Landau Noise}}^2 + \sigma_{\text{Distortion}}^2 + \sigma_{\text{Jitter}}^2 + \sigma_{\text{TDC}}^2. \tag{4.1}$$

The individual contributions are discussed in the following.

Time Walk describes the contribution caused by the effect that larger signals have a higher slew rate than lower signals. With higher slew rates, a given constant threshold is reached earlier and thus the defined time t_0 is moved to smaller times. The effect is based on the different heights of the current amplitude. This is due to the non-uniform energy deposition of charged particles in matter. The total number of created electron-hole pairs and their local density are subject to the Landau distribution and thus differ from event to event. The contribution of the *Time Walk* effect can be defined mathematically as

$$\sigma_{\text{Time Walk}} \propto \left[\frac{N}{\mathrm{d}V/\mathrm{d}t}\right]_{RMS}, \tag{4.2}$$

where N indicates the noise and $\mathrm{d}V/\mathrm{d}t$ the slew rate. Therefore, this effect is reducible with high slew rates and small noise contributions. In addition, it can be counteracted by using a proper analysis technique known as constant fraction discriminator technique, which will be explained in subsection 4.3.1.

The variation of the energy deposition affects not only the *Time Walk* contribution, but also the *Landau Noise*. The contribution of the *Landau Noise* is caused by the same physical effect. However, the variations cause additionally irregularities in the shape of the generated current signal [91]. While the *Time Walk* contribution can be reduced, the contribution due to *Landau Noise* is irreducible.

The *Distortion* contribution is caused by a non-uniform weighting field across the electrode of the device and different drift velocities of charge carriers throughout the volume of the device. Derived from Ramo-Shockley's theorem [99, 100], both

effects influence the induced current in the electrodes. As a result, the shape of the current signal depends on the hit position of the traversing particle. To reduce this contribution to the total time resolution, saturated drift velocities across the sensor are required. This is achieved with a high electric field across the device. In addition, the weighting field can be adjusted by a proper design of the device. This means, that the implant size needs to have a similar size as the pitch of the device to create a homogeneous weighting field underneath the electrode. Furthermore, to mimic a parallel plate capacitor, the electrode needs to be much larger than the thickness of the device.

The *Jitter* describes the uncertainty on the measured time when a particle traverses the device due to noise in the electronics or the signal itself. Thus, the time when the threshold is reached varies depending on the noise. The *Jitter* contribution is proportional to the system noise and inversely proportional to the slew rate, so it can be written as

$$\sigma_{\text{Jitter}} = \frac{N}{\mathrm{d}V/\mathrm{d}t}. \tag{4.3}$$

It can be reduced on the one hand by the usage of low noise readout electronics and on the other hand by a small noise and a high slew rate. However, low noise contributions can only be realised with the disadvantage of small slew rates. In contrast, large slew rates increase the effect of noise contributions due to their need for high bandwidth electronics.

TDC is an abbreviation for Time-to-Digital Converter and indicates the time uncertainty due to conversion of the analogue signal into a digital signal. As TDCs have a limited number of bins to encode time, a contribution of

$$\sigma_{\text{TDC}} = \frac{\Delta T}{\sqrt{12}}, \tag{4.4}$$

with ΔT as the bin width, is added to the total time uncertainty.

To sum everything up, the best techniques to design an optimal detector for timing measurements, a high slew rate, small noise contributions, a high electric field across the device, broad implants and a small thickness are required. The requirements to have a high slew rate are in contrast to those that are needed for small noise contributions. The chosen thickness of the device can increase or decrease certain contributions of the total time resolution as follows: On the one hand, a smaller thickness benefits higher slew rates and less *Landau Noise*, but increases on the other hand the irregularities in the weighting field and thus strengthen the *Distortion* contribution. Therefore, a trade-off between the different requirements needs to be chosen carefully to reduce the total time resolution σ_t.

4.3.1 Measurement Technique

To measure the total time resolution of an LGAD sensor, setup is used where two LGADs are placed beneath a strontium source so that the particles traverse both sensors. The strontium isotope ^{90}Sr serves as the source for β-particles due to its radioactive decay [101]. Its decay chain is:

$$^{90}_{38}\mathrm{Sr} \rightarrow {}^{90}_{39}\mathrm{Y} + \beta^-(546\,\mathrm{keV}) + \bar{\nu}_\mathrm{e} \rightarrow {}^{90}_{40}\mathrm{Zr} + \beta^-(2.288\,\mathrm{MeV}) + \bar{\nu}_\mathrm{e}.$$

The given energies are the maximum kinetic energies of the β-particles. Since the decay energy is statistically distributed on all participating components, the β-particles are not monoenergetic. The most probable value of the energy of the β-particle is somewhere between a third and half of the maximum stated energy. A schematic of the used setup is shown in Figure 4.5a.

The signals of the LGADs are collected with a single channel readout board. This readout board has internal amplification and requires a supply voltage of 2.25 V [102, 103]. To ensure that the signals of both LGADs are handled exactly the same way, two boards of the same version (version V1.4) are used at TU Dortmund University. The LGADs are glued to the board with silver epoxy for good electrical contact [103]. The boards have SMA connectors for applying the bias voltage to the LGADs and to lead out the signals to an oscilloscope (here a Tektronik MSO5204B is used). The Tektronik MSO5204B has a maximum bandwidth of 1 GHz and a sampling rate of 10 GS/s. To avoid timing differences between the used channels, the cables for connecting the output of the readout board to the oscilloscope are of equal length for both readout boards. A computer is connected via LAN with the oscilloscope to control the measurement settings and store the waveforms of the incoming signals from the readout boards.

To build the setup, the readout boards with the attached LGADs are mounted back to back in a 3D printed support. A photograph of this is presented in Figure 4.5b. For the distance of the two sensors, a trade-off between the stability of the support structure and the need to bring them as close as possible is necessary. In such a way, the distance between the two LGADs is realised to be around 1 cm in the used setup at TU Dortmund University.
The bias voltage of the used LGADs is variable. According to the former presented results, it is usually around 200 V, which is below the breakdown voltage for all different available sensor types. In further investigations, the bias voltage is increased close to the stated breakdown voltages. Since the bias voltage might be close to the breakdown voltage, the leakage currents of the used LGADs have to be monitored during the measurement to avoid damages caused by too high currents.
The frequency of signals with an amplitude higher than 10 mV varies between

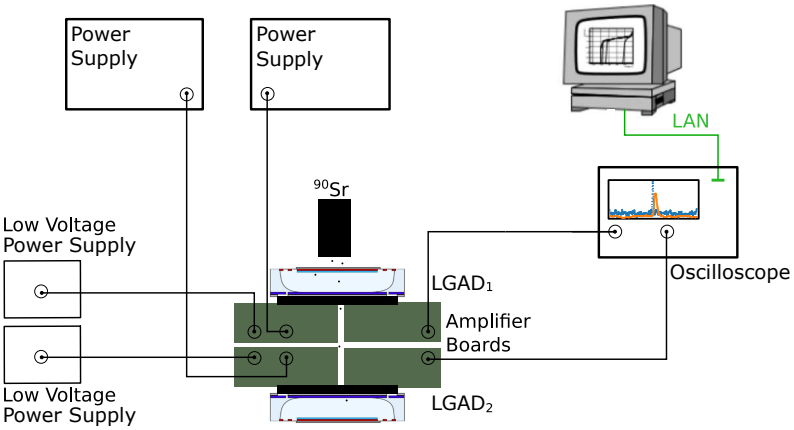

(a) Schematic of the used ^{90}Sr setup with two LGADs ([57] adapted).

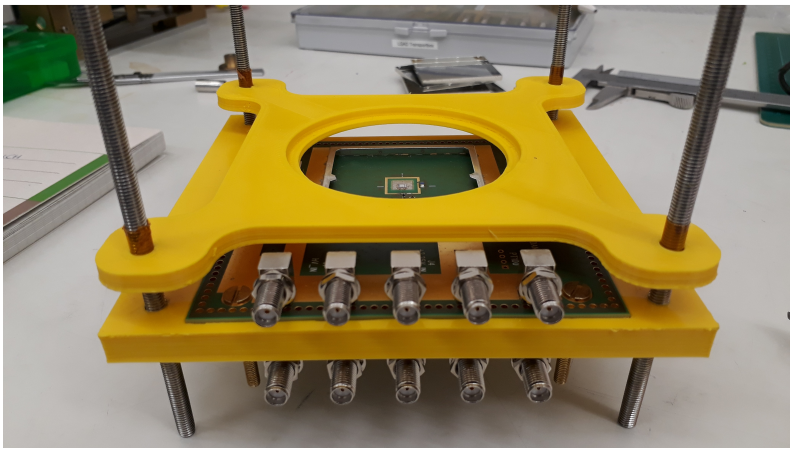

(b) Photograph of the 3D printed support for the ^{90}Sr source (upper frame) and the two LGAD readout boards (lower frame).

Figure 4.5: Details about the measurement setup, where **(a)** shows a schematic of the used circuitry and **(b)** shows a photograph of the support structure with the attached readout boards.

100 mHz and 1 Hz for a single LGAD in this setup. Since not all β-particles from the source reach the second sensor, which is installed farther away from the source, long measurement times are necessary to obtain larger statistics. The analysis is only meaningful when both LGADs have coincident signals, therefore only coincident signals are recorded. To obtain a thousand coincident signals, roughly one day is needed. The analysis is usually carried out with data sets consisting of between a thousand and ten thousand coincident signals, so a measurement can take up to more than a week.

To obtain the time resolution of a sensor, the exact times, when a particle traverses the two sensors, has to be known. For this purpose, the Constant Fraction Discriminator (CFD) technique is used in this thesis, since it minimises the effect of the time walk contribution. An example of coincident signals is depicted in Figure 4.6 to explain the CFD technique in more detail.
In the given example, a CFD value of 50% is used. In this case, the times t_{signal} and t_{trigger} indicate when the recorded signals reach the given fraction of the maximum amplitude of the signals. Within the schematic, the voltage peak of the first LGAD is nearly 5.6 mV high. With a CFD value of 50%, the threshold is about 2.8 mV for the signal. This is marked with a dashed line in the plot. Although the plot gives the impression of nearly continuous data, the oscilloscope has only limited time resolution. Therefore, the exact time when the threshold is reached by the signals is often not recorded. To extract the time precisely, a linear interpolation is done. For this purpose, the two recorded data points closest to the calculated threshold value are used. S. Pape has found, that doing so, the time resolution enhances by nearly 15 ps compared to a procedure without the linear interpolation [57].
To obtain the time resolution of the LGADs, the time difference $\Delta t = t_{\text{trigger}} - t_{\text{signal}}$ of all coincident signals in a data set is the relevant quantity. This time difference is gaussian distributed with its standard deviation giving the time resolution of the system. In theory, the mean value gives the time-of-flight t_{ToF} between the two planes for the particle traversing the planes. However, this quantity might be interfered by end-to-end delays in the circuit and cables.

4.3.2 Results of the Measurements

As stated before, the relevant quantity from the measurements is the Gaussian distributed time difference Δt. To extract the standard deviation of the distribution of Δt, the recorded time differences are plotted in a histogram and a Gaussian fit is performed afterwards. For the number of bins that are used for displaying the data, there are different possibilities available. Since there is no general rule for choosing the bin size, a rough rule of thumb suggests $\sqrt{n}$ as the number of bins, where n

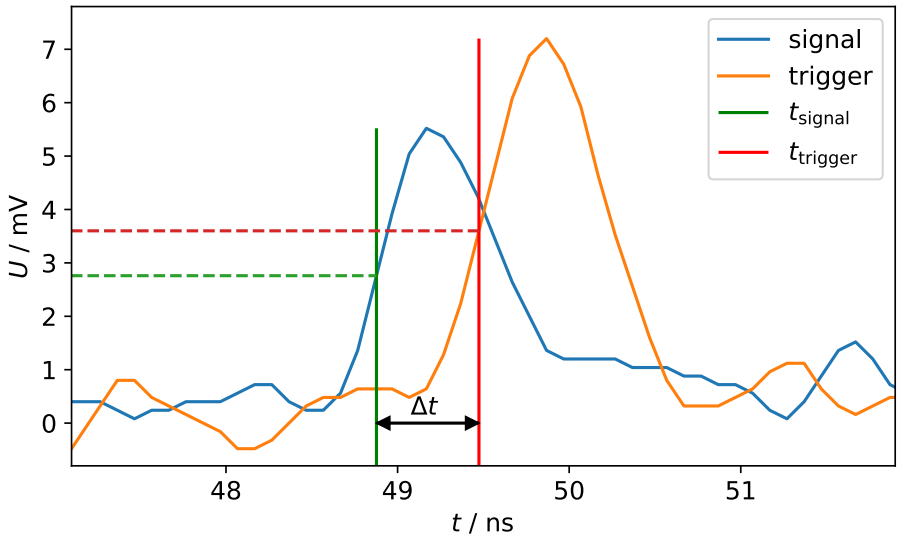

Figure 4.6: Typical waveforms of coincident signals. The voltages are the result of the measured induced currents in the two sensors, measured over an internal resistance. The LGAD closest to the ^{90}Sr source gives the signal, the second LGAD serves as the trigger. In addition to the amplitudes, the extracted times for a CFD value of 50% are displayed. The data is taken with two HPK-Type1.1 LGADs biased with 160 V.

is the number of entries. For a data set of 10000 entries, this results in 100 bins distributed from the lowest to the highest entry. However, a study to determine the optimal number of bins for the used analysis is performed instead of applying the rule of thumb. To do so, the data is plotted in histograms with different number of bins between the maximum values. Exemplary plots are shown in Figure 4.7a to Figure 4.7d. Afterwards, a Gaussian distribution with a constant offset on the y-axis for the background is fitted to the data. The results of the fit, especially the mean and standard deviation, are checked afterwards. Those results are displayed in Figure 4.7e.
The time differences are plotted in a range from −3000 ps to 3000 ps to include all measured data. This gives a total range of 6000 ps which have to be covered in the histograms with bins. The smallest number of bins used for the study is 30, the largest is 6000. If only very few bins are used to merge the data, the Gaussian distribution is not identifiable. This is true for bin numbers below 100 for the total range. With this few bins, the data can not be described properly. For more than 300 bins, the Gaussian distribution becomes clearly visible in the plots. As it can be seen in Figure 4.7e, the mean value and standard deviation of the Gaussian fit converge towards specific values for all tested bin numbers greater than 300. Since the fit parameters converge, there is no advantage in using a very high number of bins for the histogram. There is no precision gain in using more bins than 600 and, in addition, the fitting procedure takes longer for a finer binning. As a result, a bin width of 10 ps, which corresponds to a total bin number of 300 in the shown example, is used for all further histograms in this thesis.

The data taking for the setup starts, if the amplitude of the trigger is higher than 2 mV. The amplitude of the signal is also checked and the waveforms of the trigger and signal are only stored, if the signal is as well higher than 2 mV. The waveforms feature a constant background, made up of electronic noise and the chosen offset for the oscilloscope channel. This needs to be taken into account for the analysis. To determine the background level, the first and last 100 data points of each waveform are used, because no signal is expected there. They are plotted in a histogram and a Gaussian distribution is fitted to them. The resulting mean value of the Gaussian distribution gives the background level. This background level is then subtracted from the recorded waveforms for the further analysis.
The corrected waveforms are then used to extract the time of arrival. This is done for different CFD values to investigate its effect. For this purpose, the CFD value is varied from 5% up to 95% in 5% steps. The calculated time of arrival of the signal is subtracted from the calculated time of arrival of the trigger. Afterwards, the time difference Δt is plotted in a histogram. The middle of each bin and the corresponding number of bin entries are used as a pair of data points for a fit of a Gaussian distribution with an additional linear function for the background to the

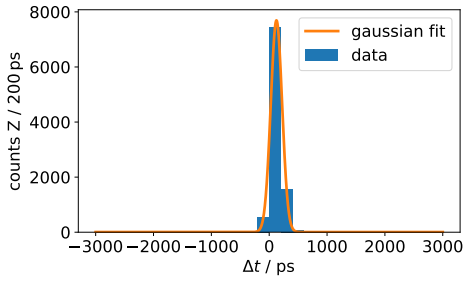

(a) 30 bins.

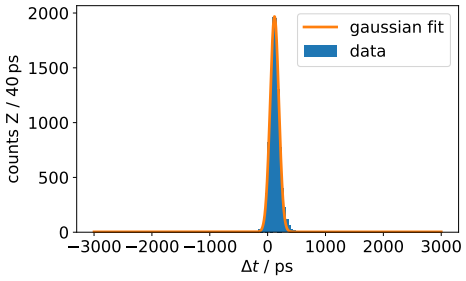

(b) 150 bins.

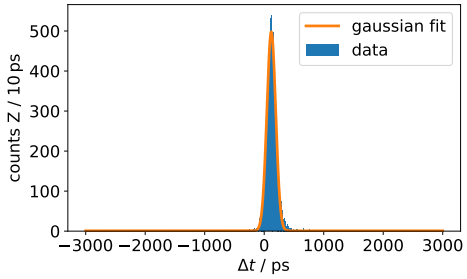

(c) 600 bins.

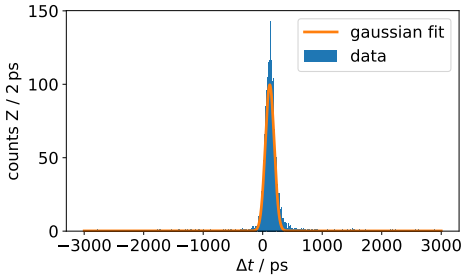

(d) 3000 bins.

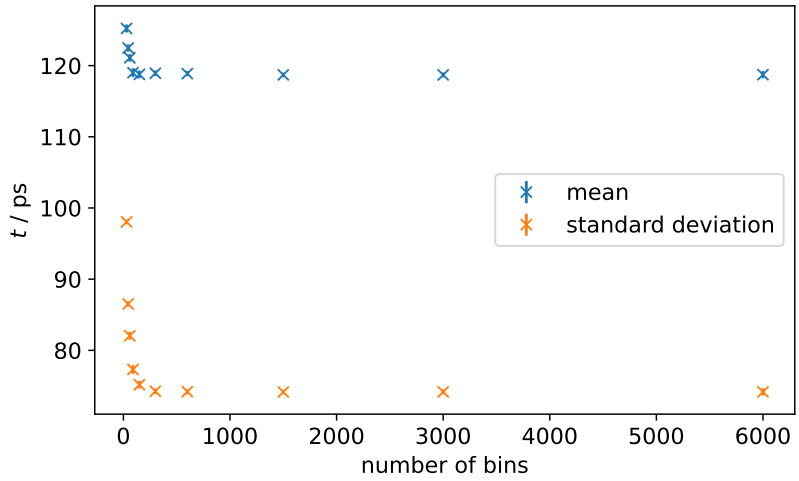

(e) Mean and standard deviation of the Gaussian fit to the distribution of Δt in dependence on the number of bins used for the histogram.

Figure 4.7: Histograms of the distribution of the time difference Δt with different bin widths are displayed in **(a)** to **(d)**. An overview of the results of the Gaussian fits for different number of bins is shown in **(e)**.

data. The fit is done in a range between −200 ps and 500 ps, because the majority of the calculated time differences Δt are in this range. The uncertainties that are calculated by the fit procedure for the mean value and the standard deviation are only the analytical uncertainties of the fit.

If two LGADs of the same type are installed in the setup, the standard deviation of the whole system $\sigma^2_{\Delta t}$ is used to calculate the time resolution of the used LGAD type. The standard formula for the timing uncertainties for the whole system is given by

$$\sigma^2_{\mathrm{LGAD1}} + \sigma^2_{\mathrm{LGAD2}} = \sigma^2_{\Delta t} - \sigma^2_{\mathrm{readout}}. \tag{4.5}$$

If the contribution of the readout chain $\sigma^2_{\mathrm{readout}}$ is negligible and the terms σ_{LGAD1} and σ_{LGAD2} are exactly the same, written as σ_{LGAD} in the following, Equation 4.5 simplifies. With these assumptions, the time resolution of a single LGAD is calculated as $\sigma_{\mathrm{LGAD}} = \sigma_{\Delta t}/\sqrt{2}$. If the time resolution of an LGAD whose time resolution is not known in advance is to be measured, a setup with one LGAD of known time resolution and the unknown LGAD can be used. In this case, Equation 4.5 can be used to calculate the time resolution of the unknown LGAD in the setup. This is done by calculating the difference between the standard deviation of the whole system $\sigma^2_{\Delta t}$ and the time resolution of the known LGAD, while the contribution of the readout chain is neglected.

The results of the presented analysis for the time resolution are displayed in Figure 4.8. The graph depicts the time resolution of all available LGAD types for different used CFD values. To begin the analysis, measurements with two LGADs of the same type are carried out. After that, one well known LGAD type is used in the setup together with an unknown LGAD. The calculation of the time resolution of the unknown LGAD is based on Equation 4.5 with a negligible part for the readout chain. The error of the calculated time resolution is given by the Gaussian error propagation:

$$\Delta\sigma_{\mathrm{LGAD1}} = \sqrt{\frac{\sigma^2_{\Delta t} \cdot (\Delta\sigma_{\Delta t})^2 - \sigma^2_{\mathrm{LGAD2}} \cdot (\Delta\sigma_{\mathrm{LGAD2}})^2}{\sigma^2_{\Delta t} - \sigma^2_{\mathrm{LGAD2}}}}. \tag{4.6}$$

In this formula, the time resolutions and their uncertainties for the whole system, $\sigma_{\Delta t}$ and $\Delta\sigma_{\Delta t}$, and for the second LGAD, σ_{LGAD2} and $\Delta\sigma_{\mathrm{LGAD2}}$, are known. For the depicted data points in Figure 4.8, an LGAD of the type HPK1.2 with a bias voltage of 200 V is used as the reference LGAD for the measurements of the types HPK2 (at 200 V) and HPK1.1 (at 200 V).
The measurements in Figure 4.8 reveal the time resolution for all available LGAD types at TU Dortmund University. For a better comparison with each other, the data is presented for a bias voltage of 200 V for all LGAD types. At this bias

voltage, the types HPK1.1 and HPK2 show a very similar time resolution. The smallest time resolution for the type HPK1.2 is around 50 ps. In the literature, a time resolution of 30 ps at this bias voltage is found [98]. Since the results differ that much from each other and another LGAD of the type HPK1.2 is available, the time resolution of the type HPK1.2 is remeasured with a second setup. Nevertheless, the best time resolution is found to be around 50 ps again. The comparison of the two data sets are presented in the appendix in Figure C.1 for completeness. For the other two types, the best time resolution is found to be around 40 ps. For HPK2, this is exactly the value that was measured by Yang et al. [98]. However, the time resolution for HPK1.1 differs from that in the literature, where a time resolution of only 60 ps is stated [98]. The differences of the measured time resolutions can be caused by several effects. Firstly, the used CFD value is not known for the analysis of Yang et al. Secondly, the temperature and the electrical circuit affect the time resolution. Details about these are not known for the data in the literature. For these reasons, it is not possible to resolve why the measurement results in this thesis differ that much from those in the literature.

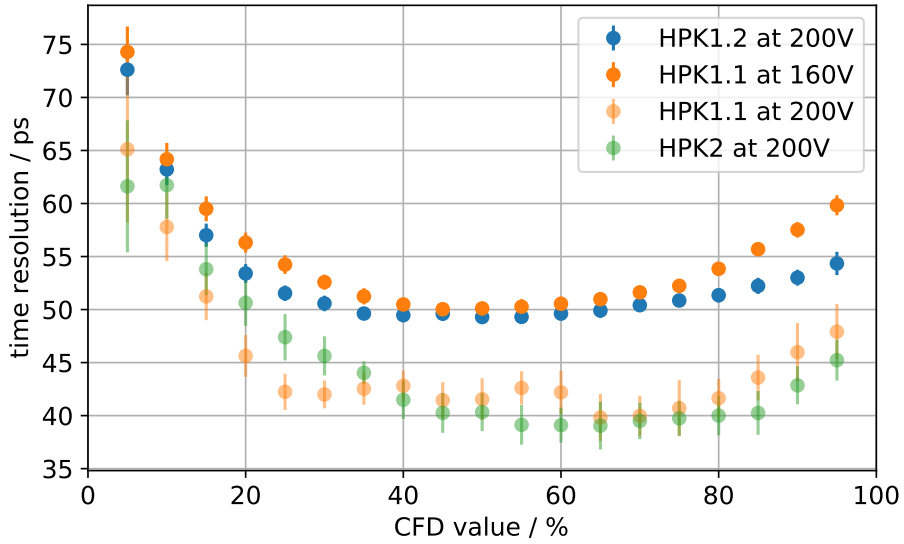

Figure 4.8: Time resolution of the different LGAD types. The bold data points mark measurements where two identical LGAD types are used and the faded data points indicate measurements where two different LGAD types are used in the setup.

As it can be seen in Figure 4.8, all curves follow the same trend. A high time resolution is observed for very low CFD values, followed by a plateau region for

CFD values between 40% to 70% where no real difference can be seen. For the highest studied CFD values, the time resolution becomes larger again. However, the largest time resolutions across the whole CFD value range are calculated for the lower CFD values. This trend is explained by the different contributions to the total time resolution from Equation 4.1 [104, 90]. The time walk effect is not corrected for when using higher CFD values. Therefore, the time resolutions worsen in this case. On the other end of the scale, the jitter becomes the most dominant part of the total time resolution, which is not counteracted with the CFD method. The best trade-off between these two extremes are the middle CFD values in the plateau region. Moreover, with CFD values between 40% to 70%, the analysis gives stable results for the time resolution.

In Figure 4.8 it can be seen, for the LGAD type HPK1.1, that the bias voltage affects the time resolution. To investigate this further, different bias voltages are applied to HPK1.1 and HPK1.2. The results of the measurements of the time resolution dependency on the bias voltage are depicted in Figure 4.9.

The results for the LGAD HPK1.1 are shown in Figure 4.9a. The breakdown voltage for this LGAD type is around 210 V. At this bias voltage, the leakage current increases exponentially and no data taking with a stable sensor condition is possible. For this reason, the maximum applied bias voltage in this study is 200 V.
The calculated time resolutions for bias voltages of 160 V and 170 V do not differ very much from each other. The best time resolution in these cases is around 55 ps. For the bias voltages of 180 V to 200 V, the calculated time resolutions follow the same trend for nearly every studied CFD value. The trend is that the time resolution improves with an increasing bias voltage. This can be observed best at CFD values above 60%. The best time resolution at a bias voltage of 200 V is around 40 ps. Compared to the time resolution at the lowest studied bias voltage of 160 V, that is an improvement of approximately 27%.
It is worth noting, that the time resolution for a bias voltage of 160 V differs in Figure 4.9a from that presented before in Figure 4.8. In Figure 4.8, the best time resolution for the sensor HPK1.1 with a bias voltage of 160 V is calculated to (50.5 ± 0.6) ps at a CFD value of 40%. In Figure 4.9a, the time resolution at a CFD value of 40% is calculated to (54.4 ± 2.4) ps. These differences arise from the fact, that two different data sets are used. The data depicted in Figure 4.8 derives from a measurement with a setup consisting of two LGADs of the type HPK1.1. However, the data in Figure 4.9a is calculated from a measurement where one HPK1.1 and one HPK1.2 biased with an external voltage of 200 V are installed in the setup. Therefore, the measurement depicted in Figure 4.8 is more reliable, since no uncertainty of an additional LGAD design affects the calculation.

The bias voltage dependent time resolution for HPK1.2 is shown in Figure 4.9b.

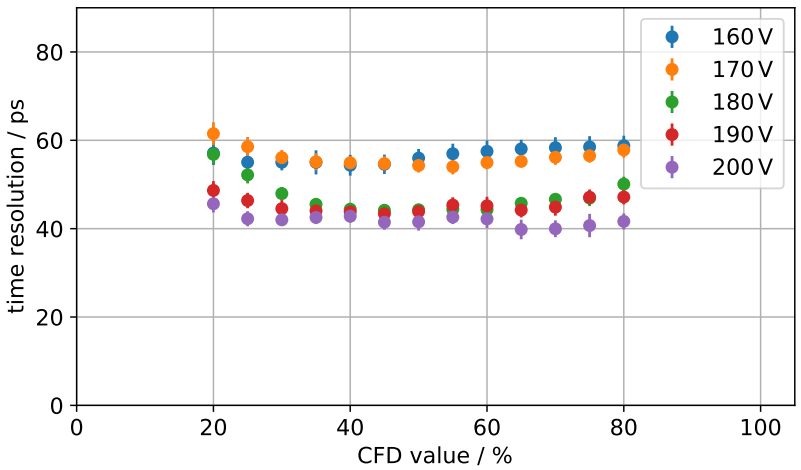

(a) Time resolution of HPK1.1.

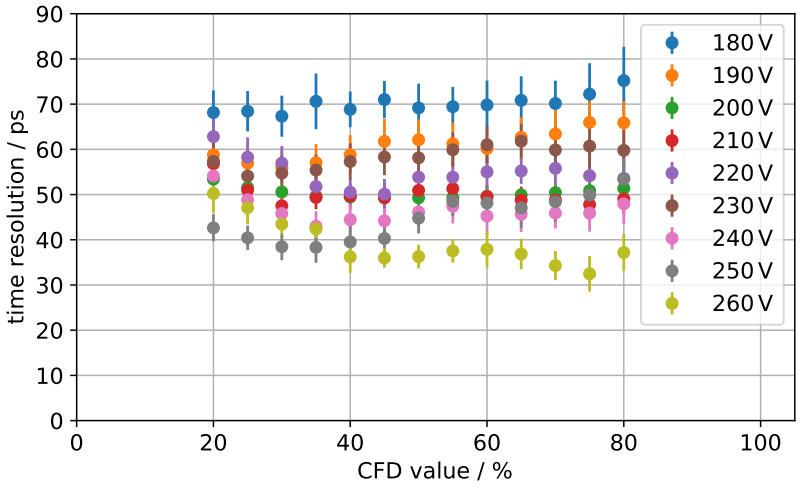

(b) Time resolution of HPK1.2.

Figure 4.9: Time resolution of the LGAD types **(a)** HPK1.1 and **(b)** HPK1.2 measured at different bias voltages. The second LGAD in the setup is always an HPK1.2 biased with 200 V.

The bias voltage for this LGAD type is varied between 180 V and 260 V. A bias voltage of 270 V was also tested, but the sensor produced too much noise to ensure a stable data taking. In addition, the leakage current increased drastically, so a stable sensor condition was not guaranteed for a longer measurement time.
The largest time resolutions are mainly measured for bias voltages below 200 V. The overall largest time resolution with a reasonable CFD value (40% to 60%) is around 70 ps at a bias voltage of 180 V. The fundamental trend across all applied bias voltages is not as clear as for the HPK1.1. One explanation for this might be different temperatures in the setup for the different measurement sequences. However, the best time resolutions are measured for the higher bias voltages. To allow a better comparison, the CFD values of 40% to 60% are examined in more detail. For those values, the best time resolution is measured with an applied bias voltage of 260 V. At this bias voltage, the time resolution is around 36 ps. This is an improvement of nearly 50% compared to the measured time resolution at a bias voltage of 180 V.

For both investigated LGAD types, the voltage dependence of the time resolution is the same: the time resolution improves drastically with an increasing bias voltage. This is explained by the fact, that a higher bias voltage corresponds to a higher internal gain [105]. For previous studied HPK sensors, for example, an exponential correlation between the gain and the bias voltage was reported for bias voltages below the breakdown voltage [106]. If the gain increases, the jitter contribution to the total time resolution decreases [90]. As the Landau noise does not depend on the gain, this component stays constant with varying bias voltage. Therefore, the time resolution converges towards this value with increasing bias voltage [90]. Since the Landau noise can not be counteracted, this limits the total time resolution.
From earlier measurements of Hamamatsu LGADs which were thicker than the tested HPK sensors in this thesis, the same trend for the time resolution is reported [105]. The time resolution measured in a testbeam setup with pions improves with an increasing bias voltage. In addition, they show a fluctuating pattern in the correlation between the time resolution and the bias voltage (as it can be seen in Figure 4.9b). These fluctuations can be larger for irradiated HPK LGADs [107].

4.4 Time-of-Flight System

The Time-of-Flight (ToF) between two detectors in a given distance L is directly proportional to the velocity of a traversing particle with mass m. A sketch of a ToF system is presented in Figure 4.10. The traversing particle induces a signal in the first detector, which is used to start an external clock. When the particle traverses

the second detector, its signal stops the clock. The resulting time difference Δt is the specific time-of-flight t_{ToF} for the particle.

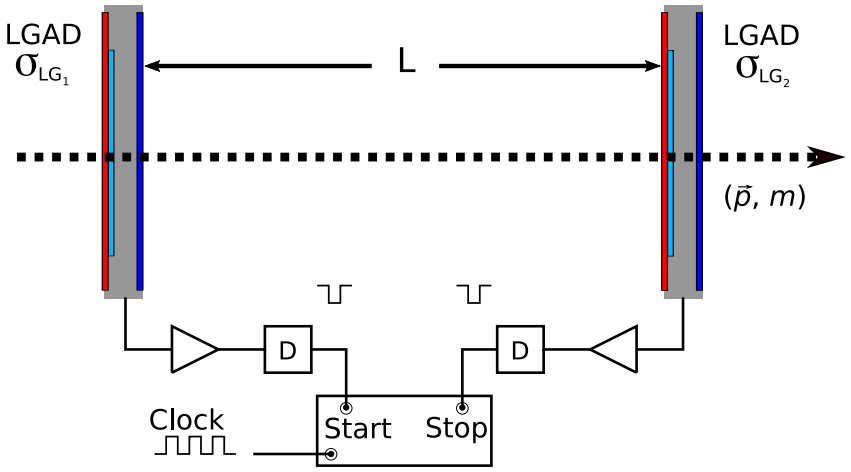

Figure 4.10: Principle of a ToF system with two LGADs with time resolutions σ_{LG_1} and σ_{LG_2} [57].

ToF systems have long been used in physics experiments [108]. The knowledge of the momentum of the particle, obtained from other detector systems in larger experiments, combined with the measured time-of-flight and the known length of the ToF system, allows to determine the mass of the traversing particle. This quantity is of great importance for the identification of produced particles, especially hadrons, in collider experiments. Particles with the same momentum but different masses require different flight times for the distance L of a ToF system [3, 109]. With this time difference, particles such as pions and kaons can be distinguished from each other.
Since the measured time-of-flight is proportional to the velocity of the particle, ToF systems are good candidates for the measurement of the energy of a traversing particle. This is important not only in high-energy physics experiments, but also in medical applications such as the particle therapy.

The treatment of cancer with protons was proposed in the middle of the last century [110]. With the precise energy loss of protons (see Figure 2.6 and the corresponding paragraph in subsection 2.2.1 for details), an irradiation of only the tumour tissue is possible. To do this, the size of the beam, i.e. its width and depth, can be modulated. In particular, range modulation, which produces spread-out Bragg peaks, is advantageous in sparing healthy tissue in front of and beyond the tumour [111]. In order to plan the treatment according to the patient's needs, information about the position of the tumour tissue is required. This is usually provided by

a conventional X-ray Computed Tomography (CT) scan. The relative stopping power of protons is then derived from this scan. However, this comes with errors of the order of 3% due to the conversion process from X-ray attenuation to proton stopping power [112, 113].
New systems such as proton radiography and proton CT systems have been proposed to overcome the conversion process, because they use the same particles, protons, for imaging and subsequent treatment [114, 115]. Precise knowledge of the proton stopping power can improve the treatment efficiency and hence patient safety, sparing even more healthy tissue around the target volume. Within a proton CT system, information about the initial and residual energy of the protons and the particle paths have to be collected. For the initial energy, the nominal beam energy is used to minimise material in front of the patient which minimises the scattering of the protons. The system to measure the residual energy of the protons after they have passed the patient could be realised as a ToF system with LGADs.

The West German Proton Therapy Centre Essen (WPE) is located close to the TU Dortmund University. This treatment facility is equipped with an IBA Proteus Plus proton therapy system [116]. The used cyclotron can deliver protons with an energy of up to 228 MeV. An energy selection system is installed to allow the use of ejected protons with lower energies. With this system, the energy of the protons is selectable between approximately 60 MeV and 228 MeV. The protons are delivered in microbunches of roughly 100 protons per bunch at a rate of 106 MHz [117]. This gives a total beam current of 2 nA or $1.24 \cdot 10^{10}$ protons per second. Within the treatment facility, there are several treatment rooms. Some use a 360° beam rotation isocentric gantry and others have a horizontally mounted nozzle [118, 119].

4.4.1 Setup Requirements and Design of a Prototype

A particle of mass m_0 and unknown total energy E traverses the distance L of the ToF system in a measured time t. The relation between these variables can be written as

$$\begin{aligned} E = \gamma m_0 c^2 &= \frac{m_0 c^2}{\sqrt{1 - \frac{L^2}{t^2 c^2}}} \\ &= \frac{m_0 c^3 t}{\sqrt{t^2 c^2 - L^2}}, \end{aligned} \tag{4.7}$$

where $v = L/t$ is used for the velocity of the particle. To determine the uncertainty of the energy measurement, the partial derivatives of E after the variables L and t

are needed, since these have measurement uncertainties σ_L and σ_t respectively. The partial derivatives result to

$$\frac{\partial E}{\partial t} = -\frac{m_0 c^3 L^2}{(t^2c^2 - L^2)^{3/2}} \quad \text{and}$$
$$\frac{\partial E}{\partial L} = \frac{m_0 c^3 t L}{(t^2c^2 - L^2)^{3/2}}.$$

These two partial derivatives are combined to give the uncertainty of the energy measurement:

$$\sigma_E = \frac{m_0 c^3 L \sqrt{L^2\sigma_t^2 + t^2\sigma_L^2}}{(t^2c^2 - L^2)^{3/2}}. \tag{4.8}$$

The image reconstruction in a pCT system relies on a correct knowledge of the energy of the detected particles. Therefore, the uncertainty of the measured energy should not exceed about 3 %, as it was explained before. To study the effect of different parameters on the uncertainty, the relative energy uncertainty $\frac{\sigma_E}{E}$ is calculated as follows:

$$\frac{\sigma_E}{E} = \frac{L\sqrt{L^2\sigma_t^2 + t^2\sigma_L^2}}{t(t^2c^2 - L^2)}. \tag{4.9}$$

With further calculations, the same quantity can be given for the kinetic energy:

$$\frac{\sigma_{E_{kin}}}{E_{kin}} = \frac{cL\sqrt{L^2\sigma_t^2 + t^2\sigma_L^2}}{(t^2c^2 - L^2)(ct - \sqrt{t^2c^2 - L^2})}. \tag{4.10}$$

All of these formulas depend on the measured time t that the particle needs to pass through the system. To investigate the characteristics of the planned setup for a prototype of a ToF system, the relative kinetic energy uncertainty is studied in more detail. For this purpose, the a priori unknown flight time of the particles t is replaced and Equation 4.10 is transposed as:

$$t = \frac{LE}{c\sqrt{E^2 - m_0^2c^4}} \tag{4.11}$$

$$\Rightarrow \frac{\sigma_{E_{kin}}}{E_{kin}} = \frac{(E^2 - m_0^2c^4)\sqrt{(c^2E^2 - m_0^2c^6)\sigma_t^2 + E^2\sigma_L^2}}{Lm_0^2c^4(E - m_0c^2)}. \tag{4.12}$$

In such a form it is possible to study the effect of different time resolutions of the setup σ_t and different setup lengths L on the relative kinetic energy uncertainty. These studies can be used to determine the features of the setup required to achieve relative kinetic energy uncertainties below 3 %.

In Figure 4.11 the progression of the relative kinetic energy uncertainty with an increasing kinetic energy can be seen. At the WPE energies between 100 MeV and

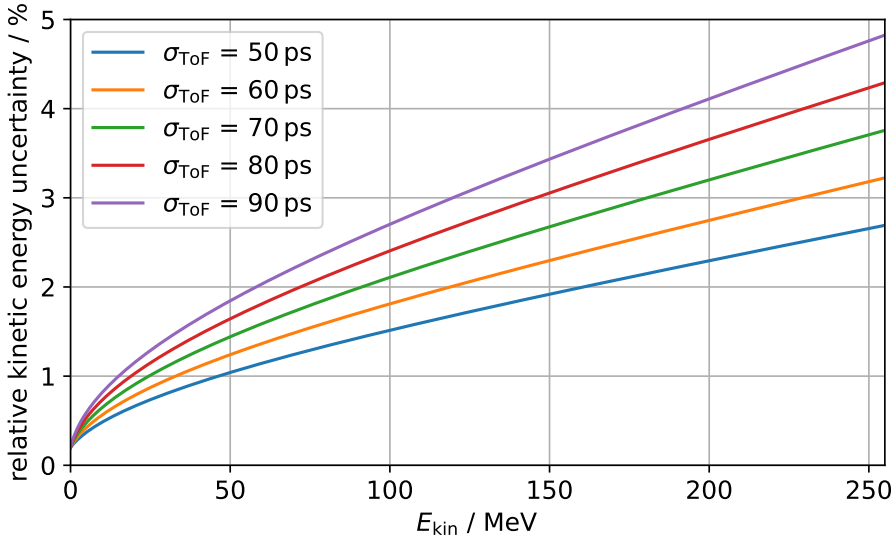

(a) Different time resolutions of the system with a fixed setup length of 1 m.

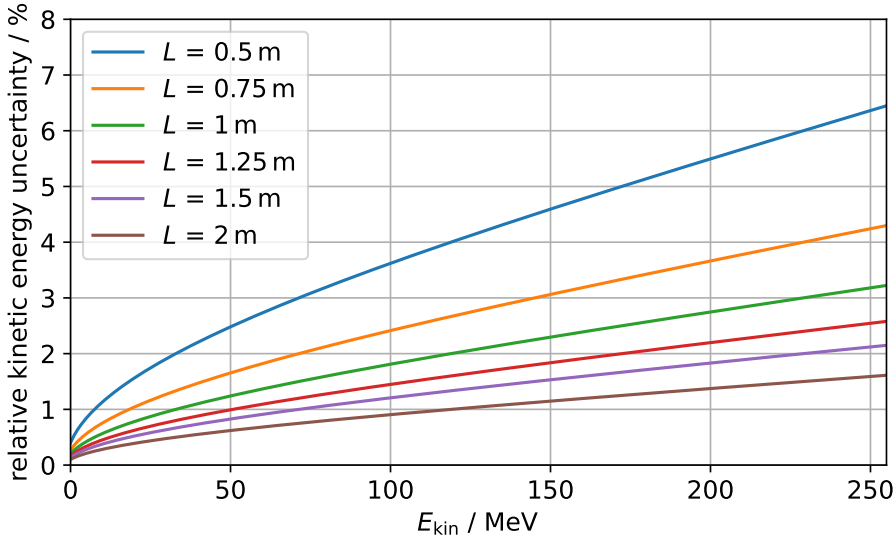

(b) Different setup lengths with a fixed time resolution of the setup of 60 ps.

Figure 4.11: The dependence of the relative kinetic energy uncertainty on different **(a)** time resolutions σ_t and **(b)** setup lengths L. An overall uncertainty for the measurement of the setup length σ_L is set to 1 mm. The time resolution σ_t of the whole system can be written as σ_{ToF} and is calculated from the time resolutions of the two used LGADs.

226 MeV can be extracted, so the values are calculated up to this upper limit. It is apparent from the plots, that a better time resolution and a longer setup length result in an overall lower relative uncertainty. To realise a system that can meet the 3 % requirement over the full energy range, time resolutions below 60 ps and a length of about 1 m are mandatory. With the available HPK 1.2 LGADs with an optimised time resolution of approximately 40 ps a time resolution of the system of about 56 ps is feasible. LGADs with a worse time resolution can still be used if the maximum energy that needs to be detected is lower. For example, if the maximum energy were less than 150 MeV, a time resolution of the entire system of 80 ps would be sufficient, which could be achieved with LGADs with a time resolution of roughly 55 ps.

As it can be seen in Figure 4.11b, a longer system length is beneficial for the relative uncertainty. However, the length of the system needs to be adjusted to the spatial restrictions. If the patient table at the WPE is used as the support for the setup, the maximum length is limited to approximately 1.5 m. However, even with this limitation in length, it is still possible to meet the 3 % requirement up to the maximum energy available at the WPE.

To test the use of LGADs in a ToF system, it was decided to use a setup with a variable length between 0.5 m to 1.5 m. In this way the energy resolution can be studied for different setup lengths as shown in Figure 4.11b. Due to the variable length of up to 1.5 m, only a horizontal arrangement of the system is feasible. The whole system is constructed with square aluminium strut profiles. These profiles are easily assembled using screws and angle brackets. The modularity of the setup is a requirement, because it has to be transported from the TU Dortmund University to the patient room of the WPE. To be transportable, the setup must be easy to disassemble and quick to reassemble. A screenshot of the setup designed in a CAD programme is shown in Figure 4.12a.
In addition to the strut profiles, holders are required for the two LGADs. These holders must be able to hold the readout cards, which have a size of approximately $10\,\text{cm} \times 10\,\text{cm}$. Since the setup is intended to be placed on the movable patient table in the treatment room at the WPE, only one of the holders requires a mechanism to align the two LGADs behind each other in the beam direction. For this reason, one of the holders is a rigid aluminium frame, which is attached with angle brackets to the strut profiles. This frame is shown on the left in the two figures in Figure 4.12. By loosening the screws that go into the profiles, the whole frame can be moved forwards and backwards within the setup. Under the readout card there is large square hole to allow the beam to pass through the setup with as little disturbance as possible. For the second holder, a metal box is designed that is attached to a XY-stage. The holder can be seen on the right hand side of Figure 4.12b. The

XY-stage is mounted on two metal bars that are fixed with screws to the back of the entire setup.

The XY-stage for the second readout card is needed to align the two planes with respect to each other and to the particle beam. A bipolar stepper motor is used in each direction of the XY-stage [120]. This stepper motor has a specified step size of 200 steps per full revolution. The stepper motors are controlled by the micro stepper motor driver A4988. The motor supply voltage for this setup is around 9 V for each stepper motor. A higher step resolution is possible with the motor driver [121]. It drops to 3200 microsteps per complete revolution with the sixteenth-step mode, which results in 0.1125° per microstep.
The motor driver is connected to a Raspberry Pi. This allows the Raspberry Pi to be controlled remotely via an Ethernet connection. This is extremely useful for the later use in the treatment room. There is a Python script on the Raspberry Pi that initiates the movement of the XY-stage. It controls the movement in each direction in large and small steps. The step sizes are checked in the laboratory with a calliper when the XY-stage is positioned so that the sliders move parallel to the floor. A large step corresponds to a movement of about 5 mm and a small step is only about 0.5 mm. The large steps are good for the rough alignment in the beginning and the small steps are then used for the final, finer steps of the alignment process.

4.4.2 Measurement with a Prototype

The setup is first assembled in the laboratory of the TU Dortmund University to check the rigidity of the connections. In addition, the XY-stage is mounted correctly in place and the step sizes are checked again. This is done, because the motors have to work against gravity in the final setup. Therefore, precise knowledge of the step sizes is required for an acceptable alignment. The step sizes are the same in each direction as given in the previous section. After these pre-tests, the setup is dismantled and taken to the WPE for a first investigation under real conditions.
Views of the setup in the patient room are shown in Figure 4.13. The whole frame without the attached readout cards on the patient table is shown in Figure 4.13a. As the patient table can be moved in all three dimensions and rotated at all angles, there is no need for a fine alignment with the beam nozzle during the initial setup phase. The frame is placed as close to the nozzle as possible. This results in a minimum distance from the nozzle to the first plane of about 15 cm. The barlock shown in Figure 4.13b is used to ensure the alignment of the whole setup frame with the beam direction. This carbon structure is attached to the patient table. It is always placed perpendicular to the long side of the patient table. The short edge

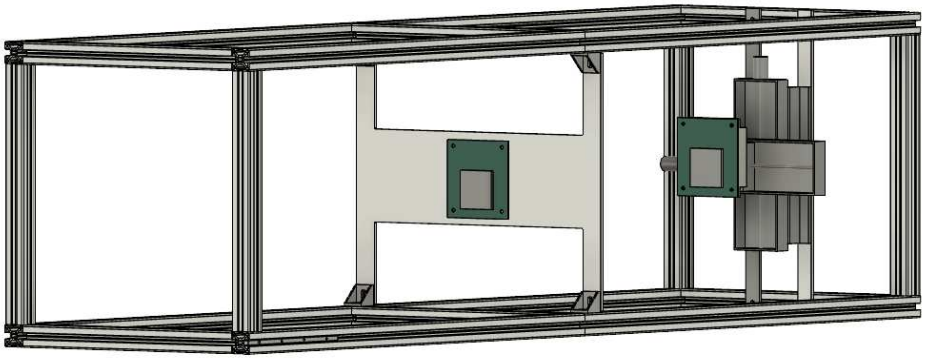

(a) Screenshot.

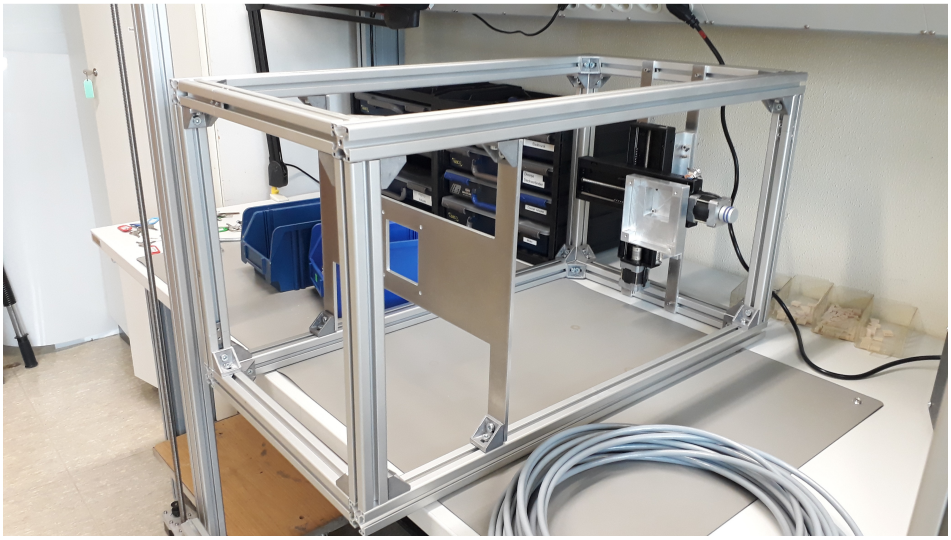

(b) Photograph.

Figure 4.12: The setup of the ToF system is presented in **(a)** as a screenshot from the CAD programme and in **(b)** as half of the full setup length in built up status without attached LGADs in the laboratory at TU Dortmund University.

of the setup is pushed against the barlock and in such a way the entire setup frame is aligned parallel to the beam direction.

The idea for the precise alignment of the setup is to use the infrastructure of the treatment room, where a laser cross from the patient positioning system is available. The movement of the patient table is then used to position the first detector plane directly in the crossing point of the lasers. This is shown in Figure 4.13c. As it can be seen, the whole setup is lifted to the correct height and the correct horizontal position. The crossing point of the laser lines is exactly in the middle of the opening hole in the cap of the readout board. The LGAD is placed under this hole, which has a diameter of about 1 cm and is covered with aluminium foil. For the positioning of the second LGAD, the laser positioning system is again used for a first rough estimate. In order to accurately align the second detector plane with the first detector, the coincidence rate during an application of the pencil beam is observed. The maximum coincidence rate should be reached when the planes are aligned with respect to the beam direction. To find the correct position, the XY-stage is used to move the last plane.

During the alignment process, the distance between the nozzle and the first detector plane was about 30 cm. The distance between the first detector plane and the second detector plane is approximately 1.1 m. This large distance was originally chosen, because this setup length was found to be one of the best choices to obtain the best energy resolution (see Figure 4.11 for more insights). The alignment was started with a pencil beam with an energy of approximately 100 MeV. The dose is about 50 Monitor Units (MU), which is a unit that is specified by the facility. This dose was applied twice, but no signal was seen in either plane.
To check the positioning of the readout cards, slices of 5 cm × 5 cm X-ray film are taped over the caps of the readout boards. The applied dose is increased to 500 MU. This dose is applied five times until both X-ray films show a pattern visible to the eye. Photographs of the X-ray films are shown in Figure 4.14. The first X-ray film (see Figure 4.14a) confirms that the plane closest to the nozzle is hit centrally by the proton beam. However, the marks on the film placed above the cap of the second readout board (Figure 4.14b) indicate a much wider beam profile, as almost the whole film is covered with marks. From this profile it is not possible to determine the exact position of the LGAD within the proton beam. To improve the alignment, a second attempt of the usage of the laser positioning system is made. The laser lines confirm that the second LGAD is not in the right position. The intersection point of the lasers and the current position are used to calculate the required shift, which is then realized with the XY-stage. However, no coincident signals are recorded on the planes afterwards when a proton beam with a dose of 50 MU is applied.

Since despite all efforts to align both detectors no signals are seen on the LGADs, a

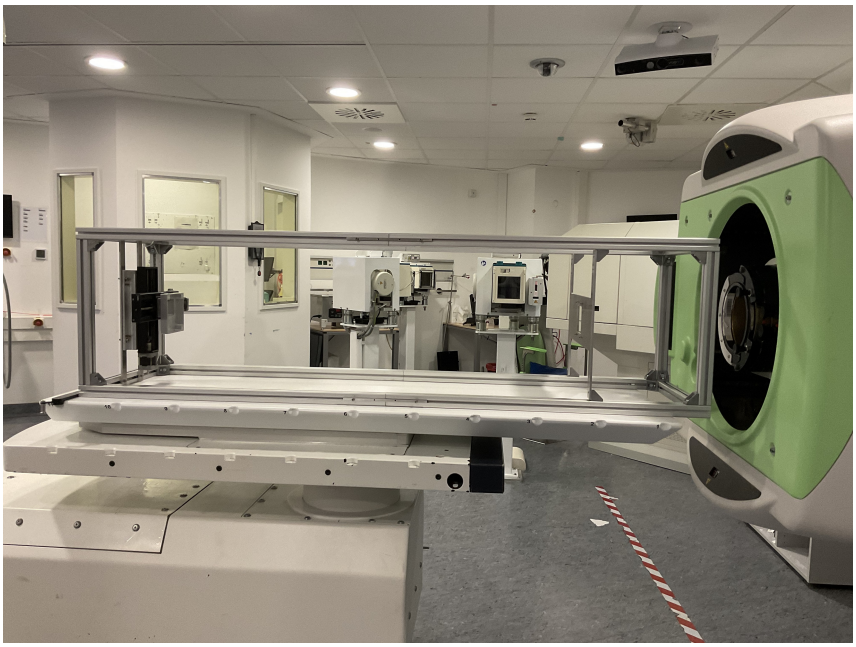

(a) Whole setup frame.

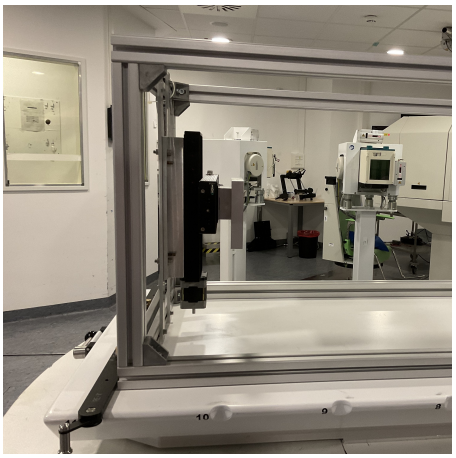

(b) Barlock for alignment.

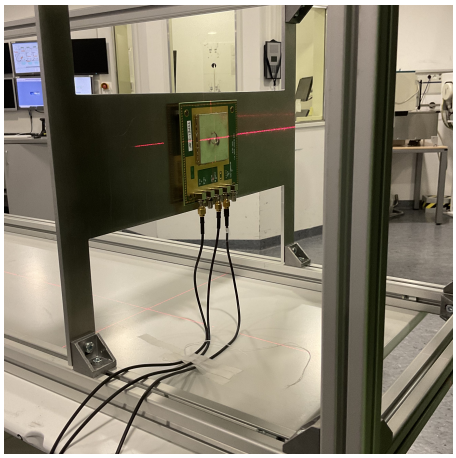

(c) Laser for alignment.

Figure 4.13: A picture of the whole frame of the setup without the installed readout cards is displayed in **(a)**. The round exit window of the nozzle can be seen on the right. The rear part of the setup with the XY-stage is shown in **(b)**. The black barlock attached to the patient table is visible at the lower left corner behind the setup frame. The laser cross used for the alignment of the first detector plane is shown in **(c)**.

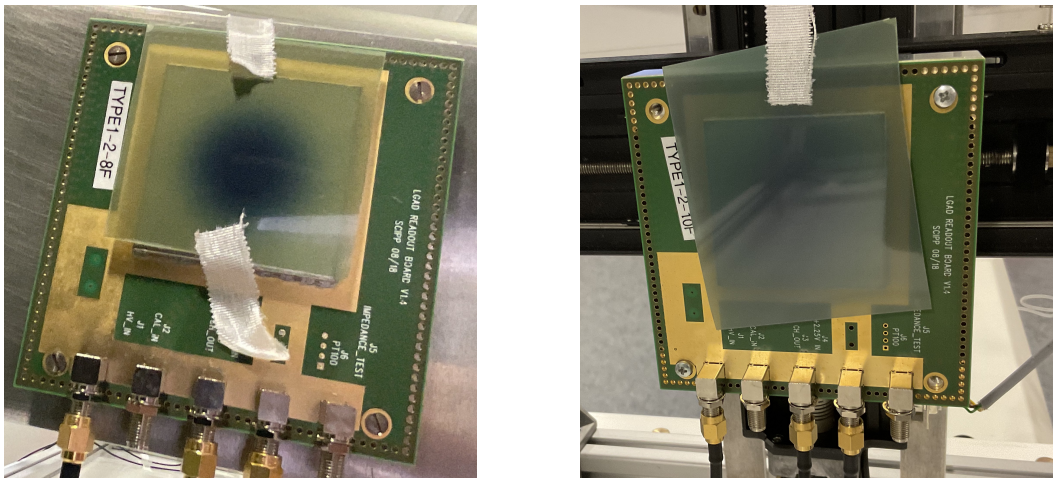

(a) X-ray film on first plane.

(b) X-ray film on second plane.

Figure 4.14: X-ray films attached to the protective caps of the readout boards on **(a)** the first detector plane and **(b)** the second detector plane. The first plane is closest to the nozzle (a distance of about 20 cm) whereas the second plane is about 1.3 m away from the beam exit window.

large debugging session is started. Up to this point the protective caps are always attached to the readout cards. To test the reaction of the LGADs to normal room light, the caps are removed. Since the energy of visible light is enough to trigger a signal in the LGAD, the current of the LGAD and the oscilloscope are observed. For both planes, the current rises when the protective caps are removed. Furthermore, when the laser is focused at the LGAD, the current increases even more. This proves that the LGADs are completely functional and react as expected to photons. However, still no signals are seen on the oscilloscope. A closer look at the oscilloscope revealed, that after the reboot at the WPE the oscilloscope was started with the default settings. For this reason the scaling and the terminating resistor were set to unsuitable values for the measurements.
After the known settings from the laboratory measurements are applied to the oscilloscope, further debugging is carried out. Several things are tried to see an effect on the signal rate. After each change, a pencil beam with a dose of 50 MU is applied to check the signals on the LGADs. First of all, the trigger level in the data acquisition software is reduced from 2 mV to 1 mV for both LGADs. However, this does not results in any recorded signals in the LGADs. As a next step, different range shifters are placed downstream of the nozzle. These are mainly made of polystyrene and are used to decrease the energy of the protons that pass through the setup [116]. Two different range shifters are tested, but nevertheless no signals

are seen. Finally, the attachment of the protective caps and the effect of normal room light during the application of the proton beam are investigated. The first signals that look like the expected curves are observed with a 51 mm range shifter, no protective caps attached to the readout boards and a trigger level of only 1 mV. The signals are shown in Figure 4.15.

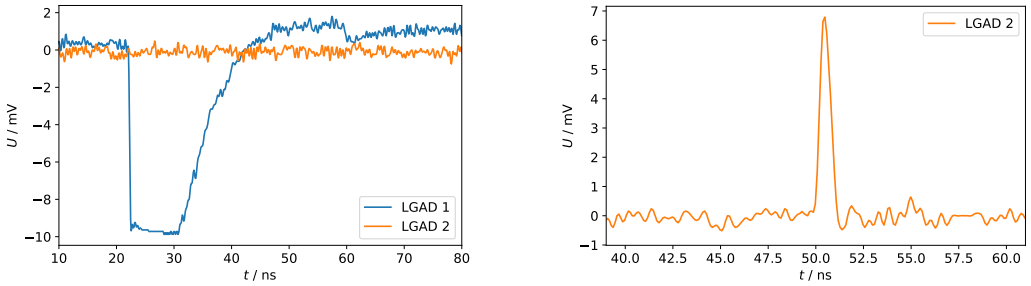

(a) Signals from first and second LGAD.

(b) Signal of second LGAD.

Figure 4.15: First recorded signals with the LGADs in the long setup, where **(a)** shows the signals of both planes when the data taking is triggered by the first LGAD and **(b)** depicts the signal of only the second LGAD when the data taking is triggered by the second LGAD. Both pictures are taken at different times, the time scale in both graphs is only for scaling purpose for the duration of the signals.

The signals shown in Figure 4.15a are recorded with the first LGAD as the trigger. The trigger level for this LGAD is set to 1 mV. For the second LGAD, there is a trigger level of 0 mV applied. With such a setting, the signal of the second LGAD is recorded regardless of its shape. In this constellation, a signal is only seen for the LGAD closest to the nozzle. Within the recorded time frame of more than 50 ns after the start of the signal on the first plane, no signal is detected on the second plane. The signal from the first LGAD has a steep rise and the fall appears to be exponential. The maximum seems to be cut off at a voltage of −10 mV. This limit is still from the default settings and was not changed before the data was taken. For this reason, the full height of the signal is not recorded and the signal shape from 22 ns to 32 ns is not caused by the physics of the particle beam, but only by electronic effects due to the oscilloscope settings. The effect of a cut-off voltage limit set in the oscilloscope is checked afterwards in the laboratory and the shape is confirmed (see Figure 4.18 for more details on this procedure). The duration of the pulse is much longer than any recorded pulse in the laboratory setup. There, pulse durations between 1 ns and 5 ns are observed. No explanation for the polarity of the pulse, which is inverted with respect to lab measurements, is found either directly at the WPE or in the later analysis process.
Since no signals are detected on the second plane during the data taking while the

first LGAD serves as the trigger, another pencil beam with a dose of 50 MU is applied to the setup. However, now the second LGAD is used as the trigger with a trigger level of 1 mV and only the signals from this LGAD are recorded to check if it is generally affected by the beam. An example of a recorded pulse can be seen in Figure 4.15b. The shape, maximum height and duration of this pulse is exactly the same as for those recorded in the laboratory setup with the ^{90}Sr source. Other recorded pulses in this configuration have the same shape with maximum heights between approximately 2.5 mV and 10 mV. For the origin of these pulses there are two possibilities: the first are secondary electrons and photons from all materials that are passed by the protons as seen in later simulations or activated material of the setup. The latter assumption also explains why such signals are only recorded after more than five hours and a cumulative dose of more than 6000 MU. Especially the XY-stage was after the measurement campaign too active to be taken directly back to TU Dortmund University, because the measured activity exceeded the limit used at the WPE.

Since there are still no coincident signals, the long setup is not used anymore to try to align the LGADs behind each other. In a second attempt, the planes are placed as close as possible to each other, which results in a distance of only 6.3 cm between them. Furthermore, the range shifter is removed from the beam exit window. A pencil beam with a dose of 50 MU is applied to the setup. The first LGAD is used to trigger the data acquisition with a trigger level of 1 mV. The signals of the second LGAD are recorded regardless of their shape or height. The only recorded signal of this setting is shown in Figure 4.16.

The signal for the front LGAD looks the same as in the long setup shown in Figure 4.15a. The height is cut off at −10 mV as before. The length of the plateau is slightly below 20 ns. In the plot in Figure 4.16 it is clearly visible that the pulse causes an overshoot of the zero line when it comes back from its maximum value. This overshoot is the reason, why the data taking is triggered. Within the recorded time frame of 100 ns, three signals are recorded by the rear detector. These three signals look exactly like the pulses previously recorded for the rear LGAD in the longer setup. The heights of the three signals are in the range of 8.1 mV to 9.3 mV. The time difference between the first and second pulse is less than the difference between the second and third pulse. This indicates that the pulses are not correlated with each other or with the particles in the proton beam.
The time difference between the start of the large signal recorded with the front LGAD and the closest signal in the rear LGAD is about 9 ns. This is much longer than the expected time-of-flight for a proton with an energy of 100 MeV. The theoretical flight time derived from Equation 4.11 is about 491 ps. Even taking into account the energy loss in air, the first sensor and the PCB material of the readout card, an increase of more than one order of magnitude is not expected. For

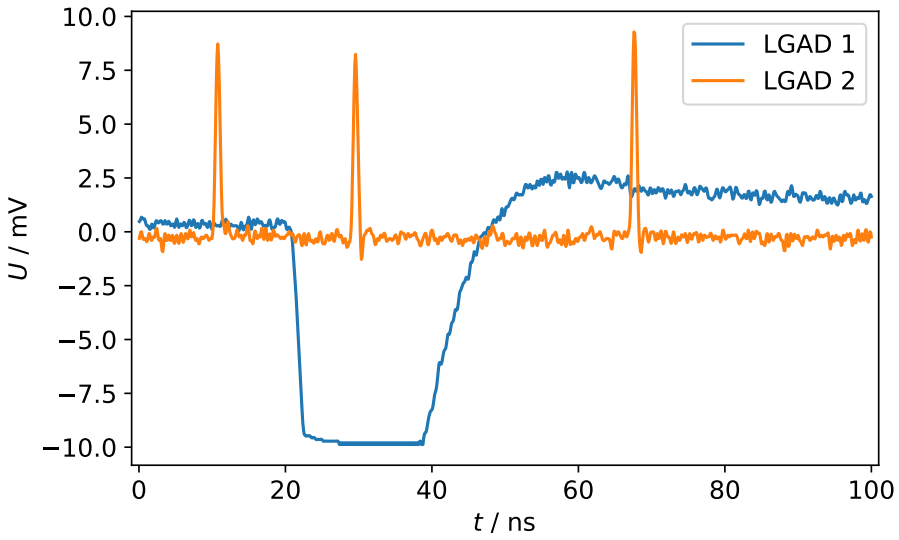

Figure 4.16: Signals of the front and rear LGAD in a setup with a length of 6.3 cm. The data taking is triggered when the signal of the first LGAD, placed closer to the nozzle than the second LGAD, is more than 1 mV.

this reason, it is safe to say that the recorded signals in the second LGAD are not correlated with the signal from the first LGAD.

For the final series of measurements with this prototype, the setup length is even further reduced. The rear LGAD is removed from the XY-stage and the readout card is taped to the back of the aluminium holder for the front LGAD. Due to the thickness of the aluminium holder and spacers, the distance between the two LGADs is reduced to approximately 3.5 cm. The aluminium holder is placed about 25 cm downstream of the nozzle. As before, a pencil beam of protons with an energy of 100 MeV and a dose of 50 MU is applied to the setup. The data acquisition is triggered by the first LGAD when a recorded signal exceeds the trigger level of 1 mV. All signals in the second LGAD are stored without a check of their height. With this setting, there is only one recorded signal in the first LGAD. The signals from the first and second LGAD are displayed in Figure 4.17.

The shapes of the signals look like those observed before. The length of the plateau region is about 22 ns, which is the longest recorded time of all three pulses observed in the first detector plane. Both signals in the second LGAD show heights of approximately 9 mV. The first recorded pulse in the rear LGAD is very close in time with the beginning of the signal in the front LGAD. A closer look at the original

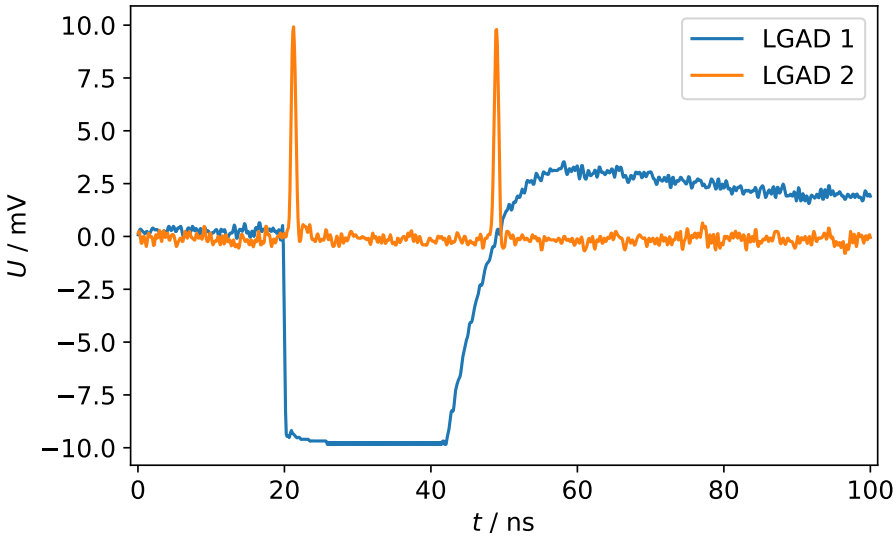

Figure 4.17: Signals of the front and rear LGAD in a setup with a length of 3.5 cm. The data taking is triggered when the signal of the first LGAD, placed closer to the nozzle than the second LGAD, is more than 1 mV.

data files reveals a time difference of about 850 ps. For protons with an energy of 100 MeV, Equation 4.11 gives a flight time of 273 ps for a distance of 3.5 cm in vacuum. Since the observed time difference is about a factor of three larger than this theoretical value, it is clear that again this is not a coincident signal caused by the same particle in both detectors.

Subsequent Troubleshooting

After the measurements at the WPE, several checks are carried out to investigate what has happened during the measurement with the prototype. The tests are done in the laboratory of the TU Dortmund University with the same LGADs that were used at the WPE.
First of all, the plateau shapes at about −10 mV for the signals observed for the first LGAD are checked. For this purpose, the setup below the ^{90}Sr source is used with an LGAD of the type HPK1.2. It is biased with 200 V as in the setup at the WPE. The oscilloscope is used to store the pure waveforms and no further analysis is performed on the recorded data. The set cut-off limit in this investigation is 8 mV. An example of a waveform is shown in Figure 4.18.

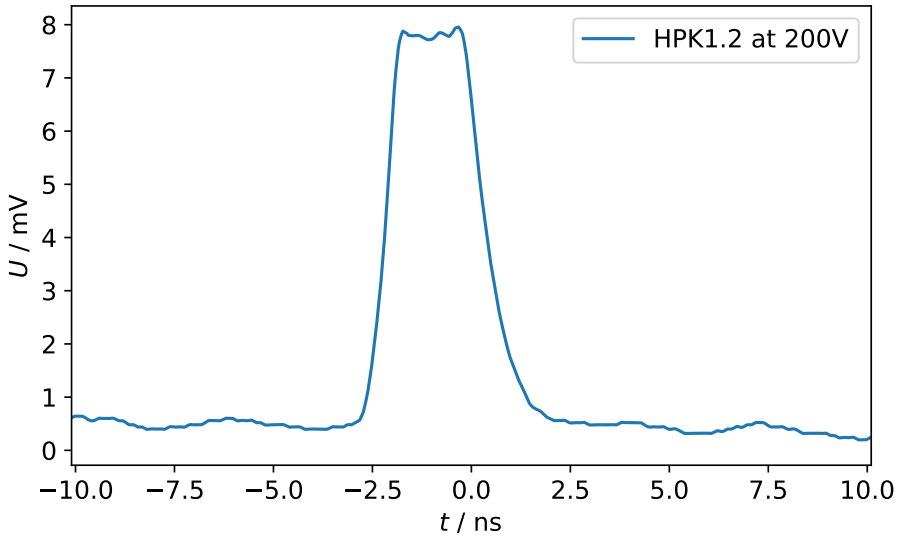

Figure 4.18: Signals of an HPK1.2 LGAD biased with 200 V in the laboratory setup beneath a ^{90}Sr source. The oscilloscope is limited to a cut-off voltage of 8 mV. The exact time scale is not relevant for the presented investigation.

This waveform shows a clear plateau region at a level of 8 mV. However, the oscilloscope does not record a constant level of 8 mV, but some fluctuations slightly below this hard limit. These fluctuations look very similar to those that were recorded for the signals in the first LGAD in the ToF setup (see for example Figure 4.15a). This investigation proves that the limited signals of the first LGAD at the WPE are indeed an artefact of an incorrectly configured voltage limit of the oscilloscope. It also proves that fluctuations in the plateau region due to a cut-off limit are to be expected and therefore the fluctuations in the signals observed in Figure 4.15 to Figure 4.17 are not correlated to any proton beam physics.
The inverted polarity of the pulse observed at the WPE could not be reproduced in the laboratory. As there is no explanation for the negative amplitude found, further investigation focuses on the question, why there were no coincident signals.

A first assumption for the absence of coincident signals is the use of different cables which connect the readout boards with the oscilloscope. Different cable lengths are expected to lead to runtime differences. As it is not possible to reconstruct which cables were used from the pictures taken on the day of the measurement, the runtime difference is checked in the laboratory.
The laboratory setup uses a pulse generator and the oscilloscope that was used at the WPE. The signal from the pulse generator is split by a T-piece directly at the

output. Cables of different lengths are attached to both ends of the T-piece and connected to two channels of the oscilloscope. For the investigation, cables with lengths from 0.45 m to 2.11 m are used. The waveforms observed on the oscilloscope are recorded and the time of arrival of each signal is taken as the 40% level of the maximum, as before for the LGAD signals. Figure 4.19 shows the measured length differences of the used cables in different measurements and the calculated length differences based on the runtime difference.

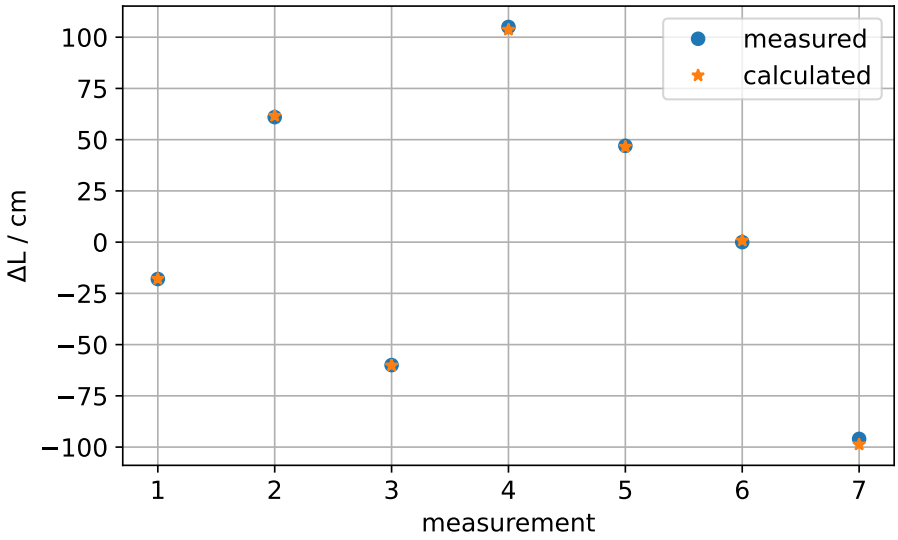

Figure 4.19: Length differences of different cables. The blue circles correspond to the lengths, more specifically length differences, measured with a measuring tape and the orange stars mark the calculated length differences based on the observed runtime differences. Values above zero indicate a longer cable for the second channel and values below zero go with a longer cable for the first channel.

All of the values are in good agreement with each other, although no uncertainties are given. The measurement with the measuring tape is not very accurate and the measured values are rounded to the nearest centimetre. However, if the signal speed of roughly $2 \cdot 10^8$ m/s (two thirds of the vacuum speed of light) is taken into account, the rounding of a few millimetres is not that relevant. The relative deviations between the measured and the calculated values are only between -1.3% and 1.0%. Solely the last measurement has a relative deviation of about 2.8%. Considering the inaccurate measurement of the cable length and the rough estimate of the speed of the signals in the cables, the relative deviations are acceptable.
The largest length difference of 1.05 m corresponds to a propagation delay of roughly 5 ns. As the cables used for the LGAD readout boards are custom made, their

lengths are known. Given the limitations of the patient room, only cables with a length of at least 1 m can be used. The longest available cable is about 2 m long, so a maximum runtime difference of 5 ns could have been present in the measurements with the prototype. However, since a time frame of 100 ns is recorded, a delay between the two planes of 5 ns is no explanation for the absence of coincident signals.

In order to gain a better understanding of the studied setup, additional simulations are performed. For this purpose, the software framework Allpix^2 is used [122]. It is specifically designed for simulations of semiconductor detectors in complex setups and offers different modules which cover individual simulation steps, e.g. the deposition of charge carriers using the Geant4 toolkit. Its main purpose is to provide a simple tool chain to simulate setups from single semiconductor detectors up to complex setups consisting of several different detectors and materials. The framework covers many steps, from the very beginning with ionising radiation to the individual response of the detectors to the hits.
With this tool, the ToF system is simulated to look for a possible reason why the test at the WPE did not work as expected. The most likely reason for the lack of coincident signals is a misalignment between the two detectors. Therefore, the effect of a shift between the two LGADs is simulated and investigated in the following.

The simulation is configured with parameters that match the known real parameters. Air is chosen as the world material. The protons of the WPE are simulated as protons with an initial energy of 100 MeV and an energy spread of approximately 650 keV [123]. A circular beam with its origin at a distance of 50 cm from the first detector is used as the source. The beam size, which gives the width of a Gaussian beam profile, is set to 5.8 mm, while the beam divergence, defined as the standard deviation of the particle angles, is 5 mrad for both axes perpendicular to the beam direction [124, 125]. The module for simulating the charge deposition in the detectors uses the *QGSP_BIC* list, a Geant4-internal list describing which physical processes are simulated [126].
The detector planes are simulated as monolithic pixel cells with dimensions of 2 mm × 2 mm. Their thickness is given as 50 µm, with a directly attached silicon support layer of 150 µm thickness with the same area as the pixel cell. Attached to the so simulated LGAD is the PCB with a thickness of 2 mm and an area of 10 cm × 10 cm. The hole beneath the LGADs is represented by a perfect cylinder with a diameter of 1.5 mm throughout the PCB. In order to further mimic the actual setup, the protective caps with their drilled hole, which is then covered with aluminium foil, are also simulated. The selected material is aluminium and the thickness of the metal sheet of the caps is set to 400 µm. This value is measured with a calliper in preparation for the simulation. For the aluminium foil, a thickness of 10 µm is chosen.

The entire simulation is comprised of five events. For each event, 100000 protons are initially simulated for the beam. Such an event is comparable to a single run collected in a testbeam campaign. The temperature is set to room temperature (20 °C), which is a crucial parameter for the module for the simulation of the propagation of the created charge carriers in the detector material.

The analysed data is derived from the Allpix^2 object PixelHit. From this object, the individual particle that causes the hit can be fetched. The information of this particle, including the identification number of the corresponding track and timing information, is extracted from the resulting root file generated by the simulation. In a further analysis, the tracks recognised by the second detector are compared to the tracks of the first detector. If the identification numbers correspond to each other, the track is recognised by both detectors and indicates therefore a coincident signal. In order to examine the impact of a misalignment between the two LGADs, a simulation with the previously described parameters is conducted. The distance between the two LGADs is set to 3.5 cm. This is the smallest studied setup length and it is anticipated that the effect of a misalignment will be more pronounced for longer setups. Accordingly, it is decided to investigate only the smallest length. The misalignment is implemented by a simple shift of the second detector in the x-direction. The shift is increased from 0 mm, which represents a perfect alignment, up to 4 mm, which is a complete misalignment. The result of the analysed simulation output is presented in Figure 4.20.

The coincidence rate is defined as the ratio of the coincident signals to the total number of recorded signals on the corresponding sensor. Five events are simulated, and each results in a slightly different total number of hits in the LGADs. The ratios shown in Figure 4.20 are the mean of these five results, with the standard deviation of the five values represented by the error bars. As expected, this ratio is highest when the sensors are perfectly aligned one behind the other. In this case the rate is about 65%. It decreases as the lateral offset increases. If the sensor centres are misaligned by 1 mm, the coincidence rate is only about 40%. For a misalignment of 2 mm, the rate decreases further to only 5% and for an even larger shift the coincidence rate is close to zero.
The simulation proves that a misalignment of just a few millimetres drastically reduces the coincidence rate. During the last measurements at the WPE, the sensors were not aligned with the laser system in a first approach, but only by eye. Therefore, a misalignment of at least 1 mm between the two LGADs is very likely. This proves that a misalignment is the most likely reason for the absence of coincident signals. On the other hand, the trend of the curve verifies the general idea of looking for the highest coincidence rate during the alignment process.

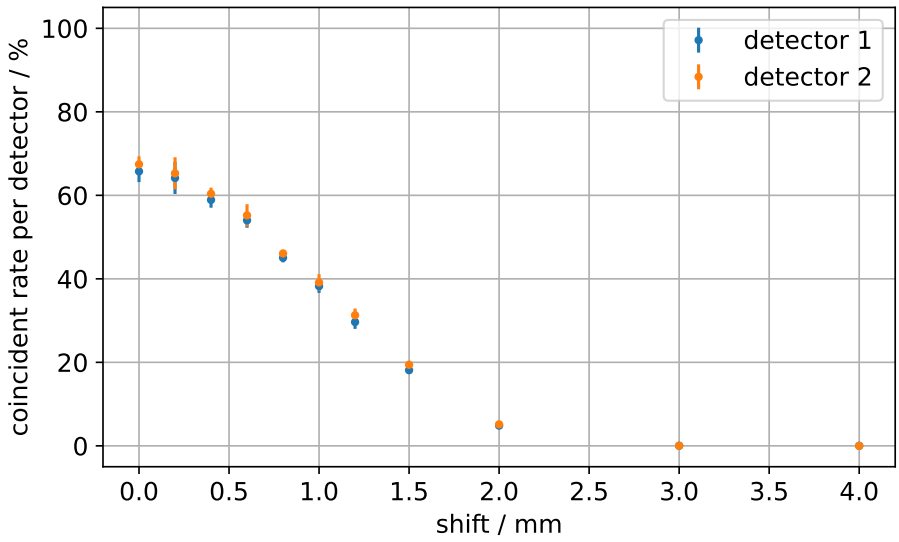

Figure 4.20: Simulated rate of coincident signals per detector plane. The beam consists of protons with an energy of 100 MeV and the distance between the two detectors is 3.5 cm. The simulation consists of five events with 100000 generated protons each.

5 Conclusion and Outlook

This thesis deals with very different topics. For this reason, a conclusion and outlook is presented for the market survey, the measurements of LGAD sensors and the first studies towards a time-of-flight system with LGADs, individually.

5.1 Market Survey

The market survey for the planar pixel sensors for the ITk detector was a huge effort. It was split between several institutes in order to meet the tight schedule. Within the market survey, sensors from several vendors were qualified for the production. This thesis presents the results for two of the six investigated vendors. One vendor, number four in the market survey, was qualified with the original requirements. The wafers of the other vendor, vendor number three, were remeasured to verify the measurement results obtained by the vendor itself. For the best possible comparability, the measurements at the TU Dortmund University were adapted to match those of the manufacturer. As a result, the measurements differed from those specified for the market survey. The measurements at the institute verified the measurements done by the vendor itself, so the electrical tests for this vendor can be trusted.

The visual inspection of all the delivered structures is the most time-consuming part. Almost no defects were found on the bump pads. Only the structures of vendor number four were found to have a sensitive metallisation. This was reported directly to the vendor. Otherwise, both vendors produced sensors of good quality. Nevertheless, there is room for improvement in this part of the quality check. Firstly, it would be beneficial to have a standardised setup for photographing the sensors. This makes it easier to compare between different institutes. Moreover, an automated image analysis for the investigation of pixel defects on larger matrices is much faster than human inspection.
When examining the thickness and bow of the structures, it was clear that both vendors were able to produce structures of uniform thickness. The delivered wafers showed no bow and only one of the diced sensors was found to have a significant bow. However, more information about the supporting layer is needed for the institutes to disentangle the real excess of material from the carrier layer and the real sensor

substrate. The standard analysis shows that a human review of conspicuous results of the analysis script is often required. In most cases the conspicuous values, for example high heights due to reflections, can be explained and the sensors are classified as good, although the analysis script gives a classification as bad.

The structures included in the wafers from vendor number three showed different depletion voltages. However, the measurements proved to be very sensitive in detecting early breakdowns and extraordinary high currents. Nevertheless, up to 27% of the structures on the wafers did not meet the market survey requirements for the leakage current or the breakdown voltage. The vendor delivered many different combinations of design features such as the biasing scheme or the pixel size. However, no correlation between the different designs and the measurement results were found. In addition, the large number of combinations was the reason why it was not possible to comment on the uniformity of the production process for this vendor. The stability of the leakage current for the measured structures was only within the requirements for the structures of the 100 µm wafer. However, all of the irradiated sensors passed the market survey requirements.
The measurements of the leakage current and breakdown voltage of the sensors from vendor number four showed very uniform results across all sensors and all sensors passed the market survey requirements. As the leakage current for these sensors was very small, the measurement setup could have been improved to measure the small currents more accurately. For this vendor, problems were observed at a high relative humidity. However, a high relative humidity is not expected in the later experiment, so long-term measurements were also performed at lower relative humidity than required for the market survey. At the lower relative humidity (around 10% instead of 40%) the sensors fulfilled the leakage current stability requirement. In addition, all of the irradiated diced sensors fulfilled the market survey requirements.

In the different testbeam campaigns, most of the measured modules passed the requirement for the particle hit detection efficiency. All unirradiated modules passed the requirement, even if they were biased with the punch-through technology. For the irradiated modules, the efficiency loss around the punch-through structures was observed as expected. For this reason, these regions were excluded from the analysis of the efficiency of these modules. With the adjusted analysis, there was only one module from the vendors investigated in this thesis that did not exceed the required efficiency of 97% for the market survey.
During the many testbeam campaigns, a number of improvements were identified. First of all, a fast reconstruction and analysis chain is very beneficial. In this way, first statements about the data quality can be made even during the ongoing measurements. This allows the measurement plan to be quickly adjusted to make more efficient use of the beam time. Secondly, some of the modules showed high leakage currents during the testbeam campaign and were therefore difficult to tune

and bias properly. If time permits, a quick measurement of the current-voltage characteristic is useful before the module is brought to the testbeam campaign. If the investigated module shows a too high leakage current in the lab, it is clear that no reasonable results can be expected and it is not worth installing the module in the testbeam setup to measure its efficiency. The third problem observed is the effect of the number of disconnected bumps. A large number of disconnected bumps leads to a very low number of tracks and therefore to doubtful analysis results. If the module is tested for this beforehand, non-promising modules can be excluded from the testbeam campaign altogether. If it is necessary to examine such a module, the measurement time for this module can be increased in order to record a higher number of tracks for the later analysis.

To summarise, the measurements for the market survey were sufficient to be used for the Final Design Review (FDR) of the planar sensors for the ITk in September 2020. Based on the results, three vendors were selected to produce the sensors for the ITk.
Vendor number three, which is FBK, is chosen for the production of 100 µm sensors with TM for biasing. The thicker sensors from this vendor did not meet all requirements of the market survey, so they were not considered good enough for the installation in the ITk. However, the second investigated vendor in this thesis, vendor number four, which is HPK, is selected to produce sensors of 150 µm thickness with polysilicon for biasing. An additional third vendor, vendor number six in the market survey, which is Micron Semiconductor Ltd and not covered in this thesis, produces sensors of both thicknesses with punch-through structures. These have shown good results with this biasing scheme in testbeam campaigns (see the thesis of T. Fitschen [79] for more details on the specific results).

5.2 Low Gain Avalanche Diodes

The LGADs at the TU Dortmund University come from two different institutes. That gives the chance to test the sensors in possible different conditions.
Their current-voltage characteristics and their depletion voltages are exactly as expected. The observed differences can all be explained by their internal structure or damage from scratches. The obtained results are in very good agreement with the values found in the literature for the available LGAD types at the TU Dortmund University.

The measurement of the time resolution of LGADs was set up in a previous master thesis, but never successfully carried out before at the TU Dortmund University. In this thesis the setup is successfully used to obtain the time resolution of all available

LGAD types. The setup is improved by a wider hole in the readout card underneath the LGAD to increase the data taking rate. As the setup is not placed in a climate chamber, the temperature and the relative humidity cannot be controlled. This is one of the reasons why an accurate comparison with measurements in the literature is not easily possible for these measurements.
The same value of the time resolution as reported in the literature can only be found for one of the LGAD types, namely type HPK2, in the used setup at the TU Dortmund University. For the type HPK1.2, the time resolution found in this work is about 66% worse than that found in the literature [98]. For the type HPK1.1, the time resolution is 33% better than that given in the literature [98]. The results are so different that no simple explanation is found to describe the discrepancy. Some parameters, such as the used CFD value or the temperature of the sensors, directly affect the time resolution. As these are not always reported in the literature, a comparison is hardly possible. Furthermore, there is no clear reference sensor available at the TU Dortmund University. Such a sensor would be an LGAD with a known very small time resolution. With such a sensor in the setup, the uncertainties caused by unknown effects of the investigated LGAD are reduced so that they only apply to the investigated sensor and not to both, as is the case with the currently used setup.

The measured rates for triggered signals are quite low (below 1 Hz) in the used setup. As it has turned out later, the radioactive source was not correctly installed in its shielding. For this reason, the energy spectrum of the recorded electrons is not identical to that expected from a ^{90}Sr source. In addition, the initial electrons may have been emitted into the shielding and only the back-scattered electrons were detected by the setup below the source.
To sum up the measurements and difficulties with the LGADs, a new measurement of the time resolution with the correctly installed radioactive source is beneficial to verify the results of this thesis. Moreover, the setup can be further improved by placing it inside a box where the environment can be controlled.

5.3 Time-of-Flight System

The measurement with the prototype of a time-of-flight system with LGADs did not work out as expected. From feasibility studies it is known that a ToF system with LGADs is able to measure the residual energy at a proton treatment facility [127]. However, the presented prototype did not provide any useful results. For this reason, this thesis focuses on the troubleshooting.

At first, the construction of the frame follows a rather simple approach. With more time and more precise tools, a setup with a better alignment capability could be designed. In particular, the alignment process can be improved with a standardised method and supporting computer scripts. The idea of alignment by the rate of coincident signals is not entirely new, and has been also used in another study [128]. If the rear sensor is moved in a systematic way and all the recorded waveforms are stored, a better analysis can be done to find a precise alignment with the front sensor.
As the most likely reason for the absence of coincident signals is a misalignment, there is another approach to overcome this. Especially for short lengths of the ToF system (below 10 cm for practical reasons), the readout boards can be fixed to the used holder before taking them to the treatment facility. In this way, the ToF system is similar to the setup with the ^{90}Sr source and this source can be used to align the sensors in the laboratory. This requires one of the sensors to be moveable in small steps. Since the coincidence rate for the laboratory setup is known, this can be used as a benchmark. The moveable LGAD is systematically moved with respect to the fixed LGAD to find the best position, which is the position with the highest coincidence rate. Once aligned, the frame with the fixed readout boards can be taken to the treatment facility and placed there in the aluminium frame. The moveable patient table can then be used to bring the centre of the ToF system to the correct height and position with respect to the proton beam. In addition to the well-known good alignment, this procedure has a second advantage. As the ToF system is already aligned within itself, there is no need for a lengthy alignment process in the treatment room. This allows the measurement time to be used more efficiently.

The use of LGADs in medical applications is a very interesting approach to combine the knowledge and expertise of the high-energy physics community and bring it to another field. A first study with LGADs for proton counting in a setup tested at a treatment facility in Italy shows promising results [129]. Furthermore, the evolution of LGADs does not stop with the small diodes presented in this thesis. Today, larger LGAD devices with dimensions of about 2.5 cm $\times$ 2.5 cm are available. Such devices can cover the entire proton beam [130].

Bibliography

[1] The ATLAS Collaboration. "Combined search for the Standard Model Higgs boson using up to 4.9 fb^{-1} of pp collision data at $\sqrt{s} = 7$ TeV with the ATLAS detector at the LHC." In: *Phys. Lett. B* 710 (2012), pp. 49–66. DOI: 10.1016/j.physletb.2012.02.044.

[2] The CMS Collaboration. "Combined results of searches for the standard model Higgs boson in pp collisions at $\sqrt{s} = 7$ TeV." In: *Phys. Lett. B* 710 (2012), pp. 26–48. DOI: 10.1016/j.physletb.2012.02.064.

[3] H. Kolanoski and N. Wermes. *Teilchendetektoren: Grundlagen und Anwendung*. Springer-Verlag Berlin Heidelberg, 2016.

[4] G. Lutz. *Semiconductor Radiation Detectors: Device Physics*. Springer-Verlag Berlin Heidelberg, 2007.

[5] S. M. Sze and Kwok K. Ng. *Physics of Semiconductor Devices*. Wiley-Blackwell, 2006.

[6] K.-H. Rohe. *Elektronik für Physiker*. 3. Auflage. Teubner Studienbücher Physik, 1987.

[7] H. Kolanoski and N. Wermes. *Particle Detectors: Fundamentals and Applications*. Oxford University Press, 2020. DOI: 10.1093/oso/9780198858362.001.0001.

[8] Particle Data Group et al. "Review of Particle Physics." In: *Progress of Theoretical and Experimental Physics* 2020.8 (2020), p. 083C01. DOI: 10.1093/ptep/ptaa104.

[9] pylandau. *SiLab-Bonn / pylandau*. URL: https://github.com/SiLab-Bonn/pylandau (visited on Aug. 2, 2022).

[10] J. H. Hubbell. "Electron–positron pair production by photons: A historical overview." In: *Radiation Physics and Chemistry* 75.6 (2006), pp. 614–623. DOI: 10.1016/j.radphyschem.2005.10.008.

[11] G. Troska. "Development and operation of a testbeam setup for qualification studies of ATLAS Pixel Sensors." PhD thesis. Technische Universität Dortmund, 2012.

[12] T. Wittig. "Slim Edge Studies, Design and Quality Control of Planar ATLAS IBL Pixel Sensors." PhD thesis. Technische Universität Dortmund, 2013.

[13] F. Hügging. "Der ATLAS-Pixelsensor - Der state-of-the-art-Pixelsensor für teilchenphysikalische Anwendungen mit extrem hohen Strahlungsfeldern." PhD thesis. Universität Dortmund, 2001.

[14] K. Motohashi et al. "Evaluation of KEK n-in-p planar pixel sensor structures for very high radiation environments with testbeam." In: *Nucl. Instrum. Meth. A* 765 (2014), pp. 125–129. DOI: 10.1016/j.nima.2014.05.092.

[15] G.-F. Dalla Betta and M. Povoli. "Progress in 3D Silicon Radiation Detectors." In: *Frontiers in Physics* 10 (2022). DOI: 10.3389/fphy.2022.927690.

[16] J. Lange et al. "3D silicon pixel detectors for the High-Luminosity LHC." In: *Journal of Instrumentation* 11.11 (2016), p. C11024. DOI: 10.1088/1748-0221/11/11/C11024.

[17] J. Lange et al. "Radiation hardness of small-pitch 3D pixel sensors up to a fluence of $3 \times 10^{16}\, n_{\mathrm{eq}}/\mathrm{cm}^2$." In: *Journal of Instrumentation* 13.09 (2018), P09009–P09009. DOI: 10.1088/1748-0221/13/09/p09009.

[18] E. Currás et al. "Study of small-cell 3D silicon pixel detectors for the high luminosity LHC." In: *Nucl. Instrum. and Meth. A* 931 (2019), pp. 127–134. ISSN: 0168-9002. DOI: 10.1016/j.nima.2019.04.037.

[19] G. Darbo. "Experience on 3D silicon sensors for ATLAS IBL." In: *Journal of Instrumentation* 10.05 (2015), pp. C05001–C05001. DOI: 10.1088/1748-0221/10/05/c05001.

[20] S. I. Parker, C. J. Kenney, and J. Segal. "3D — A proposed new architecture for solid-state radiation detectors." In: *Nucl. Instrum. Meth. A* 395.3 (1997), pp. 328–343. DOI: 10.1016/S0168-9002(97)00694-3.

[21] C. Kenney et al. "Silicon detectors with 3-D electrode arrays: fabrication and initial test results." In: *IEEE Transactions on Nuclear Science* 46.4 (1999), pp. 1224–1236. DOI: 10.1109/23.785737.

[22] M. Mathes et al. "Test Beam Characterization of 3-D Silicon Pixel Detectors." In: *IEEE Transactions on Nuclear Science* 55.6 (2008), pp. 3731–3735. DOI: 10.1109/TNS.2008.2005630.

[23] The ATLAS IBL Collaboration. "Prototype ATLAS IBL modules using the FE-I4A front-end readout chip." In: *Journal of Instrumentation* 7.11 (2012), P11010–P11010. DOI: 10.1088/1748-0221/7/11/p11010.

[24] A. L. Heggelund et al. "Radiation hard 3D silicon pixel sensors for use in the ATLAS detector at the HL-LHC." In: *Journal of Instrumentation* 17.08 (2022), P08003. DOI: 10.1088/1748-0221/17/08/P08003.

[25] M. Garcia-Sciveres. *The RD53A Integrated Circuit*. Tech. rep. Geneva: CERN, 2017. URL: http://cds.cern.ch/record/2287593.

[26] M. Daas. "Characterization and Quality Control of RD53A Readout Chips and Modules for the ATLAS ITk Pixel Detector." PhD thesis. Rheinische Friedrich-Wilhelms-Universität Bonn, 2021.

[27] M. Frohne. "Developments for a multi-module test system for ATLAS ITk pixel detector modules." Master's thesis. Rheinische Friedrich-Wilhelms-Universität Bonn, 2020.

[28] A. Dimitrievska and A. Stiller. "RD53A: A large-scale prototype chip for the phase II upgrade in the serially powered HL-LHC pixel detectors." In: *Nucl. Instrum. Meth. A* 958 (2020), p. 162091. DOI: 10.1016/j.nima.2019.04.045.

[29] N. Dinmore. *Large Hadron Collider reaches its first stable beams in 2024*. URL: https://home.cern/news/news/accelerators/large-hadron-collider-reaches-its-first-stable-beams-2024 (visited on Sept. 13, 2024).

[30] *Longer term LHC schedule*. URL: https://lhc-commissioning.web.cern.ch/schedule/LHC-long-term.htm (visited on May 2, 2022).

[31] O. S. Brüning et al. *LHC Design Report*. CERN Yellow Reports: Monographs. CERN, 2004. DOI: 10.5170/CERN-2004-003-V-1.

[32] M. Vretenar et al. *Linac4 design report*. Vol. 6. CERN Yellow Reports: Monographs. CERN, 2020. DOI: 10.23731/CYRM-2020-006.

[33] CERN. *The Proton Synchrotron Booster*. URL: https://home.cern/science/accelerators/proton-synchrotron-booster (visited on Mar. 18, 2022).

[34] H. Damerau et al. *LHC Injectors Upgrade, Technical Design Report*. 2014. DOI: 10.17181/CERN.7NHR.6HGC.

[35] CERN. *The Proton Synchrotron*. URL: https://home.cern/science/accelerators/proton-synchrotron (visited on Mar. 18, 2022).

[36] CERN. *The Super Proton Synchrotron*. URL: https://home.cern/science/accelerators/super-proton-synchrotron (visited on Mar. 18, 2022).

[37] E. Mobs. *The CERN accelerator complex - 2019. Complexe des accélérateurs du CERN - 2019*. URL: https://cds.cern.ch/record/2684277 (visited on Mar. 18, 2022).

[38] The LHCb Collaboration. "The LHCb Detector at the LHC." In: *Journal of Instrumentation* 3.08 (Aug. 2008), S08005. DOI: 10.1088/1748-0221/3/08/s08005.

[39] The ALICE Collaboration. "The ALICE experiment at the CERN LHC." In: *Journal of Instrumentation* 3.08 (Aug. 2008), S08002. DOI: 10.1088/1748-0221/3/08/s08002.

[40] The CMS Collaboration. "The CMS experiment at the CERN LHC." In: *Journal of Instrumentation* 3.08 (Aug. 2008), S08004. DOI: 10.1088/1748-0221/3/08/s08004.

[41] The ATLAS Collaboration. "The ATLAS Experiment at the CERN Large Hadron Collider." In: *Journal of Instrumentation* 3.08 (Aug. 2008), S08003. DOI: 10.1088/1748-0221/3/08/s08003.

[42] J. Pequenao. "Computer generated image of the whole ATLAS detector." 2008. URL: https://cds.cern.ch/record/1095924.

[43] A. Ahmad et al. "The silicon microstrip sensors of the ATLAS semiconductor tracker." In: *Nucl. Instrum. Meth. A* 578.1 (2007), pp. 98–118. DOI: 10.1016/j.nima.2007.04.157.

[44] I. Gorelov et al. "A measurement of Lorentz angle and spatial resolution of radiation hard silicon pixel sensors." In: *Nucl. Instrum. Meth. A* 481.1 (2002), pp. 204–221. DOI: 10.1016/S0168-9002(01)01413-9.

[45] A. Eli Phoboo. *A New Sub Detector for ATLAS*. URL: https://atlas.cern/updates/news/new-sub-detector-atlas (visited on Apr. 13, 2022).

[46] M. Capeans et al. *ATLAS Insertable B-Layer Technical Design Report*. Tech. rep. Geneva: CERN, 2010. URL: https://cds.cern.ch/record/1291633.

[47] *Technical Design Report for the ATLAS Inner Tracker Strip Detector*. Tech. rep. Geneva: CERN, 2017. URL: http://cds.cern.ch/record/2257755.

[48] *Technical Design Report for the ATLAS Inner Tracker Pixel Detector*. Tech. rep. Geneva: CERN, 2017. URL: https://cds.cern.ch/record/2285585.

[49] The ATLAS Collaboration. *Peak Interactions per Crossing in 2018*. URL: https://twiki.cern.ch/twiki/bin/view/AtlasPublic/LuminosityPublicResultsRun2 (visited on Apr. 25, 2022).

[50] The ATLAS Collaboration. *ITk Pixel Layout Updates*. 2020. URL: https://atlas.web.cern.ch/Atlas/GROUPS/PHYSICS/PLOTS/ITK-2020-002/ (visited on Apr. 20, 2022).

[51] *Expected tracking and related performance with the updated ATLAS Inner Tracker layout at the High-Luminosity LHC*. Tech. rep. Geneva: CERN, 2021. URL: http://cds.cern.ch/record/2776651.

[52] A. L. Heggelund on behalf of the ATLAS Collaboration. "Overview of the ATLAS ITk pixel detector." In: *Journal of Instrumentation* 18.02 (2023), p. C02014. DOI: 10.1088/1748-0221/18/02/C02014.

[53] *Technical Design Report: A High-Granularity Timing Detector for the ATLAS Phase-II Upgrade*. Tech. rep. Geneva: CERN, 2020. URL: https://cds.cern.ch/record/2719855.

[54] T. Fritzsch et al. "Packaging of radiation and particle detectors." In: *56th Electronic Components and Technology Conference 2006*. 2006, 5 pp. DOI: 10.1109/ECTC.2006.1645664.

[55] ITk Planar Pixel Sensor MS Group. *ITk Planar Pixel Sensor MS - 14-02-2020 - Figure 05*. URL: https://atlas.web.cern.ch/Atlas/GROUPS/PHYSICS/PLOTS/ITK-2020-001/ (visited on Jan. 13, 2023).

[56] KEYENCE DEUTSCHLAND GmbH. *Messkopf für 3D-Profilometer VR-3200*. URL: https://www.keyence.de/products/microscope/macroscope/vr-3000/models/vr-3200/ (visited on Jan. 23, 2023).

[57] S. Pape. "Studies towards a Time-of-Flight system using LGAD sensors." Master's thesis. Technische Universität Dortmund, 2020.

[58] S. Dungs et al. *E4control, A Python Based Software for Device Controlling and Data Taking*. URL: https://github.com/sdungs/E4control (visited on Feb. 24, 2023).

[59] Hewlett-Packard Japan, LTD. *HP 4284A Precision LCR Meter Operation Manual*. Sixth Edition. 1998.

[60] Keysight Technologies. *Impedance Measurement Handbook - A Guide to Measurement Technology and Techniques*. 6th Edition. 2020.

[61] *Price Enquiry - Technical Specification - Production of Planar Pixel Sensors for the ATLAS ITk*. Internal documentation for the ATLAS ITk Market Survey (revision status of November 2018).

[62] Birmingham Instrumentation Laboratory for Particle physics and Applications. *Irradiation facility*. URL: http://www.ep.ph.bham.ac.uk/general/SiliconLab/irradiationfacility.html (visited on Apr. 20, 2023).

[63] *Technical Specification and Acceptance Criteria for the Planar Pixel Sensors for the ITk project*. Internal documentation for the ATLAS ITk Market Survey (revision status of June 2017).

[64] R. Diener et al. "The DESY II test beam facility." In: *Nucl. Instrum. Meth. A* 922 (2019), pp. 265–286. DOI: 10.1016/j.nima.2018.11.133.

[65] H. Jansen et al. "Performance of the EUDET-type beam telescopes." In: *EPJ Techniques and Instrumentation* 3.1 (2016), p. 7. DOI: 10.1140/epjti/s40485-016-0033-2.

[66] J. Baudot et al. "First test results Of MIMOSA-26, a fast CMOS sensor with integrated zero suppression and digitized output." In: *2009 IEEE Nuclear Science Symposium Conference Record (NSS/MIC)*. 2009, pp. 1169–1173. DOI: 10.1109/NSSMIC.2009.5402399.

[67] D. Cussans. *Description of the JRA1 Trigger Logic Unit (TLU), v0.2c*. 2009. URL: https://api.semanticscholar.org/CorpusID:61414353.

[68] M. Garcia-Sciveres et al. "The FE-I4 pixel readout integrated circuit." In: *Nucl. Instrum. and Meth. A* 636.1 (2011), pp. 155–159. DOI: 10.1016/j.nima.2010.04.101.

[69] P. Ahlburg et al. "EUDAQ — a data acquisition software framework for common beam telescopes." In: *Journal of Instrumentation* 15.01 (2020), P01038. DOI: 10.1088/1748-0221/15/01/P01038.

[70] M. Wagner. "Investigations of Planar n^+-in-n ATLAS Silicon Sensors with Modified Pixel Implantations." PhD thesis. Technische Universität Dortmund, 2020.

[71] *EUTelescope - a generic beam telescope data analysis framework*. URL: https://eutelescope.github.io/ (visited on May 30, 2023).

[72] T. Bisanz, A. Morton, and I. Rubinskiy. *EUTelescope 1.0: Reconstruction Software for the AIDA Testbeam Telescope*. 2015. URL: http://cds.cern.ch/record/2000969.

[73] *TBMon2, The ATLAS Pixel testbeam analysis framework*. URL: https://gitlab.cern.ch/tbmon2 (visited on Dec. 1, 2023).

[74] *ILC Soft*. URL: https://ilcsoft.desy.de/portal/ (visited on Dec. 1, 2023).

[75] T. Bisanz et al. "EUTelescope: A modular reconstruction framework for beam telescope data." In: *Journal of Instrumentation* 15.09 (2020), P09020–P09020. DOI: 10.1088/1748-0221/15/09/p09020.

[76] C. Kleinwort. "General broken lines as advanced track fitting method." In: *Nucl. Instrum. Meth. A* 673 (2012), pp. 107–110. DOI: 10.1016/j.nima.2012.01.024.

[77] V. Blobel. "Software alignment for tracking detectors." In: *Nucl. Instrum. Meth. A* 566.1 (2006), pp. 5–13. DOI: 10.1016/j.nima.2006.05.157.

[78] A. Gisen. "Quad module prototypes and design improvement studies of planar n^+-in-n silicon pixel sensors for the ATLAS Inner Tracker upgrade." PhD thesis. Technische Universität Dortmund, 2018.

[79] T. Fitschen. "Search for semileptonic vector boson scattering with the ATLAS Detector using LHC Run-II data." PhD thesis. Université Paris-Saclay and University of Birmingham, 2022.

[80] T. Heim. "YARR - A PCIe based Readout Concept for Current and Future ATLAS Pixel Modules." In: *Journal of Physics: Conference Series* 898.3 (2017), p. 032053. DOI: 10.1088/1742-6596/898/3/032053.

[81] R. H. Taibah. "Upgrade of the ATLAS tracking detector in preparation for the High-Luminosity phase of the LHC : Planar pixel module characterisation and calibration for the current and future ATLAS inner tracker." PhD thesis. Université de Paris, 2021.

[82] S. Möbius. "Pixel Detector Studies for the ATLAS ITk Upgrade for the HL-LHC." PhD thesis. Georg-August-Universität Göttingen, 2022.

[83] F. Crescioli on behalf of ITk Paris Cluster. *Planar pixel sensors for ATLAS ITk and beyond*. Talk presented at the French-Ukrainian Workshop. URL: https://indico.ijclab.in2p3.fr/event/6532/#12-planar-pixel-sensors-for-at (visited on Sept. 29, 2024).

[84] K. Nakamura et al. "Development of a radiation tolerant fine pitch planar pixel detector by HPK/KEK." In: *Nucl. Instrum. Meth. A* 924 (2019), pp. 64–68. DOI: 10.1016/j.nima.2018.09.015.

[85] T. Isidori et al. "Performance of a low gain avalanche detector in a medical linac and characterisation of the beam profile." In: *Physics in Medicine & Biology* 66.13 (2021), p. 135002. DOI: 10.1088/1361-6560/ac0587.

[86] W. Krüger et al. "LGAD technology for HADES, accelerator and medical applications." In: *Nucl. Instrum. Meth. A* 1039 (2022), p. 167046. DOI: 10.1016/j.nima.2022.167046.

[87] V. Monaco et al. "Performance of LGAD strip detectors for particle counting of therapeutic proton beams." In: *Physics in Medicine & Biology* 68.23 (2023), p. 235009. DOI: 10.1088/1361-6560/ad02d5.

[88] R. S. Quimby. "Photodiode Detectors." In: *Photonics and Lasers*. John Wiley & Sons, Ltd, 2006. Chap. 14, pp. 249–279. DOI: 10.1002/0471791598.ch14.

[89] G. Pellegrini et al. "Technology developments and first measurements of Low Gain Avalanche Detectors (LGAD) for high energy physics applications." In: *Nucl. Instrum. Meth. A* 765 (2014), pp. 12–16. DOI: 10.1016/j.nima.2014.06.008.

[90] H. F.-W. Sadrozinski, A. Seiden, and N. Cartiglia. *4-Dimensional Tracking with Ultra-Fast Silicon Detectors*. 2017. arXiv: 1704.08666 [physics.ins-det].

[91] N. Cartiglia et al. "Tracking in 4 dimensions." In: *Nucl. Instrum. Meth. A* 845 (2017). Ed. by G. Badurek et al., pp. 47–51. DOI: 10.1016/j.nima.2016.05.078.

[92] H. F.-W. Sadrozinski et al. "Sensors for ultra-fast silicon detectors." In: *Nucl. Instrum. Meth. A* 765 (2014), pp. 7–11. DOI: 10.1016/j.nima.2014.05.006.

[93] *Technical Proposal: A High-Granularity Timing Detector for the ATLAS Phase-II Upgrade*. Tech. rep. Geneva: CERN, 2018. URL: https://cds.cern.ch/record/2623663.

[94] N. Cartiglia et al. "Beam test results of a 16 ps timing system based on ultra-fast silicon detectors." In: *Nucl. Instrum. Meth. A* 850 (2017), pp. 83–88. DOI: 10.1016/j.nima.2017.01.021.

[95] W. Riegler and G. Aglieri Rinella. "Time resolution of silicon pixel sensors." In: *Journal of Instrumentation* 12.11 (2017), P11017–P11017. DOI: 10.1088/1748-0221/12/11/p11017.

[96] N. Cartiglia et al. "Design optimization of ultra-fast silicon detectors." In: *Nucl. Instrum. Meth. A* 796 (2015), pp. 141–148. DOI: 10.1016/j.nima.2015.04.025.

[97] M. Ferrero et al. *An Introduction to Ultra-Fast Silicon Detectors: Design, Tests, and Performances*. 2021. DOI: 10.1201/9781003131946.

[98] X. Yang et al. "Layout and performance of HPK prototype LGAD sensors for the High-Granularity Timing Detector." In: *Nucl. Instrum. Meth. A* 980 (2020), p. 164379. DOI: 10.1016/j.nima.2020.164379.

[99] W. Shockley. "Currents to Conductors Induced by a Moving Point Charge." In: *Journal of Applied Physics* 9.10 (1938), pp. 635–636. DOI: 10.1063/1.1710367.

[100] S. Ramo. "Currents Induced by Electron Motion." In: *Proceedings of the IRE* 27.9 (1939), pp. 584–585. DOI: 10.1109/JRPROC.1939.228757.

[101] W. Stolz. *Radioaktivität*. Vieweg+Teubner Verlag Wiesbaden, 1996.

[102] N. Cartiglia et al. "Beam test results of a 16ps timing system based on ultra-fast silicon detectors." In: *Nucl. Instrum. Meth. A* 850 (2017), pp. 83–88. DOI: 10.1016/j.nima.2017.01.021.

[103] V. Gkougkousis. *UcscSingleChannel*. URL: https://twiki.cern.ch/twiki/bin/view/Main/UcscSingleChannel (visited on Apr. 17, 2024).

[104] F. Carnesecchi et al. "Beam test results of 25 and 35 µm thick FBK ultra-fast silicon detectors." In: *The European Physical Journal Plus* 138.1 (2023), p. 99. DOI: 10.1140/epjp/s13360-022-03619-1.

[105] F. Carnesecchi et al. "Development of ultra fast silicon detector for 4D tracking." In: *Nucl. Instrum. Meth. A* 936 (2019), pp. 608–611. DOI: 10.1016/j.nima.2018.09.110.

[106] H. F.-W. Sadrozinski. *Timing Measurements on Ultra-fast Silicon Detectors.* Talk presented at the 12th "Trento" Workshop on Advanced Silicon Radiation Detectors, Trento. URL: https://indico.cern.ch/event/587631/contributions/2471694/ (visited on May 29, 2024).

[107] A. Vakili et al. "Analysis of the performance of low gain avalanche diodes for future particle detectors." In: *Journal of Instrumentation* 18.07 (2023), P07052. DOI: 10.1088/1748-0221/18/07/P07052.

[108] W. Klempt. "Review of particle identification by time of flight techniques." In: *Nucl. Instrum. Meth. A* 433.1 (1999), pp. 542–553. DOI: 10.1016/S0168-9002(99)00323-X.

[109] M. C. S. Williams. "Particle identification using time of flight." In: *Journal of Physics G: Nuclear and Particle Physics* 39.12 (2012), p. 123001. DOI: 10.1088/0954-3899/39/12/123001.

[110] R. R. Wilson. "Radiological use of fast protons." In: *Radiology* 47 (1946), pp. 487–491. DOI: 10.1148/47.5.487.

[111] A. R. Smith. "Proton therapy." In: *Physics in Medicine & Biology* 51.13 (2006), R491. DOI: 10.1088/0031-9155/51/13/R26.

[112] E. Clements. *A new kind of detector technology that could lead to discoveries in particle physics may also lead to better 3D images of the human body and help cancer patients.* URL: https://www.symmetrymagazine.org/article/april-2012/pursuing-protons-medical-imaging (visited on Dec. 1, 2024).

[113] M. Yang et al. "Comprehensive analysis of proton range uncertainties related to patient stopping-power-ratio estimation using the stoichiometric calibration." In: *Physics in Medicine & Biology* 57.13 (2012), p. 4095. DOI: 10.1088/0031-9155/57/13/4095.

[114] U. Schneider and E. Pedroni. "Proton radiography as a tool for quality control in proton therapy." In: *Medical Physics* 22.4 (1995), pp. 353–363. DOI: 10.1118/1.597470.

[115] M. Esposito et al. "CMOS Active Pixel Sensors as energy-range detectors for proton Computed Tomography." In: *Journal of Instrumentation* 10.06 (2015), p. C06001. DOI: 10.1088/1748-0221/10/06/C06001.

[116] I. Schilling. "From High Energy Physics to Hospital — Investigation of the ATLAS IBL Pixel Detector for Applications in Proton Therapy." PhD thesis. Technische Universität Dortmund, 2023.

[117] G. Pausch et al. "Scintillator-Based High-Throughput Fast Timing Spectroscopy for Real-Time Range Verification in Particle Therapy." In: *IEEE Transactions on Nuclear Science* 63.2 (2016), pp. 664–672. DOI: 10.1109/TNS.2016.2527822.

[118] IBA Proton Therapy. *Westdeutsches Protonentherapiezentrum Essen*. URL: https://www.iba-protontherapy.com/iba-center/westdeutsches-protonentherapiezentrum-essen-0 (visited on Dec. 1, 2024).

[119] Universitätsmedizin Essen - Westdeutsches Protonentherapiezentrum (WPE). *Die Protonentherapie: Eigenschaften und Wirkung*. URL: https://www.wpe-uk.de/eigenschaften-und-wirkung/ (visited on Dec. 1, 2024).

[120] Pololu Robotics & Electronics. *Stepper Motor: Bipolar, 200 Steps/Rev, 42×38mm, 2.8V, 1.7 A/Phase*. URL: https://www.pololu.com/product/2267 (visited on Nov. 10, 2024).

[121] Pololu Robotics & Electronics. *A4988 Stepper Motor Driver Carrier*. URL: https://www.pololu.com/product/1182 (visited on Nov. 10, 2024).

[122] S. Spannagel et al. "Allpix2: A modular simulation framework for silicon detectors." In: *Nucl. Instrum. Meth. A* 901 (2018), pp. 164–172. DOI: 10.1016/j.nima.2018.06.020.

[123] C. Bäumer et al. "Measurement of absolute activation cross sections from carbon and aluminum for proton therapy." In: *Nucl. Instrum. Meth. B* 440 (2019), pp. 75–81. DOI: 10.1016/j.nimb.2018.11.020.

[124] I. Schilling et al. "Characterization of pixelated silicon detectors for daily quality assurance measurements in proton therapy." In: *Journal of Physics: Conference Series* 2374.1 (2022), p. 012178. DOI: 10.1088/1742-6596/2374/1/012178.

[125] I. Schilling et al. "Measuring the Beam Energy in Proton Therapy Facilities Using ATLAS IBL Pixel Detectors." In: *Instruments* 6.4 (2022). DOI: 10.3390/instruments6040080.

[126] Geant4 Collaboration. *QGSP_BIC*. URL: https://geant4-userdoc.web.cern.ch/UsersGuides/PhysicsListGuide/html/reference_PL/QGSP_BIC.html (visited on Nov. 20, 2024).

[127] F. Ulrich-Pur et al. "Feasibility study of a proton CT system based on 4D-tracking and residual energy determination via time-of-flight." In: *Physics in Medicine & Biology* 67.9 (2022), p. 095005. DOI: 10.1088/1361-6560/ac628b.

[128] A. Vignati et al. "A new detector for the beam energy measurement in proton therapy: a feasibility study." In: *Physics in Medicine & Biology* 65.21 (2020), p. 215030. DOI: 10.1088/1361-6560/abab58.

[129] R. Sacchi et al. "Test of innovative silicon detectors for the monitoring of a therapeutic proton beam." In: *Journal of Physics: Conference Series* 1662.1 (2020), p. 012002. DOI: 10.1088/1742-6596/1662/1/012002.

[130] O. A. M. Villarreal et al. "Characterization of large LGAD sensors for proton counting in particle therapy." In: *Journal of Instrumentation* 17.09 (2022), p. C09022. DOI: 10.1088/1748-0221/17/09/C09022.

Danksagung

An dieser Stelle möchte ich mich bei einer Reihe von Menschen bedanken, ohne die diese Arbeit nicht möglich gewesen wäre.
An erster Stelle natürlich meinem Erstgutachter, Herrn Prof. Dr. Kröninger, an dessen Lehrstuhl ich die Möglichkeit bekommen habe, über dieses Thema schreiben zu können. Vielen Dank, dass Sie auch unter den seltsamsten Umständen optimistisch bleiben und auch eine lange verschollene Doktorandin wieder auf den richtigen Weg zum Abschluss gebracht haben. Vielen Dank auch an Herrn Prof. Dr. Dr. Rhode für die spontane Bereitschaft, diese Arbeit zu korrigieren und zu bewerten.

Dem gesamten Lehrstuhl E4 bin ich für die angenehme Atmosphäre sehr dankbar. Mike und Andrea, euch gilt mein Dank für alles, was mir organisatorisch oder technisch sonst über den Kopf gewachsen wäre. Ohne euch kann keine Abschlussarbeit beendet werden und ihr wisst garantiert, dass ihr so unendlich viel wichtiger seid als alles LehrbuchWissen, um eine Abschlussarbeit fertigstellen zu können! Insbesondere bevor das soziale Leben durch eine globale Pandemie auf den Kopf gestellt wurde, haben Kuchenrunden, Eispausen im Sommer und gute Gespräche im Büro dafür gesorgt, dass ich auch in schwierigen Zeiten weitermachen wollte. Hier sind vor allem meine langjährigen Bürokollegen Mareike, Felix und Mike zu nennen, die mich direkt am Anfang meiner Masterarbeit zum DESY geschleppt haben. Dadurch hatte ich einen Narren an der Halbleiterphysik gefressen und bin einfach noch viele weitere Jahre geblieben. Und vielen Dank auch an Christopher und Marta, die diese Arbeit fleißig mit guten Kommentaren versehen haben!
Gute Kollegen machen einem das Leben leichter während der Promotion, aber jede Doktorarbeit braucht die richtige Betreuung. Den Löwenanteil hatte dabei im Tagesgeschäft Jens. Ohne Deinen Input, Deine Korrekturen, Deine Bereitschaft für Diskussionen und Deine emotionale Aufbauarbeit wäre diese Arbeit garantiert noch immer nur eine halbfertige Datei auf meinem Computer! Daher gilt Dir das allergrößte Dankeschön - und die neu geschaffene Bezeichnung als mein “Doktor-Onkel”.

Die Daten, die in dieser Arbeit dargestellt sind (und noch zusätzlich viel mehr, die es nicht in die Arbeit geschafft haben), wurden mit sehr vielen Menschen zusammen während verschiedener Messungen aufgenommen. Ob im Labor in Dortmund, am DESY in Nachtschichten oder am WPE, ein großes Dankeschön an alle Datensammler, Testbeam-Koordinatoren und psychologische Beistände in viel zu langen

Nachtschichten: Koji, Jörn, Marco, Francesco, Sebastian, Christopher, Silke, Tobias, Maria, Marius, Alina, Max ... Solche Datenmengen lassen sich nicht mal eben generieren und alleine hätte ich keine Chance gehabt.

Neben der Arbeit habe ich natürlich auch noch ein Leben, auch wenn es manchmal so schien, als würde dafür nicht mehr viel Zeit bleiben. In diesem Teil meines Lebens hat mich meine Familie immer unterstützt, sei es mit Essen, aufmunternden Worten oder einem geschwisterlichen Wettstreit um den ersten Doktortitel der Familie - den ich leider verloren habe. Eine besondere Erwähnung hat sich dabei meine Tante Bärbel verdient, die mir in für mich sehr wichtigen Momenten den unbedingt notwendigen verbalen Tritt in den Hintern gegeben hat. Wenn ich Dir nicht versprochen hätte, etwas zu schreiben, dann hätte ich es wohl auch nicht gemacht!
Vielen Dank auch an meine Freunde, dass sie sich jahrelang mein Gejammer angehört haben, aber auch immer gute Durchhalteparolen vorbringen konnten. Ich verspreche, ab jetzt nie wieder über die Doktorarbeit zu meckern und nur noch Urlaubstipps auszutauschen ;)

Alex ... von allen hier genannten Personen hast Du mit mir wohl am meisten durchgemacht. Du hast mich in allen Phasen (von himmelhoch jauchzend bis zu Tode betrübt, von euphorisch lose Fäden zusammensuchend wie ein hektisches Eichhörnchen kurz vor Wintereinbruch bis lethargisch auf dem Sofa liegend, weil ich mit der Arbeit abgeschlossen hatte) erlebt und ertragen, was wohl gleichzeitig der Vorteil und Nachteil einer Ehe ist. Nachdem wir uns vor dreißig schon den Lebenstraum vom Wohnen am Strand erfüllt haben, bin ich gespannt, was wir jetzt noch anfangen werden! Ab jetzt bin ich auch wieder mit meiner ungeteilten Aufmerksamkeit dabei - versprochen!

A Additional Measurements for the ITk Market Survey

A.1 Measurements of Complete Wafers

Table A.1: List with all detected defects on structures of the thin wafer at reception. SC indicates sensors with the single chip size, DC refers to the double chip size and Q stands for the quads. The letter 'n' is used, if no defects are found.

sensor	residues of liquids	scratches		short-circuited pixels
		$< 5\,\mathrm{mm}$	$> 5\,\mathrm{mm}$	
SC1	n	1	n	n
SC8	n	3	n	9
SC10	n	n	n	2
SC15	n	n	n	2
DC2	n	n	n	11
DC7	y	n	n	n
DC9	y	n	n	n
Q1	y	n	n	n
Q2	n	n	n	2

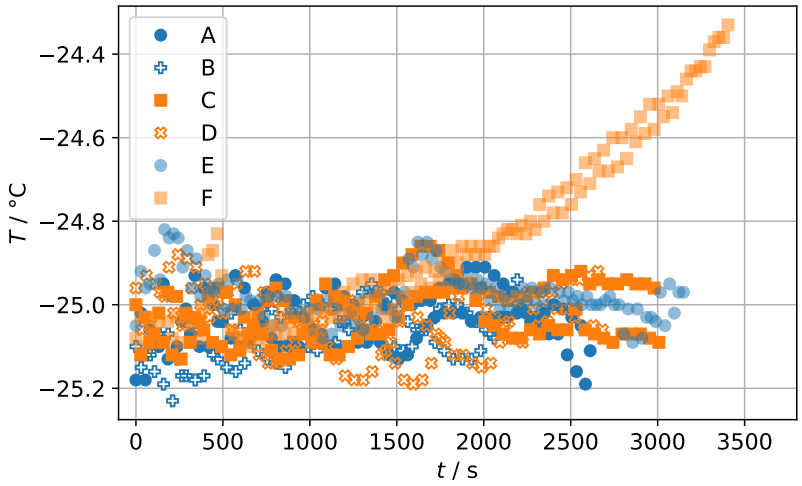

(a) Measured temperature during the IV scan for the different irradiated sensors. The temperature refers to the measured temperature by that PT1000 sensor which is closest to the investigated sensor. Within the market survey it was decided that a deviation of $\pm 1\,°C$ from the desired temperature of the sensor of $T_{\text{sensor}} = -25\,°C$ is accepted. During all measurements this requirement is fulfilled.

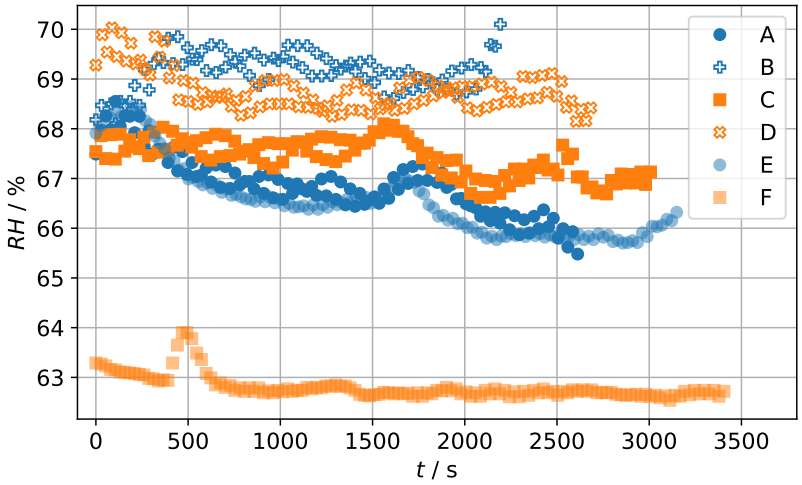

(b) Measured relative humidity during the IV scan for the different irradiated sensors. The requirement for the market survey is a relative humidity below 50% which is not fulfilled with any measurement.

Figure A.1: Measured data for **(a)** the environmental values of the temperature and the **(b)** relative humidity during the IV scans of the irradiated sensors.

Table A.2: List with all detected defects on structures of the thick wafer at reception. SC indicates sensors with the single chip size, DC refers to the double chip size and Q stands for the quads. The letter 'n' is used, if no defects are found.

sensor	residues of liquids	scratches		short-circuited pixels
		$< 5\,\mathrm{mm}$	$> 5\,\mathrm{mm}$	
SC1	n	6	n	n
SC3	n	n	n	3
SC4	n	1	n	n
SC8	n	1	n	n
SC16	n	n	n	3
DC4	n	1	n	n
DC7	y	3	n	n
DC8	n	n	n	3
DC9	y	n	n	n
Q1	y	n	n	20
Q2	n	n	n	3
Q3	n	5	2	n

Table A.3: List with all detected defects on structures of the thin wafer after all measurements are performed. SC indicates sensors with the single chip size, DC refers to the double chip size and Q stands for the quads. The letter 'n' is used, if no defects are found. The numbers in brackets give the difference to the detected quantities at reception and a dash within the brackets indicates no change at all.

sensor	residues of liquids	scratches		short-circuited pixels
		$< 5\,\mathrm{mm}$	$> 5\,\mathrm{mm}$	
SC1	n	4 (+3)	n	n
SC4	n	1 (+1)	n	n
SC7	n	1 (+1)	n	n
SC8	n	3 (-)	n	9 (-)
SC10	n	2 (+2)	n	2 (-)
SC12	n	1 (+1)	n	n
SC13	n	1 (+1)	n	n
SC15	n	1 (+1)	n	2 (-)
DC1	n	1 (+1)	n	n
DC2	n	n	n	17 (+6)
DC4	n	1 (+1)	n	n
DC5	n	1 (+1)	n	n
DC6	n	1 (+1)	n	n
DC7	y (-)	1 (+1)	n	n
DC8	n	1 (+1)	n	n
DC9	y (-)	n	n	n
Q1	y (-)	1 (+1)	n	n
Q2	n	n	n	2 (-)
Q3	n	1 (+1)	n	n

Table A.4: List with all detected defects on structures of the thick wafer after all measurements are performed. SC indicates sensors with the single chip size, DC refers to the double chip size and Q stands for the quads. The letter 'n' is used, if no defects are found. The numbers in brackets give the difference to the detected quantities at reception and a dash within the brackets indicates no change at all.

sensor	residues of liquids	scratches		short-circuited pixels
		$< 5\,\mathrm{mm}$	$> 5\,\mathrm{mm}$	
SC1	n	6 (-)	n	n
SC3	n	n	n	3 (-)
SC4	n	1 (-)	n	n
SC5	n	1 (+1)	n	n
SC8	n	1 (-)	n	n
SC13	n	1 (+1)	n	n
SC14	n	1 (+1)	n	n
SC16	n	1 (+1)	n	3 (-)
DC1	n	1 (-)	n	n
DC4	n	1 (-)	n	n
DC6	n	1 (+1)	n	n
DC7	y (-)	5 (+2)	n	n
DC8	n	n	n	3 (-)
DC9	y (-)	1 (+1)	n	n
DC10	n	2 (+2)	n	n
Q1	y (-)	1 (+1)	n	20 (-)
Q2	n	1 (+1)	n	3 (-)
Q3	n	6 (+1)	2 (-)	n

Table A.5: Fit parameters of the straight line fits to determine the misalignment of the chuck during the height measurements. The fit procedure uses the *scipy.curve_fit* function with the formula $y = a \cdot x + b$. Moreover, the measurement uncertainties of $\pm 3\,\mu m$ for the heights are taken into account. The values refer to the five horizontal and vertical line scans for the thin and thick wafer.

wafer	line scan	slope a / 1×10^{-5}	vertical intercept b / µm
thin	horizontal 1	-0.5 ± 0.4	0.4 ± 0.5
	horizontal 2	-2.5 ± 0.4	0.9 ± 0.5
	horizontal 3	0.0 ± 0.4	0.3 ± 0.5
	horizontal 4	1.1 ± 0.4	-2.1 ± 0.5
	horizontal 5	1.7 ± 0.4	-1.8 ± 0.5
	vertical 1	0.5 ± 0.4	-0.8 ± 0.5
	vertical 2	-1.3 ± 0.4	-0.6 ± 0.5
	vertical 3	-1.4 ± 0.4	-0.9 ± 0.5
	vertical 4	1.6 ± 0.4	-1.2 ± 0.5
	vertical 5	5.0 ± 0.4	-6.1 ± 0.5
thick	horizontal 1	-3.9 ± 0.4	5.0 ± 0.5
	horizontal 2	-4.4 ± 0.4	4.3 ± 0.5
	horizontal 3	-0.6 ± 0.4	0.9 ± 0.5
	horizontal 4	-1.7 ± 0.4	2.0 ± 0.5
	horizontal 5	3.1 ± 0.4	-3.1 ± 0.5
	vertical 1	-3.1 ± 0.4	1.5 ± 0.5
	vertical 2	-3.1 ± 0.4	1.2 ± 0.5
	vertical 3	-2.1 ± 0.4	1.5 ± 0.5
	vertical 4	-1.0 ± 0.4	0.8 ± 0.5
	vertical 5	3.4 ± 0.4	-3.2 ± 0.5

Table A.6: Fit parameters of the straight line fits to determine the misalignment of the chuck during the measurements of the bow. The fit procedure uses the *scipy.curve_fit* function with the formula $y = a \cdot x + b$. Moreover, the measurement uncertainties of $\pm 3\,\mu m$ for the heights are taken into account. The values refer to the five horizontal and vertical line scans for the thin and thick wafer.

wafer	line scan	slope a / 1×10^{-5}	vertical intercept b / µm
thin	horizontal 1	-1.9 ± 0.4	0.4 ± 0.5
	horizontal 2	-1.8 ± 0.4	0.2 ± 0.5
	horizontal 3	1.2 ± 0.4	-2.1 ± 0.5
	horizontal 4	0.4 ± 0.4	-1.5 ± 0.5
	horizontal 5	2.6 ± 0.4	-2.8 ± 0.5
	vertical 1	0.9 ± 0.4	-1.2 ± 0.5
	vertical 2	-1.0 ± 0.4	-0.8 ± 0.5
	vertical 3	-1.2 ± 0.4	-1.5 ± 0.5
	vertical 4	1.4 ± 0.4	-1.2 ± 0.5
	vertical 5	4.2 ± 0.4	-5.2 ± 0.5
thick	horizontal 1	-2.9 ± 0.4	2.3 ± 0.5
	horizontal 2	-3.2 ± 0.4	3.1 ± 0.5
	horizontal 3	-0.5 ± 0.4	1.5 ± 0.5
	horizontal 4	-1.0 ± 0.4	0.6 ± 0.5
	horizontal 5	1.4 ± 0.4	-1.3 ± 0.5
	vertical 1	-0.4 ± 0.4	1.2 ± 0.5
	vertical 2	-1.6 ± 0.4	-0.2 ± 0.5
	vertical 3	-1.3 ± 0.4	-0.6 ± 0.5
	vertical 4	-0.7 ± 0.4	-1.6 ± 0.5
	vertical 5	4.4 ± 0.4	-6.6 ± 0.5

A.2 Measurements of Diced Sensors

This section presents the measurements and results for an additional vendor that delivered diced sensors for the ITk market survey. The vendor delivered the required 20 double chip size sensors (DCs) and 10 single chip size sensors (SCs). These sensors have a nominal thickness of 150 µm. As a characteristic of this manufacturer, all sensors feature at least two different pixel designs. The main difference is the biasing scheme, so that half of the pixels of each sensor are biased using polysilicon bias resistors. Another difference is the size of the pixel implants. However, the different pixel sizes are only implemented on the SCs. Additionally, these sensors have under bump metallisation (UBM), whose quality has to be checked during the visual inspection.

A.2.1 Visual Inspection

The quality of the 30 delivered sensors has to be checked immediately upon receipt. As these sensors come with UBM, special attention is paid to the quality of the UBM during the visual inspection. To document the UBM status, the sensors are photographed with an optical microscope with a hundredfold magnification. With the same magnification, the entire surface of each sensor is observed to detect any striking features or damages. The defects and irregularities are documented with with even higher magnification photographs.

A detailed list of the detected permanent defects found on each sensor at reception is presented in Table A.7. Special attention should be paid to the size of the detected scratches. Compared to the wafers (see subsection 3.2.1), the average size of the scratches is one order of magnitude smaller. This smaller value to class the scratches is chosen, because the diced sensors have only been at the vendor before, so less damage is expected. Another difference is that none of the diced sensors show any liquid residue or short-circuited pixels. Therefore, these categories are not listed in Table A.7.

All of the detected scratches are only on the edges of the sensors, so none of them touch the pixel matrix. In addition, most of these scratches with sizes smaller than 0.5 mm are point like. Therefore, no severe effect on the behaviour of the sensors is expected from them.
The numbers for the pixels with damaged UBM pads refer to pixels where the UBM appears to be either dirty or smeared. A picture of such a region with damaged UBM pads is shown in Figure A.2a. These regions are noticeable during the investigation under the optical light microscope as the reflection of the light is different there. Overall, there are no missing UBM pads or short circuits between two adjacent

Table A.7: List with all detected permanent defects on the diced sensors at reception. SC indicates sensors with the single chip size, DC refers to the double chip size. The letter 'n' is used, if no defects are found.

sensor	scratches		damaged UBM
	$< 0.5\,\mathrm{mm}$	$> 0.5\,\mathrm{mm}$	
SC1	4	n	45
SC2	1	n	n
SC3	4	n	n
SC4	2	n	n
SC5	n	n	5
SC6	4	n	n
SC7	6	n	7
SC9	3	n	n
SC10	2	n	n
DC1	6	n	12
DC2	2	n	22
DC3	3	n	2
DC4	3	n	54
DC5	9	n	n
DC6	3	n	30
DC7	2	n	41
DC8	1	n	49
DC9	4	n	54
DC10	15	n	1
DC11	3	n	n
DC12	6	n	35
DC13	7	n	55
DC14	6	n	n
DC15	3	n	n
DC16	8	n	1
DC17	3	n	n
DC18	2	n	6
DC19	n	n	3
DC20	n	n	6

pixels on any of the sensors. The largest number of damaged UBM pads on a SC is observed for SC1, where approximately 45 pixels are affected. This is compared to the total number of pixels on an SC ($400 \times 192 = 76800$) only 0.05%. Within the market survey, a percentage of up to 0.1% of pixels with damaged UBM pads is accepted. This SC is therefore rated good. For the DCs, DC13 has the most damaged UBM pads. Since a double chip has about twice as many pixels as a SC, the percentage of damaged UBM pads compared to the total number of UBM pads is again small enough for the DC to be rated as good as well.
The edges of the diced sensors are very sharp. Only for one sensor there is a chipped edge detected which is shown in Figure A.2b. This crack has a length of approximately 150 µm and is in the lower left corner of the sensor SC10. The market survey disregards sensors with chips larger than 40 µm. However, this value refers to the length of the chip perpendicular to the direction of the dicing line. Since the detected chip is parallel to the dicing line and not that large in the direction towards the pixel matrix, the presence of the chip does not affect the status of this chip as good for the visual inspection. Since chips at the edges of a sensor can affect the current-voltage characteristics of a sensor by allowing a current to flow across the edge, the sensor with the chip must be investigated carefully during the electrical measurements.
To summarise the results, the diced sensors are of very good quality overall and all are considered good in terms of the requirements of the market survey. Nevertheless, the UBM seems to be very sensitive. On some sensors, traces can be seen in the overall photograph that indicate non-uniform UBM pads. However, in close-ups of the traces, no obvious difference can be seen between pixels within and outside the trace. Therefore, it is assumed that the UBM pad quality will get worse during handling the sensors and particularly prudent handling is necessary.

The sensors are placed in small gel packs for shipping, from which they need to be detached for the measurements of their electrical behaviour. Therefore, they need to be lifted out of the gel pack. Unfortunately, the placement of the sensors inside the gel pack is very tight, as it is shown in Figure A.3. The average spacing between two sensors is less than 2 mm, in some cases it is only about 1.6 mm. This does not leave much room for any tool to help lifting the sensors.

To ease lifting the sensors, there are three options tested. The first, intuitive solution is the usage of vacuum tweezers. However, this comes with the downside of damaging the UBM pads by the rubber nozzles of the vacuum tweezers. Such round marks from a circular shaped rubber nozzle is shown in Figure A.4a. Additionally, since the nozzles are only pushed onto the metal tube of the vacuum tweezers, the nozzles sometimes ride up the metal tube and the tube then touches the sensor surface. This leads to severe scratches in the pixel matrix which do not destroy only the metallisation of the UBM pads, but also the layers beneath. Such a deep scratch

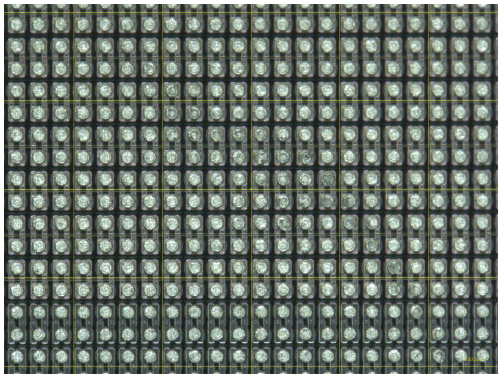

(a) Non-uniform UBM, 300x magnification.

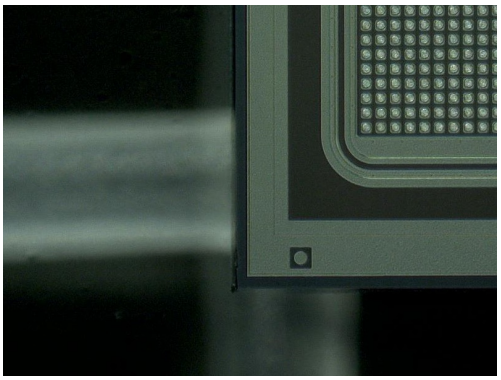

(b) Close-up of a chipped edge, 100x magnification.

Figure A.2: Photographs of observed defects and anomalies on delivered diced sensors. The rectangular pixels on the left have a size of 25 µm × 100 µm, the square pixels on the right have a pitch of 50 µm × 50 µm. These sizes can serve for scaling within the photographs.

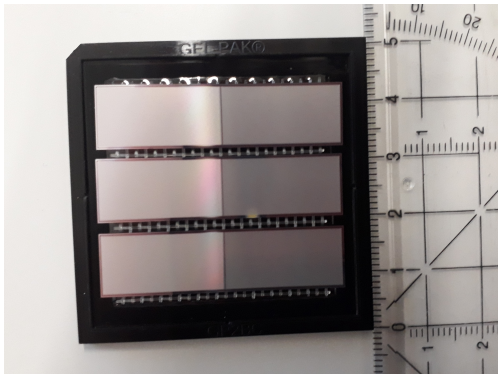

(a) Gel pack used for shipping.

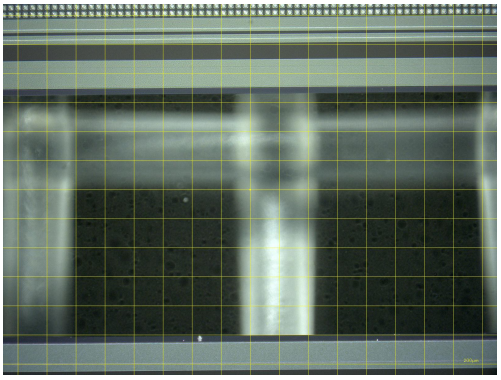

(b) Close-up of two sensors in gel pack.

Figure A.3: Photographs of the diced DC sensors in the gel pack used for shipping. In **(a)** a centimetre ruler is placed next to the gel pack to emphasise the small gap between the sensors. In **(b)** a picture taken with an optical microscope and a yellow grid with the edge lengths of 200 µm is displayed.

is shown in Figure A.4b. Since the usage of vacuum tweezers comes with many disadvantages, they are not used after testing this method to prevent damaging the UBM pads on more sensors.
Another attempt was the usage of regular plastic or metal tweezers. Since the sensor surface should not be touched with anything, the tips of the tweezers have to be wrapped around the sensor. However, this is particularly difficult, because the width between the tips of the used tweezers is smaller than the width of the sensor. Therefore, the tips have to be manually pressed apart from each other to be wrapped around the sensor edges. This comes with the downside, that if one of the tips slips off the edge, the tips move towards each other and scratch in that way across the sensor surface. A photograph of such a scratch is shown in Figure A.4c. It can be clearly seen, that the UBM pads are damaged and in some cases the metallisation of the UBM pads is smeared together (visible at the bottom of the scratch in the photograph). As a consequence, regular tweezers are not used to lift the sensors, because the damage is too severe.
The third and last tested option is to form a small tray with a piece of paper or Kapton, that is then slid beneath the sensor. Since Kapton pieces seem to be more stable than pieces of paper, a tray of paper was only tested once. The disadvantage of this technique is the fact, that the piece of Kapton has to be broader than the sensor width. Therefore, the formed tray may touch the neighbouring sensors inside the gel pack. Especially if it is handled unwarily, the piece of Kapton can scratch across the sensor surface and lead to large-scale damage of the UBM pads. An overview of such damaged UBM pads is shown in Figure A.4d. In contrast to the scratches caused by the metal tube of the vacuum tweezers and the regular tweezers, there is only the damaged metallisation of the UBM pads, but no deeper scratch is done.

During the testing of the usage of the different tools for handling the sensors, some of the DCs are damaged. The vacuum tweezer was tested only on DC3, which shows marks of the rubber nozzle and especially deep scratches caused by the metal tube of the vacuum tweezers. Another DC (DC5) was damaged by a plastic tweezer, whose tip scratched across the pixel matrix and DC1 was accidently touched by a metal tweezer when sensor DC2 was meant to be lifted. However, the metal tweezers were also tested on DC1, where a slipping of the tweezers lead to a slip mark on the DC as well as a chip at the bottom of this sensor. Nevertheless, the most damaged sensor is DC2, where metal tweezers were tested again and left three scratch marks. In addition, this sensor was touched by a piece of Kapton, which led to the large-scale damaged UBM pads shown in Figure A.4d. Since the disadvantages of the usage of tweezers in any form are severe deep scratches, it was decided to use the Kapton trays for the lifting of the sensors. After practicing the handling with a piece of Kapton and dummy sensors, none of the other sensors show any signs of severe

(a) Marks from rubber nozzle of vacuum tweezers, 100x magnification.

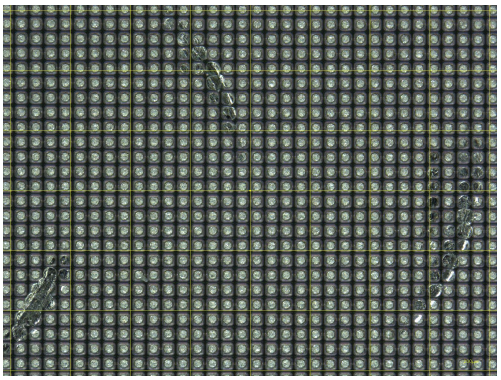

(b) Close-up of scratches by metal tube of vacuum tweezers, 300x magnification.

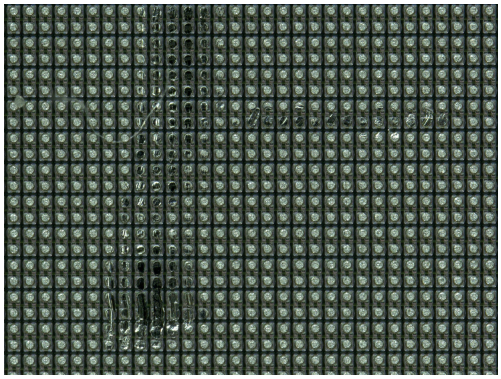

(c) Close-up of scratch due to slipped tweezers tip, 300x magnification.

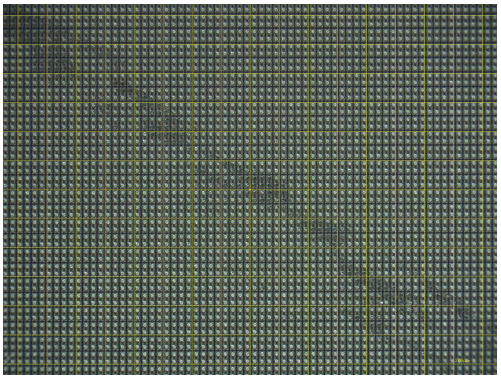

(d) Damaged UBM pads due to touch of Kapton piece, 100x magnification.

Figure A.4: Photographs of observed defects after handling the sensors with different tools.

permanent damage. Nevertheless, cautious handling of these sensors is absolutely necessary.

After all measurements including the electrical tests are finished, a final visual inspection is done to document the new defects on the sensors. A detailed list with the detected damages is shown in Table A.8. It is worth noting, that only those sensors that were discussed before in the paragraph about the difficult handling show severe damages.
For the SC sized sensors, all new scratches are mainly point like, meaning their dimensions are usually smaller than 50 µm × 50 µm. Moreover, these scratches are only at the edges of the sensors, so none of them damages the pixel matrix. In contrast to the scratches of the wafers, there is no scratch in proximity of the contact pad. This is explained by the size of the contact pads, which are for the diced sensors in both directions 1.5 times larger than for the structures on the wafers. Therefore, the needle is much more likely to be placed in the correct location. Since these sensors are only handled with a tray formed out of Kapton, there are no new cracks at the sensor edges. Only one sensor has additionally damaged UBM pads. This can be tracked down to a contact with the Kapton tray. The sensors SC6 and SC9 show a larger number of smaller new scratches. For both sensors, the scratches are at their right side, outside of the pixel matrix and away from the guard rings. Therefore, it is assumed that they do not affect the electrical behaviour of the sensors.
For the DCs number 1, 2, 3 and 5 no new point like scratches smaller than 0.5 mm are taken into account, because these sensors feature severe damage from testing the handling options and those are expected to have a greater influence on their quality. The DC sized sensors DC1 and DC2 that were handled with the metal tweezers, show additionally chips at their edges (nine new chips on DC1 and seven chips on DC2). However, only for DC1 three of the new chips have a size larger than 50 µm perpendicular to the dicing street, which is the relevant size for the market survey requirement. Since this damage was due to handling issues, this does not affect the qualification of the manufacturer. The DCs number 1, 2, 3 and 5 show a large increase in the number of damaged UBM pads. All of these are caused by scratches that are received during handling. Especially DC2 shows a large increase of more than 1700 new damaged UBM pads. A great amount of these (around 1500) are caused by the scratches by the Kapton tray. The other damaged UBM pads (even for DC4 and DC13) are due to scratches from tweezers. Since for the DCs with numbers greater than 5 no handling testing was performed, they show usually a much better trend. The main part of the scratches are only smaller than 0.5 mm and all are located at the edges of the sensors.

Table A.8: List with all detected permanent defects on the diced sensors during the final visual inspection. SC indicates sensors with the single chip size, DC refers to the double chip size. The letter 'n' is used, if no defects are found. The numbers in brackets give the difference to the detected quantities at reception and a dash within the brackets indicates no change at all.

sensor	scratches		damaged UBM
	$< 0.5\,\mathrm{mm}$	$> 0.5\,\mathrm{mm}$	
SC1	4 (-)	n	45 (-)
SC2	1 (-)	n	n
SC3	6 (+2)	n	4 (+4)
SC4	2 (-)	n	n
SC5	2 (+2)	n	5 (-)
SC6	12 (+8)	n	n
SC7	6 (-)	n	7 (-)
SC8	6 (+6)	n	n
SC9	13 (+10)	n	n
SC10	5 (+3)	n	n
DC1	8 (+2)	4 (+4)	191 (+179)
DC2	5 (+3)	4 (+4)	1790 (+1768)
DC3	5 (+2)	2 (+2)	288 (+286)
DC4	6 (+3)	1 (+1)	88 (+34)
DC5	9 (-)	1 (+1)	420 (+420)
DC6	8 (+5)	n	30 (-)
DC7	2 (-)	n	41 (-)
DC8	3 (+2)	n	49 (-)
DC9	9 (+5)	n	54 (-)
DC10	15 (-)	n	1 (-)
DC11	5 (+2)	n	n
DC12	8 (+2)	n	35 (-)
DC13	14 (+7)	1 (+1)	88 (+33)
DC14	6 (+4)	n	n
DC15	8 (+5)	n	n
DC16	10 (+2)	n	1 (-)
DC17	3 (+1)	n	n
DC18	2 (+4)	n	6 (-)
DC19	5 (+5)	n	3 (-)
DC20	2 (+2)	n	6 (-)

A.2.2 Measurements of Thickness and Bow

The same setup that was described in subsection 3.2.1 for the measurements of the wafers is used to measure the thickness and bow of the diced sensors. Only the chuck to hold the sensors has to be replaced, since the big chuck for whole wafers does not include small structures to hold diced sensors. A properly sized smaller chuck is used, where single chip sized and double chip sized sensors can be hold down. The measurement of the thickness and bow has to be performed for at least two double chip sized sensors. Since the first measurements revealed some unexpected results, four additional sensors are measured to validate those measurements.

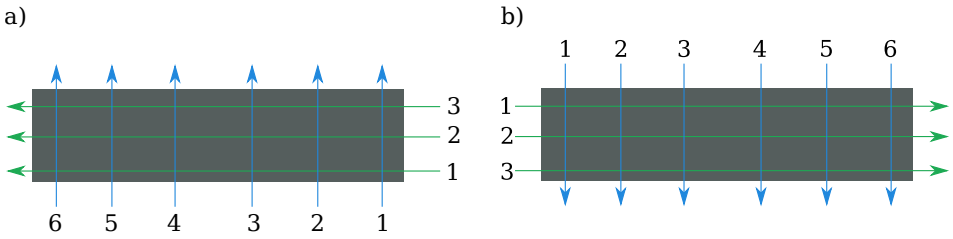

Figure A.5: Distribution of the line scans across the DCs. The scheme under a) is valid for the measurements of DC1 and DC2. The other sensors were measured with the scheme of b). The blue arrows indicate the vertical line scans, while the green arrows symbolise the horizontal measurements. The arrows declare the direction of the measured profile.

The sensors are measured along nine lines, three of them in the horizontal direction and the remaining six in the vertical direction. This large number of vertical scans is chosen, since the DCs feature two pixel designs. Therefore, the layout of the sensor is different on its right and left side. To cover potential differences in the thickness, each side is covered with three vertical line scans. The distribution of the line scans is depicted in Figure A.5.
Since the diced sensors are measured on a different chuck and the taken line scans differ in the proportion of covered chuck length and sensor length, the analysis scheme of the data sets has to be adapted. Firstly, to handle all data sets equally, only the first and last 21 data points are used to fit the chuck. These points equal a measured length of roughly 0.25 mm on each side of the chuck. Since the used chuck features more grooves within close proximity to the sensors, this small range is the only option to treat all line scans equally.
Secondly, the diced sensors do not have large edges of bare silicon. Therefore, there are less reflections at the sensor edges. These regions of reflections have been used in subsection 3.2.1 to define the region of interest (ROI) to determine the requested parameters for the ITk market survey. If in the data set missing values are present due to reflections at bare silicon, the same procedure as for the wafers is used. Then,

the ROI starts roughly 0.5 mm (which results from 42 data points with a spacing of 11.8 µm in the scan direction) after the last gap on the left side of the scan and ends approximately 0.5 mm before the first gap on the right side of the scan. However, if no gaps are in the data set, a sliding window technique is used to determine the edge of the sensor. To do so, a window which covers 30 consecutive data points is moved across the data set and searches for locations where the difference between the first measured height and the last measured height is more than 150 µm. The ROI starts then roughly 0.8 mm after the detection of the sensor edge and ends roughly 0.8 mm before the sensor edge. These values are the result of the 30 data points wide window and a safety margin of additionally 42 data points to exclude possible reflection artefacts, which equal approximately 350 µm and 500 µm respectively.

The results of the analysis for the six measured sensors can be seen in Table A.9, Table A.10 and Table A.11. It is important to note that the measurement directions of the line scans differ between the data sets. The sensors DC3 to DC6 are measured in the same way. However, the first sensors DC1 and DC2 are measured with different distributed line scans. This is shown in Figure A.5.

First of all, the slope for the alignment of the chuck is two orders of magnitude greater than for the wafer measurements (compare with Table A.5 and Table A.6). This is due to the fixture of the smaller chuck which is not properly suited for the mounting plate of the macroscope. Nevertheless, the overall tilting of the chuck is not that relevant, since it does not affect the measurements. In the same way, the high negative values for the vertical intercept of the correction calculation are of no importance. They are caused by the definition of a reference point within the data taking. Since the data is corrected for the chuck misalignment, these values are only relevant for the analysis scheme, but do not affect the relevant parameters for the market survey.
The sensor thickness deviation of the diced sensors should not be more than 15 µm to be accepted within the market survey. For all measurements, the horizontal line scan which covers the top of the sensor (horizontal 3 for DC1 and DC2 and horizontal 1 for the other DCs) and the two vertical line scans in the middle of the sensor (vertical 3 and 4) show the maximum deviations. These maximum deviations are mainly greater than the 15 µm requirement. One example of such a horizontal line scan is shown in Figure A.6. The plot reveals an excess of material or a bump in the middle of the upper half of the sensor. This is also validated within the vertical line scans number 3 and 4 (see Figure A.7). However, there is no reasonable explanation why this is present in the middle of the sensors. Moreover, as it can be seen in Figure A.6, the right side of the sensor seems to be slightly thicker than the left side of the sensor. This is the same for all measured sensors, so it might be caused by the different pixel designs, which differ on the left and right side of the DC sensors. Since all other measured thickness deviations are within the specifications

and this excess of material seems to be a systematic feature of these sensors, they are still used for further measurements within the market survey.
The nominal thickness of these sensors is known to be about 150 µm. All of the mean measured heights for DC1 and DC2 differ only by 5 µm. Moreover, the measured mean values are between approximately 154 µm and 160 µm for these two sensors, which is maximum 7% thicker than it would be expected. For the other sensors, the measured mean heights of all line scans differ by approximately 10 µm within a single sensor. However, since DC3 to DC6 show the biggest bumps in their profiles, which are seen in the biggest deviations of the measured heights, these higher values are expected. If the problematic line scans with the known bump are excluded from the discussion, the maximum difference of the measured mean heights within a single sensor decreases to roughly 7 µm. In addition, even for those four sensors the maximum additional height to the expected height of 150 µm are only 14 µm. Compared to the expected thickness, this is an excess of roughly 9% which is acceptable in the production process.

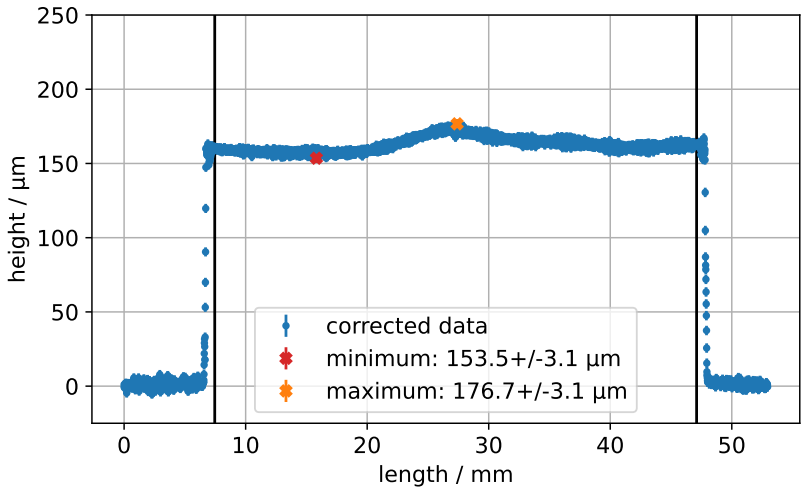

Figure A.6: Corrected data for the height measurement of the first horizontal line scan of the DC4. Each measured value has an uncertainty of approximately 3 µm, which is too small to be easily visible in the plot.

If the vendor delivers diced sensors, it is required to measure the bow of at least two double chip size sensors for the ITk market survey. Since the thickness is measured for six DCs, the same six DCs are used for the measurement of the bow as well. The measurement procedure is the same as for the wafers: the DCs are placed on the chuck, but the vacuum is not applied, and nine line scans are done. The analysis of the taken data follows the same scheme as for the thickness measurement. However,

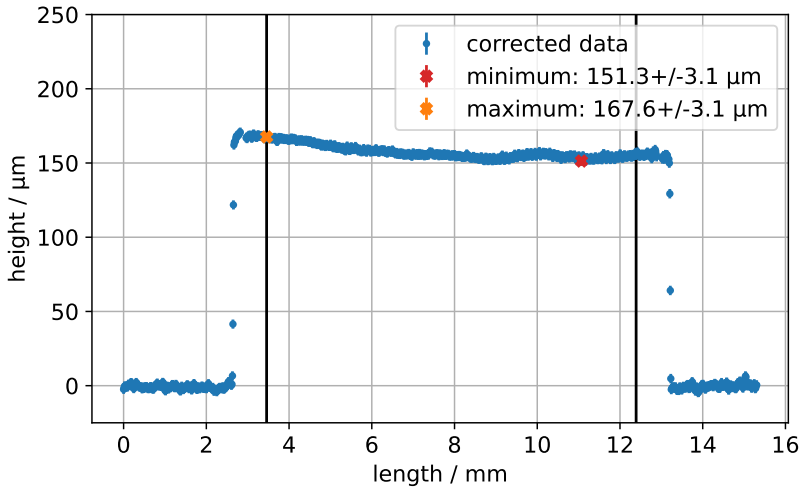

(a) Sixth height profile.

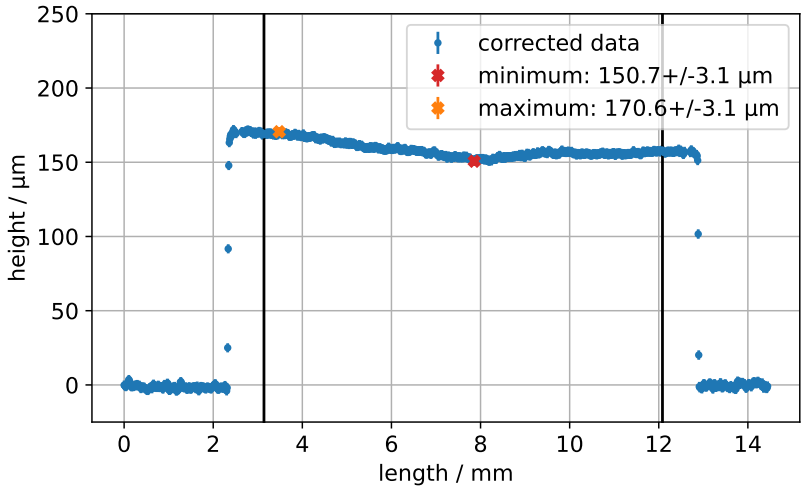

(b) Seventh height profile.

Figure A.7: Corrected data of the height measurements for DC4. The profiles depicted in **(a)** and **(b)**, corresponding to vertical line scans left to the middle and right to the middle respectively, validate a bump on the sensor. Since the scans are performed from the top towards the bottom, it is clearly visible, that the material excess is only present in the top half of the sensor.

Table A.9: Parameters of the analysis of the height measurement of the diced sensors DC1 and DC2. The fit procedure uses the *scipy.curve_fit* function with the formula $y = a \cdot x + b$. Moreover, the measurement uncertainties of $\pm 3\,\mu\text{m}$ for the heights are taken into account. The values refer to the three horizontal and six vertical line scans.

sensor	line scan	slope a / 1×10^{-3}	vertical intercept b / µm	mean height / µm	maximum deviation / µm
DC1	vertical 1	3.08 ± 0.06	-862.2 ± 0.7	155.7 ± 0.8	6 ± 4
	vertical 2	2.96 ± 0.05	-872.3 ± 0.7	154.4 ± 0.8	10 ± 4
	vertical 3	2.97 ± 0.05	-887.3 ± 0.7	158.7 ± 0.8	19 ± 4
	vertical 4	2.87 ± 0.05	-891.7 ± 0.7	156.4 ± 0.8	10 ± 4
	vertical 5	2.78 ± 0.05	-901.2 ± 0.7	155.5 ± 0.8	9 ± 4
	vertical 6	2.96 ± 0.06	-909.2 ± 0.7	156.0 ± 0.8	9 ± 4
	horizontal 1	-1.249 ± 0.019	-845.3 ± 0.7	156.4 ± 0.8	13 ± 4
	horizontal 2	-1.250 ± 0.019	-832.2 ± 0.7	156.0 ± 0.8	14 ± 4
	horizontal 3	-1.266 ± 0.019	-820.0 ± 0.7	159.2 ± 0.8	17 ± 4
DC2	vertical 1	2.82 ± 0.06	-708.4 ± 0.7	157.1 ± 0.8	9 ± 4
	vertical 2	3.01 ± 0.05	-713.7 ± 0.7	155.9 ± 0.8	8 ± 4
	vertical 3	2.93 ± 0.06	-722.1 ± 0.7	158.6 ± 0.8	20 ± 4
	vertical 4	3.05 ± 0.06	-725.3 ± 0.7	156.9 ± 0.8	14 ± 4
	vertical 5	3.00 ± 0.05	-732.8 ± 0.7	154.4 ± 0.8	10 ± 4
	vertical 6	2.92 ± 0.06	-733.4 ± 0.7	154.6 ± 0.8	10 ± 4
	horizontal 1	-0.689 ± 0.018	-693.1 ± 0.7	156.1 ± 0.8	18 ± 4
	horizontal 2	-0.713 ± 0.018	-683.0 ± 0.7	157.3 ± 0.8	14 ± 4
	horizontal 3	-0.754 ± 0.018	-668.9 ± 0.7	159.8 ± 0.8	21 ± 4

Table A.10: Parameters of the analysis of the height measurement of the diced sensors DC3 and DC4. The fit procedure uses the *scipy.curve_fit* function with the formula $y = a \cdot x + b$. Moreover, the measurement uncertainties of $\pm 3\,\mu\text{m}$ for the heights are taken into account. The values refer to the three horizontal and six vertical line scans.

sensor	line scan	slope a / 1×10^{-3}	vertical intercept b / µm	mean height / µm	maximum deviation / µm
DC3	horizontal 1	-0.192 ± 0.017	-427.6 ± 0.7	161.0 ± 0.8	23 ± 4
	horizontal 2	-0.143 ± 0.017	-438.8 ± 0.7	156.8 ± 0.8	18 ± 4
	horizontal 3	-0.173 ± 0.017	-451.7 ± 0.7	156.7 ± 0.8	15 ± 4
	vertical 1	-2.94 ± 0.06	-412.2 ± 0.7	151.4 ± 0.8	7 ± 4
	vertical 2	-2.83 ± 0.06	-411.4 ± 0.7	150.5 ± 0.9	7 ± 4
	vertical 3	-2.95 ± 0.06	-416.8 ± 0.7	159.8 ± 0.8	14 ± 4
	vertical 4	-2.74 ± 0.06	-421.3 ± 0.7	157.0 ± 0.8	18 ± 4
	vertical 5	-2.92 ± 6.00	-413.8 ± 0.7	153.8 ± 0.9	9 ± 4
	vertical 6	-2.96 ± 0.06	-419.0 ± 0.7	154.0 ± 0.8	9 ± 4
DC4	horizontal 1	2.744 ± 0.018	-466.4 ± 0.7	162.7 ± 0.8	23 ± 4
	horizontal 2	2.790 ± 0.018	-488.8 ± 0.7	157.2 ± 0.8	13 ± 4
	horizontal 3	2.775 ± 0.017	-508.2 ± 0.7	156.2 ± 0.8	13 ± 4
	vertical 1	-5.05 ± 0.06	-416.6 ± 0.7	153.7 ± 0.8	8 ± 4
	vertical 2	-5.02 ± 0.06	-393.6 ± 0.7	154.0 ± 0.9	6 ± 4
	vertical 3	-5.03 ± 0.06	-376.8 ± 0.7	157.1 ± 0.8	16 ± 4
	vertical 4	-5.12 ± 0.07	-363.8 ± 0.7	158.4 ± 0.8	20 ± 4
	vertical 5	-4.94 ± 0.06	-334.9 ± 0.7	155.3 ± 0.9	9 ± 4
	vertical 6	-5.07 ± 0.06	-317.5 ± 0.7	156.0 ± 0.8	11 ± 4

Table A.11: Parameters of the analysis of the height measurement of the diced sensors DC5 and DC6. The fit procedure uses the *scipy.curve_fit* function with the formula $y = a \cdot x + b$. Moreover, the measurement uncertainties of $\pm 3\,\mu m$ for the heights are taken into account. The values refer to the three horizontal and six vertical line scans.

sensor	line scan	slope a / 1×10^{-3}	vertical intercept b / µm	mean height / µm	maximum deviation / µm
DC5	horizontal 1	2.989 ± 0.018	-595.8 ± 0.7	163.8 ± 0.8	22 ± 4
	horizontal 2	3.026 ± 0.018	-617.3 ± 0.7	157.0 ± 0.8	11 ± 4
	horizontal 3	2.970 ± 0.018	-636.3 ± 0.7	156.9 ± 0.8	11 ± 4
	vertical 1	-5.29 ± 0.06	-550.5 ± 0.7	154.3 ± 0.8	7 ± 4
	vertical 2	-4.91 ± 0.06	-527.1 ± 0.7	153.0 ± 0.8	9 ± 4
	vertical 3	-5.16 ± 0.07	-509.7 ± 0.7	157.9 ± 0.8	15 ± 4
	vertical 4	-5.21 ± 0.06	-491.5 ± 0.7	159.8 ± 0.8	20 ± 4
	vertical 5	-5.16 ± 0.06	-465.0 ± 0.7	155.9 ± 0.8	12 ± 4
	vertical 6	-4.99 ± 0.07	-445.8 ± 0.7	154.5 ± 0.8	10 ± 4
DC6	horizontal 1	2.805 ± 0.018	-455.0 ± 0.7	163.8 ± 0.8	22 ± 4
	horizontal 2	2.788 ± 0.018	-475.7 ± 0.7	157.4 ± 0.8	13 ± 4
	horizontal 3	2.834 ± 0.018	-497.1 ± 0.7	158.1 ± 0.8	12 ± 4
	vertical 1	-5.22 ± 0.06	-412.9 ± 0.7	154.0 ± 0.8	6 ± 4
	vertical 2	-5.08 ± 0.06	-393.8 ± 0.7	154.9 ± 0.8	7 ± 4
	vertical 3	-4.60 ± 0.06	-377.0 ± 0.7	160.3 ± 0.8	21 ± 4
	vertical 4	-5.58 ± 0.06	-348.9 ± 0.7	157.9 ± 0.8	15 ± 4
	vertical 5	-5.04 ± 0.06	-329.7 ± 0.7	155.3 ± 0.8	8 ± 4
	vertical 6	-4.90 ± 0.06	-313.0 ± 0.7	159.9 ± 0.8	8 ± 4

since the mean height is not meaningful in this measurement, it is not calculated and only the minimum and maximum value inside the ROI are localised. The bow is then defined as the difference of those two heights. The results of the analysis are shown in Table A.12, Table A.13 and Table A.14.

The sensor bow must not exceed 12.5 µm for the double chip size sensors to be accepted within the market survey. Within the measurement uncertainties, only the measured bows of DC1 fulfil this requirement. For all other measured sensors, at least three measured bows are too high to be accepted. However, taken into account that even for the height measurements where the sensors are held down, the minimum height deviation across all sensors was about 6 µm, the 12.5 µm requirement can be adjusted for these sensors. Therefore a maximum bow of 18 µm seems a reasonable criterion for these sensors. With this new criterion, DC2, DC5 and DC6 are classified as good, since the measured bows of these sensors are in good agreement with a 18 µm bow, taken the measurement uncertainties into account.
As a result, only DC3 and DC4 would be classified as bad, because they show a maximum bow greater than that. For DC4 the horizontal line scan number 1 is the problematic one with a maximum bow of 26 µm. Compared with the formerly measured height deviation of 23 µm during the height measurement, this is however no indication for a too large bow. Therefore, this DC is classified as good after a check with the previously recorded data. Nevertheless, this is not the case for DC3. Even compared with its thickness deviation of 23 µm a bow of 57 µm is not acceptable. A graph of the measured profile is shown in Figure A.8. The additional vertical measurements reveal a curvature with its highest point in the top left corner of this sensor, while the lowest point is in the bottom right corner of this sensor. Since this curvature can not be found in the previous height measurements of this sensors, the sensor is classified as bad regarding the bow measurement of the market survey. With this result it might be rejected for further processing steps like the flip chip process. Nevertheless, taken all gained information into account, five out of six investigated sensors comply with the requirements of the ITk market survey. Especially the investigation of the bow shows that it is sometimes necessary to check conspicuous results of the standard analysis scripts. In such a way, results that would raise a qualification as bad can be explained and are converted to a good categorisation.

A.2.3 Electrical Tests

The electrical properties of the diced sensors are measured as well. This includes the analysis of the depletion voltage V_{depl} and the breakdown voltage V_{bd}. Moreover, the leakage current at a specific bias voltage is investigated and the long-term stability

Table A.12: Parameters of the analysis of the measurement of the bow of the diced sensors DC1 and DC2. The fit procedure uses the *scipy.curve_fit* function with the formula $y = a \cdot x + b$. Moreover, the measurement uncertainties of $\pm 3\,\mu m$ for the heights are taken into account. The values refer to the three horizontal and six vertical line scans.

sensor	line scan	slope a / 1×10^{-3}	vertical intercept b / µm	height / µm minimum	height / µm maximum	bow / µm
DC1	vertical 1	3.02 ± 0.06	-867.8 ± 0.7	160.9 ± 3.1	172.4 ± 3.1	11 ± 4
	vertical 2	2.83 ± 0.05	-878.9 ± 0.7	155.5 ± 3.1	166.1 ± 3.1	11 ± 4
	vertical 3	2.80 ± 0.06	-890.8 ± 0.7	158.1 ± 3.1	171.7 ± 3.1	14 ± 4
	vertical 4	2.65 ± 0.06	-894.1 ± 0.7	159.0 ± 3.1	173.7 ± 3.1	15 ± 4
	vertical 5	2.86 ± 0.05	-903.5 ± 0.7	159.7 ± 3.1	170.6 ± 3.1	11 ± 4
	vertical 6	2.71 ± 0.05	-909.5 ± 0.7	160.2 ± 3.1	174.0 ± 3.1	14 ± 4
	horizontal 1	-1.152 ± 0.019	-850.4 ± 0.7	152.4 ± 3.1	166.9 ± 3.2	14 ± 4
	horizontal 2	-1.143 ± 0.019	-839.7 ± 0.7	157.7 ± 3.1	174.7 ± 3.2	17 ± 4
	horizontal 3	-1.154 ± 0.019	-826.5 ± 0.7	157.9 ± 3.1	174.7 ± 3.2	17 ± 4
DC2	vertical 1	2.87 ± 0.06	-710.2 ± 0.7	164.8 ± 3.1	178.6 ± 3.1	14 ± 4
	vertical 2	2.90 ± 0.06	-716.0 ± 0.7	156.4 ± 3.1	168.5 ± 3.1	12 ± 4
	vertical 3	3.12 ± 0.06	-724.8 ± 0.7	157.4 ± 3.1	169.8 ± 3.2	12 ± 4
	vertical 4	2.80 ± 0.06	-727.1 ± 0.7	156.6 ± 3.1	170.3 ± 3.2	14 ± 4
	vertical 5	2.82 ± 0.05	-734.7 ± 0.7	153.5 ± 3.1	168.1 ± 3.2	15 ± 4
	vertical 6	3.10 ± 0.06	-736.0 ± 0.7	153.5 ± 3.1	164.2 ± 3.2	11 ± 4
	horizontal 1	-0.668 ± 0.019	-697.3 ± 0.7	154.2 ± 3.1	174.0 ± 3.1	20 ± 4
	horizontal 2	-0.688 ± 0.018	-686.1 ± 0.7	159.3 ± 3.1	177.5 ± 3.1	18 ± 4
	horizontal 3	-0.671 ± 0.019	-674.5 ± 0.7	159.8 ± 3.1	181.7 ± 3.1	22 ± 4

Table A.13: Parameters of the analysis of the measurement of the bow of the diced sensors DC3 and DC4. The fit procedure uses the *scipy.curve_fit* function with the formula $y = a \cdot x + b$. Moreover, the measurement uncertainties of $\pm 3\,\mu m$ for the heights are taken into account. The values refer to the three horizontal and six vertical line scans.

sensor	line scan	slope a / 1×10^{-3}	vertical intercept b / µm	height / µm minimum	height / µm maximum	bow / µm
DC3	horizontal 1	2.945 ± 0.018	-479.1 ± 0.7	165.6 ± 3.2	222.2 ± 3.1	57 ± 4
	horizontal 2	2.966 ± 0.018	-501.4 ± 0.7	161.8 ± 3.2	217.8 ± 3.1	56 ± 4
	horizontal 3	2.911 ± 0.018	-520.1 ± 0.7	154.8 ± 3.2	211.9 ± 3.1	57 ± 4
	vertical 1	-5.19 ± 0.06	-426.7 ± 0.7	200.6 ± 3.2	218.0 ± 3.1	17 ± 4
	vertical 2	-5.14 ± 0.06	-403.4 ± 0.7	185.8 ± 3.2	204.2 ± 3.1	18 ± 4
	vertical 3	-4.93 ± 0.06	-384.9 ± 0.7	174.2 ± 3.2	193.0 ± 3.1	19 ± 4
	vertical 4	-5.17 ± 0.06	-368.8 ± 0.7	169.1 ± 3.2	184.3 ± 3.1	15 ± 4
	vertical 5	-5.11 ± 0.06	-340.3 ± 0.7	157.3 ± 3.1	176.1 ± 3.1	19 ± 4
	vertical 6	-5.12 ± 0.06	-322.2 ± 0.7	153.6 ± 3.1	171.8 ± 3.1	18 ± 4
DC4	horizontal 1	2.911 ± 0.018	-603.7 ± 0.7	161.7 ± 3.1	187.3 ± 3.2	26 ± 4
	horizontal 2	2.904 ± 0.018	-625.0 ± 0.7	160.8 ± 3.1	180.6 ± 3.2	20 ± 4
	horizontal 3	2.905 ± 0.018	-643.0 ± 0.7	154.3 ± 3.1	174.3 ± 3.2	20 ± 4
	vertical 1	-5.24 ± 0.06	-559.3 ± 0.7	161.3 ± 3.1	176.0 ± 3.1	15 ± 4
	vertical 2	-5.02 ± 0.06	-537.4 ± 0.7	155.1 ± 3.2	170.1 ± 3.1	15 ± 4
	vertical 3	-5.09 ± 0.07	-519.0 ± 0.7	154.1 ± 3.2	171.4 ± 3.1	17 ± 4
	vertical 4	-4.91 ± 0.07	-494.8 ± 0.7	152.4 ± 3.2	170.0 ± 3.1	18 ± 4
	vertical 5	-5.18 ± 0.06	-472.1 ± 0.7	156.8 ± 3.2	173.8 ± 3.1	17 ± 4
	vertical 6	-5.11 ± 0.06	-455.2 ± 0.7	164.3 ± 3.2	181.3 ± 3.1	17 ± 4

Table A.14: Parameters of the analysis of the measurement of the bow of the diced sensors DC5 and DC6. The fit procedure uses the *scipy.curve_fit* function with the formula $y = a \cdot x + b$. Moreover, the measurement uncertainties of $\pm 3\,\mu m$ for the heights are taken into account. The values refer to the three horizontal and six vertical line scans.

sensor	line scan	slope a / 1×10^{-3}	vertical intercept b / µm	height / µm minimum	height / µm maximum	bow / µm
DC5	horizontal 1	2.967 ± 0.018	-594.2 ± 0.7	164.8 ± 3.1	183.3 ± 3.2	19 ± 4
	horizontal 2	2.963 ± 0.018	-613.7 ± 0.7	159.0 ± 3.1	177.9 ± 3.2	19 ± 4
	horizontal 3	2.949 ± 0.018	-634.4 ± 0.7	155.0 ± 3.1	173.0 ± 3.2	18 ± 4
	vertical 1	-5.20 ± 0.06	-551.5 ± 0.7	160.4 ± 3.2	177.8 ± 3.1	17 ± 4
	vertical 2	-5.24 ± 0.06	-529.9 ± 0.7	155.5 ± 3.1	173.1 ± 3.1	18 ± 4
	vertical 3	-5.17 ± 0.06	-508.5 ± 0.7	155.3 ± 3.2	172.0 ± 3.1	17 ± 4
	vertical 4	-5.17 ± 0.07	-493.4 ± 0.7	159.2 ± 3.2	173.6 ± 3.1	14 ± 4
	vertical 5	-5.25 ± 0.06	-461.2 ± 0.7	157.4 ± 3.2	173.6 ± 3.1	16 ± 4
	vertical 6	-5.05 ± 0.07	-445.7 ± 0.7	165.1 ± 3.2	181.1 ± 3.1	16 ± 4
DC6	horizontal 1	2.756 ± 0.017	-334.3 ± 0.7	168.9 ± 3.1	186.0 ± 3.2	17 ± 4
	horizontal 2	2.801 ± 0.018	-357.2 ± 0.7	161.6 ± 3.1	180.0 ± 3.2	18 ± 4
	horizontal 3	2.807 ± 0.018	-373.9 ± 0.7	156.7 ± 3.1	173.1 ± 3.2	16 ± 4
	vertical 1	-4.95 ± 0.06	-285.5 ± 0.7	162.9 ± 3.2	179.5 ± 3.1	17 ± 4
	vertical 2	-5.09 ± 0.06	-263.4 ± 0.7	155.3 ± 3.2	172.9 ± 3.1	18 ± 4
	vertical 3	-5.37 ± 0.06	-241.4 ± 0.7	156.7 ± 3.2	172.0 ± 3.1	15 ± 4
	vertical 4	-4.86 ± 0.06	-230.3 ± 0.7	158.9 ± 3.2	176.8 ± 3.1	18 ± 4
	vertical 5	-5.21 ± 0.06	-202.2 ± 0.7	160.8 ± 3.2	174.5 ± 3.1	14 ± 4
	vertical 6	-4.88 ± 0.07	-186.9 ± 0.7	165.5 ± 3.2	182.0 ± 3.1	17 ± 4

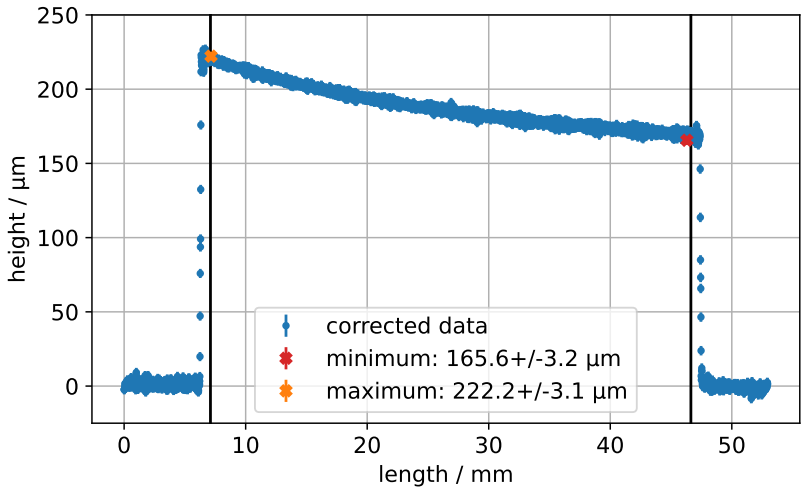

Figure A.8: Corrected data for the measurement of the bow of the first horizontal line scan of the third DC. Each measured value has an uncertainty of approximately 3 µm, which is too small to be easily visible in the plot.

is observed for 48 hours.
This section also includes measurements of irradiated sensors. Since the irradiated sensors were already measured at TU Dortmund before their irradiation as well, a direct comparison is possible.

The first results concern the depletion voltage. The measurements are carried out in the same setup as described in subsubsection 3.2.2. For the measurement, the LCR meter is used in the $C_P - D$ mode. An alternating voltage with a frequency of 1 kHz and an amplitude of $V_{\text{rms}} = 100\,\text{mV}$ is used. The bias voltage is increased in 5 V steps up to a maximum bias voltage of 200 V. At each measurement point, the capacitance is measured five times and the delay between setting the voltage and starting the measurement is set to 5 s. The measurement environment is aimed to be at 20 °C and a relative humidity of $(40 \pm 10)\%$.
The results of these measurements can be found in Table A.15. The data is analysed as stated in subsubsection 3.2.2.

As it can be seen in Table A.15 and Figure A.9a, the results are very uniform for all sensors for the measurements with a frequency of 1 kHz. Especially when the results are rounded to the nearest measurement point, most of the data set is described with only two neighboured voltage points (75 V and 80 V). Only one sensor (DC1) shows a lower depletion voltage. Within the market survey, the sensors are qualified as good, if their depletion voltage is less than 100 V. This is true for all delivered

sensors.
For a comparison, the same sensors are investigated with a frequency of 10 kHz as well. The results are also presented in Table A.15. Additionally, the results are plotted in Figure A.9b. It is very obvious, that the variation in the analysis results is larger compared to the measurement at 1 kHz. For some sensors, the data taking was not even possible. The unstable data taking might be an explanation for the larger measurement uncertainties that are present for this subset of measurements.

The depletion voltage was also measured by the vendor. There, the measurement was carried out on test structures on the full wafer. Values for the depletion voltage between (76.9 ± 0.6) V and (80.5 ± 0.6) V resulted.
Since the market survey requires a measurement with 1 kHz, only this subset will be compared to the results of the vendor's measurement. Nearly all values comply with those values, if the measurement uncertainties are taken into account. Only one sensor (SC2) shows a depletion voltage, which is slightly too large. Nevertheless, this proofs, that the sensors are produced in a very uniform quality that fulfils the market survey requirements.

The next results are gained from the IV measurements at the reception. The used setup for these measurements is the same as in subsubsection 3.2.2. The measurements are carried out with an increasing bias voltage in 5 V steps up to a maximum voltage of 600 V. This procedure is only interrupted, if the leakage current increases the set current limit of 1 µA. In these cases, the bias voltage is slowly ramped down. At each bias voltage, the leakage current is measured ten times. The delay, after which the measurements start after setting the correct bias voltage, is 10 s. The measurement environment is aimed to be at 20 °C and a relative humidity of (40 ± 10)%.
The results of these measurements can be found in Table A.16. The data is analysed as stated in subsubsection 3.2.2. However, the additional requirement of three consecutive steps with an increase of the leakage current of more than 20% is not needed for these measurements.

The market survey requires a breakdown voltage V_{bd} of more than $V_{\mathrm{depl}} + 70$ V. As it can be seen in Table A.16, all sensors fulfil this requirement. Moreover, for none of the sensors, a breakdown is found up to a bias voltage of 600 V.
The threshold for the leakage current per area I_{leak}/A is 0.75 µA/cm^2. The leakage current for these sensors is examined at a bias voltage of $V_{\mathrm{depl}} + 50$ V. Since the depletion voltage of all sensors is very uniform, a depletion voltage of $V_{\mathrm{depl}} = 80$ V is used for all sensors. Therefore, the leakage current listed in Table A.16 is measured at a bias voltage of 130 V. All measured leakage currents per area are well below the given limit.

Table A.15: Results of the CV measurements of the diced sensors. The column labelled *analysis* gives the results of the fit algorithm. The column labelled with *rounded* shows the values from the analysis rounded to the nearest measurement point and the stated uncertainty is given as the step width of the corresponding measurement.

	1 kHz			10 kHz	
sensor	V_{depl} / V analysis	V_{depl} / V rounded	sensor	V_{depl} / V analysis	V_{depl} / V rounded
SC1	78.6 ± 0.6	80 ± 5	SC1	76.1 ± 0.6	75 ± 5
SC2	82.5 ± 0.7	80 ± 5	SC2	82.4 ± 0.9	80 ± 5
SC3	78.9 ± 0.7	80 ± 5	SC3	82.5 ± 1.9	80 ± 5
SC4	81.3 ± 0.7	80 ± 5	SC4	80.0 ± 1.7	80 ± 5
SC5	77.3 ± 0.7	75 ± 5	SC5	74.7 ± 2.8	75 ± 5
SC6	77.1 ± 0.7	75 ± 5	SC6	67.2 ± 1.2	65 ± 5
SC7	77.1 ± 0.8	75 ± 5	SC7	74.1 ± 2.1	75 ± 5
SC8	76.3 ± 0.7	75 ± 5	SC8	73.2 ± 1.5	75 ± 5
SC9	77.4 ± 0.6	75 ± 5	SC9	74.3 ± 1.6	75 ± 5
SC10	80.3 ± 0.7	80 ± 5	SC10	67.4 ± 2.1	65 ± 5
DC1	71.8 ± 1.0	70 ± 5	DC1	75.5 ± 0.8	75 ± 5
DC2	78.9 ± 0.8	80 ± 5	DC2	76.8 ± 0.8	75 ± 5
DC3	77.2 ± 0.7	75 ± 5	DC3	72.2 ± 1.5	70 ± 5
DC4	79.2 ± 0.6	80 ± 5	DC4	72.7 ± 1.8	75 ± 5
DC5	77.5 ± 0.5	75 ± 5	DC5	72.1 ± 2.0	70 ± 5
DC6	75.8 ± 0.4	75 ± 5	DC6	70.7 ± 1.6	70 ± 5
DC7	78.3 ± 0.6	80 ± 5	DC7	76.0 ± 0.4	75 ± 5
DC8	80.4 ± 0.7	80 ± 5	DC8	74.4 ± 0.7	75 ± 5
DC9	77.1 ± 0.5	75 ± 5	DC9	72.8 ± 0.8	75 ± 5
DC10	78.0 ± 0.6	80 ± 5	DC10	74.0 ± 1.8	75 ± 5
DC11	76.4 ± 0.4	75 ± 5	DC11	71.4 ± 1.3	70 ± 5
DC12	81.1 ± 0.7	80 ± 5	DC12	-	-
DC13	79.6 ± 0.7	80 ± 5	DC13	82.5 ± 1.0	80 ± 5
DC14	80.8 ± 1.0	80 ± 5	DC14	-	-
DC15	77.2 ± 0.7	75 ± 5	DC15	71.5 ± 2.5	70 ± 5
DC16	76.2 ± 0.6	75 ± 5	DC16	75.4 ± 0.7	75 ± 5
DC17	77.7 ± 0.6	80 ± 5	DC17	-	-
DC18	80.8 ± 0.6	80 ± 5	DC18	-	-
DC19	80.4 ± 0.7	80 ± 5	DC19	-	-
DC20	81.3 ± 0.6	80 ± 5	DC20	81.0 ± 0.8	80 ± 5

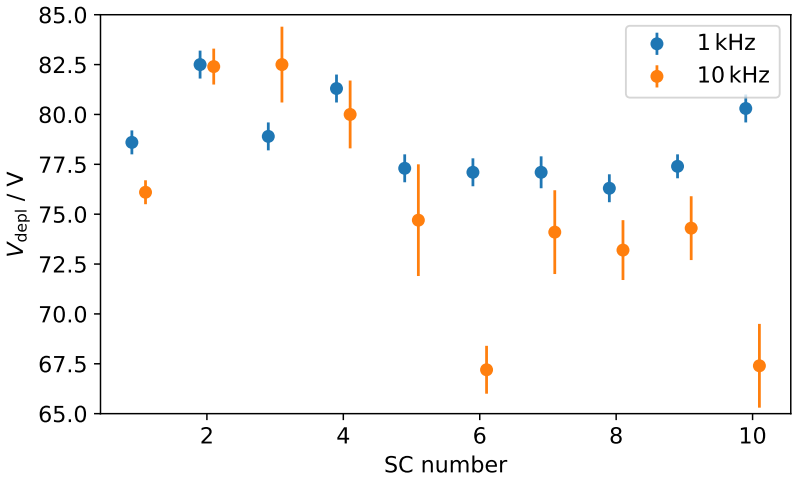

(a) Depletion voltages of the SCs.

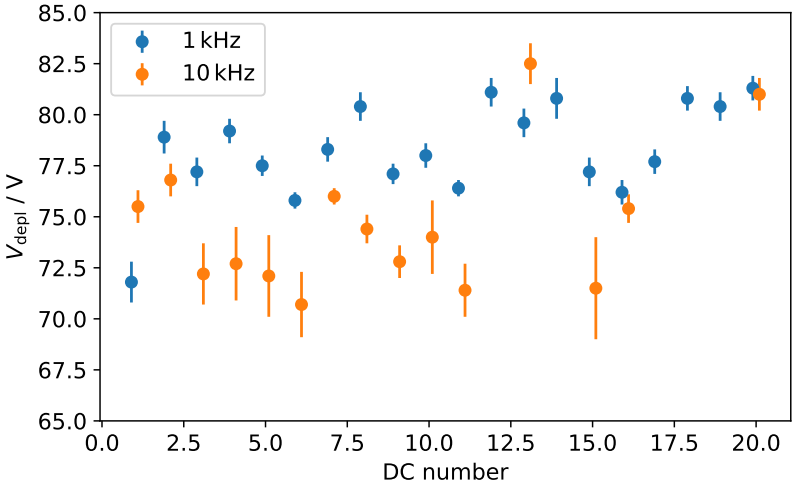

(b) Depletion voltages of the DCs.

Figure A.9: Depletion voltages V_{depl} of the measured diced sensors. The analysis results of the measurements with 1 kHz and 10 kHz are shown for comparison.

To sum up the results of the IV measurements, the sensors of this vendor show a very uniform electrical behaviour. None of them shows a breakdown and even the leakage current per area is very similar across all sensors. Concerning the IV measurements, all sensors fulfil the market survey requirements.

Some of the sensors have severe damage from previous handling. To investigate, if the damage affects the classification of these sensors within the market survey, they are remeasured after the damage has happened. For this reason, the capacitance-voltage and the current-voltage characteristics are measured another time.
A comparison of the depletion voltages before and after the mechanical damage is shown in Table A.17. The biggest difference can be seen for DC1, where the depletion voltage increases of roughly 5 V. The differences for the other two sensors, DC2 and DC3, are only approximately 1 V. In general, all sensors still fulfil the market survey requirement ($V_{\mathrm{depl}} < 100\,\mathrm{V}$). Moreover, the measured and rounded depletion voltages still fit in the grand scheme that was found before.

The current-voltage characteristic is checked again and the results are plotted in Figure A.10. DC1 was damaged by metal tweezers and DC3 was damaged by vacuum tweezers. For these sensors (shown in Figure A.10b and Figure A.10c), the leakage currents have the exact same behaviour as in the undamaged state. The small deviations in the height of the leakage current can be traced back to slightly different temperatures in the measurement setup.
Only for DC2, which features scratches from metal tweezers and damaged UBM pads by a contact with a sheet of Kapton foil, the leakage current is different after the mechanical damage. As it can be seen in Figure A.10a, the leakage current increases drastically for bias voltages of more than 400 V. Moreover, for this curve, a breakdown is detected by the analysis script at a bias voltage of 430 V. Nevertheless, this sensor still fulfils the requirements of the market survey. The leakage current per area at a bias voltage of 130 V is still low enough and although a breakdown is detected, it is at a very high bias voltage. Within the market survey, sensors are accepted, if their breakdown voltage is higher than $V_{\mathrm{depl}} + 70\,\mathrm{V}$. Since 430 V is well above 150 V, which is the threshold for the sensors of this vendor, this sensor is still considered as good.

The measurement of the long-term stability of the leakage current is performed in the same setup as it was used for the other electrical measurements. The leakage current is measured at a constant bias voltage of $V_{\mathrm{depl}} + 50\,\mathrm{V}$, which means, that all sensor are measured at a bias voltage of 130 V. The market survey requires an investigation of the leakage current for 48 hours and data points every ten minutes. Therefore, every ten minutes, the leakage current is measured ten times to determine the standard deviation of the mean current at this moment. If the original taken measurements cover more than 48 hours, only the first 48 hours of the data set are

Table A.16: Results of the IV measurements of the diced sensors. The stated leakage currents per area I_{leak}/A are measured at a bias voltage of 130 V.

sensor	I_{leak}/A / µA/cm^2	V_{bd} / V
SC1	0.004 60 ± 0.000 14	>600
SC2	0.004 59 ± 0.000 10	>600
SC3	0.003 64 ± 0.000 10	>600
SC4	0.003 46 ± 0.000 08	>600
SC5	0.004 56 ± 0.000 10	>600
SC6	0.004 59 ± 0.000 10	>600
SC7	0.005 37 ± 0.000 12	>600
SC8	0.004 78 ± 0.000 09	>600
SC9	0.003 52 ± 0.000 12	>600
SC10	0.003 66 ± 0.000 08	>600
DC1	0.004 15 ± 0.000 04	>600
DC2	0.004 30 ± 0.000 07	>600
DC3	0.002 76 ± 0.000 10	>600
DC4	0.002 68 ± 0.000 07	>600
DC5	0.002 861 ± 0.000 034	>600
DC6	0.002 77 ± 0.000 04	>600
DC7	0.004 53 ± 0.000 08	>600
DC8	0.004 10 ± 0.000 07	>600
DC9	0.002 98 ± 0.000 06	>600
DC10	0.004 07 ± 0.000 05	>600
DC11	0.002 72 ± 0.000 05	>600
DC12	0.002 88 ± 0.000 17	>600
DC13	0.004 52 ± 0.000 12	>600
DC14	0.002 49 ± 0.000 08	>600
DC15	0.004 18 ± 0.000 08	>600
DC16	0.003 67 ± 0.000 20	>600
DC17	0.004 41 ± 0.000 34	>600
DC18	0.0054 ± 0.0011	>600
DC19	0.0036 ± 0.0005	>600
DC20	0.003 78 ± 0.000 27	>600

Table A.17: Depletion voltages of sensors before and after the mechanical damage.

	before damage			after damage	
sensor	V_{depl} / V analysis	V_{depl} / V rounded	sensor	V_{depl} / V analysis	V_{depl} / V rounded
DC1	71.8 ± 1.0	70 ± 5	DC1	76.9 ± 0.5	75 ± 5
DC2	78.9 ± 0.8	80 ± 5	DC2	78.0 ± 0.6	80 ± 5
DC3	77.2 ± 0.7	75 ± 5	DC3	78.5 ± 0.6	80 ± 5

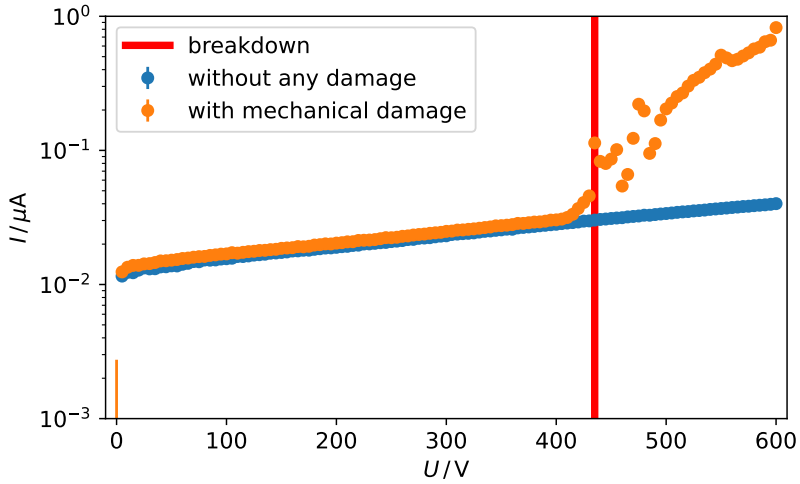

(a) DC2.

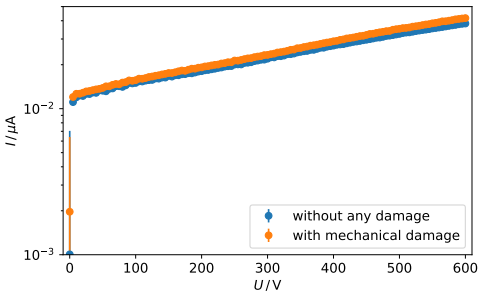

(b) DC1.

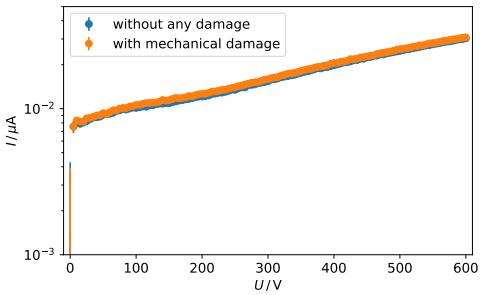

(c) DC3.

Figure A.10: Current-voltage characteristics before and after mechanical damage for different sensors. The sensor DC2 (in **(a)**) is damaged by metal tweezers and a Kapton foil, DC1 (shown in **(b)**) is damaged by metal tweezers and DC3 (shown in **(c)**) has marks from vacuum tweezers.

used for the analysis in this thesis.
Within the analysis, the variation between any two measurement points in a measurement has to be smaller than 25% to fulfil the market survey requirement. The variation is defined as the difference between the largest and smallest measured leakage current divided by the maximum current. Since the sensors might show some kind of build up effect, the very first data point (measured at the beginning of the measurement) is excluded from the analysis and only data points with measurement times of more than 10 minutes are used.
The measurement is meant to be carried out at a temperature of (20 ± 1)°C and a relative humidity of (40 ± 10)%. Both requirements are not always met. Detail about this will be given in the following.

The first measured sensors are SC8 and SC9. The results of these measurements are plotted in Figure A.11. It is obvious, that the temperature is higher than allowed and the humidity inside the climate chamber decreases below the threshold. A reason for this could not be found by the time the measurements were taken. For later measurements, the temperature and humidity control inside the climate chamber works better, so that those parameters are better controllable.
Both sensors show striking current peaks. They were measured one after the other, so for the first sensor SC8 it was unclear, what caused these peaks. Since the second sensor SC9 shows the same peaks, it is clear, that this is an effect of the environment and not a feature of the single sensor. When the measurement times are converted to daytimes, it becomes clear, that the peak is always present between noon and six o'clock in the evening.
The laboratory has windows facing south-west. Although the climate chamber itself is lightproof, there are passages for cables and hoses. For applying dry air to the climate chamber, a transparent hose is used on the side of the climate chamber, which is not facing the windows. This transparent hose is the reason why light is able to affect the current measurement inside the climate chamber. For later measurements, the hose is covered in black duct tape. After this adjustment, no more current peaks caused by sunlight are detected.

Since the peaks are approximately 1.5 times larger than the mean current, those measurements do not fulfil the requirements of the market survey.
For SC8 a leakage current of roughly 9 nA is expected. The mean leakage current over the whole 48 hours is (7.479 ± 0.017) nA. The lowest measured current is (6.81 ± 0.29) nA and the highest current, measured in the second peak, is about (9.65 ± 0.29) nA. This results in a variation of (29 ± 4)%, which is larger than allowed for the market survey.
From the previous IV measurements, a leakage current around 7 nA is expected for SC9. The mean leakage current of (7.336 ± 0.018) nA is close to this expectation. The extreme values of this measurement are (6.27 ± 0.30) nA for the lowest measured

current and (9.5 ± 0.4) nA for the maximum leakage current. The variation for this measurement is therefore $(34 \pm 4)\%$, which is again too large to be acceptable within the market survey.

In the improved setup, where the transparent hose is covered and the temperature and humidity are better controlled, another SC is measured. The results for SC10 are shown in Figure A.12. The temperature and the relative humidity inside the climate chamber are much stabler now.
A mean leakage current of approximately 7 nA is expected and a mean leakage current of (6.521 ± 0.021) nA is measured. The minimum leakage current that is measured is (6.06 ± 0.17) nA and the maximum current is (6.92 ± 0.25) nA. This gives a maximum variation of only $(12 \pm 4)\%$. Therefore, this sensor fulfils the requirement of the market survey.

The improved setup was also used to measure the long-term stability of the leakage current of two DC sensors. The results of these measurements are shown in Figure A.13. Both measurements show drastic increases of the leakage current over the measurement time of 48 hours. Although the IV characteristics state, that a leakage current of 11 nA for DC9 and 14 nA for DC16 are expected, these low values are not measured at all. The leakage current of DC9 rises from approximately 15 nA up to 40 nA. This results in a maximum variation of roughly 60%. For DC16 the increase is even higher. The current rises from nearly 200 nA to more than 800 nA. This is a variation of more than 70%. Both sensors obviously do not comply with the market survey requirement.
Current increases at a high relative humidity inside the climate chamber are also observed in Göttingen [82]. There, the leakage current seems to be a function of the relative humidity. In the thesis of S. Möbius [82], the current increases and decreases in accordance with the relative humidity, which is not observed in the measurements presented in Figure A.13. Nevertheless, the relative humidity around 40% or more seems to be problematic for these sensors. For this reason, both sensors are remeasured at a lower humidity.

The results of the measurement of the leakage current at a lower humidity are shown in Figure A.14. For both measurements, the humidity settles around 10% after 10 hours of measurement time and the leakage current stays stable over the complete 48 hours.
The expected values for the leakage current of 11 nA for DC9 and 14 nA for DC16 are met. The mean leakage currents are (10.56 ± 0.07) nA and (13.51 ± 0.11) nA, respectively. These values are confirmed by the measurements from Göttingen. There 10 nA and 12.5 nA are reported for these sensors at a bias voltage of 125 V and a relative humidity of only 2%. Therefore, these measurements are consistent with each other.

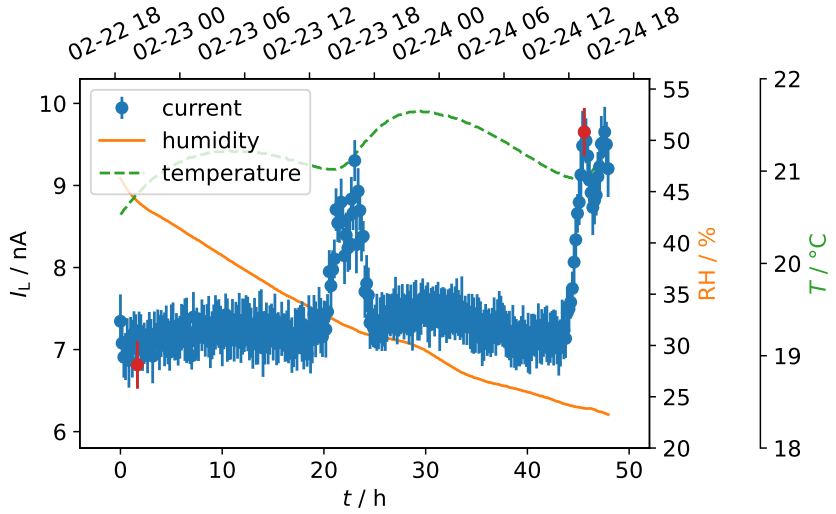

(a) SC8.

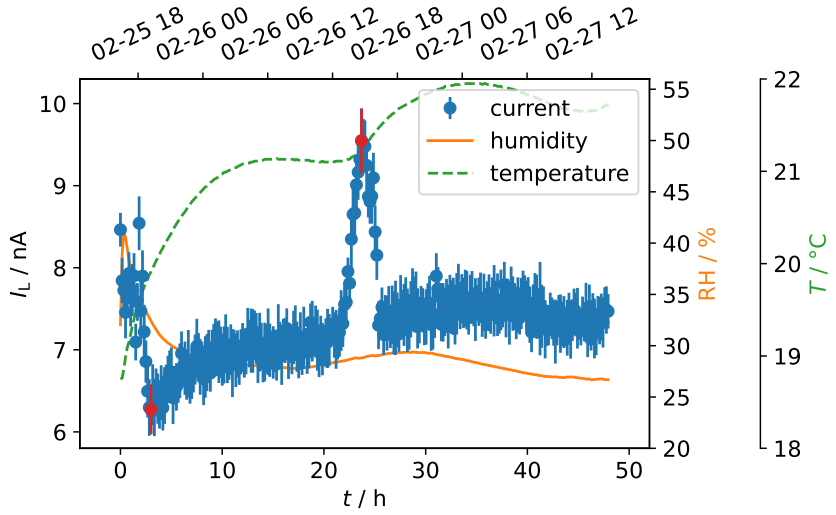

(b) SC9.

Figure A.11: Data of the It measurement of two single chip sized sensors, **(a)** shows the It measurement for SC8 and **(b)** for a second SC, namely SC9. Besides the leakage current at a bias voltage of 130 V, the temperature of the sensor and the humidity inside the climate chamber are displayed. At the top of the plot, the daytime of the measurement is given as well. The red data points mark the minimum and maximum measured leakage currents in the data set.

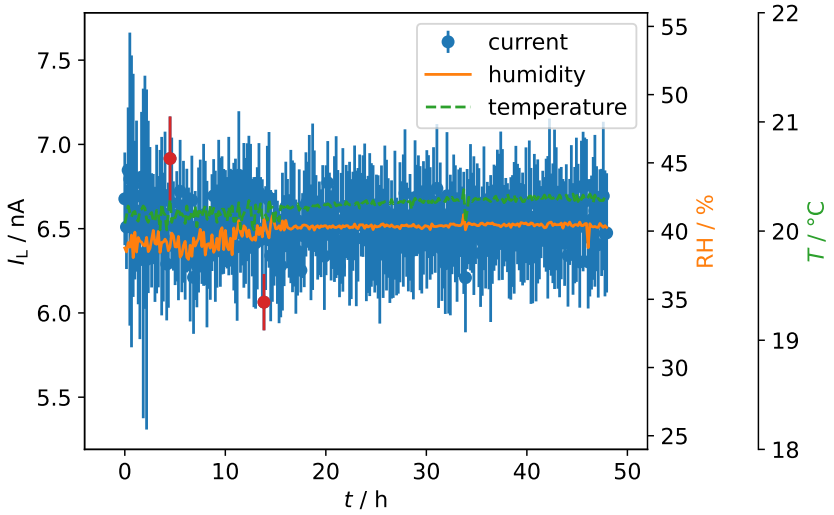

Figure A.12: Data of the It measurement of SC10. The temperature of the sensor and the humidity inside the climate chamber are displayed, as well as the leakage current measured at a bias voltage of 130 V. The red data points mark the minimum and maximum measured leakage currents in the data set.

The lowest measured current for DC9 is (8.4 ± 2.0) nA, which shows a relative uncertainty of more than 20%. The highest leakage current for this sensor is (12 ± 6) nA, which has an even larger relative uncertainty of 50%. This results in a maximum variation of (30 ± 40)%. The large uncertainty is a result of the large uncertainties of the extreme values. The analysis script classes this sensor as bad. However, since the uncertainties of the relevant measurement points are very large and comply with the mean measured leakage current, the sensor is classified as good after a human check. The same classification is true for sensor DC16. The lowest current is (11 ± 5) nA, with a relative uncertainty of 45%, and the highest current is (16 ± 5) nA (a relative uncertainty of more than 30%). The calculated variation is (31 ± 35)%. The extreme values comply again with the mean value, if their uncertainties are taken into account.

After a human check, all sensors measured in the improved setup fulfil the market survey requirement. The effect of the relative humidity on the long-term stability of the leakage current is not considered a problem, so the data taken at the lower humidity (shown in Figure A.14) verifies the good quality of the DC sensors.

Four of the characterised sensors are sent to Birmingham to be irradiated. The irradiation fluences are the same as for the sensors presented in subsection 3.2.3: approximately $2 \cdot 10^{15}\, n_{\mathrm{eq}}/\mathrm{cm}^2$ and $5 \cdot 10^{15}\, n_{\mathrm{eq}}/\mathrm{cm}^2$. The sensors are first charac-

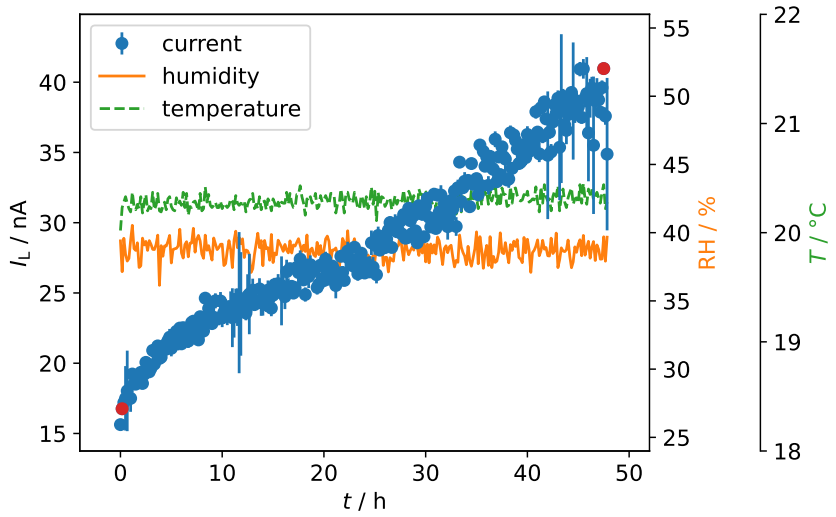

(a) DC9.

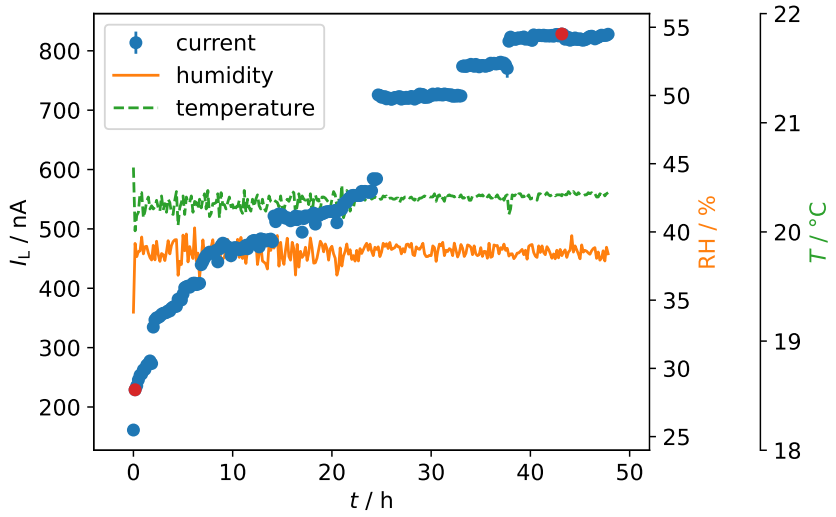

(b) DC16.

Figure A.13: Data of the It measurement of two double chip sized sensors, **(a)** shows the It measurement for DC9 and **(b)** for a second DC, namely DC16. Besides the leakage current at a bias voltage of 130 V, the temperature of the sensor and the humidity inside the climate chamber are displayed. The red data points mark the minimum and maximum measured leakage currents in the data set.

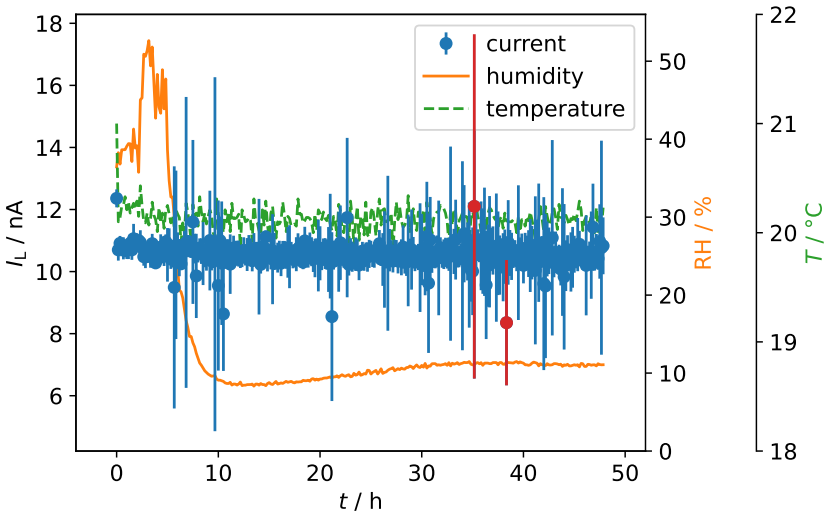

(a) DC9.

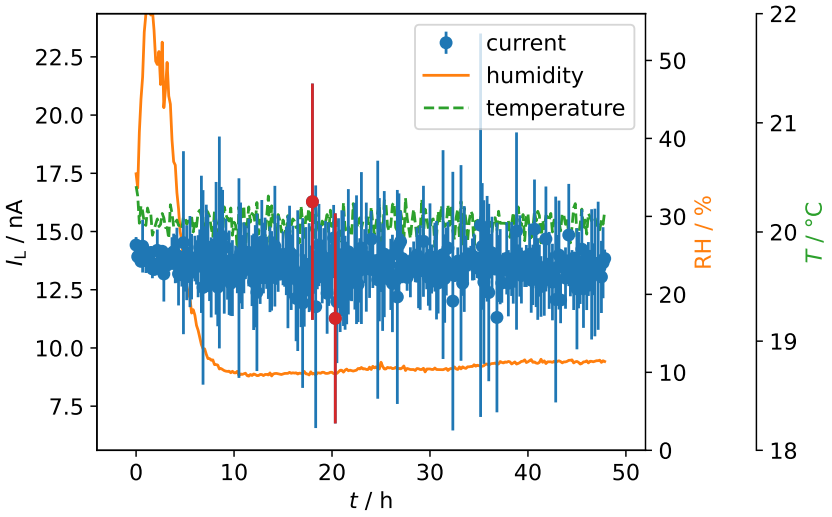

(b) DC16.

Figure A.14: Data of the It measurement of two double chip sized sensors at low humidity, where **(a)** shows the It measurement for DC9 and **(b)** for a second DC, namely DC16. Besides the leakage current at a bias voltage of 130 V, the temperature of the sensor and the humidity inside the climate chamber are displayed. The red data points mark the minimum and maximum measured leakage currents in the data set.

terised in Göttingen [82], where additional annealing studies are carried out, and then shipped to TU Dortmund. Therefore, the sensors have undergone an annealing of at least 10 days at room temperature.

The measurement is carried out in the aforementioned climate chamber setup. The leakage current is measured in 5 V steps with 10 repetitions per voltage step and the delay, after which the measurement starts after setting the bias voltage, is set to 10 s. The maximum applied bias voltage is 800 V for those sensors that are irradiated to $5 \cdot 10^{15}\, n_{\mathrm{eq}}/\mathrm{cm}^2$. Although for the sensors that are irradiated to $2 \cdot 10^{15}\, n_{\mathrm{eq}}/\mathrm{cm}^2$ a lower investigation point is used, they are measured up to a maximum bias voltage of 1000 V. If the leakage current exceeds 100 µA, the measurement is stopped and the voltage is ramped down.
The sensor temperature is meant to be as close as possible to $T_{\mathrm{sensor}} = -25\,^{\circ}\mathrm{C}$. For this purpose, the climate chamber is set to $T_{\mathrm{set}} = -25\,^{\circ}\mathrm{C}$. The different sensor temperatures are displayed in Figure A.15a. Within the market survey, a deviation of $\pm 1\,^{\circ}\mathrm{C}$ is tolerated. Only the temperatures for SC9 and SC10 are in the beginning of the measurement too low to meet the requirement. Since the measurements are used only as the cross-check for measurements done in a probe station in Göttingen, this is not a problem.
However, the humidity inside the climate chamber, which should be lower than 50% during the measurement, does not meet the requirement at all. The data for this is shown in Figure A.15b.

The current-voltage characteristics of the different sensors are shown in Figure A.16. A list with the leakage current scaled to the sensor area and the breakdown voltage is given additionally in Table A.18.
Those sensors, that are irradiated to $2 \cdot 10^{15}\, n_{\mathrm{eq}}/\mathrm{cm}^2$, need to have a breakdown voltage larger than 400 V to meet the requirement for the market survey. This is true for both investigated sensors. The leakage current does not show any steep increases. The measurement for SC9 does not reach the current limit up to a bias voltage of 900 V. For sensor SC10 the contact is interrupted for bias voltages larger than 860 V. Therefore, this value is given as the lower limit for the breakdown voltage. The higher irradiated sensors need breakdown voltages higher than 600 V to fulfil the market survey requirement. This is again true for both measured sensors.
The second examined criterion of the market survey is the leakage current per area. For the lower irradiated sensors, the leakage current is examined at a bias voltage of 400 V and for the higher irradiated sensors it is examined at 600 V. Both sensors irradiated to $2 \cdot 10^{15}\, n_{\mathrm{eq}}/\mathrm{cm}^2$ fulfil the requirement clearly. A maximum leakage current per area of $25\,\mu\mathrm{A}/\mathrm{cm}^2$ is allowed and both show at a bias voltage of 400 V a leakage current, that is only half as high. The higher irradiated sensors are allowed a leakage current per area of maximum $45\,\mu\mathrm{A}/\mathrm{cm}^2$. Only SC6 is close to this limit, as it is seen in Figure A.16. Nevertheless, even this sensor fulfils the market survey

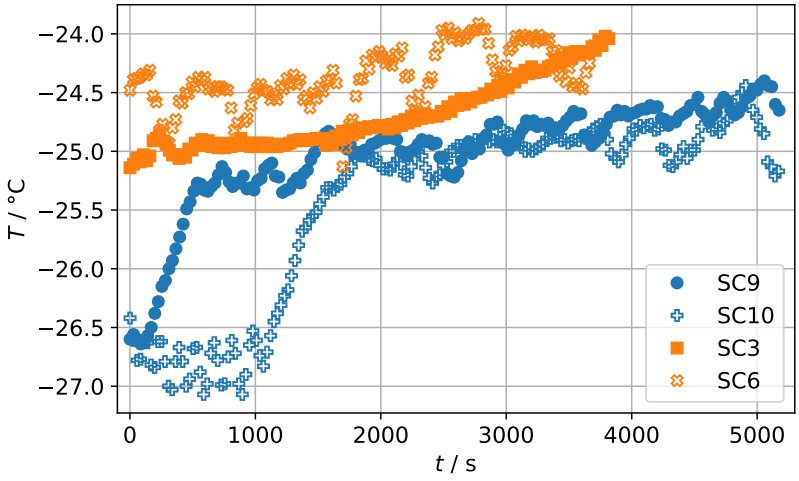

(a) Sensor temperatures.

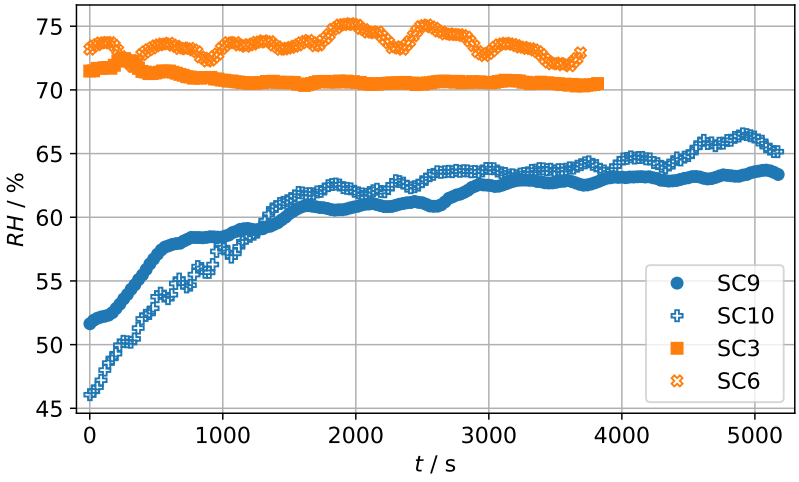

(b) Relative humidity during measurements.

Figure A.15: Measured data for the environmental values of the **(a)** temperature and **(b)** the relative humidity. The data points in blue refer to the measurements of those sensors, that are irradiated to a fluence of $2 \cdot 10^{15}\, n_{\mathrm{eq}}/\mathrm{cm}^2$. The orange markers indicate measurements for sensors irradiated to a fluence of $5{\cdot}10^{15}\, n_{\mathrm{eq}}/\mathrm{cm}^2$.

requirement (see Table A.18). To sum this up, all sensors are qualified as good within the market survey.

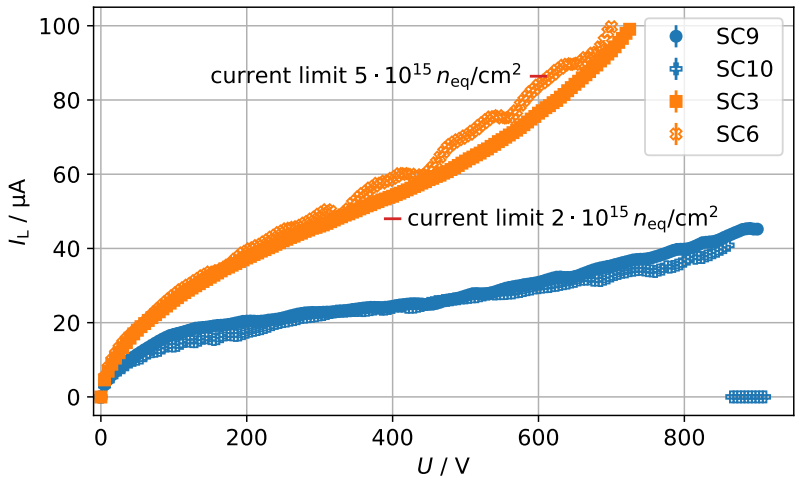

Figure A.16: Current-voltage characteristics of the irradiated sensors. The blue markers refer to those sensors that are irradiated to a fluence of $2 \cdot 10^{15}\, n_{eq}/cm^2$ and the orange markers depict the sensors irradiated to $5 \cdot 10^{15}\, n_{eq}/cm^2$. Additionally, the corresponding current limits are displayed in the plots. The measurement uncertainties defined as the standard deviation of the measured leakage currents per bias voltage are plotted as well, but are too small to be seen.

Table A.18: Detailed list with the relevant data of the leakage current measurements of the irradiated sensors. Given are the values for the leakage current I_L scaled to the area of the sensors A and the breakdown voltage V_{bd} of the sensors.

thickness	fluence	sensor name	I_L/A / µA/cm^2	V_{bd} / V
150 µm	$2 \cdot 10^{15}\, n_{eq}/cm^2$	SC9	12.585 $\pm$ 0.007	>900
		SC10	12.425 $\pm$ 0.016	>860
	$5 \cdot 10^{15}\, n_{eq}/cm^2$	SC3	39.4135 $\pm$ 0.0028	725 $\pm$ 5
		SC6	43.318 $\pm$ 0.009	700 $\pm$ 5

B Parameters for Testbeam Software

The given examples in the following sections have to be adjusted depending on the pixel dimensions of the installed modules in the testbeam setup.

B.1 EUTelescope

The following code snippet provides details about the configuration file used for the reconstruction. Information about the modules in other files, such as the gear file, can be obtained from the details provided in the main part of the thesis. All other used files and parameters are kept in their default state.

```
# general setup
[DEFAULT]
    # Which planes should be excluded from reconstruction
    ExcludePlanes =

[converter]
    # How many events for noisy pixel analysis
    NoOfEvents = 100000
    # Details of telescope
    M26SensorVec = 0 1 2 3 4 5
    FiringFreqCutM26 = 0.005
    # Details of DUTs and reference module
    APIXSensorVec = 110 112 21
    FiringFreqCutAPIX = 0.001

[hitmaker]
    # ID of fixed sensor for correlation and alignment
    FixedPlane = 3
    # Number of events used for Correlator and PreAligner
    NoEvents = 100000
    # Residual cuts for Correlator and PreAligner
    ResidualsXMin = -3. -3. -3. -10. -10. -3. -3. -3. -10.
```

```
    ResidualsXMax = 3. 3. 3. 10. 10. 3. 3. 3. 10.
    ResidualsYMin = -3. -3. -3. -10. -10. -3. -3. -3. -10.
    ResidualsYMax = 3. 3. 3. 10. 10. 3. 3. 3. 10.

[alignGBL]
    MaxTrackCandidatesTotal = 100000
    Iteration = 0
    # Number of alignment constants used. Available
    # modes are: XYShiftsRotZ, XYZShiftsRotXYZ
    AlignMode = XYZShiftsRotXYZ
    # Details of setup
    UpstreamTriplet = 0 1 2
    LastUpstreamSensor = 2
    DownstreamTriplet = 3 4 5
    # Details of alignment mode
    FixedPlanes = 0 5
    FixedZShift = 0 1 2 110 112 3 4 5 21
    # res = pitch/sqrt(12)
    resMim = 0.0052
    resRD531X = 0.0289
    resRD531Y = 0.0072
    resRD532XY = 0.0144
    resFEI4X = 0.0722
    resFEI4Y = 0.0144
    # DUT0 is 50x50 and DUT1 is 25x100
    # Note: in this nomenclature (AxB) A is in y-direction
    # and B in x-direction
    ResolutionX = %(resMim)s %(resMim)s %(resMim)s
                  %(resRD532XY)s %(resRD531X)s %(resMim)s
                  %(resMim)s %(resMim)s %(resFEI4X)s
    ResolutionY = %(resMim)s %(resMim)s %(resMim)s
                  %(resRD532XY)s %(resRD531Y)s %(resMim)s
                  %(resMim)s %(resMim)s %(resFEI4Y)s
    # Cuts applied during alignment
    UpstreamTripletCut= 0.2
    DownstreamTripletCut= 0.2
    UpstreamSlopeCut= 3.0
    DownstreamSlopeCut= 3.0
    TripletMatchingCut= 0.5
    DUTCuts = 1.0 1.0
```

```
[alignGBL1]
    MaxTrackCandidatesTotal = 100000
    Iteration = 1
    # Number of alignment constants used. Available
    # modes are: XYShiftsRotZ, XYZShiftsRotXYZ
    AlignMode = XYZShiftsRotXYZ
    # Details of setup
    UpstreamTriplet = 0 1 2
    LastUpstreamSensor = 2
    DownstreamTriplet = 3 4 5
    # Details of alignment mode
    FixedPlanes = 0 5
    FixedZShift = 0 1 2 110 112 3 4 5 21
    # res = pitch/sqrt(12)
    resMim = 0.0052
    resRD531X = 0.0289
    resRD531Y = 0.0072
    resRD532XY = 0.0144
    resFEI4X = 0.0722
    resFEI4Y = 0.0144
    # DUT0 is 50x50 and DUT1 is 25x100
    # Note: in this nomenclature (AxB) A is in y-direction
    # and B in x-direction
    ResolutionX = %(resMim)s %(resMim)s %(resMim)s
                  %(resRD532XY)s %(resRD531X)s %(resMim)s
                  %(resMim)s %(resMim)s %(resFEI4X)s
    ResolutionY = %(resMim)s %(resMim)s %(resMim)s
                  %(resRD532XY)s %(resRD531Y)s %(resMim)s
                  %(resMim)s %(resMim)s %(resFEI4Y)s
    # Cuts applied during alignment
    UpstreamTripletCut= 0.2
    DownstreamTripletCut= 0.2
    UpstreamSlopeCut= 3.0
    DownstreamSlopeCut= 3.0
    TripletMatchingCut= 0.5
    DUTCuts = 1.0 1.0

[alignGBL2]
    MaxTrackCandidatesTotal = 100000
    Iteration = 2
    # Number of alignment constants used. Available
```

```
    # modes are: XYShiftsRotZ, XYZShiftsRotXYZ
    AlignMode = XYZShiftsRotXYZ
    # Details of setup
    UpstreamTriplet = 0 1 2
    LastUpstreamSensor = 2
    DownstreamTriplet = 3 4 5
    # Details of alignment mode
    FixedPlanes = 0 5
    FixedZShift = 0 1 2 110 112 3 4 5 21
    # res = pitch/sqrt(12)
    resMim = 0.0052
    resRD531X = 0.0289
    resRD531Y = 0.0072
    resRD532XY = 0.0144
    resFEI4X = 0.0722
    resFEI4Y = 0.0144
    # DUT0 is 50x50 and DUT1 is 25x100
    # Note: in this nomenclature (AxB) A is in y-direction
    # and B in x-direction
    ResolutionX = %(resMim)s %(resMim)s %(resMim)s
                  %(resRD532XY)s %(resRD531X)s %(resMim)s
                  %(resMim)s %(resMim)s %(resFEI4X)s
    ResolutionY = %(resMim)s %(resMim)s %(resMim)s
                  %(resRD532XY)s %(resRD531Y)s %(resMim)s
                  %(resMim)s %(resMim)s %(resFEI4Y)s
    # Cuts applied during alignment
    UpstreamTripletCut= 0.03
    DownstreamTripletCut= 0.03
    UpstreamSlopeCut= 2.00
    DownstreamSlopeCut= 2.00
    TripletMatchingCut= 0.20
    DUTCuts = 0.3 0.3

[fitGBL]
    UpstreamTriplet = 0 1 2
    LastUpstreamSensor = 2
    DownstreamTriplet = 3 4 5
    # Planes which should be excluded from track fitting
    # standard=unbiased tracks->exclude all DUTs:
    DUTPlanes = 110 112 21
    # res = pitch/sqrt(12)
```

```
resMim = 0.0052
resRD531X = 0.0289
resRD531Y = 0.0072
resRD532XY = 0.0144
resFEI4X = 0.0722
resFEI4Y = 0.0144
# DUT0 is 50x50 and DUT1 is 25x100
# Note: in this nomenclature (AxB) A is in y-direction
# and B in x-direction
ResolutionX = %(resMim)s %(resMim)s %(resMim)s
              %(resRD532XY)s %(resRD531X)s %(resMim)s
              %(resMim)s %(resMim)s %(resFEI4X)s
ResolutionY = %(resMim)s %(resMim)s %(resMim)s
              %(resRD532XY)s %(resRD531Y)s %(resMim)s
              %(resMim)s %(resMim)s %(resFEI4Y)s
# Cuts applied
UpstreamTripletCut = 0.03
DownstreamTripletCut = 0.03
UpstreamSlopeCut = 2.00
DownstreamSlopeCut = 2.00
TripletMatchingCut = 0.20
DUTCuts = 0.3 0.3
OutputPlanes = 110 112 21
```

B.2 TBMon2

The following code snippet provides details about the main configuration file used for the analysis of the reconstructed tracks. The default values of all other parameters not mentioned explicitly in this section remain unchanged. These can be found online by registered CERN users [73].

```
# general setup
    useRecoZ = true;
    recoGEAR = true;

# DUT handling
# the analysed DUT
    lv1Min = 10;
    lv1Max = 20;
    noisyNeighborColRadius = 1;
    noisyNeighborRowRadius = 1;
    maskDeadPixels = true;
    # 200 is used with pixel dimension of 100 µm
    # 100 with the smaller dimensions
    matchX = 100;
    matchY = 200;
    # 50 is used with pixel dimension of 100 µm
    # 25 with the smaller dimensions
    matchPixelMarginX = 25;
    matchPixelMarginY = 50;
    matchDUT = true; # to analyse the DUT

# DUT handling
# the additional DUT in the setup
    lv1Min = 0;
    lv1Max = 31;
    noisyNeighborColRadius = 1;
    noisyNeighborRowRadius = 1;
    maskDeadPixels = true;
    # 200 is used with pixel dimension of 100 µm
    # 100 with the smaller dimensions
    matchX = 100;
    matchY = 200;
    # 50 is used with pixel dimension of 100 µm
```

```
    # 25 with the smaller dimensions
    matchPixelMarginX = 25;
    matchPixelMarginY = 50;
    matchDUT = false;

# FEI4 reference sensor
    lv1Min = 0;
    lv1Max = 15;
    noisyNeighborColRadius = 1;
    noisyNeighborRowRadius = 1;
    maskDeadPixels = true;
    # 500 is used with pixel dimension of 250 µm
    # 100 with the pixel dimension of 50 µm
    matchX = 500;
    matchY = 100;
    # 125 is used with pixel dimension of 250 µm
    # 25 with the pixel dimension of 50 µm
    matchPixelMarginX = 125;
    matchPixelMarginY = 25;
    matchDUT = false;

# preprocessor EuBuildTrack
    chi2 = 50;
```

C Appendix

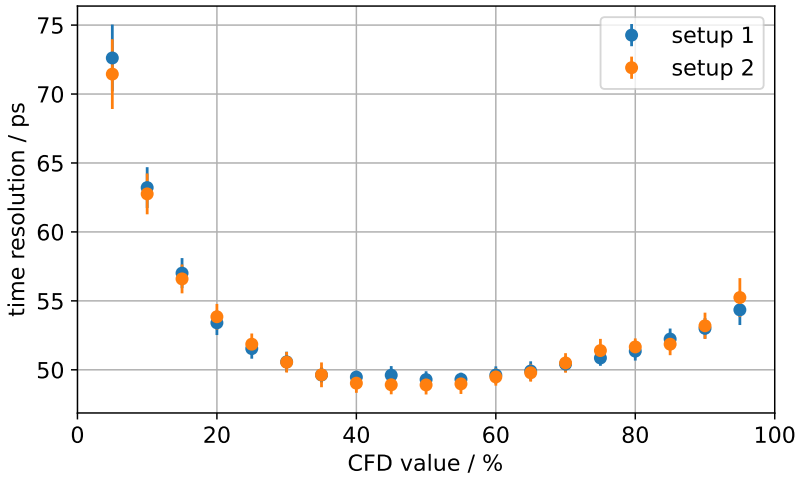

Figure C.1: Time resolution of the LGAD of type HPK1.2. The first setup consists of the two sensors HPK1.2-10F and HPK1.2-8F, the second of the sensors HPK1.2-P3-1N and HPK1.2-8F. The first named sensor is installed closest to the ^{90}Sr source and gives the signal, whereas the second sensor serves as the trigger. In both setups, the bias voltage for all sensors is 200 V. The difference between the sensor HPK1.2-8F and HPK1.2-P3-1N is only the metallisation layout on top of the surface. The sensors HPK1.2-8F and HPK1.2-10F are two sensors with exactly the same layout.

C.1 Conference Contributions

Valerie Hohm: *Test beam results of irradiated silicon sensors with modified pixel layout.* Talk at the "7th Beam Telescopes and Test Beams Workshop", January 2019, CERN, Geneva, Switzerland

Valerie Hohm: *Qualifizierungsmessungen im Rahmen der ATLAS-ITk-Pixel Market-Survey.* Talk at the "DPG-Frühjahrstagung 2019", March 2020, Aachen, Germany

Valerie Hohm: *Overview of beam tests for the ATLAS ITk planar sensor market survey.* Talk at the "8th Beam Telescopes and Test Beams Workshop", January 2020, Tbilisi, Georgia

Valerie Hohm: *Overview of the ATLAS ITk Planar Pixel Sensor Market Survey.* Online talk at the "ATLAS D-Meeting", September 2020, Berlin, Germany

Valerie Hohm: *First measurements with an LGAD equipped prototype of a Time-of-Flight system.* Online talk at the "DPG-Frühjahrstagung 2021", March 2021, Dortmund, Germany

Valerie Hohm: *Entwicklung eines Time-of-Flight-Systems mit Halbleitersensoren zur Anwendung in der Protonentherapie.* Talk at the "52. Herbstschule für Hochenergiephysik Maria Laach", August 2021, Bad Honnef, Germany

Valerie Hohm: *Studies towards a Time-of-Flight system equipped with LGADs.* Online talk at the "DPG-Frühjahrstagung 2022", March 2022, Heidelberg, Germany

C.2 (Co-)Supervised Theses

Lara Bußmann: *Simulation eines Time-of-Flight Systems zur Protonenradiographie.* Bachelor thesis, TU Dortmund University, August 2020

Felix Georg: *Charakterisierung von Silizium-Photomultipliern zur Intensitätsmessung eines Laseraufbaus.* Bachelor thesis, TU Dortmund University, September 2020

Sebastian Pape: *Studies towards a Time-of-Flight system using LGAD sensors.* Master thesis, TU Dortmund University, September 2020

Caroline Bonk: *Entwicklung eines Systems zur Überwachung der Laserintensität in einem Aufbau zur Detektorentwicklung.* Bachelor thesis, TU Dortmund University, August 2021

Christopher Krause: *Track reconstruction for low energy protons using Corryvreckan.* Master thesis, TU Dortmund University, September 2021